Laboratoire
de Génie Civil
et géo-Environnement

Université de Lille

Développement d'organo-argiles performants pour une purification efficace de l'eau

Development of advanced organoclays for efficient water purification

THÈSE

présentée et soutenue publiquement le 13/06/2025

pour obtenir le grade de

DOCTEUR en Mécanique, génie mécanique, génie civil de l'Université de Lille

Par

Lilan ZHANG

Composition du jury

Président	Fabrizio Cleri	Professeur, Université de Lille
Rapporteur	Matt Probert	Professeur, University of York (United Kingdom)
Rapporteur	Siham Kamali-Bernard	Professeur, INSA Rennes
Examinateur	Annan Zhou	Professeur, Royal Melbourne Institute of Technology (Australia)
Examinateur	Wei Yang	Professeur, Hunan University (China)
Direction de thèse	Ali Zaoui	Professeur, Université de Lille

UNIVERSITÉ DE LILLE

École doctorale n°632 : Sciences de l'Ingénierie et des Systèmes – ENGYS

Laboratoire de Génie Civil et Géo-Environnement – LGCgE ULR4515

Bât. ESPRIT, Cité Scientifique, Av. Paul Langevin - 59 655 Villeneuve d'Ascq Cedex

Abstract

By 2050, over half of the global population will be affected by water shortages, leading to serious concerns in human health, economic and ecological sectors. Reuse of wastewater and desalination of seawater are two effective ways to overcome the water supply deficit in the coming decades. Physical adsorption and nanofiltration are ubiquitous and scalable water purification techniques, and advanced sustainable materials for these methods are urgently needed to be investigated to improve efficiency. Clay minerals, particularly montmorillonite (MMT), are promising candidates due to their natural abundance, high cation exchange capacity, and tunable layered structure. However, their limited adsorption efficiency for anionic pollutants and inherent permeability-selectivity trade-offs in membrane applications hinder their broader adoption. This thesis addresses these gaps by developing organic-modified MMT composites, MMT-filled polymeric membranes, and bioinspired MMT membranes for enhanced adsorption and nanofiltration efficiency. Molecular dynamics (MD) simulations are employed to investigate adsorption mechanisms, composite stability, and diffusion dynamics. The main work of this thesis includes:

1) Investigation of interlayer adsorption of surfactant hexadecyltrimethylammonium (HDTMA) modified MMT for cationic methylene blue (MB) dyes.
2) Study of coating mechanisms of biopolymer chitosan (CHT) on MMT and evaluation of the thermal stability of the composite.
3) Examination of surface adsorption of CHT-MMT for MB under various pH conditions;
4) Study of adsorption mechanisms and desorption process of anionic methyl orange (MO) dye on HDTMA-MMT and CHT-MMT;
5) Evaluation of the role of exfoliated MMT nanosheets as fillers in polyamide (PA) membrane;
6) Design of novel bioinspired MMT membranes assisted by carbon nanotubes (CNT)

for adsorptive filtration.

For adsorption properties, MD results show that HDTMA modification enhances MB adsorption of MMT only at $w > 50\%$, as low w ($< 50\%$) causes site-blocking effects. In contrast, CHT-MMT overcomes this limitation and achieves stable multilayer adsorption of MB at high pH with an immobilization efficiency of 80% (158.79 mg/g) owing to its functional amide and hydroxyl groups. For MO adsorption, CHT-MMT utilizes hydrogen bonding, while HDTMA-MMT relies on hydrophobic interactions and surface roughness to stabilize dye molecules. The two organoclays effectively enhance cationic dye adsorption and address the limitations of natural clays in capturing anionic dyes from water.

For membrane applications, MMT nanofillers help to enhance crosslinking efficiency and hydrophilicity of PA membranes, while dopamine modification contributes to a better dispersion of MMT in PA. To further overcome the selectivity-permeability, a bioinspired MMT membrane with a fern-like structure is designed, where CNTs act as an axis to stabilize the interlayer spacing of MMT. This innovative membrane, combining adsorption function and hierarchical structure, creates intralayer channels (< 2 nm) for high water flux (180–300 $L \cdot m^{-2} \cdot h^{-1} \cdot bar^{-1}$) and excellent MB rejection (> 97%).

This research provides fundamental insights into the design of advanced organoclay materials by elucidating molecular-level adsorption and membrane filtration mechanisms, suggesting a new solution for the design of next-generation organoclay-based membranes to address global water scarcity.

Résumé

D'ici 2050, plus de la moitié de la population mondiale sera touchée par des pénuries d'eau, posant de graves problèmes pour la santé humaine, l'économie et l'écologie. La réutilisation des eaux usées et le dessalement de l'eau de mer sont deux solutions efficaces pour pallier le déficit d'approvisionnement en eau dans les décennies à venir. L'adsorption physique et la nanofiltration sont des techniques de purification de l'eau omniprésentes et évolutives, nécessitant urgemment l'étude de matériaux durables avancés pour améliorer leur efficacité. Les minéraux argileux, notamment la montmorillonite (MMT), sont prometteurs grâce à leur abondance naturelle, leur forte capacité d'échange cationique et leur structure en couches ajustable. Cependant, leur faible efficacité d'adsorption des polluants anioniques et les compromis entre perméabilité et sélectivité dans les applications membranaires limitent leur adoption. Cette thèse comble ces lacunes en développant des composites MMT modifiés organiquement, des membranes polymériques remplies de MMT et des membranes bioinspirées pour une adsorption et une nanofiltration optimisées. Des simulations de dynamique moléculaire (MD) explorent les mécanismes d'adsorption, la stabilité des composites et la dynamique de diffusion. Les principaux travaux incluent :

1) Étude de l'adsorption interlaminaire de la MMT modifiée par le surfactant HDTMA pour les colorants cationiques comme le bleu de méthylène (MB).
2) Analyse des mécanismes de revêtement du biopolymère chitosan (CHT) sur la MMT et évaluation de la stabilité thermique du composite.
3) Examen de l'adsorption de surface de CHT-MMT pour le MB sous diverses conditions de pH.
4) Étude des mécanismes d'adsorption et de désorption du colorant anionique orange de méthyle (MO) sur HDTMA-MMT et CHT-MMT.
5) Évaluation du rôle des nanosheets de MMT exfoliées comme charges dans les membranes en polyamide (PA).

6) Conception de membranes bioinspirées assistées par des nanotubes de carbone (CNT) pour une filtration adsorbante.

Les résultats MD montrent que la modification par HDTMA améliore l'adsorption du MB par la MMT uniquement à w > 50 %, les faibles valeurs (w < 50 %) provoquant un blocage des sites. En revanche, CHT-MMT surmonte cette limite, atteignant une adsorption multicouche stable du MB à pH élevé avec une efficacité d'immobilisation de 80 % (158.79 mg/g) grâce à ses groupes amide et hydroxyle. Pour le MO, CHT-MMT exploite les liaisons hydrogène, tandis que HDTMA-MMT repose sur des interactions hydrophobes et la rugosité de surface. Ces organoargiles améliorent l'adsorption des colorants cationiques et pallient les limites des argiles naturelles pour les colorants anioniques.

Pour les membranes, les nanofillers MMT augmentent l'efficacité de réticulation et l'hydrophilie des membranes PA, la modification par dopamine améliorant la dispersion de la MMT. Pour surmonter le compromis perméabilité-sélectivité, une membrane bioinspirée à structure en fougère est conçue, les CNT stabilisant l'espacement interlaminaire de la MMT. Cette membrane innovante, combinant adsorption et structure hiérarchique, crée des canaux intralamellaires (< 2 nm) pour un flux élevé (180–300 $L \cdot m^{-2} \cdot h^{-1} \cdot bar^{-1}$) et un rejet du MB supérieur à 97 %.

Cette recherche offre des insights fondamentaux sur la conception de matériaux organoargileux avancés, élucidant les mécanismes d'adsorption et de filtration membranaire au niveau moléculaire, et propose une solution pour des membranes de nouvelle génération face à la pénurie d'eau mondiale.

Publications

Published journal papers:

Zhang L., et al. Journal of Hazardous Materials, 2023, 442: 130107

Zhang L., et al. Journal of Membrane Science, 2024, 123303.

Zhang L., et al. Journal of Water Process Engineering, 2024, 57: 104651.

Zhang, L. et al. Applied Clay Science, 2024, 261, 107571.

Zhang L., et al. Applied Clay Science, 2023, 243: 107089.

Zhang, L., et al. Applied Clay Science, 2021, 201, 105961.

Zhang L., et al. Journal of Industrial and Engineering Chemistry, 2025

Zhang L., et al. Ultra-selective bioinspired CNT@MMT dual-channel membrane for highly flux water purification. (under review).

Acknowledgements

First and foremost, I would like to express my deepest gratitude to my supervisor, Professor Ali Zaoui, for his invaluable guidance, encouragement, and support throughout my PhD journey at the University of Lille. His profound expertise and insightful feedback have been essential to the completion of this thesis. I appreciate his patience to me and mentorship, which has not only motivated me to strive for excellence in my work but also inspired me to pursue an academic career.

I am also incredibly grateful to Dr. Wassila Sekkal, for the guidance and advice she gave me in every group meeting. Her keen insights and helpful discussions have enriched my research experience and provided me with valuable perspectives. I deeply appreciate her encouragement and willingness to share her knowledge.

I would like to express my sincere thanks to the members of my PhD jury, Prof. Matt Probert, Prof. Siham Kamali-Bernard, Prof. Annan Zhou, Prof. Fabrizio Cleri, and Prof. Wei Yang, for their time and effort in reviewing my thesis, attending my defense, and providing valuable comments that significantly improved my research.

I would also like to acknowledge my colleagues in the LGCgE laboratory, Dr. Yan Zhu, Dr. Zhu Xiaodong, Dr. Wei Pengchang, Mr. Jia Jiwei, Ms. Niu Weiwei, and Mr. Lin Jiyu, for their collaboration and friendship. I am thankful for the countless discussions we had, whether on technical matters or daily life.

I would like to extend my gratitude to my master's supervisor, Dr. Yuanyuan Zheng, for her constant support for my study and life.

Finally, a special thanks goes to my family, my husband Dr. Wan Jianhong, my parents, my sisters, and my parents-in-law. Their unwavering support and love have been my foundation throughout this journey. I am truly fortunate to have such a caring and encouraging family.

Contents

List of Figures

List of Tables

General introduction

Ⅰ. Water pollution and purification techniques

Water pollution caused by organic pollutants and heavy metals has been a critical global issue, significantly impacting human health and environment. Synthetic dyes are among of the most common ubiquitous and persistent pollutants in wastewater, discharged from industries, such as textile (54%), dyeing (21%), paper (10%), tannery (8%), and dye manufacturing (7%) [1]. According to the Council for Textile Recycling, less than 25% of textile waste is reused annually [2]. Dye concentrations in wastewater typically range from 10 to 250 mg/L, with some case exceeding 1000 mg/L [3-5]. To meet international standard, the direct discharge of dyes must be restricted to less than 1 mg/L [6-8]. Dyes are divided into four categories, including direct, reactive, acidic, and basic dyes, and the coexistence of various dyes makes dye removal from water more challenging [9]. Notably, the highest rates of toxicity were observed in the basic and diazo direct dyes [10]. According to charge characteristics, basic dyes are cationic, such as methylene blue (MB), crystal violet, and rhodamine B [11-13], and many azo dyes are anionic, such as methyl orange (MO), Congo red, Eriochrome black T, etc. [14-15]. Effective removal of dye contaminants is essential to safeguarding environmental and public health.

Conventional wastewater treatments include biological, chemical, and physical methods, encompassing a wide range of techniques, including adsorption, filtration, reverse osmosis, ion exchange, chemical precipitation, photodegradation, and solvent extraction [16]. As chemical and biological techniques are generally involved in high energy consumption and technical support [17], physical processes like adsorption and filtration are regarded as scalable approaches for water purification [18]. Adsorption is a surface process whereby an adsorbate is accumulated on the surface of an adsorbent. There is a growing focus on developing eco-friendly and high-efficiency adsorbent materials. In filtration methods, nanofiltration membranes remove organic contaminants and large divalent ions from water by adsorption or size exclusion mechanisms with pore sizes ranging from 1~10 nm [19]. Permeability and selectivity are the two main challenges that need to be addressed in the design of nanofiltration

membranes.

Ⅱ. Environmental applications of clay minerals

Compared to conventional adsorbents like activated carbon, which are costly options for industrial-scale applications and regeneration, non-conventional materials derived from natural, waste, or engineered sources have emerged as promising alternatives. Clay minerals stand out for their excellent adsorption and structural properties in contaminant removal, particularly in adsorption and filtration processes.

Clay minerals such as montmorillonite, muscovite, kaolinite, and quartz minerals, are favorable as adsorbents due to the hydrophilicity nature and permanent negative charges that come from isomorphic substitutions [20-21]. These negative charges are compensated by counterions, making natural clays highly suitable for removing cationic and hydrophilic pollutants through ionic interaction and cation exchange mechanisms. However, natural clays show low affinity to anionic and hydrophobic pollutants, posing a challenge for the adsorption of anionic dyes. In real-world scenarios, where various dyes often coexist, this limitation restricts the applicability of natural clay adsorbents. To address this gap, research has focused on enhancing clay minerals' adsorption capacity and extending their applications to anionic dye removal. A promising method is surface modification with organic modifiers, which aim to transform the negative and hydrophilic clay surfaces to positive and hydrophobic nature via ion exchange [22-23]. Surfactants and polymers are the two primary types of modifiers employed. Surfactants, with long hydrophobic carbon chains, and polymers, with multiple active chemical groups, offer different structural advantages for organic dyes. Given this, the potential of surfactant- and polymer-modified clays for the efficient uptake of organic dyes warrants comprehensive investigation [24-26].

On the other hand, clay minerals can be exfoliated due to their layered structure and weak interlayer forces. Their nanosheets have strong mechanical strength and a hydrophilic nature, which enable them to serve as effective nanofillers of polymeric nanomembranes to regulate their structure and improve their membrane performance.

Polyamide (PA), one of the most widely used commercial membranes, is synthesized via interfacial polymerization (IP) [27]. The incorporation of clay nanosheets into the organic or aqueous phase during the IP process can modulate the synthesis of PA membranes [28-29]. However, the fundamental regulatory mechanisms remain unclear and this is a critical gap that needs to be addressed to fully exploit the potential of clay minerals for the optimization PA membranes.

Furthermore, exfoliated nanosheets of clay minerals can be reconstructed into two-dimensional lamellar membranes (2DLMs). These membranes utilize their nanoconfined interlayer channel to provide pathways for mass-selective transport, which can be regulated by surface charge or interlayer height [30-31]. However, fabricating 2DLMs with controllable nanochannels and ensuring their long-term stability remains a significant challenge. A widely adopted strategy to address these issues is the intercalation of guest species, such as alkali-metal cations, small organic cations, surfactants, polymers, or nanoparticles, to support and bridge adjacent layers after exfoliation [32-33]. However, introducing interlayer modifiers may adversely affect mass transport kinetics within these nanochannels, thus necessitating careful assessment of the introduced species [33-34]. Additionally, reconstructed membranes also face issues such as non-uniform channels caused by reassembly defects, alongside scalability challenges due to the complexity and time demands of the fabrication process. To overcome these obstacles, innovative structures and fabrication methods of clay membranes need to be further developed to achieve high efficiency and sustainability.

Clay minerals hold great promise for environmental applications in water treatment owing to their adsorption capabilities, structural versatility, and potential for modification. However, challenges such as their low affinity for anionic dyes, their unclear role as nanofillers in polymeric membranes, and the instability of 2DLMs, underscore the need for further research and innovation. Advancing the design and application of clay-based materials will contribute significantly to developing sustainable and efficient solutions for water purification.

Ⅲ. Nanoscale simulation research

Molecular dynamics (MD) method provides a deep understanding of atomic interaction and dynamic transport in adsorption and filtration systems. By providing precise atomic-level information, MD makes the adsorption sites and structural changes visualized. It is also crucial to understand the diffusion of water and pollutants across membranes with controlled nanopores and channels. Although existing experimental studies can provide valuable insights into adsorption efficiency from physicochemical characteristics, adsorption kinetics, and isotherms analysis [35-36], however, detailed mechanisms of dye removal by organoclays are still scarcely explored in experimental research. MD has been widely employed to complement experimental findings, aiding in the interpretation of adsorption data by investigating the most stable adsorption configurations and adsorption energies of dye molecules on adsorbent surfaces [15, 37-40]. Research increasingly relies on MD simulations to study the mechanisms of organic modification of clay minerals, as well as the relationships between adsorption and filtration performance and the structural properties of organoclays.

Ⅳ. Thesis organization

In this thesis, we aim to develop versatile organoclays for efficient adsorption and filtration in water purification using MD simulations. First, to address the limited adsorption capacity for anionic pollutants, we focus on the organic modification of montmorillonite (MMT) to enhance its adsorption capacity and efficiency for both cationic methylene blue (MB) and anionic methyl orange (MO) dyes. Two different organic modifiers were studied: the surfactant hexadecyltrimethylammonium bromide (HDTMA-Br) and the biopolymer chitosan (CHT). The adsorption mechanisms, composite stability, and the effects of pH and organic loadings on adsorption performance were evaluated. Then, to overcome permeability-selectivity trade-off in nanomembranes, we focus on developing MMT-filled polymeric membranes and novel bioinspired MMT-based lamellar membranes. We explore the potential of exfoliated MMT nanosheets as nanofillers in PA membranes by studying the regulatory

mechanisms of MMT for PA formation. Most importantly, we propose a non-exfoliated MMT membrane with carbon nanotube (CNT) bonded to clay edges to stabilize interlayer channels and create intralayer channels for mass transport.

The thesis is divided into two parts. Part I is devoted to materials and methodology, and Part II presents the results of MD simulations and the ensuing discussion. The detailed chapter organization is as follows:

The chapter 1 provides an introduction to the structural properties of dyes and clay minerals. It also discusses the adsorption properties and membrane performance of clay minerals in addressing water contamination, emphasizing the role of organic modifications. Then, the chemical structures and properties of surfactant HDTMA and polymer CHT are introduced.

In chapter 2, we introduced the principles of MD method and the simulation settings, including boundary conditions, time integration, system energy and force fields, energy minimization, and ensemble. Analysis methods, such as mean square distribution, radius distribution function (RDF), hydrogen bonding analysis, and non-covalent interaction analysis, are also detailed.

The chapter 3 evaluates the effectiveness of HDTMA-modified MMT for the adsorption of cationic MB dye in comparison with unmodified Na-MMT. Adsorption mechanisms are analyzed in terms of adsorption energy, interlayer configuration, RDF and noncovalent interactions. The effects of interlayer water content and HDTMA loading levels are also discussed.

In chapter 4, the synthesis of CHT-modified MMT composites and their thermal stability in aqueous solutions are investigated. The coating process of CHT at various pH on MMT is studied. The coating mechanisms and the optimum pH condition are discussed. Then, immersion simulations for the dry the CHT-MMT composite are conducted at various temperatures and the adhesion rate of NH_3^+ groups from CHT to the MMT surface is analyzed in detail to evaluate the composite stability.

The chapter 5 focuses on the adsorption mechanisms and capacity of CHT-MMT for cationic MB removal under different pH conditions. Adsorption characteristics and

mechanisms are analyzed. An evaluation method to quantify the immobilization ability of CHT-MMT surfaces for MB adsorption is proposed based on dye diffusion coefficients. Results also compare with that on unmodified MMT surface.

The chapter 6 investigates the effectiveness of both HDTMA- and CHT-modified MMT for the adsorption of cationic MB dye. This chapter employs equilibrium and non-equilibrium MD methods to investigate the adsorption mechanisms and desorption process of MO. The effects of organic loading and surface charge of MMT are evaluated. Bonding analysis confirms the structural stability of two organoclays during adsorption.

The chapter 7 explores exfoliated MMT nanosheets as nanofillers to tailor the structure and performance of PA membranes. The effects of MMT modifications with organophilic dopamine (DA) on PA formation are discussed. The regulatory mechanisms of MMT nanosheets during the IP process are analyzed, highlighting their influence on monomer movement and crosslinking efficiency. Salt separation simulations indicate that the addition of MMT creates more hydrophilic pathways to facilitate water transport.

In chapter 8, we introduce a novel non-exfoliated MMT membrane to address the permeability-selectivity balance. The design inspired by the structure of ferns, utilizes hydroxylated carbon nanotubes (CNT(OH)) bonded to the edges of MMT layers to create dual-selective channels: stable interlayer channels (<1 nm) for ion selectivity and intralayer channels (<2 nm) for organic adsorption and large water permeation. Filtration simulation results are compared with the performance of existing membranes to demonstrate the effectiveness of the proposed MMT membrane.

In the end, a summary of the thesis will be given.

Part I: Material and methodology

Chapter 1

Clay-based materials for dye adsorption and filtration applications

1.1 Organic dyes

Methylene blue (MB) is a cationic dye commonly used for biological staining. It has a blue color, which originates from its phenothiazine structure. The aromatic moiety of MB is planar and its chemistry formula is $C_{16}H_{18}N_3SCl$. The structure is shown in Fig. 1-1(a).

Azo dyes, comprising 60-70% of organic dyes used in textile, food, and leather industries, represent one of the most important categories among synthesis dyes [41-42]. These dyes contain at least one azo bond (−N=N−) connecting aromatic rings [43]. Most azo dyes are anionic due to the presence of sulfonate groups ($-SO_3^-$). Methyl orange (MO), an anionic azo dye, is widely used as a pH indicator. Its chemical formula is $C_{14}H_{14}N_3SO_3Na$, and its structure is illustrated in Fig. 1-1(b).

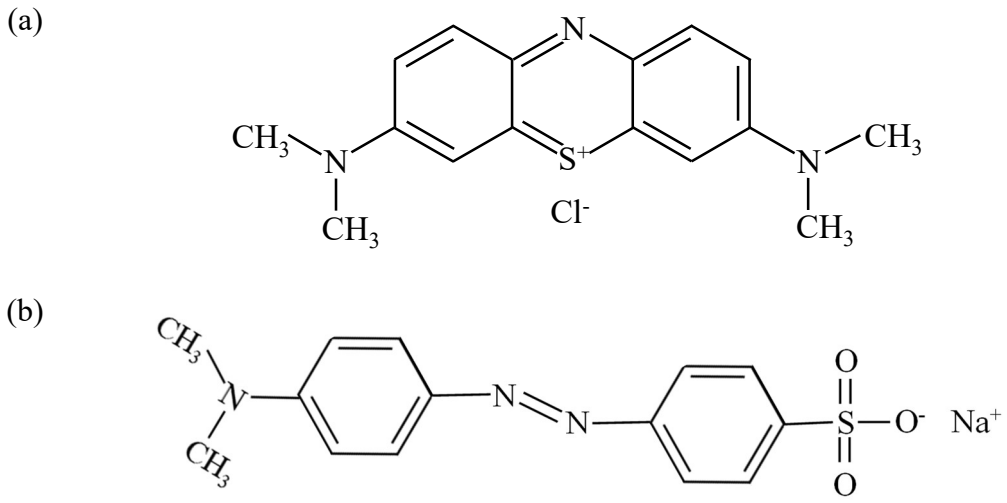

Fig. 1-1 Molecular structures of (a) cationic MB and anionic MO

1.2 Clay minerals

Clay minerals are naturally occurring hydrous aluminosilicates, formed primarily through weathering and hydrothermal alteration of silicate minerals. They are the most abundant materials in the Earth's crust and play critical roles in various environmental, industrial, and geological processes. Clay minerals have layered structures composed of tetrahedral silicate and octahedral aluminate sheets stacked in a 1:1 or 2:1

configuration along the [001] direction. Most 2:1-type clays, such as montmorillonite (MMT) and vermiculite, have two tetrahedral sheets sandwiching one octahedral sheet. These clays swell easily when exposed to water because of the weak interlayer interaction between adjacent layers, which allows water molecules and cations to intercalate. In contrast, 1:1-type clays (e.g. kaolinite) are non-swelling due to the strong hydrogen bonding layers.

Natural clays usually carry negative charges due to isomorphic substitutions, such as the replacement of octahedral Al^{3+} by Mg^{2+} and tetrahedral Si^{4+} by Al^{3+}. This charge imbalance allows clay minerals to attract and exchange cations from their surrounding environment through ionic interaction and cation exchange mechanisms [44]. The adsorption capacity of clay minerals is directly related to its cation exchange capacity (CEC), which is defined as the amount of the exchangeable cations [45]. CEC is expressed as milli-equivalents of charge per 100 grams of clay.

MMT is the major component of bentonite clay, and its high swelling capacity and excellent adsorption properties make it a valuable material in water treatment [46]. The widely studied clay prototype, Wyoming-type Na-montmorillonite (Na-MMT), has the unit cell formula of $Na_{0.75}[Si_{7.75}Al_{0.25}](Al_{3.5}Mg_{0.5})O_{20}(OH)_4$ [47-48], with spatial parameters of a = 5.18 Å, b = 8.98 Å, c = 15.00 Å, $\alpha = \beta = \gamma = 90$ [49]. Its net charge is −0.75 e, and its formula weight is 735.5 g. Thus, the calculated CEC of this Na-MMT is 102 meq/100 g. Fig. 1-2 shows the crystal structure of the 4a × 3b × 1c Na-MMT supercell.

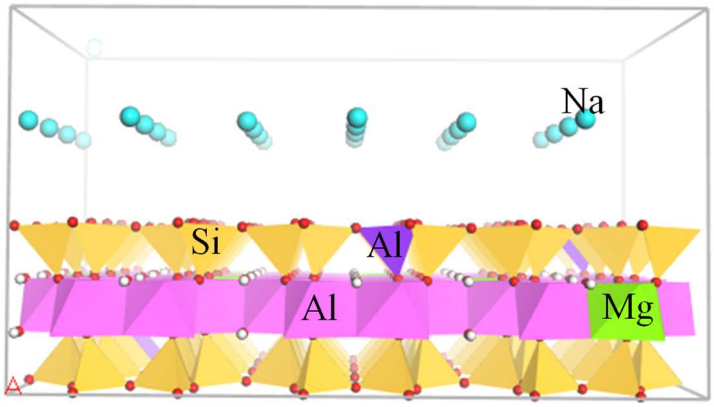

Fig. 1-2 Crystal structure of 4*a* × 3*b* × 1*c* Na-MMT. Note that yellow is for Si tetrahedral; purple is for Al-substituted tetrahedral; pink is for Al octahedral; green is for Mg-substituted octahedral.

1.3 Adsorption properties with organic modification

1.3.1 Organic modification

Raw clay minerals are effective to adsorb cationic and hydrophilic pollutants because of their crystal structure and negative charge. On the other hand, these characteristics also limit their industrial applications in removal of anionic and hydrophobic pollutants from aqueous media. Over the years, numerous strategies have been employed to improve the adsorption efficiency of clay-based adsorbents, including, organic modification [50-51], acid activation [12,52], calcination [53], and magnetization supported by magnetic nanoparticles [14,54]. Among these, organic modification has attracted considerable attention for eliminating organic and inorganic contaminants from wastewater [55]. As shown in Fig. 1-3, the interlayer counter cations (i.e., Na^+, K^+, Ca^{2+}) of clay minerals can be easily exchanged by surfactants or polymers to synthesize organoclays with hydrophobic and organophilic characteristics [56].

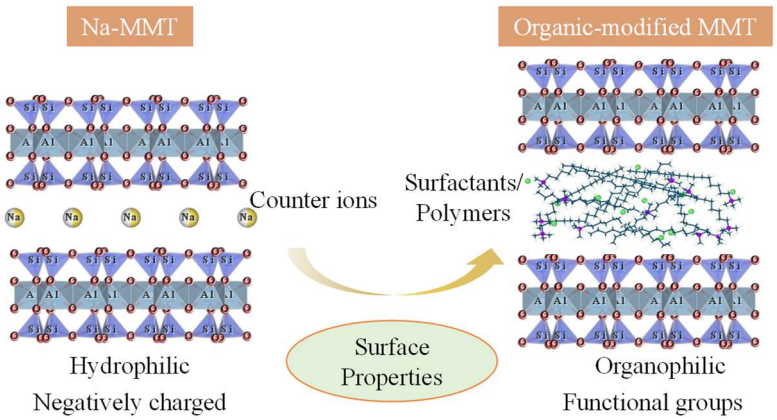

Fig. 1-3 Scheme of organic modification of MMT.

Synthesized organoclays have potential for selective adsorption by utilizing

modifiers with functional groups specifically chosen for their chemical compatibility with targeted pollutants, thereby enhancing binding efficiency between organoclays and pollutants [57]. When selecting organoclays, careful consideration must be given to both the type of organic modifier and its loading amount, as these factors significantly influence adsorption performance [58]. Additionally, environmental conditions such as pH, temperature and dye concentrations can be optimized to further improve the adsorption process.

1.3.2 Surfactants

Significant researchers have focused on the utilization of swelling clays, such as MMT, synthesized with surfactants [59-63]. In many cases, surfactants usually coexist with dyes in textile wastewater and affect the adsorption process [64]. Quaternary ammonium compounds (QACs) are the most widely used cationic surfactants for clay modification. QACs have a hydrophilic head group and a lipophilic alkyl chain with various lengths [65]. For example, one of the long-chain QACs, HDTMA ($C_{19}H_{42}N^+$) consists of a nitrogen-head with a net positive charge of *e* and a non-charged alkyl tail, as shown in Fig. 1-4.

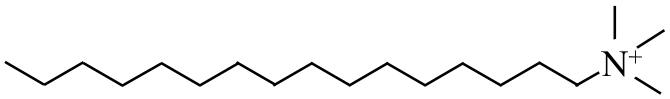

Fig. 1-4 Chemical structure of HDTMA cation ($C_{19}H_{42}N^+$)

Cationic surfactant modifications such as HDTMA, cetyltrimethylammonium bromide (CTAB), and cetylpyridinium bromide hexadecyl are effective for the uptake of anionic dyes [50], [66-67]. Gamoudi et al. [68] demonstrated that the anionic MO adsorption onto $HDPy^+$-modified clay is governed predominantly by hydrophobic interaction and anionic exchange mechanisms.

However, the availability of using cationic surfactant-modified clays for cationic dye adsorption is still questionable. Although anionic surfactants are more suitable for

cationic dyes, their incorporation into the interlayer space of clay minerals is challenging without ion pairs (H_3O^+) or counterions like Na^+ and Ca^{2+} [69]. Consequently, research has primarily focused on cationic surfactants. It is reported that several cationic QACs modified MMT were tested with less efficiency for cationic MB removal in comparison with raw MMT. And the higher QACs concentrations on the sorbent clay is the less the MB dye uptake [70]. This is because the QACs would firstly occupy the cation-exchange sites on the clay surface, thus impeding the adsorption process of MB. Nevertheless, some opposite conclusions were obtained in the recent five years. Experimental studies indicated that montmorillonite modified by HDTMA can be successfully applied for the adsorption of MB [71]. HDTMA-bentonite also showed higher dye removal efficiency in comparison to raw bentonite under all conditions [13]. Another study showed that kaolinite modified with cationic CTAB surfactant can be a highly efficient adsorbent for the treatment of groundwater contaminated with MB dye [72].

To advance the development of organoclays, there is a need to further research into adsorption mechanisms of cationic HDTMA-modified MMT to optimize the adsorption performance for both cationic and anionic dye.

1.3.3 Polymers

Recent research has increasingly focused on biopolymers, which are environmentally friendly, biodegradable, and contain multiple active chemical groups that provide abundant adsorption sites for contaminants [73]. Chitosan (CHT) is one of the most popular is biopolymer. Due to the abundance of functional groups and charge adjustability, CHT exhibits excellent affinity to cationic, anionic, and non-ionic contaminants and has been increasingly explored for new composite adsorbent materials [74-79]. Furthermore, the combination of clays and chitosan can remedy some of their drawbacks as single adsorbents. For example, CHT enhances the adsorption of anionic and non-ionic pollutants in clay-based adsorbents; while clays can increase the mechanical properties of CHT-based adsorbents. Recent studies have highlighted the

potential of CHT-modified clay in eliminating acids, dyes (e.g. reactive orange 16 dye, MB, reactive dye RR222, Congo red), pharmaceutical contaminants, and selenium [80-84]. In particular, CHT-clay composites have been effectively utilized for adsorptive dye removal in various forms, including membranes, membrane nanofillers, adsorbents, beads, and hydrogels [74, 85-91].

CHT is synthesized by the deacetylation and protonation process of chitin [92]. The raw polymer, chitin, is the second most available natural organic resource on Earth, which is commercially extracted from marine crustaceans (shrimps, crabs, squids) [93-94]. An idealized deacetylation degree of 100% means that all acetylamino groups (-$NHCOCH_3$) in original chitin are chemically converted to amino groups (-NH_2), as shown in Fig. 1-5.

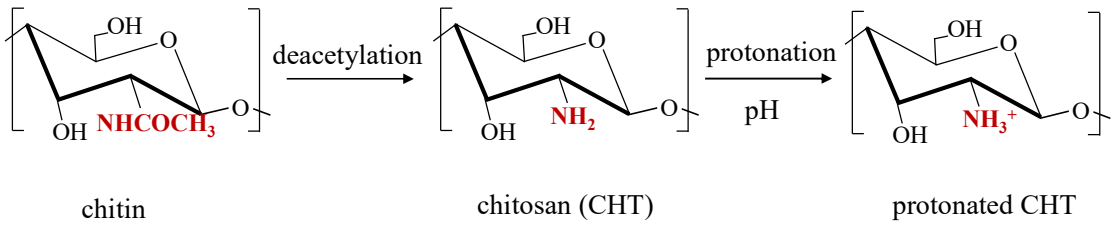

Fig. 1-5 Chemical structure of chitosan.

CHT carries large amounts of hydroxyls (-OH) and amino (-NH_2) groups, and its adsorption behavior is strongly pH-dependent due to the protonation and deprotonation of amino groups. At acidic pH levels, the neutral amino groups (-NH_2) are protonated to positively charged NH_3^+ [9]. The number of protonated sites (-NH_3^+) depends on pH values and the protonation constant pK_a of amine groups which is 6.5 in chitosan, and can be calculated according to (1-1) [95, 96]. Theoretically, at pH values of 3.5, 6.5 and 9.5, the protonation rates of CHT are 100%, 50% and 0, corresponding to strongly acidic, weakly acidic and strongly alkaline conditions, respectively [95-97].

$$N_{\text{protonated}} = \frac{10^{pk_a - pH}}{1+10^{pk_a - pH}} N_{\text{total}} \quad (1\text{-}1)$$

where $N_{\text{protonated}}$ is the number of protonated sites (-NH_3^+) and N_{total} is the total number

of NH_2 groups in CHT.

Further investigation is required to val|date the stability of CHT-MMT composites to ensure long-term efficiency, and to elucidate the interactions between dyes and CHT-MMT composites under varying environmental pH conditions to optimize their adsorption performance.

1.4 Filtration and separation performance with MMT

Nanofiltration (NF) membranes, typically with nanoscale thickness and pore sizes ranging from 1~10 nm, are engineered with unique structural or functional properties to control the movement of particles, molecules, or ions, primarily for filtration and separation processes. For example, these membranes are often designed to reject organic contaminants and large divalent ions from water while allowing smaller monovalent salts, such as NaCl, to pass through [19]. However, achieving high water permeation and precise selectivity remains a significant challenge in the design of nanofiltration membranes. Nanomembranes can be fabricated from various materials, including polymers, ceramics, metals, or composites, and are characterized by their high surface area-to-volume ratio and precise pore structures. Swelling clay minerals, such as MMT, can be readily exfoliated into 1-nm thin nanosheets that can be added into polymeric membranes and reconstructed as 2DLMs, playing a vital role in nanomembrane technology.

1.4.1 Clay-embedded polyamide membranes

The incorporation of nanomaterials has emerged as one of the most straightforward and reliable approaches for modifying the structure and performance of polymeric membranes. Economical aluminosilicates such as nanoclays possess many advantages, including hydrophilicity, excellent adsorption ability, and non-toxicity, that make them a sustainable option for assisting polymeric membrane design. Clay-based nanocomposites have been successfully integrated into commercial polymer

membranes such as polyamide (PA), polyvinylidene fluoride, and polyethersulfone to create novel thin film composite membranes (TFC) [98-100]. Polyamide (PA), featuring a thickness ranging from 50 to 100 nm, is a dominant material in TFC membranes, particularly in deep water processing such as desalination for drinking water production [101-102]. Recent studies have demonstrated the promise of clays as fillers added to the organic/aqueous solution for PA membranes. For example, Dong et al. [103], for the first time, demonstrated the efficacy of clay nanosheets like montmorillonite (MMT) and layered double hydroxide (LDH) as filler materials, effectively tailoring surface properties and enhancing fouling resistance and water flux of PA-based membranes. Additionally, Zhao et al. [104] reported a novel Zn–Al LDH modified PA TFC membranes with denser, leaf-like morphologies and increased surface hydrophilicity.

These clay components improve membrane microstructures and enhance permeability, fouling resistance, and separation performance [105-108]. However, the potential of nanoclays as PA fillers is underexplored compared to carbon-based inorganic materials. The reason could be attributed to the poor dispersion of unexfoliated MMT in organic solutions. It is reported that they are highly likely to form aggregates on the PA membrane surface, leading to a negative impact on the selectivity properties [109]. To address dispersion problem, Tian et al. found for the first time that exfoliated MMT is well dispersed in aqueous solutions and is compatible with MPD monomers, which is beneficial for PA formation [110]. Their findings demonstrate that the incorporation of exfoliated MMT effectively overcomes the classical trade-off between membrane permeability and selectivity. Another way to improve the dispersity of MMT in polymeric matrix is through organic modification. Surfactant-modified MMT, for instance, has been reported to exhibit favorable dispersion in the TMC solution, contributing to higher water flux and antifouling properties when embedded in the PA layer [111]. Moreover, the polydopamine (PDA) coating endows zeolitic imidazolate framework-8 nanoparticles with good dispersibility in water and hydrochloric acid resistance, preventing them from agglomerating and degrading the crystalline structure in the selective layer, thereby increasing the permeability and fouling resistance of the

polymeric membrane [112-113].

While the incorporation of nanomaterials is extensively utilized to enhance polymeric membrane performance, the underlying mechanisms driving these enhancements in the PA layer remain insufficiently understood. Furthermore, the potential of aluminosilicates, particularly MMT, remains underutilized. To fully unlock their potential as cost-effective and sustainable fillers, future research should prioritize the development of effective dispersion strategies for MMT in PA, including exfoliation and organic modification.

1.4.2 Lamellar clay membranes

Lamellar membranes, composed of parallel stacked layers of nanometer-thick sheets with inter- and intra-lamellar nanochannels, have emerged as promising tools for advanced filtration and separation technologies. Over the past decade, various new lamellar membranes, including MXene, MoS_2, and boron nitride, have been developed [114-119]. Their adjustable channel sizes and chemical properties enable precise rejection or degradation of a wide range of contaminants, including organic pollutants, heavy metals, and salts, making them more versatile and effective than traditional nanoporous membranes. However, many 2D nanomaterials are still costly to produce, so there is a need to develop more economical 2D membranes using less expensive raw materials. Additionally, to minimize toxicity and prevent recontamination, environmentally friendly materials such as clays and layered double hydroxides should be prioritized [120].

Lamellar clay minerals present significant advantages owing to their natural abundance, cost-effectiveness, and chemical stability. Their nanoscale interlayer space provides pathways for mass-selective transport, which can be regulated by the surface charge or channel height [30-31]. Conventional top-down fabrication methods for clay-based membranes involve exfoliating layered clays into single nanosheets, which are then reassembled into orderly lamellar membranes. However, a critical challenge in this process lies in forming controllable nanochannels and maintaining their long-term stability. One prevalent solution is intercalating guest species, such as surfactants and

polymers, to control interlayer spacing and mitigate swelling damage [32-33]. On the other hand, introducing interlayer modifiers may adversely affect mass transport kinetics within these nanochannels, thus necessitating careful assessment of the introduced species [33-34].

Therefore, research should focus on developing green fabrication methods for lamellar clay membranes to achieve high efficiency and sustainability in both structure and performance.

Chapter 2

Molecular dynamic simulation method

2.1 Introduction of molecular dynamic method

Molecular Dynamics (MD) is a numerical simulation method used to study the behavior of materials at the molecular or atomic level. MD has a wide range of applications in the fields of physics, chemistry, biology and materials. In physics, MD is used to study phase transitions, expansion, and transport process. In chemistry, it helps explore reaction mechanisms, such as catalysis and polymer-crosslinking reactions. In biology, MD is of great significance for life sciences, drug design, and protein research. In materials science, MD is extensively applied to study geological materials (e.g., clay minerals), nanomaterials, structural materials (e.g., cement), semiconductors and functional materials. MD can dynamically visualize molecular behaviors on a computer screen, allowing an intuitive understanding of the evolution of the system under specific conditions. Regarding adsorption and filtration properties of clay-based materials, it is important to explore intermolecular interactions through MD simulations.

The fundamental principle of MD is based on Newtonian classical mechanics to compute the trajectories of atoms and molecules in phase space. The method relies on the assumption that atoms are inert spheres and atomic interactions depend on solely by their interaction distances. Quantum effects are often neglected unless quantum MD methods are employed. Accurate interaction between atoms is premise for success MD simulations, and such interaction are defined as force fields. Given an initial atomic configuration, it is able to solve the equations of motion under potential interactions and external constrains to simulate the trajectory of the system over time. By extracting samples from the evolutionary trajectory and calculating the configuration integral of the system, the equilibrium thermodynamic and transport properties can be determined by means of statistical analysis to predict macroscopic properties and behaviors.

The computational process is outlined below and the primary steps of MD simulations are illustrated in Fig. 2-1:

1) Define the representative system and boundary conditions;

2) Choose an appropriate potential energy function to describe the interactions between particles;

3) Set the initial positions and velocities of the particles in the system. For clay minerals, the spatial coordinates of atoms can be obtained through X-ray diffraction experiments;

4) Implement the simulation algorithm to compute interparticle forces, as well as the velocities and positions of each particle over time. The forces acting on each particle are derived from the gradient of the potential energy with respect to atomic coordinates. Given the known mass of each atom, Newton's Second Law is applied to compute the acceleration of each atom. By selecting an appropriate time step Δt (typically 1 fs for hydrogen-containing systems), the acceleration is integrated to obtain atomic velocities, which are further integrated to yield atomic displacements and determine the new configuration of the system. The potential energy of this new configuration is recalculated, and the process is iteratively repeated until the desired simulation duration is achieved.

5) Once the system reaches equilibrium, statistical methods are employed to derive macroscopic parameters and transport properties.

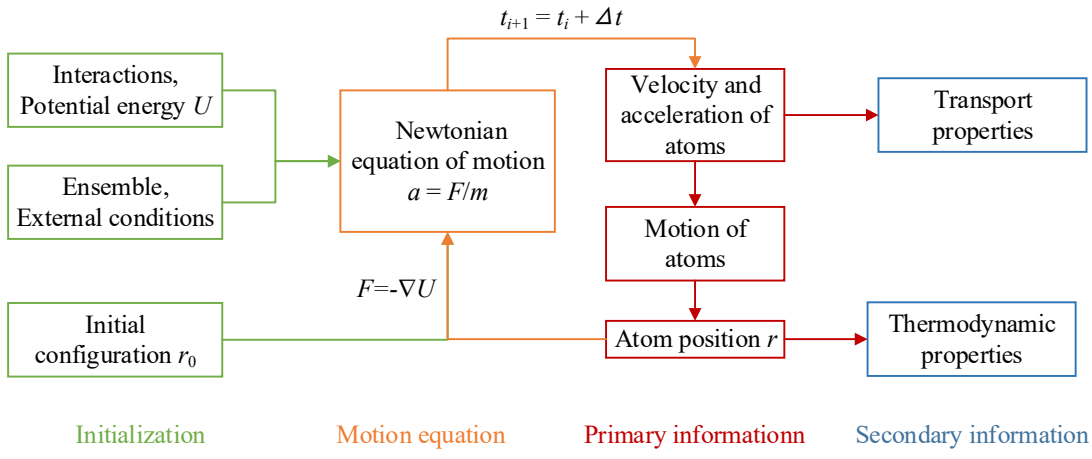

Fig. 2-1 MD flow-chart. F represents the force acting on an atom, m is mass of atom, and a is its acceleration.

2.2 Modelling and simulation settings

2.2.1 Atomic systems and boundary conditions

In MD method, modern computational capabilities can handle atomic systems containing thousands to millions of atoms. Typically, a representative unit of material with a finite simulation box is used for simulations. However, small systems differ from the behaviors of macroscopic materials due to size and surface effects. To mimic the behavior of infinite or bulk systems within a finite system, boundary conditions are applied.

Periodic boundary conditions (PBCs) are widely used to approximate an infinite system by replicating the simulation box in specific directions. The principle works as follows: when a particle moves across the boundary of the simulation box, its periodic image enters through the opposite boundary to replace it. Taking a two-dimensional system as an example, this concept is illustrated in Fig. 2-2. PBCs help eliminate boundary effects, ensure a constant number of atoms in the system, and enable the system to behave like bulk material. Different types of PBCs can be employed depending on the dimensionality of the system. For example, three-dimensional PBCs can be used to simulate bulk materials and two-dimensional PBCs are suitable for surfaces and thin film material. By carefully selecting representative cells and boundary conditions, macroscopic phenomena can be predicted from nanoscale simulations. Atoms interact with their neighboring atoms within a specified cut-off distance (r). To avoid interactions with their periodic images, r must be set to no more than half the minimum dimension (d) of the simulation box. In particular, when studying surface problems, it is common to use three-dimensional PBCs along with a sufficient vacuum region ($> r$) in the simulation box in the direction perpendicular to the surface to approximately simulate a non-periodic condition in that direction.

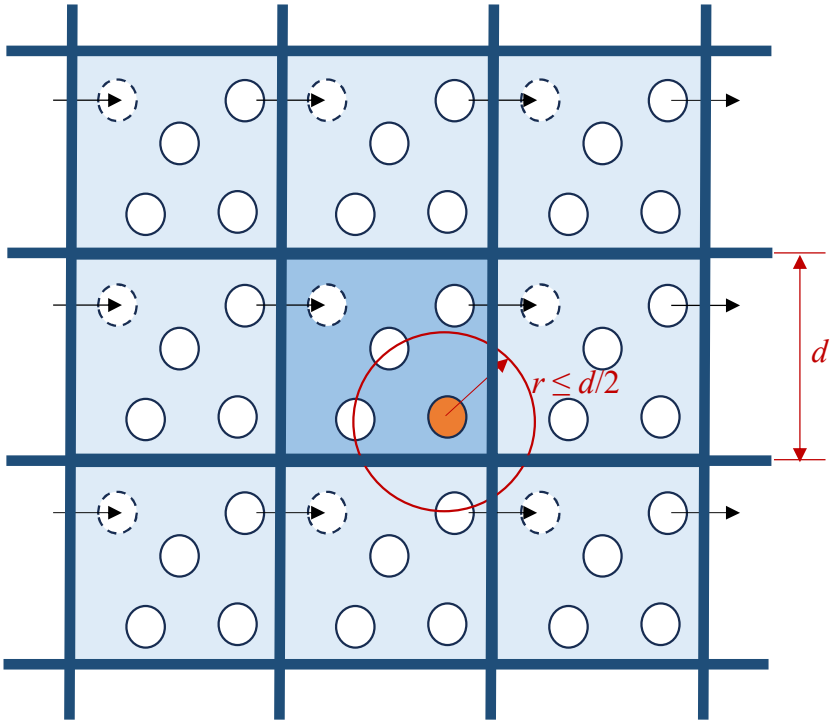

Fig. 2-2 Periodic images of a central cell. Dashed circles represent periodic images of the atom. The red circle defined by the cut-off distance shows the neighboring atoms that interact with the central orange atom.

2.2.2 Time integration

The time step in an MD simulation determines the duration between successive calculations of particle positions and velocities. Typically, time steps on the order of 1–2 fs are used, as they are small enough to accurately capture the fast atomic vibrations. An appropriate timestep Δt is crucial for accuracy and efficiency. To update atomic positions and velocities over time, time integration algorithms, such as the Verlet, Leap-Frog, and Velocity Verlet algorithms are used to solve the equations of motion iteratively. The Verlet integration algorithm approximates the new atomic position at $t + \Delta t$ based on the current and previous positions:

$$r_i(t+\Delta t) = r_i(t) + \frac{\Delta t}{1!}\cdot \dot{r}_i(t) + \frac{\Delta t^2}{2!}\cdot \ddot{r}_i(t) + \frac{\Delta t^3}{3!}\cdot \dddot{r}_i(t) + O(\Delta t^4) \tag{2-1}$$

$$r_i(t-\Delta t) = r_i(t) - \frac{\Delta t}{1!}\cdot \dot{r}_i(t) + \frac{\Delta t^2}{2!}\cdot \ddot{r}_i(t) - \frac{\Delta t^3}{3!}\cdot \dddot{r}_i(t) + O(\Delta t^4) \tag{2-2}$$

where $r_i(t)$ is the position of atoms at time t, $\dot{r}_i(t)$ is the velocity, $\ddot{r}_i(t)$ is the acceleration. Adding these two expansions gives

$$r_i(t+\Delta t) = 2r_i(t) - r_i(t-\Delta t) + \Delta t^2 \cdot \frac{F_i}{m_i} \tag{2-3}$$

However, because the Verlet algorithm does not compute velocity directly, atomic velocities are estimated via finite difference. An improved version of the Verlet method, the Velocity Verlet algorithm, updates both positions and velocities simultaneously:

$$r_i(t+2\Delta t) = r_i(t+\Delta t) + \frac{\Delta t}{1!}\cdot \dot{r}_i(t+\Delta t) + \frac{\Delta t^2}{2!}\cdot \ddot{r}_i(t+\Delta t) + O(\Delta t^3) \tag{2-4}$$

Combining (2-1) and (2-4), then we get:

$$r_i(t+2\Delta t) = r_i(t+\Delta t) + \frac{\Delta t}{1!}\cdot (\dot{r}_i(t) + \dot{r}_i(t+\Delta t)) + \frac{\Delta t^2}{2!}\cdot (\ddot{r}_i(t) + \ddot{r}_i(t+\Delta t)) + O(\Delta t^3) \tag{2-5}$$

We also have:

$$v_i(t) = \frac{r_i(t+2\Delta t) - r_i(t)}{2\Delta t} + O(\Delta t^2) \tag{2-6}$$

Combining (2-5) and (2-6), then we get:

$$v_i(t+\Delta t) = v_i(t) + \frac{F_i(t+\Delta t) + F_i(t)}{2m}\cdot \Delta t \tag{2-7}$$

The Leap-Frog method updates velocity at half-integer time steps:

$$v_i(t+\frac{\Delta t}{2}) = v_i(t-\frac{\Delta t}{2}) + \frac{F_i(t)}{m}\cdot \Delta t \tag{2-8}$$

$$r_i(t+\Delta t) = r_i(t) + v_i(t+\frac{\Delta t}{2})\cdot \Delta t \tag{2-9}$$

Finally, velocity at $t+\Delta t$ is obtained as:

$$v_i(t+\Delta t) = v_i(t+\frac{\Delta t}{2}) + \frac{F_i(t+\Delta t)}{2m}\cdot \Delta t \tag{2-10}$$

In this thesis, all simulations are performed using the Velocity Verlet algorithm to solve the equation of motion.

2.2.3 System energy and force fields

The total energy in a MD system consists of kinetic energy and potential energy. The kinetic energy (*Ke*) of the system is associated with the motion of the atoms and molecules. It is given by:

$$Ke = \frac{1}{2}\sum_i m_i v_i^2 \tag{2-11}$$

The potential energy of the system arises from the interactions between atoms. A force field is a mathematical description of the position-dependent potential energy of atomic systems. The total potential of the system is described by both bonded and non-bonded interactions:

$$U_{\text{total}} = U_{\text{bonded}} + U_{\text{non-bonded}} \tag{2-12}$$

Bonded interactions refer to the energy associated with the relative positions of atoms that are covalently bonded. These interactions are usually described by four terms: bond stretching, angle bending, dihedral angles, and out-of-plane terms:

$$U_{\text{bonded}} = U_{\text{bond stretch}} + U_{\text{angle bend}} + E_{\text{Dihedral}} + E_{\text{out-of-plane}} \tag{2-13}$$

Non-bonded interactions include short-range van der Waals forces (VDW), representing weak interactions between atoms or molecules, and long-range Coulombic electrostatic forces, describing the interactions between charged particles. It is worth noting that the interaction between a pair of bonded atoms is primarily specified by the bonded potentials, meaning that the non-bonded interaction between these atoms should be excluded or reduced.

$$U_{\text{non-bonded}} = U_{\text{VDW}} + U_{\text{coul}} \tag{2-14}$$

Commonly used empirical force fields include CLAYFF, CVFF, COMPASS, PCFF, AMBER, CHARMM, GROMOS, and OPLS. These are all no-reactive force fields, assuming that chemical bonds in the system are fixed. Consequently, these traditional force fields cannot describe bond breaking and formation during simulations. Intermolecular interactions are controlled by non-bonded interactions. The choice of force fields for simulation systems is critical in achieving accurate results.

2.2.3.1 Force field for phyllosilicates

CLAYFF [121] is specifically designed to model the structure and dynamics of hydrated phyllosilicates. In CLAYFF, most interatomic interactions are treated as nonbonded, which includes 12-6 Lennard-Jones (L-J) potentials for VDW interactions and electrostatic potentials for interactions between charged particles.

$$U_{\mathrm{VDW}} = 4\varepsilon_{ij}\left[\left(\sigma_{ij}/r_{ij}\right)^{12} - \left(\sigma_{ij}/r_{ij}\right)^{6}\right] \tag{2-15}$$

where r_{ij} is the distance between atom i and j, ε_{ij} is the depth of the potential well and σ_{ij} is the distance at which the inter-particle potential is zero. The L-J parameters ε_{ij} and σ_{ij} between atom i and j are calculated by the Lorentz-Berthelot's mixing rule [122], based on the self-interaction parameters of atoms i (σ_i, ε_i) and j (σ_j, εj):

$$\sigma_{ij} = \frac{\sigma_i + \sigma_j}{2}, \quad \varepsilon_{ij} = \sqrt{\varepsilon_i \varepsilon_j} \tag{2-16}$$

The electrostatic potential is given by:

$$U_{\mathrm{coul}} = \frac{e^2 q_i q_j}{4\varepsilon_0 r_{ij}} \tag{2-17}$$

where q_i and q_j are the charges of atom i and j respectively; ε_0 is the dielectric constant.

Bond stretching and angle bending terms are evaluated only for hydroxyl groups, described by simple harmonic terms:

$$U_{\mathrm{bond}} = k_1\left(r_{ij} - r_0\right)^2 \tag{2-18}$$

$$U_{\mathrm{angle}} = k_2\left(\theta_{ijk} - \theta_0\right)^2 \tag{2-19}$$

where k_1 and k_2 is a force constant, r_0 represents the equilibrium oxygen−hydrogen bond length; θ_{ijk} is the bond angle for the metal−oxygen−hydrogen and hydrogen−oxygen−hydrogen in water; θ_0 represents the equilibrium bond angle.

2.2.3.2 Force fields for organic-clay composite systems

CVFF [123] (Consistent Valence Force-Field) is focused on simulating organic,

polymeric, and biopolymeric systems. CVFF and CLAYFF belong to Class I force fields, which assume that bonded and non-bonded interactions can be described using simple analytical functions, typically harmonic or Lennard-Jones potentials. CVFF and CLAYFF are fully compatible because of the same 12-6 L-J potential expressions and harmonic bond and angle terms. As a result, their combination is one of the most widely used hybrid force fields for modeling organic-clay composite systems, successfully describing intermolecular interactions between clay minerals, water, and organic molecules.

PCFF (Polymer-Consistent Force Field) and COMPASS (Condensed-phase Optimized Molecular Potentials for Atomic Simulation Studies) force field [124] are extensively utilized for complex polymeric systems, such as CHT [125-126]. They may cover polymer functional groups that are not presently available in many Class I force fields. However, PCFF and COMPASS are Class II force fields, which incorporate cross-term interactions (e.g., bond-bond, bond-angle, and angle-torsion coupling). Also, they use 9-6 L-J potential expressions, making them difficult to be compatible with CLAYFF.

To address this issue, the INTERFACE force field (IFF) was developed as the first uniform force field for inorganic and polymeric hybrid systems. IFF derives parameters for biomolecules, polymers, and solvents from their respective parent force fields (CHARMM, PCFF, CVFF) [127]. IFF-PCFF has been applied to simulate various clay minerals, and its accuracy has been extensively tested in terms of cell parameters, density, surface tension, etc. [127-130]. The VDW energy expression is based on the PCFF using a 9-6 potential. The total potential energy is calculated as follows:

$$U = \sum_{ij,\text{bond}} \frac{1}{2} K_{r,ij} \left(r_{ij} - r_0 \right)^2 + \sum_{ijk,\text{angle}} \frac{1}{2} K_{\theta,ijk} \left(\theta_{ijk} - \theta_0 \right)^2 + E_{\text{Dihedral}} + E_{\text{out-of-plane}}$$
$$+ \frac{1}{4\pi\varepsilon_0\varepsilon_r} \sum_{\substack{ij,\text{coul} \\ (1,2 \text{ and } 1,3 \text{ excl})}} \frac{q_i q_j}{r_{ij}} + \sum_{\substack{ij,\text{VDW} \\ (1,2 \text{ and } 1,3 \text{ excl})}} \varepsilon_{ij} \left[2 \left(\frac{\sigma_{ij}}{r_{ij}} \right)^9 - 3 \left(\frac{\sigma_{ij}}{r_{ij}} \right)^6 \right] \quad (2\text{-}20)$$

where 1,2 pair of atoms means that pair atom is directly bonded to each other, and 1,3 pair of atoms means that pair atom is bonded via one intermediate bond. In 9-6 L-J term,

ε_{ij} and σ_{ij} are calculated with a sixth power combination rule:

$$\sigma_{ij} = \left(\frac{\sigma^6{}_i + \sigma^6{}_j}{2} \right)^{\frac{1}{6}}, \quad \varepsilon_{ij} = \frac{2\sqrt{\varepsilon_i \varepsilon_j}\,\sigma^3{}_i \sigma^3{}_i}{\sigma^6{}_i + \sigma^6{}_j} \tag{2-21}$$

2.2.3.3 Reactive force field

ReaxFF is a reactive force field designed to model chemical reactions, including bond breaking and formation. It has been developed to model interatomic interactions in a wide range system, including clay minerals, silica, and biomolecules [131-136]. ReaxFF is highly flexible to be applied in organic-clay systems to investigate polymerization and degradation of organic molecules, or reactive process on the clay surfaces. ReaxFF is initially proposed by van Duin et al. [137]. It accounts for both bonded interactions, using bond-order dependent potentials, and non-bonded interactions, such as VDW and Coulombic energies between atoms. One key difference from non-reactive force fields is the use of bond orders to dynamically calculate bond energies. In empirical force fields, bonds are static and predefined so that bond orders are discrete. ReaxFF does not rely on predefined bonds and instead calculates bond orders dynamically as a continuous function of interatomic distance. Therefore, ReaxFF allows it to model reaction mechanisms and structural changes in real time. Additionally, ReaxFF employs a charge equilibration method to compute partial atomic charges at each iteration, ensuring accurate treatment of electrostatic interactions. The total potential of a system is described by a sum of contributions:

$$U_{\text{total}} = U_{\text{bond}} + U_{\text{over}} + U_{\text{angle}} + U_{\text{torsion}} + U_{\text{VDW}} + U_{\text{coulomb}} + U_{\text{specific}} \tag{2-22}$$

where U_{bond} is the bond formation energy, as a function of instance distance between atoms;

U_{over} is the energy penalty preventing the over-coordination stability of atoms, maintaining realistic atomic coordination numbers;

U_{angle} is the angular associated with the three-body valence angle;

U_{torsion} is torsional energies the four-body torsional angle strains;

U_{VDW} is the van der Waals energy;

$U_{coulomb}$ is the Coulombic contribution between partially charged atoms;
$U_{specific}$ represents the specific contributions such as lone-pair interactions, hydrogen bonding, and conjugation effects.

2.2.4 Energy minimization

Before starting an MD simulation, it is often necessary to perform energy minimization for initial systems that may have high potential energy. This process aims to adjust the positions of atoms in the system to eliminate any unfavorable interactions or high-energy configurations, leading to a more stable starting structure. The goal is to bring the system to a local potential energy minimum, where the forces acting on atoms are nearly zero. Common algorithms for energy minimization include steepest descent and conjugate gradient methods [138]. The steepest descent method moves atoms along the direction of the steepest decrease in potential energy. It is simple and robust but converges slowly near the minimum. The conjugate gradient method is more efficient for systems that are near equilibrium, as it determines the new direction as a linear combination of the previous direction and the current gradient.

2.2.5 Ensemble

An ensemble in MD refers to a statistical collection of system states that are used to model the thermodynamic properties of a system under various conditions. Without any constraints to a MD system, a microcanonical ensemble (NVE) is generated. In this ensemble, the number of particles (N), volume (V), and system energy (E) are constant, meaning there is no exchange of energy or particles with the environment, making it ideal for studying isolated systems.

To create a desired temperature environment, the MD system is coupled to a heat bath (thermostat), allowing energy exchange and maintaining a constant temperature. The most popular thermostats include Nosé-Hoover [139], Langevin [140], and Berendsen [141]thermostats. The canonical ensemble (NVT), with constant N, V, and temperature (T), is typically implemented using the Nosé–Hoover thermostat. This thermostat

introduces a dynamic friction variable ξ derived from an extended Hamiltonian formalism, which modulates the particle velocities based on deviations from the target kinetic energy. The equations of motion are extended accordingly to ensure proper canonical sampling.

$$\frac{d\mathbf{r}_i}{dt} = \mathbf{v}_i \tag{2-23}$$

$$\frac{d\mathbf{v}_i}{dt} = \frac{\mathbf{F}_i}{m} - \xi \mathbf{v}_i \tag{2-24}$$

$$\frac{d\xi}{dt} = \frac{1}{Q}\left(\sum_i m_{\mathrm{i}} \frac{v^2{}_i}{2} - \frac{3N+1}{2} k_B T_{\mathrm{target}} \right) \tag{2-25}$$

Where ξ is a thermostat friction coefficient. Q is the eligible damping parameter. $\sum_i m_{\mathrm{i}} \frac{v^2{}_i}{2}$ is the kinetic energy of the system at T_i. $\frac{3N+1}{2} k_B T_{\mathrm{target}}$ is the average kinetic energy at the target temperature, where 3N+1 is used instead of 3N because of the added degree of freedom ξ.

For simulations at constant pressure, the system must be allowed to exchange volume with its surroundings. This is achieved using a barostat, which couples the simulation box to a pressure reservoir. The isothermal-isobaric ensemble (NPT) maintain constant *N*, *T*, and pressure (*P*). It is useful to simulate systems at constant environmental conditions like room temperature and atmospheric pressure, as well as to study phase transitions. Barostats can be implemented in different forms depending on whether the simulation box shape is fixed or allowed to deform. The fixed-shape barostats (e.g., Andersen–Hoover) scale the box isotropically or anisotropically while preserving its overall shape. The Andersen method introduces a fictitious volume degree of freedom, governed by a "piston" mass; in the Andersen–Hoover variant, this is coupled to a Nosé–Hoover thermostat for simultaneous control of pressure and temperature. In contrast, variable-shape barostats (e.g., Parrinello–Rahman) allow the box to change both shape and size, enabling independent control of shear and normal stresses. This makes them suitable for simulating anisotropic materials and structural

transitions. In this work, the NPT ensemble is used with an Andersen–Hoover barostat coupled to a Nosé–Hoover thermostat to maintain constant temperature and pressure.

2.3 Analysis methods

MD simulations generate the trajectories of all atoms in the system over time. Analysis of these trajectories provides insight into the structural, dynamic, and thermodynamic properties of the system. Some common analysis methods are introduced below.

2.3.1 Mean squared displacement and diffusion coefficients

Mean squared displacement (MSD) is used to study the dynamic characteristics of atoms or molecules within a system. It is a measure of the average squared distance that a particle moves over time:

$$MSD(t) = \frac{1}{N}\sum_{i=1}^{N}\left(\vec{r}_i(t) - \vec{r}_i(0)\right)^2 \tag{2-26}$$

where N is the number of particles to be averaged, vector $\vec{r}_i(t)$ denotes the position of particle i at time t and $\vec{r}_i(0)$ for initial position [142]. For diffusive systems like liquids, the MSD increases linearly with time at long time scales. When particles are bound or adsorbed, the MSD tends to plateau, indicating limited particle motion.

Diffusion coefficient **(**D**)** can help to quantify the mobility of particles. A higher diffusion coefficient indicates faster diffusion. D is extracted from the slope of the MSD versus time at long times, based on the Einstein equation [143]:

$$D = \frac{MSD(t)}{2dt} \tag{2-27}$$

where $d = 3$ for three-dimensional system and $d = 2$ for two-dimensional system.

2.3.2 Radial distribution function and coordination number

The radial distribution function (RDF), also known as $g(r)$, is a common structural indicator to reflect interaction distance between particles and structural arrangement of atoms or molecules [44], [144]. It is defined as the normalized density of a particle presented around the target particle at a distance r, In a solid, RDF exhibits sharper, well-defined peaks due to the regular arrangement of atoms and for a liquid or gas, $g(r)$ is close to 1 for all r, indicating no structured arrangement. Mathematically, RDF is given by:

$$g(r)_{ij} = \frac{n(r)_j}{p_j V} \approx \frac{n_j(r)}{4\pi p_j r^2 \Delta r} \tag{2-28}$$

where $n(r)_j$ is the average number of atom type j around atom type i found in a spherical shell of thickness Δr, at distance r from an atom of type i. ρ_j is the number density of atom type j, and r is the distance between atom type i and j.

Coordination number (CN) determines the number of surrounding particles of the target particle by integrating the $g(r)$ up to a specific distance r, which is typically chosen as the distance of the first minimum in $g(r)$.

$$CN_{ij} = 4\pi p_j \int_0^{r_{\text{cutoff}}} g(r) r^2 dr \tag{2-29}$$

where r_{cutoff} is the distance of the first minimum in $g(r)$.

2.3.3 Noncovalent interaction

Noncovalent interaction (NCI) analysis is employed to visualize and quantify weak, noncovalent interactions in molecular systems. These interactions include VDW forces, hydrogen bonds, π–π stacking, and steric repulsion. The NCI approach relies on the concept that noncovalent interactions can be characterized by the electron density and its first derivative, known as reduced density gradient (RGD). The RDG function is a dimensionless quantity that describes the deviation from a homogeneous electron distribution and is calculated as follows [145]:

$$RDG(r) = \frac{1}{2(3\pi)^{1/3}} \frac{|\nabla\rho(r)|}{\rho(r)^{4/3}} \tag{2-30}$$

where $\rho(r)$ is the electron density at position r. $\nabla\rho(r)$ is the gradient of the electron density. Low values of ρ and $RDG(r)$ indicate regions of noncovalent interactions.

sign(λ_2)ρ can be used to determine the nature of the interactions, where λ_2 is the sign of the second eigenvalue of the Hessian matrix of the electron density ($\nabla^2\rho$). $\lambda_2 < 0$ means attractive interactions (e.g., hydrogen bonds, π–π stacking), $\lambda_2 > 0$ means repulsive interactions (steric repulsion), and $\lambda_2 = 0$ corresponds to weak VDW forces. The $RDG(r)$ against sign(λ_2)ρ scatter plot, combined with isosurface visualizations of the spatial distribution of noncovalent interactions, help identify interaction regions and distinguish between attractive, repulsive, and weak dispersive forces in molecular systems.

Part II: Results

Chapter 3

Interlayer adsorption of cationic MB dye on HDTMA-modified MMT

3.1 Introduction

The effectiveness of using cationic surfactant-modified clay for cationic dye adsorption is still questionable. It is reported that several cationic QACs modified MMT were tested with less efficiency for MB removal in comparison with raw MMT. And the higher QACs concentrations on the sorbent clay is the less the MB dye uptake [70]. This is because the QACs would firstly occupy the cation-exchange sites on the clay surface, thus impeding the adsorption process of MB. Nevertheless, some opposite conclusions were obtained in the recent five years. Experimental studies indicated that MMT modified by HDTMA can be successfully applied for the adsorption of MB [71]. HDTMA-bentonite also showed higher dye removal efficiency in comparison to raw bentonite under all conditions [13]. Another study showed that kaolinite modified with cationic CTAB surfactant can be a highly efficient adsorbent for the treatment of groundwater contaminated with MB dye [72].

Despite some simulation research have been done on investigating the microstructure of QACs surfactant-based organoclays [146-147], or the pollutant-organoclay interaction without considering the effect of water [148-149], specific computational studies on MB adsorption by surfactant-MMT adsorbent are still very limited in references due to the vast database of adsorbents and pollutants. In this regard, more efforts need to be made to predict the mechanism as well as the adsorption process of MB in real wastewater.

The objective of this chapter is to examine the effectiveness of HDTMA-MMT for the removal of MB dye. MD simulations will be carried out to investigate the configurations and diffusion characteristics of interlayer species. The RDF between clay, surfactants and MB dyes will be analysed to reflect the bonding interaction. The NCI approach will be conducted to identify the weak inter-molecular interactions. For the purpose of comparison, the same method will be also conducted on hydrated Na-MMT in the absence of surfactants.

3.2 Computational details

3.2.1 Modeling details

The clay prototype is Wyoming-type Na-MMT with the formula of $Na_{0.75}[Si_{7.75}Al_{0.25}](Al_{3.5}Mg_{0.5})O_{20}(OH)_4$ [47-48]. The corresponding CEC is 102 meq/100 g. The clay adsorbent model consists of one layer of 8-unit cells in the *x*-direction and 4-unit cells in the *y*-direction.

HDTMA-MMT adsorbent was modelled by replacing exchangeable Na^+ ions in Na-MMT with $HDTMA^+$ cations in amounts of 100% and 75% of the MMT's CEC. Water content (*w*) is defined as the mass ratio of water molecules (M_w) and clay supercell (M_{MMT}), which is chosen of 0, 13%, 25%, 38%, 50%, 63% and 75% in this study, corresponding to 0, 5, 10, 15, 20, 25 and 30 water molecules per unit cell. Four MB dye molecules ($4MB^+$+$4Cl^-$) were put into the MMT interlayer space to obtain adsorbent-dye composites.

The chemical structure of $HDTMA^+$ and MB dye can be seen in Fig. 3-1, as well as two examples of initial unmodified and modified adsorbent-dye nanocomposites. Noting that the initial position and arrangement of MB molecules are the same in all cases.

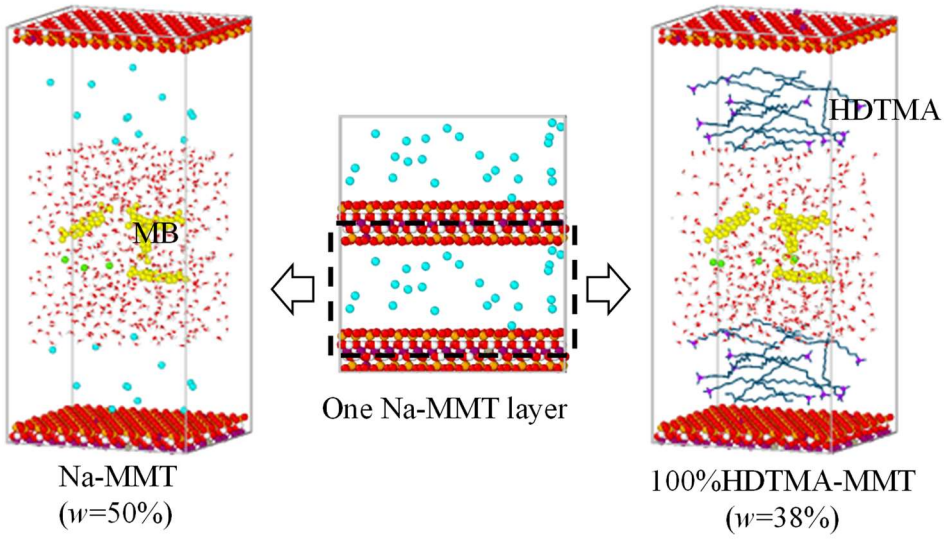

Fig. 3-1 The chemical structure of $HDTMA^+$ and MB dye. Examples of initial clay-dye

system of hydrated unmodified Na-MMT (w=50%) and 100%HDTMA-modified MMT (w=38%). Note: for interlayer species, blue - Na ions, white - H in water, red - O in water, yellow – MB cations, green - Cl^- in MB molecules, dark blue - alkyl chains of HDTMA, purple - N in HDTMA head groups.

3.2.2 Simulation methods

In this study, CLAYFF [121] was used to define atomic interactions of Na-MMT, while CVFF [123] was for MB and HDTMA. Water molecules is represented by the single point charge SPC model [150], which is consistent with CLAYFF and CVFF. The partial charges for the HDTMA surfactant were derived from the values calculated by Böcker et al [151]. For the MB cations, we used the Mulliken charge values [39] calculated at the B3LYP/LanL2DZ in the aqueous phase. The Lorentz-Berthelot mixing rule [122] was used to obtain the L-J parameters between different atoms. The particle mesh Ewald (PME) summation [152] was employed for the long-range electrostatic interactions with an accuracy of 0.0001 kcal.mol^{-1}.

Table 3-1 The average basal spacing (Å) of each clay adsorbent system without dyes.

w	Unmodified	Modified MMT (No. of $HDTMA^+$)	
(M_w/M_{MMT})	Na-MMT	75% CEC (n = 18)	100% CEC (n = 24)
0		18.12 (Fig. 3-2(a))	19.03 (Fig. 3-2(a))
13%		19.36	22.11 (22.47 [61])
25%	15.51 (15.5 [153])	22.62	25.24 (25.21 [61])
38%	18.8 (18.5 [153])	25.66	28.16 (28.02 [61])
50%	21.97	29.00	31.27
63%	25.1		
75%	28.29		

Minimization procedure was firstly implemented for all the clay absorbent systems and absorbent-dye systems. Then the NPT ensemble was used for 2 ns at 298 K and 1 atm. The clay layer was allowed to free swell. All the systems reached their equilibrium

state in the first 1 ns. In the last 1 ns, average basal spacings of absorbent and absorbent-dye systems were calculated.

As shown in Table 3-1, our results of basal spacing of adsorbent are consistent with prior studies. It is observed that the basal spacing of dry modified MMT is 18.12 ~ 19.03 Å when HDTMA intercalated in proportion of 75% ~ 100% CEC. Our results are comparable to other experimental and calculational values in dry conditions, as exhibited in Fig. 3-2(a). This is also in good agreement with some MD studies, which proved that HDTMA surfactant arranges in bilayer pattern in dry smectites with layer charge between 0.5 and 1.0 e per unit cell, and the corresponding basal spacing ranges at 17.7~19.8 Å [146-147]. For clay-dye composites, it is observed from Fig. 3-2(b) that higher amount of water molecules or HDTMA cations results in a larger basal spacing of MMT.

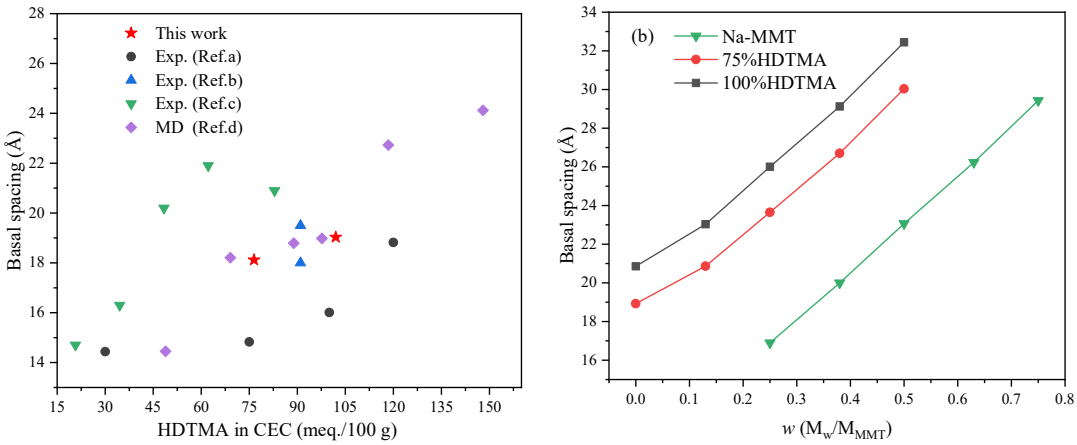

Fig. 3-2 (a) The basal spacings of dry MMT/bentonite adsorbent with different amounts of HDTMA intercalation; (b) The basal spacings of clay-dye composites at various *w*. Reference: a [154], b [155], c [156], d [149].

3.3 Results

3.3.1 Adsorption energy

The interaction energy E_{int} between adsorbate (four MB molecules) and clay adsorbents can be calculated as follow:

$$E_{int} = E_{total}\text{-}(E_{adsorbent}+E_{MB}) \quad (3\text{-}1)$$

where E_{total} is the potential energy of the adsorbent-dye composite after equilibrium; $E_{adsorbent}$ and E_{MB} are the potential energy of the clay adsorbent composites (without MB molecules) and the four MB molecules, respectively. For clarity, (3-2) and (3-3) show the detail energy component in modified and unmodified clay systems, respectively.

$$E_{int} = E_{MMT+water+HDTMA+MB}\text{-}(E_{MMT+water+HDTMA}+E_{MB}) \quad (3\text{-}2)$$

$$E_{int} = E_{MMT+water+MB}\text{-}(E_{MMT+water}+E_{MB}) \quad (3\text{-}3)$$

The adsorption energy E_{ads} is defined as the average interaction of a single MB molecule adsorbed in the interlayer of Na-MMT or surfactant-MMT. The E_{ads} can be obtained from E_{int} divided by the number of MB molecules:

$$E_{ads} = E_{int}/N_{i}MB \quad (3\text{-}4)$$

The obtained E_{ads} are negative values in all cases, as exhibited in Fig. 3-3, indicating the spontaneity of the MB adsorption onto both unmodified and modified clay systems. The highest absolute value of E_{ads} suggests that the adsorption process is more stable [157]. A chemical adsorption binding with chemical bond will formed when the adsorption energy is in the range of 100-1000 kJ/mol [158]. It can be seen in Fig. 3-3 that the absolute values of all the E_{ads} are more than 100 kJ/mol, which indicates that MB adsorbed in clay nanopore is a chemisorption process.

It is also found that the E_{ads} increases as w in the same surfactant amount. The adsorption energy of unmodified Na-MMT is larger than that in HDTMA-modified MMT within a small interlayer space. However, no noticeable difference was observed when the basal spacing exceeds 25 Å, corresponding to w > 50% in Na-MMT. The adsorption efficiency of cationic dye has a little enhancement with the intercalation of cationic surfactant when the d_{001} > 25 Å. In three adsorbent systems, the highest adsorption energy always obtained at w = 50%. In particularly, dry HDTMA-modified MMT has relatively low adsorption efficiency compared to the E_{ads} in other cases approximately ranging from -210 to -250 kJ/mol.

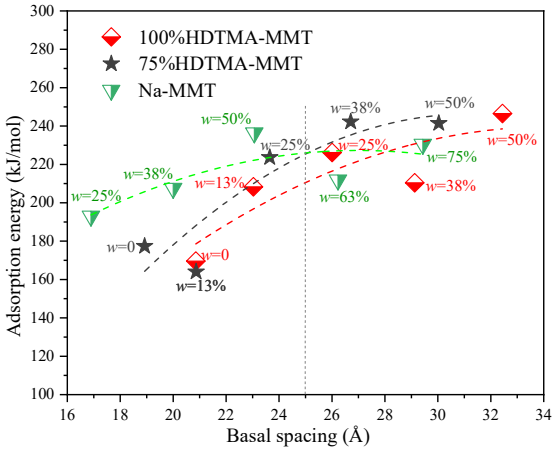

Fig. 3-3 The adsorption energy E_{ads} as a function of the basal spacing.

3.3.2 Diffusion characteristics

100% HDTMA-MMT adsorbents are chosen to study the surfactant performance. Mean square displacement (MSD) curves shown in Fig. 3-4 express the diffusion characteristics of water molecules and MB cations within MMT interlayer spaces. Generally, the mobility of water molecules in all cases are much larger than that of MB molecules. The MSD values of ring nitrogen atom in MB molecules are less than 1 nm^2 over the simulation periods in Na-MMT, indicating a high attraction of dyes and the clay.

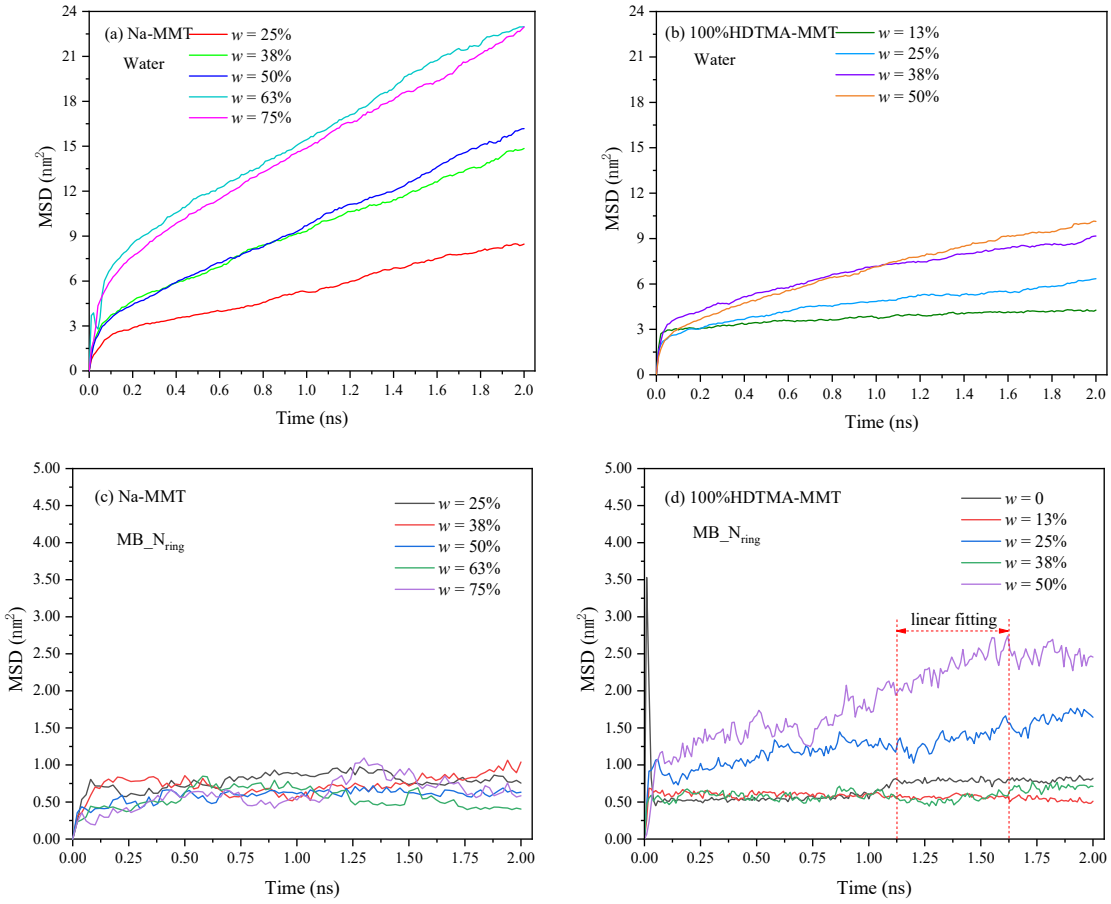

Fig. 3-4 Average MSD of water molecules and ring nitrogen atoms in MB molecules within the interlayer space of Na-MMT and 100%HDTMA-MMT systems.

The self-diffusion coefficients of water molecules (D_w) and ring nitrogen atom in MB cations (D_{MB}) are obtained by linear fitting MSD curves (1.125~1.625 ns) [143]. Calculated diffusion coefficients are presented in Table 3-2. It is difficult to fit MSD curves of MB in Na-MMT adsorbents so that there are absences of D_{MB} values in some cases. The calculated D_w is (6.44~15.6) × 10^{-10} m^2/s for Na-MMT interlayers, while ranges from 0.87 × 10^{-10} to 5.44 × 10^{-10} m^2/s for 100%HDTMA-MMT interlayers. The obtained D_w in Na-MMT are similar to reported values of (2.22~14) × 10^{-10} m^2/s with water content of 10% ~ 30% [159-160]. With the same surfactant amount, the more water content w, the larger D_w. It can be easily found that the cationic HDTMA plays an important role in reducing the D_w within MMT interlayer space. All the diffusion coefficients of MB are on the order of 10^{-10} m^2/s, which is consistent with other

computational results in clay minerals and mesoporous silica [161-163]. The existence of hydrophobic surfactants may result in the rise of mobility of MB cations, for example, the case of w = 25% and w = 50%. The possible reason is that surfactants will weaken the attraction of MB dyes and MMT by affecting MB configurations.

Table 3-2 Diffusion coefficient of water molecules and ring nitrogen atom in MB cations (10^{-10} m^2/s).

Adsorbent	D	w (M_{water}/M_{MMT})						
		0	13%	25%	38%	50%	63%	75%
Na-MMT	D_w			6.44 (6.3~9.0 [153])	8.35	10.02	15.60	11.86
	D_{MB}			-	0.39	-	-	-
100%HDT MA-MMT	D_w		0.87	1.10	3.79	5.44		
	D_{MB}	0.04	0.04	1.23	0.36	2.11		

3.3.3 Interlayer configurations

To visualize the interlayer interaction, the final configurations of unmodified MMT-dye systems and 100%HDTM-MMT-dye systems are shown in Fig. 3-5.

It is observed that water molecules and $N(CH_3)_3$ head groups of $HDTMA^+$ are in the first layer adhered onto MMT siloxane surfaces, which indicated that MMT has high attraction to both water and ammonium head groups. MB cations present five types of orientation which reveals different interaction modes between MB and MMT surfaces.

Fig. 3-6 depicts the main configurations of MB dyes near clay surfaces. MB cations are attracted onto the MMT surface in a nearby horizontal position in Type 1, Type 2 and Type 3. The positions of $N(CH_3)_2$ groups or aromatic rings make a distinct contribution in these MB orientations paralleled to basal plane of MMT. For Type 4 and Type 5, MB cations are oblique to the Si-O surface interacting with one or two MMT surfaces simultaneously through CH_3 groups.

Atomic *z*-density profiles ρ of nitrogen atoms of $N(CH_3)_2$ groups in the last 20-ps MD simulation were computed to further quantify MB distributions, as shown in Fig. 3-7. Black dash lines represent the position of lower and upper basal surfaces of MMT. The nearest distance of ρ(N) peaks to the lower and upper clay surface were approximately measured as x_1 and x_2, respectively, and recorded in Table 3-3. When $x_1/x_2 > 7$, there is no direct interaction between clay and dye. Thus, the quantity of five MB orientations in each case are counted up and reported in Table 3-3 according to MB configurations in Fig. 3-5. It can also be figured out that the orientation Type 1 and Type 3 correspond to $3.5 < x_1/x_2 < 4$ and $5 < x_1/x_2 < 6$, respectively, while and the rest corresponds to $4 < x_1/x_2 < 5$.

From Table 3-3, most of MB molecules are parallel to mineral surface (orientation Type 1~3) in Na-MMT interlayer space, which allows as more adsorption sites as possible to attach on the surface. But for 100% HDTMA-MMT, MB configurations distinctly depend on the water content. MB cations can interact with Si-O surface in a horizontal and inclined position at low *w*, where the basal spacing of MMT is relatively small. As the water content increases, it is observed from the top view of interlayer species in Fig. 3-5 that organic HDTMA molecules are closely linked and forming hydrophobic aggregates. As a result, MB molecules can hardly reach adsorption sites of MMT due to the mobility constraint from the surfactants.

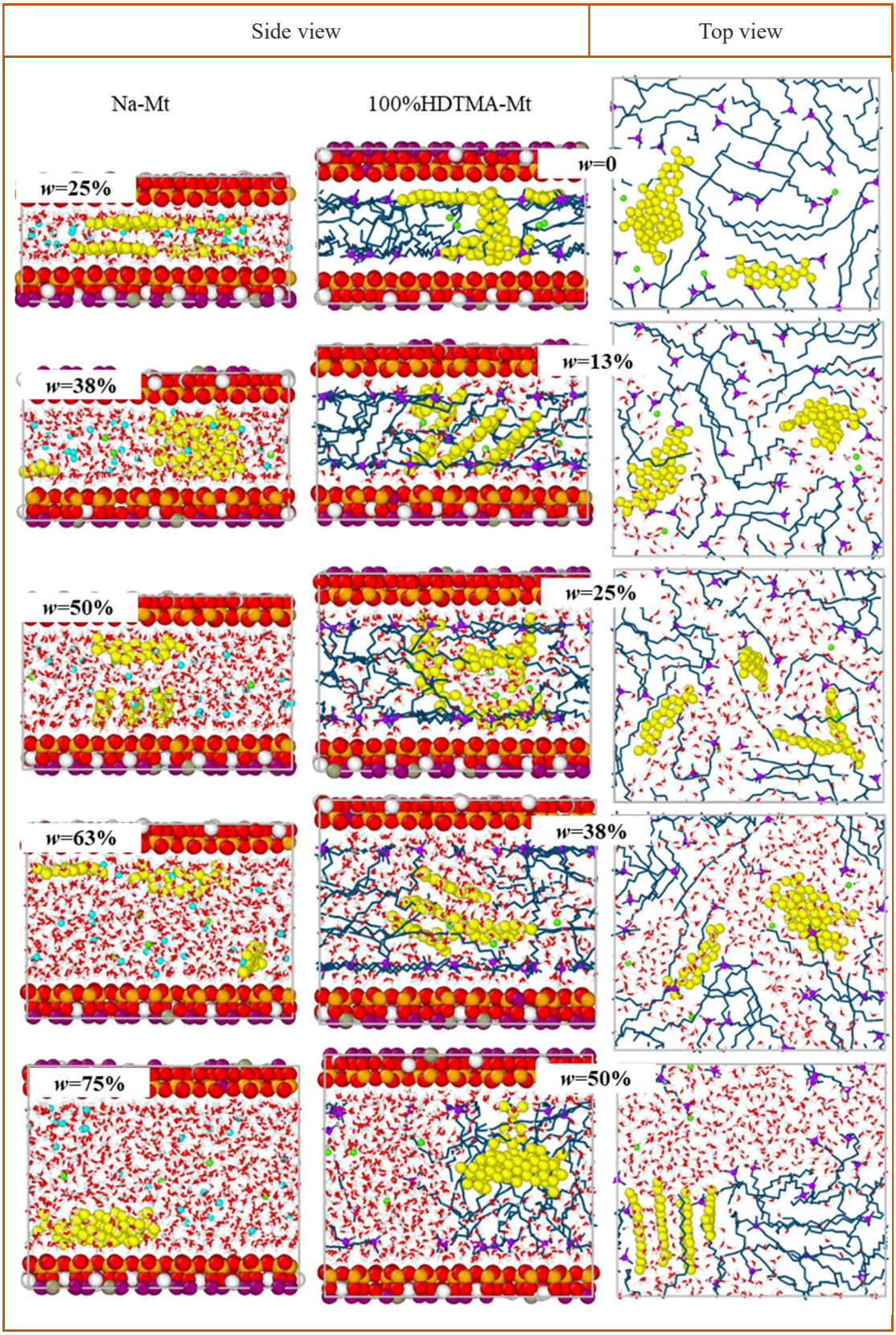

Fig. 3-5 Snapshots of final configurations in Na-MMT and 100% HDTMA-MMT in different water conditions. For clear express, MMT layer is removed for top view of the distribution of interlayer species in 100% HDTMA-MMT. Note: for interlayer

species, white - H in water, red - O in water, yellow - MB^+ cations, green - Cl^- in MB molecules, dark blue - alkyl chains of HDTMA, purple - N in $HDTMA^+$ head groups.

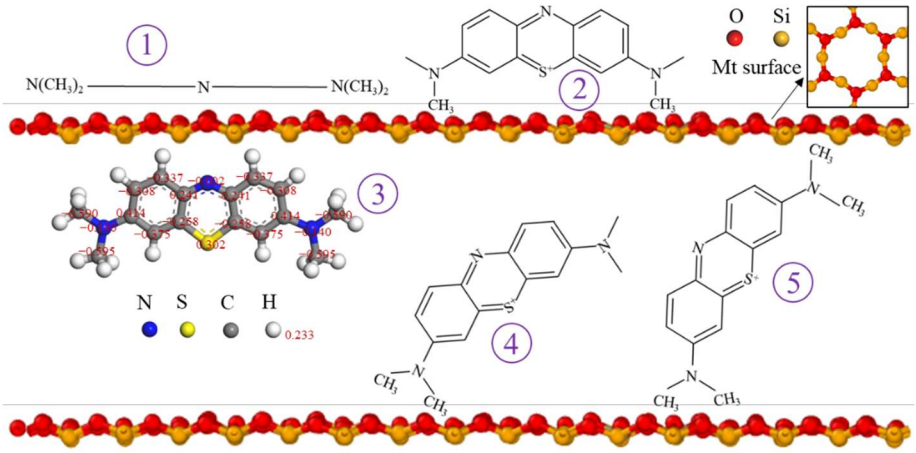

Fig. 3-6 Five types of molecular orientations of MB cations absorbed on Si-O surface of MMT. Atomic charges of MB cation are shown in Type 3. Type 1: MB interacts with one MMT surface via all the $N(CH_3)_2$ groups and aromatic ring; Type 2: MB interacts with one MMT surface via two $N(CH_3)_2$ groups; Type 3: MB interacts with one MMT surface via N atoms in aromatic moiety; Type 4: MB interacts with one MMT surface via one $N(CH_3)_2$ group; Type 5: MB interacts with two MMT surfaces simultaneously via two $N(CH_3)_2$ groups.

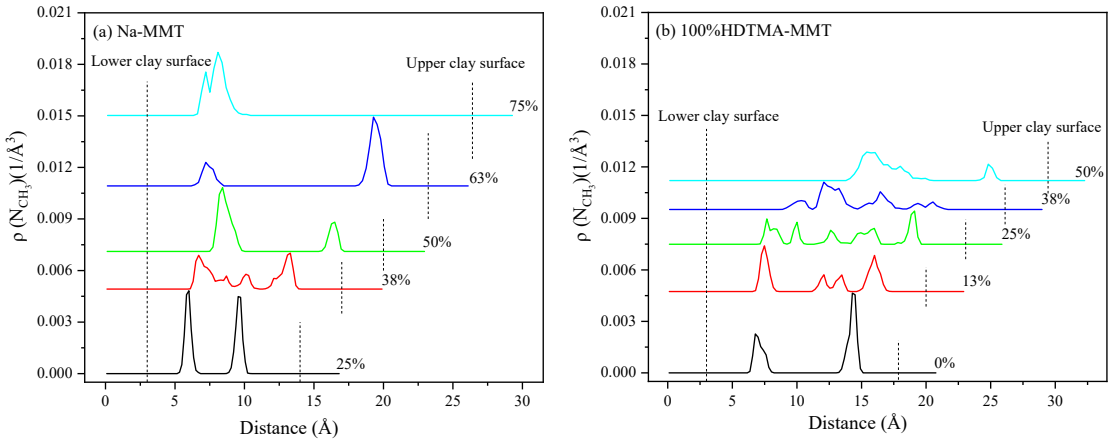

Fig. 3-7 Atomic *z*-density profiles ρ of nitrogen atoms of $N(CH_3)_2$ groups.

Table 3-3 The nearest distance x_1 and x_2 (unit Å) of ρ(N) peaks to the lower and upper clay surface and the quantity of each type of MB orientations.

Adsorbent	w	x_1	x_2	Type 1	Type 2	Type 3	Type 4	Type 5
Na-MMT	25%	3.5	3.9	4	-	-	-	-
	38%	3.7/5.7	3.7	1	1	1	1	-
	50%	5.4	3.5	1		3	-	-
	63%	4.2	3.9	1	3	-	-	-
	75%	4.2/5.1	-	-	1	3	-	-
100%HDT MA-MMT	0	3.8	3.5	2	1	-	-	1
	13%	4.5	4.0	-	1	-	2	1
	25%	4.6	3.9	-	-	1	2	-
	38%	>7	5.6	-	-	-	-	-
	50%	>7	4.6	-	-	-	1	-

3.3.4 Intermolecular interactions

RDFs were calculated based on the last 20000 instantaneous trajectories (20 ps) to reflect the interlayer bonding interaction.

3.3.4.1 Interaction between dye and MMT

It can be concluded from Fig. 3-6 that MB molecules are most likely to adhere onto clay surface through $N(CH_3)_2$ groups. Fig. 3-8 shows the radial distribution function g(r) of oxygen atoms on MMT surface (O_{MS}) with carbon atoms in CH_3 groups (C_{CH_3}) in Na-MMT and 100% HDTMA-MMT systems.

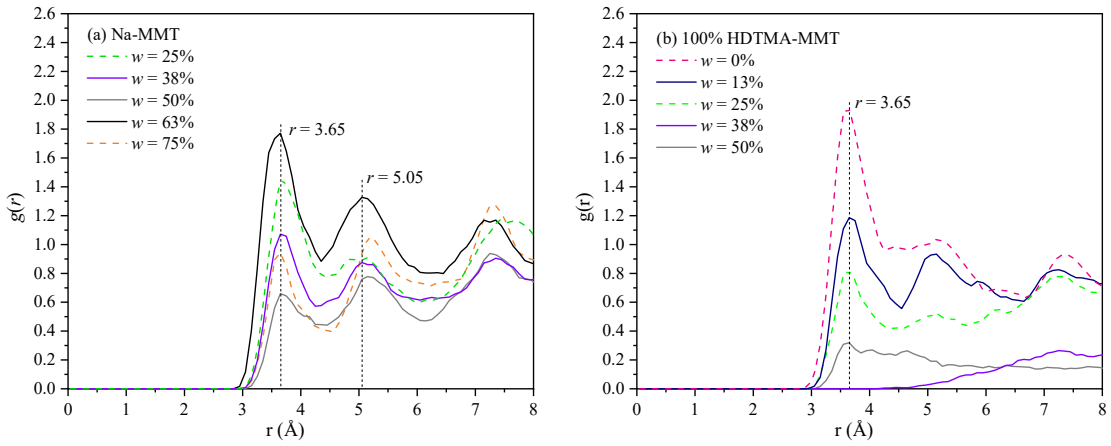

Fig. 3-8 The radial distribution function g(r) of O_{MS} with carbon atoms in CH_3 groups on Na-MMT and 100%HDTMA-MMT adsorbents.

It is seen that the minimum interaction distance of O_{MS}…C_{CH_3} is the same (r = 3.65 Å) in unmodified and modified MMT systems. This suggests that the CH_3 groups of MB attracted to Si-O surfaces via strong electrostatic interaction. The peak values of g(r) can quantify the adsorbed CH_3 groups near basal surfaces of MMT and reflect the orientations of MB dyes.

As shown in Fig. 3-8(a), the smaller peak values of g(r) are found at w = 50% and w = 75% without surfactant where higher E_{ads} are obtained. In this regard, MB configuration Type 3 with N atoms in the aromatic ring orientating towards MMT surface makes a great contribution to strengthen the dye-clay interaction. In 100%HDTMA-MMT systems (Fig. 3-8(b)), the peak values of g(r) are in the order of w = 0 > 13% > 25% > 50%, suggesting that less CH_3 groups of MB interact directly with MMT as w increases. In particular, no short-range interaction can be observed between O_{MS} and C_{CH_3} at w = 38%. This validates that no MB cations are among five types of orientations in this case.

The lowest E_{ads} at w = 25% in Na-MMT and at w = 0 in 100%HDTMA-MMT can be attributed to interaction Type 1. Even though some CH_3 groups of MB tightly attached onto Si-O surface in these two types of positions, the repulsive interaction between the aromatic ring and MMT surface is possibly where the negative effect

comes from.

3.3.4.2 Interaction between dye and surfactant

From the RDF based on the center of mass of $HDTMA^+$ and MB^+ cations (Fig. 3-9), the two organic phases are at an average distance of 5.25 Å at w = 25%. But for other cases, no clear peaks can be observed. It is suggested that the intermolecular force between MB^+ and $HDTMA^+$ cations is via weak van der Waals force.

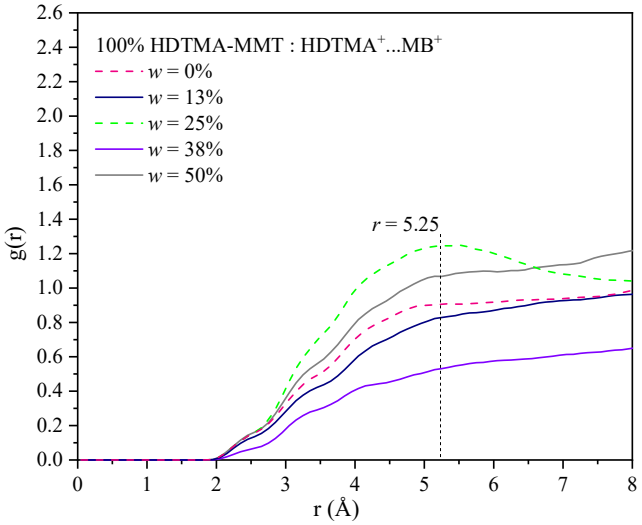

Fig. 3-9 The radial distribution function g(r) of $HDTMA^+$…MB^+ cations.

3.3.4.3 Interaction between water, surfactant and MMT

The RDF between O_{MS} and water molecules and $HDTMA^+$ are presented in Fig. 3-10. It is observed from Fig. 3-10(a) that the g(r) of O_{MS}…H_{Water} shows the first peak located at around 1.85 Å and for O_{MS}…O_{Water} is at r_2 = 3.35 Å in both Na-MMT and 100%HDTMA-MMT adsorbents at w = 50%. It was found from Fig. 3-5 that water molecules are in the first layer adsorbed onto the MMT interface. This is because H_{Water} are oriented towards MMT surface to form strong hydrogen bonds with O_{MS} by acting as H-bond acceptor. The existence of HDTMA surfactant has little effect on the arrangement of water molecules near the MMT surface.

(a) MMT - Water (b) MMT - HDTMA

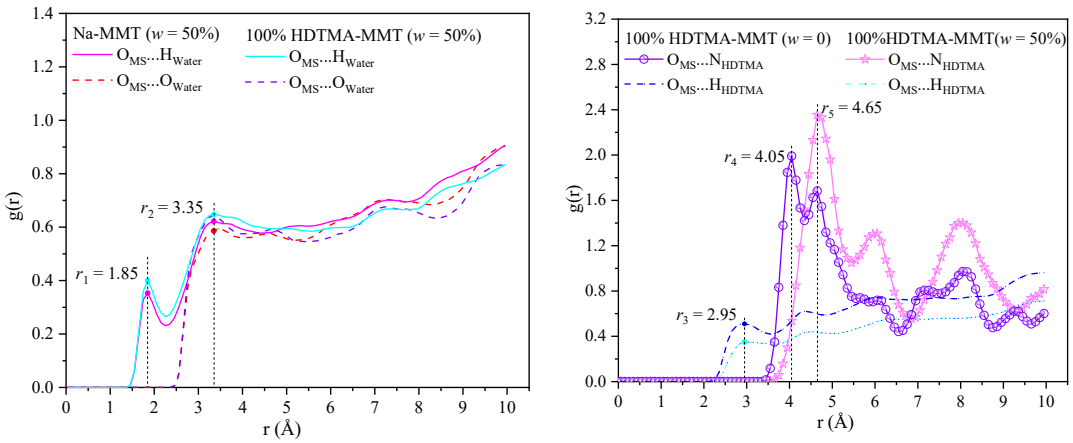

Fig. 3-10 The $g(r)$ of various atoms at distance r: (a) water molecules and (b) HDTMA molecules with oxygen atoms of the MMT surface (O_{MS}).

In 100%HDTMA-MMT adsorbents (Fig. 3-10(b)), it is noticed that the distance of hydrogen atoms in $HDTMA^+$ to the MMT surface is approximately 2.95 Å. According to Jeffery [164], H-bonds with $H_{HDTMA}…O_{MS}$ distances in the interval of 2.5~3.2 Å are moderate and mostly electrostatic interaction. The minimum distance of O_{MS} -N_{HDTMA} r_4 = 4.05 Å in dry condition. It increases to r_5 = 4.65 Å at w = 50%. Comparing with r_1, water molecules have higher affinity with MMT surface than $HDTMA^+$. Due to the negative charge of nitrogen atom (-0.56) of $HDTMA^+$, the interaction between N and MMT surface can be attributed to van der Waals forces. Therefore, the positive charge $N(CH_3)_3$ head groups are strongly attracted to MMT surfaces via both strong electrostatic interaction (O_{MS}-H_{HDTMA}) and van der Waals forces (O_{MS}-N_{HDTMA}).

3.3.5 Noncovalent interaction (NCI)

Based to the final molecular coordinates, the electron density can be computed from a quantum chemical calculation by Gaussian. The obtained wavefunction information is then used as input to calculate the RDG with respect to the sign $(\lambda_2)\rho$ using Multiwfn program [165] and rendered by VMD 1.9.2 program [166], as shown in Fig. 3-11. The shattered spikes of the RGD scatter graph of the MB, HDTMA and MMT

complex which selected in the final configuration of 100%HDTMA-MMT system, located in the negative valued sign (λ_2)*ρ area, which indicated that a strong attraction between the involved molecules. The blue and green RDG surfaces indicated weak hydrogen bonds and van der Waals interactions between Si-O atoms on MMT surface and N(CH_3) group of both MB and HDTMA. The main interaction (green) between MB and HDTMA is van der Waals interaction. The results of NCI analysis are consistent with the above RDF analysis.

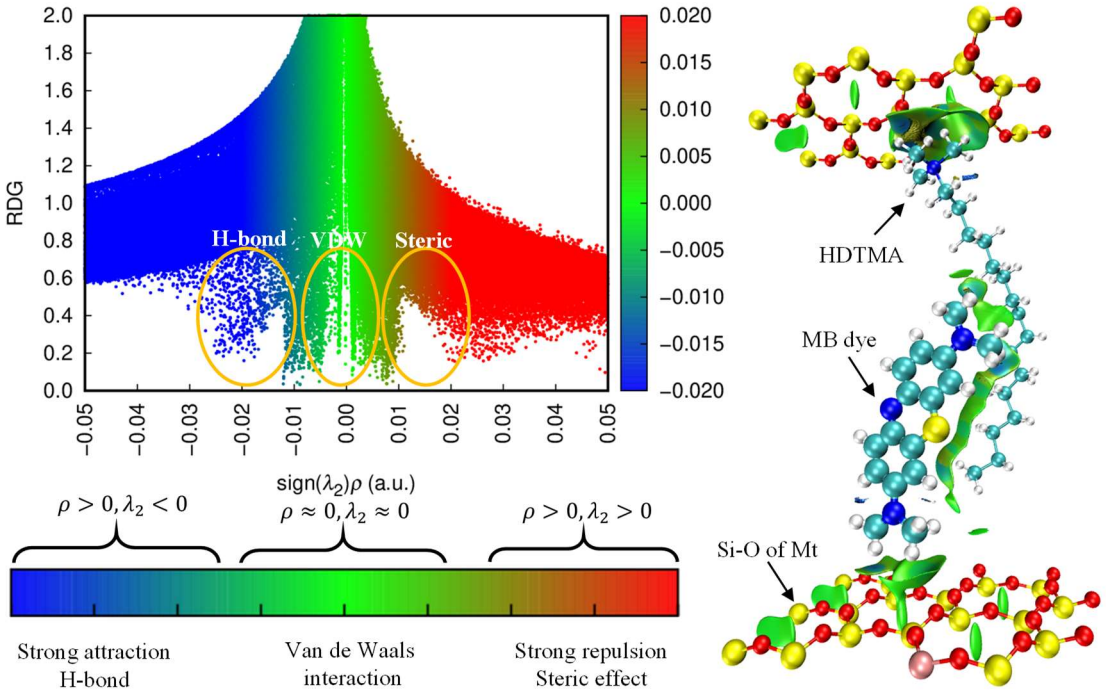

Fig. 3-11 RDG isosurface map with isovalue of 0.6 of MB, HDTMA and Si-O surface of MMT. The value of sign (λ_2)ρ surfaces is represented by filling color according to the color bar. For clarity, the RDG isosurface is shown only in the range of -0.015 < sign (λ_2)ρ > 0.01.

3.4 Discussions

3.4.1 Adsorption mechanism of MB onto MMT inner surfaces

The interaction strength and the adsorption efficiency of MB are associated with

their molecular orientations on MMT surfaces. As a result of the analysis from above five sections, the adsorption mechanism of MB includes both chemisorption and physisorption.

Chemical adsorption process comes from strong electrostatic interactions between positive CH_3 groups and oxygen atoms of the negative tetrahedral layer of MMT. Strong electrostatic interaction is considered as chemical adsorption in some reference [167-168]. From Table 3-3, the strong electrostatic interaction based on CH_3-O_{MS} is the dominant driving force and easy to achieved as it steers all MB configurations except Type 3.

Physical adsorption comes from VDW force and weak electrostatic interaction, which are attributed to negative nitrogen atoms in $N(CH_3)_2$ groups and positive sulfur atoms in the aromatic ring interacting with negative MMT surfaces, respectively. In addition to Type 3, N atoms in the aromatic ring orientating towards MMT surface may create Lewis acid-base interactions with MMT. It is proposed that nitrogen atom in the aromatic ring of MB would act as Lewis base to strongly interact with Al-O octahedron (Lewis acid) of clay sheet [169].

In earlier experimental studies, it is widely recognized that ion exchange is the most important mechanism for MB uptake by swelling clay and is classified as a chemical reaction [170-173]. Yener et al [174] also proved that the irreversible ion exchange and reversible physical adsorption of MB^+ cations on the activated clay occurred simultaneously. Accordingly, the present study gives a detailed explanation for adsorption mechanism of MB from an atomic point of view.

3.4.2 Effects of the HDTMA on adsorption efficiency of MB

It can be concluded from the obtained high adsorption energy that cationic surfactant-modified clay is effective in dye water treatment especially at high *w*. The optimum water content in the present work was obtained at w = 50%, suggesting that enhancing the adsorption capacity cannot be always achieved by increasing interlayer spacings. No evident enhancement can be found from the calculated E_{ads} of cationic MB by HDTMA-modified MMT compared with Na-MMT. The possible reason is that

the cationic surfactants not only play a positive role in enlarging the interlayer space of MMT, but also a negative effect on the reduction of adsorption sites for dyes.

With low water content (w < 50%), unmodified clay adsorbent shows higher adsorption efficiency of dye molecules compared to the modified MMT. The functional groups ($N(CH_3)_3$) of HDTMA have high affinity to MMT surface and occupy the adsorption sites, leading to a reduction in reactive sites for MB. Furthermore, since the two organic compounds do not strongly interact with each other, the presence of surfactant has a certain impact on molecular orientations of MB.

With large water content (w > 50%), modified-MMT adsorbent has a potential to improve the adsorption capacity of dye molecules. Unmodified Na-MMT adsorbent may not achieve higher adsorption capacity as basal spacing increases. Since dye molecules prefer to be parallelly adhered on Na-MMT surfaces to form a single adsorption layer, so that only limited dye molecules would be efficiently adsorbed and other dye molecules will just have weak interaction with clay adsorbent. However, for modified-MMT, HDTMA molecules tend to aggregate and separate with water due to their hydrophobic characteristics. As a result, more MB would be "physically" surrounded by the HDTMA alkyl chains and remained within MMT interlayer space with lower mobility.

In short, the change of microstructure of clay adsorbent by intercalation of cationic surfactant will not have much effect on improving the adsorption capacity. The effective surfactants should contain multiple functional groups that can not only easily interact with the clay mineral but also strongly attract cationic dyes.

3.5 Conclusions

In this chapter, the interlayer adsorption characteristics of HDTMA-MMT and natural clay for cationic MB dye cations were studied. The following conclusions can be drawn:

(1) The adsorption energy of MB on both HDTMA-MMT and Na-MMT absorbent were obtained more than 100 kJ/mol and up to 250 kJ/mol, indicating the

effectiveness of two types of adsorbents in dye water treatment. This study also validates that nature MMT have great efficiency for uptake of multi-pollutants containing dyes and surfactants.

(2) Interlayer configuration revealed that MB molecules have five main orientations towards MMT surfaces which were distinctly affected by the water content. MB can be parallel and oblique to the mineral surfaces in the presence of HDTMA. However, MB molecules tend to interact with Na-MMT interlayer surfaces in a horizontal mode (Type 1~3). This indicates that only limited amounts of dyes will be adsorbed via first layer adsorption on unmodified MMT plane surfaces.

(3) As a result of dye molecular orientations, RDF and NCI studies, the adsorption mechanism of MB includes strong electrostatic interaction (as chemisorption) between CH_3 groups of MB and oxygen atoms of MMT surfaces. Sulfur and nitrogen atoms in the aromatic ring of MB can created weak electrostatic forces (as physisorption) and Lewis acid-base interactions with MMT surfaces.

(4) The intercalation of cationic surfactant cannot significantly improve the adsorption efficiency of MB. At low water content (w < 50%), the positive $N(CH_3)_3$ head groups of HDTMA molecules were tightly attached to the MMT surface via electrostatic interaction, occupying the adsorption sites and causing a decrease of active sites for MB. However, with higher water content, their long-length alkyl chains would aggregate and surround MB molecules due to the hydrophobic interaction with water, thereby reducing the diffusion and mobility of MB to contact with MMT.

Chapter 4

Synthesis and thermal stability of CHT-MMT nanocomposites

4.1 Introduction

In Chapter 3, cationic surfactants may not provide significant enhancement in the adsorption of cationic dyes because they may occupy some adsorption sites on clay surfaces. Much attention has been focused on various biopolymers that contain multiple active chemical groups and that are harmless to nature [73]. CHT contains plenty of hydroxyls (-OH) and amino (-NH_2) groups so that CHT exhibits excellent affinity to cationic, anionic, and non-ionic contaminants [74]. In this regard, CHT is more advantaged as a clay modifier than surfactants.

Novel CHT-clay nanocomposites have been cumulatively explored in adsorption and filtration applications for dyes and metal ions purification in recent twenty years [98], [175-183]. For instance, Daraei et al. [98] reported a novel TFC membrane prepared by organoclay/CHT nanocomposite coated on the commercial polyvinylidene fluorid microfiltration membrane. They proved that this novel TFC membrane was capable of removing dyes from water. Zhu et al. [175] reported that a novel nanomembrane coated by CHT-MMT nanosheets has better performance in dye purification. Zhang et al. [184] proved that carboxymethyl chitosan (CMC)-MMT hybrid composite exhibited higher adsorption capacity on Pb(II) and Congo Red than Na-MMT and CMC alone. Most of the research in this field is aimed at the adsorption performance of CHT/clay-based nanomembranes. However, little attention has been paid to these hybrid materials themselves in terms of their structural stability in real operation since a large range of pH and temperature always occurs in industrial effluents.

One of the imperfections of CHT is its poor thermal stability. It has been extensively reported that clay-based polymer nanocomposites (CPN) have better mechanical and thermal properties compared to neat polymer membranes [185-188]. Martínez-Camacho et al. [189] found that the glass transition temperature of CHT films with clay nanoparticles is between 200 and 250 °C and the decomposition of amino units may occur at 135~300 °C. The presence of clay particles usually made the composite more resistant to degradation when compared to CHT [190]. In spite of the existing experimental studies on the thermal properties of these CPN mixtures, what

should be paid more attention to is membranes' structural stability when they are working, typically said, when they are exposed and immersed in water with various temperatures. However, it is still rarely discussed in earlier published articles.

The pH condition plays a non-negligible role in the microstructure of CHT-MMT composites. It is observed from an atomic simulation that CHT with all amino groups protonated quickly coated on MMT surface in a monolayer form in water solvent [191]. Similarly, Tiraferri et al. [192] found that CHT at a pH of 8 does not adsorb to oppositely charged silica surfaces. Whereas, in mildly acidic solutions formed rigid and thin adsorption monolayers, and in neutral solutions, layers became significantly thicker (~10 nm).

Understanding the coating interaction between CHT and clay can provide ideas for the fabrication and regeneration of CHT-MMT membranes. Darder et al. [193] investigated a bilayer structure of CHT on the surface of clay platelets. They found that the first CHT layer is adsorbed through a cationic exchange procedure, while the second layer is adsorbed through hydrogen bonding interaction between amino and hydroxyl groups in the CHT chain. Previous molecular dynamic simulations showed the order of interaction of three functional groups of carboxymethyl CHT with the MMT surface followed by OH > COOH > NH_2 [184]. Wang et al. [194] studied the molecular adhesion of chitin and CHT to montmorillonite at different degrees of acetylation and protonation under fully hydrated conditions and evaluate the effect of counter ions. Their simulation results revealed a small variation of the total molecular adhesion as a function of degrees of acetylation. There are still limited computational research focused on the combination mechanisms of CHT-MMT nanocomposites in consideration of pH effects.

Consequently, coating mechanisms for CHT-MMT with respect to aqueous pH and thermal stability of CHT-MMT composites should be fully investigated in this chapter to ensure its adsorption performance. The distribution and diffusion characteristics of CHT with various pH values in the coating process will be studied, and the corresponding adhesion mechanisms of CHT-MMT composites will be discussed. The structural changes of dry CHT-MMT composites in an aqueous medium will be

explored in view of immersion and temperature effects.

4.2 Computational details

4.2.1 System Setup

The PCFF-IFF force field was herein applied to define CHT-MMT interaction and force field parameters for CHT were taken from PCFF. The suitability of IFF force field in simulating interactions between clay minerals and organic components has been widely validated [195-198]. The atomic charges of CHT were assigned by the COMPASS force field.

The Na-MMT model is based on the chemical composition of $Na_{0.75}[Si_{7.75}Al_{0.25}](Al_{3.5}Mg_{0.5})O_{20}(OH)_4$. The MMT substrate consists of a 16*a* × 6*b* × 1*c* supercell with 3912 atoms and a size of 8.29 nm × 5.39 nm in the *xy*-plane. Thus, there are 72 sodium ions to balance the negative charges of the substrate. Since clay-CHT nanocomposites have been experimentally synthesized by mixing clay and CHT solutions [199], the MMT-water solution system herein was constructed following the scheme in Fig. 4-1. First, the water solution with 7000 water molecules based on the flexible SPC model in PCFF was equilibrated under NPT ensemble at room temperature and atmospheric pressure for 100 ps. The obtained water density is about 1.03 g/cm^3 (Fig. 4-1(a)), confirming the suitability of the chosen force field. Then, the water solution was added to the Na-MMT surface obtained after a minimization procedure Fig. 4-1(b)). Fig. 4-1(c) shows the equilibrated MMT-water system under NVT ensemble (298 K) for 1 ns.

A CHT molecular chain consists of 10 repeating units with an idealized deacetylation degree of 100%. In terms of pH, the adsorption plane [0 0 1] of the clay mineral is almost unaffected by the environmental pH, whereas only the edge surfaces would be affected [194]. Further, the extra H^+ and OH^- are ignored in the strongly acidic and basic solution. The monolayer coating of CHT biopolymer onto MMT clay layers is achieved by ion exchange process [193]. The cationic CHT can be either neutralized in

the system by replacing counterions (Na^+) from the MMT or by adding negative chloride ions [191], [194]. Considering that in real practice ions should usually be washed out, positive charges in CHT molecules were herein balanced by removing corresponding number of Na^+. Regarding the cation exchange capacity of MMT, six CHT molecules with up to 60 e positive charges were added to the equilibrated MMT-water system, as shown in Fig. 4-1(d). The charged fraction of CHT monomer calculated based on (1-1) and the number of CHT chains and Na ions are given in Table 4-1.

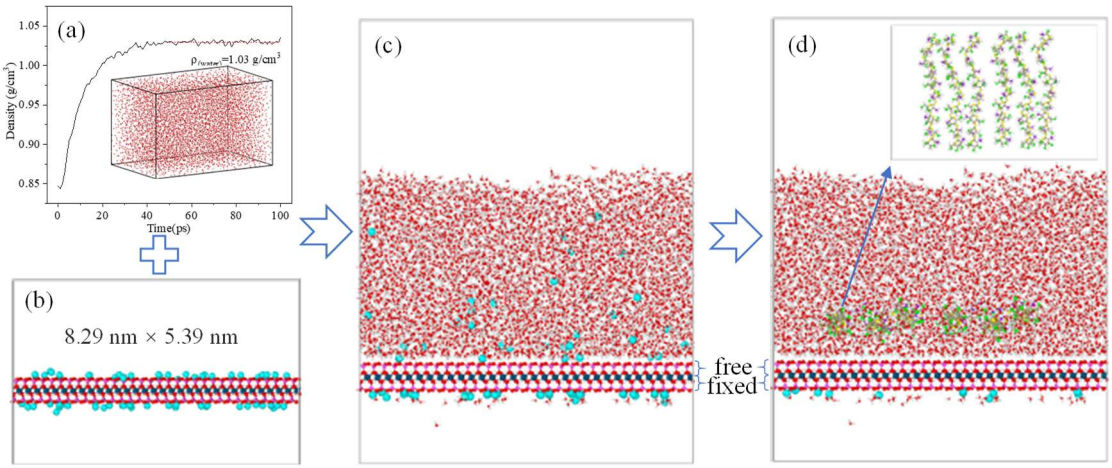

Fig. 4-1 (a) Density evolution of water solution; (b) Equilibrated the Na-MMT monolayer. (c) Equilibrated MMT-water system. (d) Initial CHT-MMT solution system at pH = 3.5.

Table 4-1 The charged fraction of CHT and the number of counterions corresponding to pH level.

pH	A CHT chain	Number of CHT chains	Number of Na^+
3.5	$[-NH_3^+-]_{10}$	6	12
6.5	$[-NH_2-NH_3^+-]_5$	6	42
9.5	$[-NH_2-]_{10}$	6	72

4.2.2 Simulation process

NVT ensemble was applied to CHT-MMT solution systems for 2 ns with a timestep of 1 fs. The temperature was set at 298 K. The long-range electrostatic interactions were calculated by the particle mesh Ewald (PME) summation with an accuracy of 0.0001 kcal.mol^{-1} [152] . The initial distance between the center of mass of six CHT chains and the clay surface was set at 10 Å. The fabrication of clay-CHT nanomembranes in experiments usually ends with a drying process for mixture solutions [175], [199-200]. Accordingly, water molecules will be totally and partially removed from equilibrated CHT-MMT solution system for drying and then systems ran for another 2 ns to obtain dry and wet (w=11.7 *wt*%) CHT-MMT nanomembranes.

4.3 Results and discussions

4.3.1 Distribution and diffusion characteristics: pH effects

Fig. 4-2 shows snapshots of three steady systems at different pH levels in an aqueous and fully dry condition. It can be noticed that CHT chains with abundant NH_3^+ groups aggregate near clay while chains with plentiful NH_2 groups disperse in solution. The CHT thickness near the surface is 1.4 nm, 2.7 nm, and 4.0 nm at pH 3.5, 6.5, and 9.5, respectively. Fig. 4-3(a) depicts the interaction energy between CHT polymers and the MMT including pairwise and long-range Coulombic energy. It is found that a higher pH value along with a lower charge density of CHT results in weaker CHT-MMT interaction and diminished CHT-MMT adhesiveness. It seems that CHT chains without any protonation (at pH 9.5) fail to adsorb to the negatively charged MMT surface since their attraction energy is quite small in an aqueous solution. CHT chains are found from Fig. 4-2 in a more dispersive morphology in a basic state on the MMT surface. A similar experimental phenomenon was found by Tiraferri et al. [192] that CHT at a pH of 8 does not adsorb to silica. They pointed out that this was attributed to CHT aggregating at this pH due to its reduced aqueous solubility.

Once water molecules were removed from systems, CHT and sodium ions

immediately stuck at the MMT surface as their interaction energy instantly increases at 2 ns. However, CHT-MMT interaction at a pH 9.5, where a high amount of Na^+ ions existed, has no significant enhancement in dry state even though CHT backbones were clustered at the surface. This is because sodium ions tend to locate between CHT and MMT, and act as a bridge for them by attracting OH and NH_2 groups, as can be seen from Fig. 4-3 (b). Na^+ ions serve as a "glue" assisting polymer chains coating onto MMT [194], these ions -on the other hand- prevent direct interactions between CHT and MMT.

Furthermore, pH value can also influence the CHT distribution on the MMT surface. From Fig. 4-2, the dry CHT-MMT composite possesses 1.5 nm thickness in a strong and weak acidic condition, while it is 1.9 nm thickness in an alkaline condition. Our results are similar to Tiraferri's [192] experimental ones, which show that CHT formed rigid and thin adsorption monolayers (≈ 0.5 nm, $w \approx 60\%$) near silica surface in mildly acidic solutions. Lee et al. [201] also found that CHT are physisorbed on mica surface at pH 8.5 with significantly increased surface roughness. Fig. 4-2 also exhibits the top view of three dry composites. The coverage rates of CHT chains are 40.5%, 36.5%, and 32.9% at pH = 3.5, 6.5 and 9.5, respectively. It can be observed that CHT backbones can well spread and coat onto the MMT surface in acidic conditions. A relatively uniform distribution can be found at pH = 3.5 compared with pH = 6.5. However, CHT backbones would roll up and would not flatten onto the clay surface at pH = 9.5.

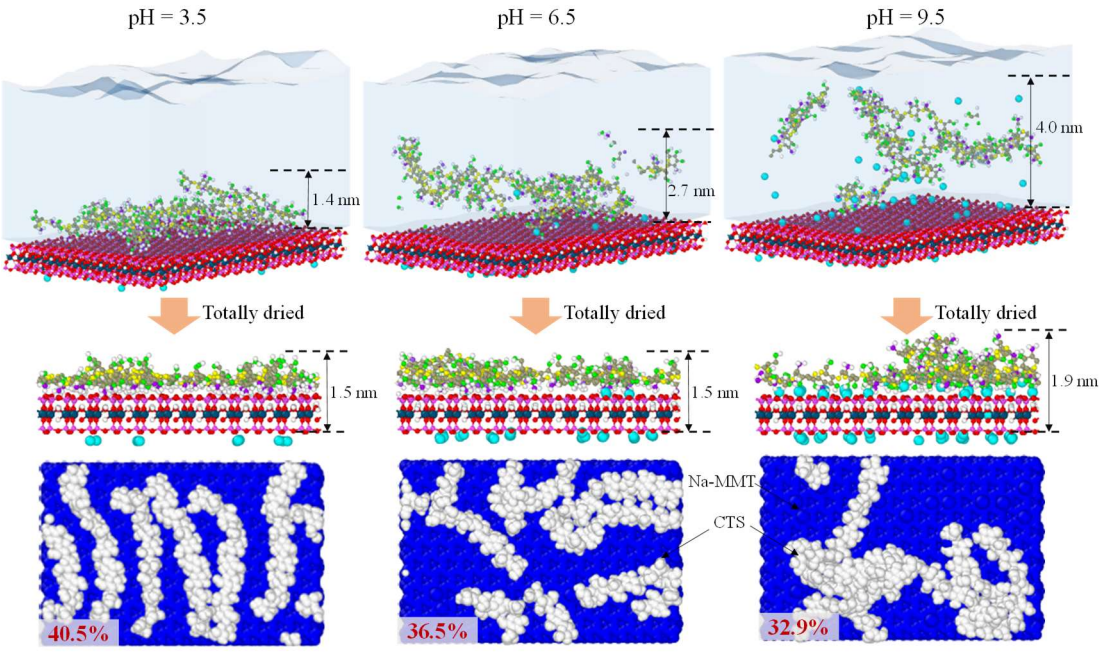

Fig. 4-2 Snapshots of equilibrated systems in water solution and dry condition. Color code in three top views of dry CHT-MMT composites: navy is for Na-MMT; white is for CHT chains. Atoms are displayed in their van der Waals radii for crystal MMT [202] and nonbonded contact distances for organic CHT: N-1.64 Å, O-1.58 Å, H-1.10 Å, C-1.77 Å [203].

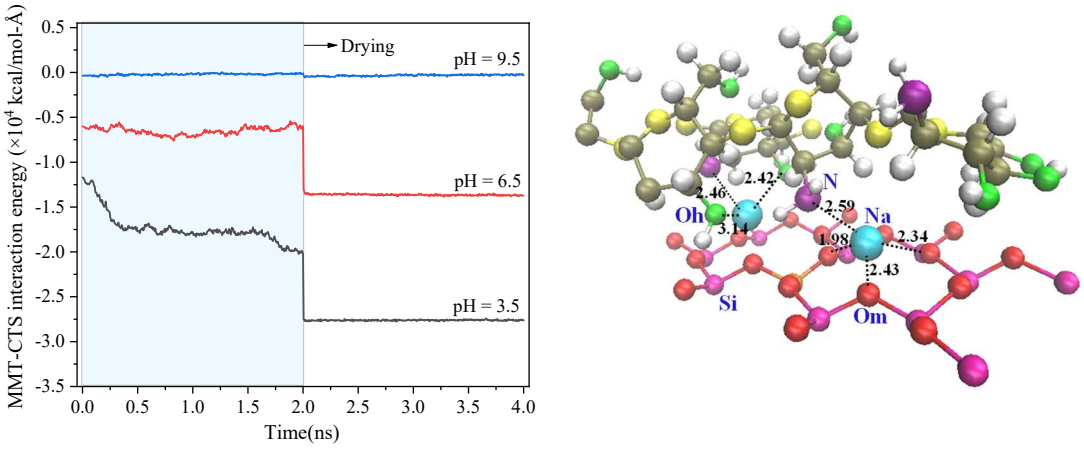

Fig. 4-3 (a) The interaction energy between the MMT and CHT; (b) Snapshot of dry CHT-MMT segment at pH=9.5. Om: oxygen atom of MMT; Oh: oxygen atom of OH group; N: nitrogen atom of NH_2 group.

To evaluate the mobility of CHT, the mean-squared displacement (MSD) of amine

groups (-NH_3^+ and -NH_2) and hydroxyl groups are studied as shown in Fig. 4-4(a) and (b), respectively. The self-diffusion coefficients (D) were estimated by the 1/6 linear slope (dashed line in Fig. 4-4) of MSD versus time in the region of 1 ~ 2 ns. Particularly, the diffusions of CHT in pure water (Fig. 4-5) were also studied as a comparison to evaluate the role of the MMT in the solubility of CHT chains. Table 4-2 lists D values of amino groups in water with and without MMT. The obtained D_{amine} and $D_{hydroxyl}$ values at pH = 9.5 are larger than that at pH = 6.5. The lowest mobility of -NH_3^+ and -OH groups is found at pH = 3.5. It is noticed from Fig. 4-4 that they are mostly diffusive in water with increasing pH. Moreover, $D_{amine} < D_{hydroxyl}$ was always found at the same pH. The diffusivity of amine and hydroxyl groups is controlled by electrostatic interactions with the negatively charged clay mineral. The affinity on the MMT surface is followed by -NH_3^+ > -NH_2 > -OH. After fully drying, these MSD curves keep relatively unchanged in all cases, suggesting that the CHT chains is highly restricted by the MMT surface even at pH = 9.5.

From Table 4-2, the negative slopes of MSD curves in water-MMT system at pH 3.5 and in pure water system at pH 9.5 indicate that CHT backbones are insoluble. Configurations of CHT in Fig. 4-5 also show that CHT is dispersive and soluble in acidic solutions, which is in agreement with previous study [204]. The underlying cause of the dispersion is the electrostatic repulsive interaction between the CHT chains, which carry more positive charges as pH decreases [205]. The CHT chains aggregate at pH 9.5, mainly due to hydrophobic attractions. Indeed, the hydrophilic functional groups (-OH and -NH_2) present in CHT cannot sufficiently change its hydrophobic nature [206]. In the presence of clay minerals, however, electrostatic attraction of the MMT is strong enough to gather these dispersed CHT chains to the MMT surface. At basic pH, CHT chain becomes more rigid and immobile due to the deprotonation, making them difficult to rearrange especially with the existence of clay attraction [201]. Therefore, our study reveals the completely different morphology of CHT in pure water and near clay mineral surfaces.

Therefore, we can conclude that CHT chains coat on the MMT surface mainly

contributed to -NH_3^+, while hydroxyl groups and neutral amino groups exhibit fewer contributions. Regarding this, it is better to control the solution in acidic condition to ensure 100% protonation of CHT in order to get well-coating CHT-MMT nanocomposites.

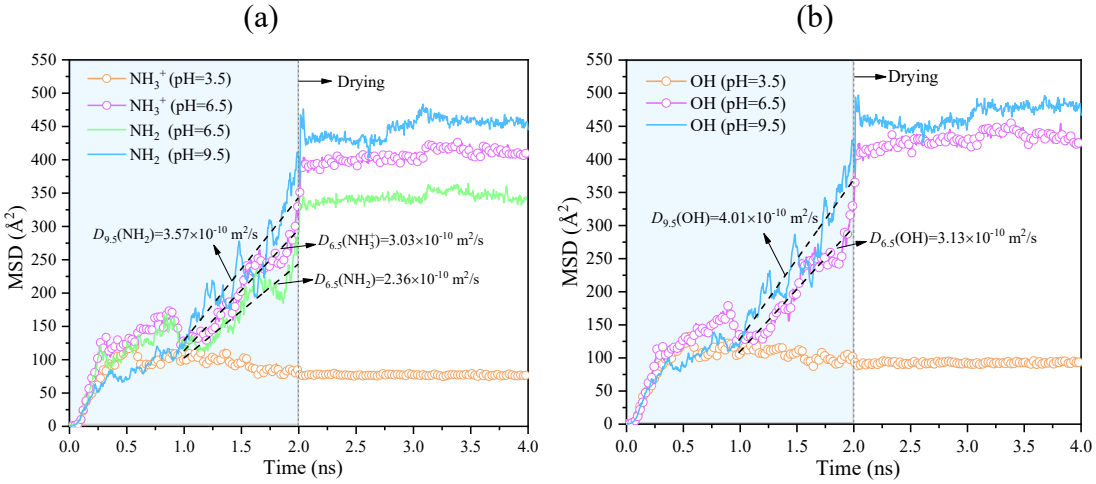

Fig. 4-4 MSD curves of (a) -NH_2/ -NH_3^+ and (b) -OH groups of CHT in water-MMT solution and dry condition.

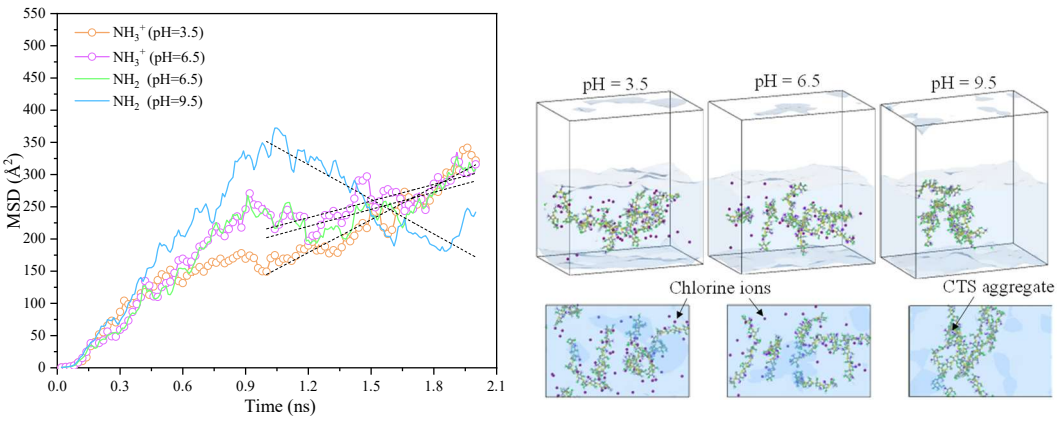

Fig. 4-5 MSD curves of amino groups in pure water with different pH values and corresponding configurations in the absence of MMT.

Table 4-2 Self-diffusion coefficient (D) of neutral and charged amino groups in water-MMT and pure water system. (in m^2/s)

system	pH	3.5	6.5	9.5
water+MMT	$D_{NH_3^+}$	negative	3.03	-
water+MMT	D_{NH_2}	-	2.36	3.57
pure water	$D_{NH_3^+}$	2.84	1.44	-
pure water	D_{NH_2}	-	1.47	negative

4.3.2 Coating mechanisms in CHT-MMT fabrication

According to the above discussion, a well-coated clay surface is expected to acquire in a strong acidic condition. Structural evolution in the drying procedure was illustrated by the case of pH = 3.5. Three snapshots of equilibrated MMT-CHT in different hydration states are visualized in Fig. 4-6, including state B in the aqueous solution, state D with a moisture content of 11.7 *wt*%, and state E in the fully dry condition. Dry and hydrated MMT-CHT are simulated by deleting all and partial (with 4 Å water thickness left) water molecules from state B. Fig. 4-7 shows the corresponding interaction energy between MMT and CHT in three systems, as well as the distance (r) between the center of mass of six CHT chains and the montmorillonite surface (MS).

It is seen from configurations at the state B that only a limited number of $-NH_3^+$ (in purple) and -OH (in green) groups of CHT will adhere to the MMT surface in the water solution. The distance (r) of CHT-MS decreases from 10 Å to 8.1 Å to 6.7 Å in the aqueous solution. As can be seen from the state B to state C1 and state C2, CHT backbones suddenly collapse onto the clay after water removal as the r suffers a rapid drop and then keep a steady value of 4.5 Å and 3.4 Å in hydrated and dry conditions, respectively. The MMT-CHT interaction accordingly becomes stronger as their separation distance shortens. More pronated amino groups can be adsorbed on the MS with reduced water content, as seen in the front and side views of CHT-MMT. The

lower interaction energy between MMT and CHT reveals a more stable MMT-CHT composite which can be achieved with less water. CHT backbones can fully spread on the clay only in a totally dry condition in state E. It is suggested that a drying process is necessary to obtain a well-coated nanocomposite as water plays a hinder role in the combination of MMT and CHT.

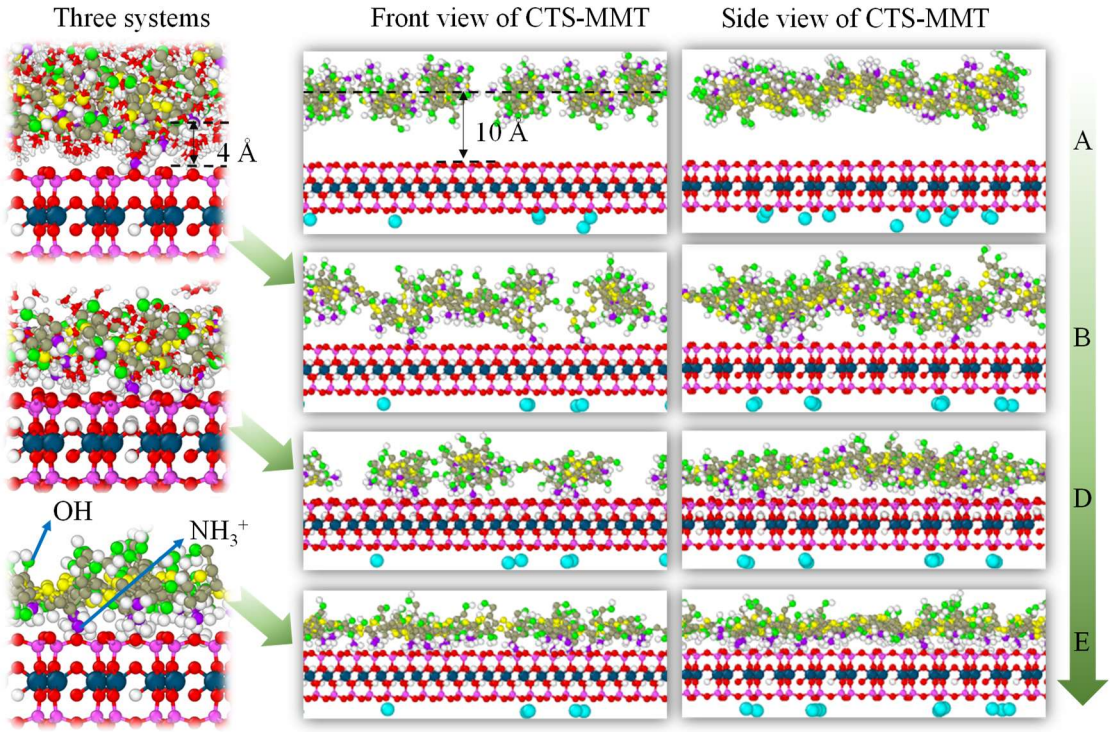

Fig. 4-6 Snapshots of the system at different hydration states. For clarity, water molecules are removed to show CHT-MMT in front and side views. Note: the state A and state B for the initial and equilibrated state of the MMT-CHT solution system, respectively; the state D and state E for the equilibrated state of hydrated and dry MMT-CHT system, respectively.

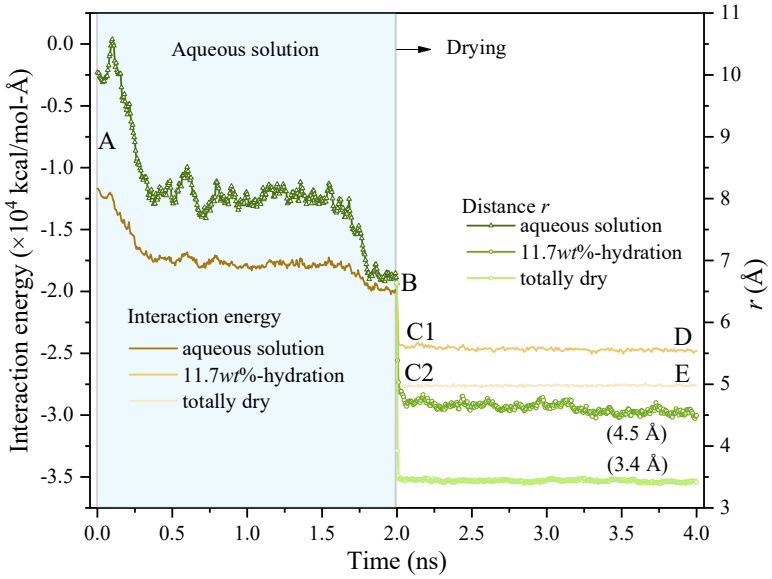

Fig. 4-7 Interaction energy between MMT and CHT, and the distance between the center of mass of CHT and montmorillonite surface (MS). Note: the state C1 and state C2 for the MMT-CHT composite after deleting partial and all water from state B.

The bonding interactions of -NH_3^+ and -OH groups of CHT with oxygen atoms of MMT surface are further verified by RDFs and coordination number (N) of O-N pairs and O-Ho pairs at the state B, D, and E, as depicted in Fig. 4-8. It is found that $g_{O\text{-}N}(r)$ curves present sharp peaks within 2.5 Å at state D and state E, corresponding to a strong electrostatic interaction between pair atoms. Previous studies have also reported that the electrostatic attraction between the -NH_3^+ group and the negatively charged Na-MMT surface provides the thermodynamic driving force for the organo-mineral complexation [207-208]. Furthermore, Zhu et al. [209] performed density functional calculations on the adsorption of glycine with -NH_3^+ endings on kaolinite surfaces, and their electron density difference results showed that no direct bonds were formed between NH_3^+ and negatively charged clay surfaces, but that strong electrostatic interactions occurred. The coordination number $N_{O\text{-}N}$ follows the order: $N_B << N_D = N_E = 0.06$. From $g_{O\text{-}Hw}(r)$ curves, it is found that the first layer of water is located at around 2.65 Å, which is slightly larger than $r_{O\text{-}N}$. With water dissipation, it is achievable for -NH_3^+ groups penetrating the first water layer to be adsorbed on the clay so that $N_{O\text{-}N}$ is dramatically increased. The O-Ho interaction distance is about 1.7 Å in both hydrated

and dry CHT-MMT composite systems with the same coordination number $N_{O\text{-}Ho}$ of 0.02. The value of $N_{O\text{-}Ho}$ is three times smaller than $N_{O\text{-}N}$. The first peak of $g_{O\text{-}Ho}(r)$ at the state B is found located at 3.22 Å, indicating that OH groups have no interaction with the clay.

Therefore, it can be concluded that the clay surface is more appealing to $-NH_3^+$ groups than -OH groups due to a much larger coordination number of O-N pairs. The CHT-MMT interaction is basically produced by electrostatic and hydrogen bonding interactions attributed to $-NH_3^+$ groups. There is a possible buoyancy effect in the aqueous solution, which consequently prevents the interaction of CHT-MMT, that is why a drying process is needed in its fabrication.

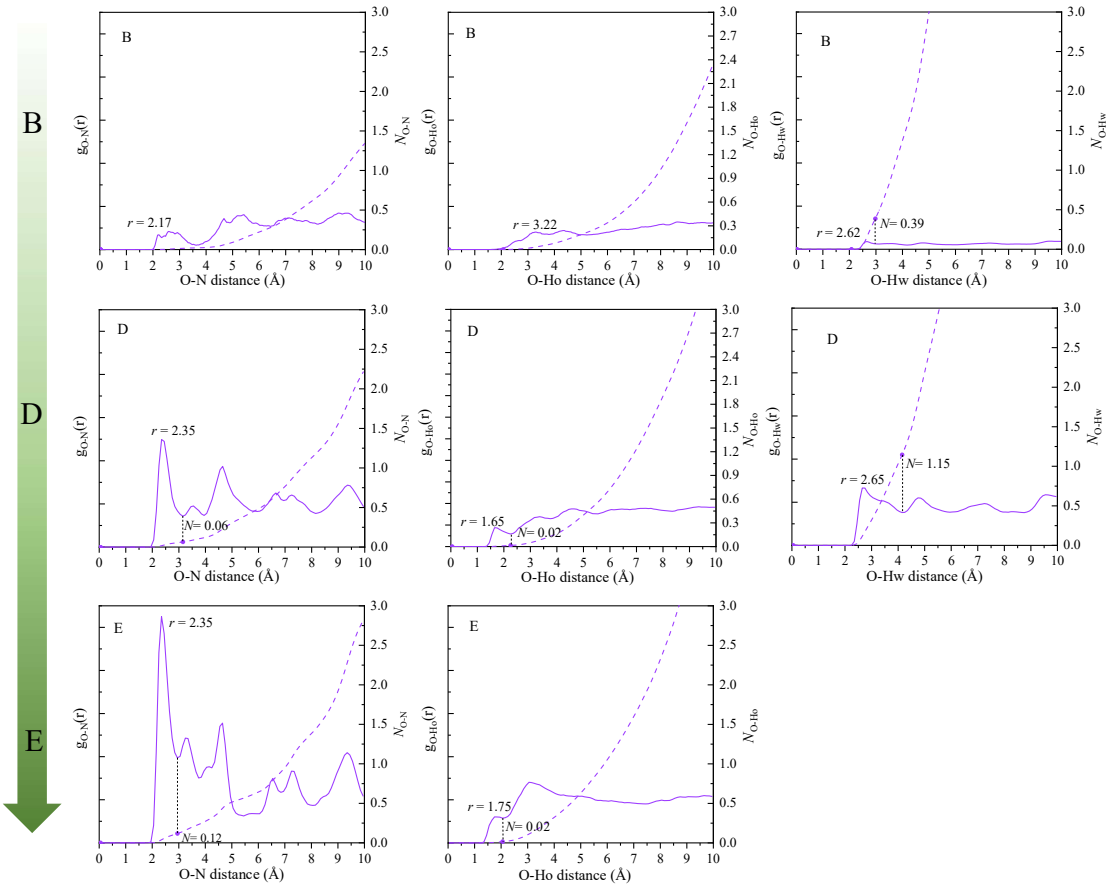

Fig. 4-8 RDF curves and coordination number (N) between O-N pairs, O-Ho pairs and O-Hw pairs at the state B in an aqueous medium, the state D with 11.7 *wt*% hydration, and the state E in dry condition.

4.3.3 Thermal stability of the CHT-MMT nanosheet

CHT is soluble in acidic media and this weakens the stability of CHT films. The solubility of CHT is a serious concern for its applications in an aqueous environment. In this regard, MD simulations were performed on structural responses of the dry CHT-MMT nanocomposite in an aqueous solution with various temperatures. The bulk water was initially placed right on top of the dry composite region (DCR). This composite is obtained at pH=3.5 with about 1.5 nm thick. The initial system is described in Fig. 4-9. The minimization operation was first conducted and then two different heating procedures were implemented under NVT ensemble. The first one was to control temperature linearly rising from 0 K to 800 K for 2 ns in order to foresee the structural change of this organoclay at extremely high temperatures. The second one was under a set of fixed temperatures of 273 K, 298 K, 348 K, and 398 K for 2 ns, respectively, which are common temperatures in effluent. To prevent water evaporation or migration beyond the initial *z*-bound at high temperatures, a non-periodic and fixed boundary in the *z*-direction is imposed accompanied by a virtual reflecting wall over the water solution, as shown in Fig. 4-9.

The high thermal stability of this organoclay is evidenced by the elevated temperature required to obliterate the organic modifier from the clay substrate. Hence, the adhesion rate of nitrogen atoms, which is defined as the proportion of the number of NH_3^+ groups within the first coordination shell of O_{MS} ($r_{O\text{-}N}$ = 2.35 Å), is calculated to reflect the desorption of CHT. The number of water molecules entering the dry composite region (DCR) is recorded, as seen in Fig. 4-9(c).

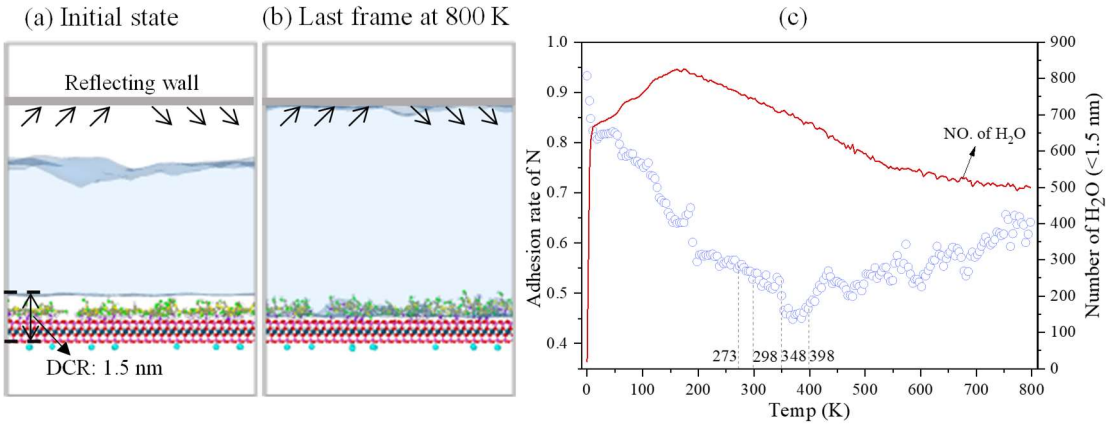

Fig. 4-9 Schematic of the initial system (a) and the snapshot of the last frame (b) in the first heating mode; (c) The evolution of adhesion rate of N and number of H_2O entering DCR with temperature from 0~800 K.

In the rapid heating process, a continuing loss of the adhesion rate of protonated amino groups is observed from Fig. 4-9 until temperature up to 400 K, suggesting that CHT chains became unstable and would be peeled off from the clay surface. However, the number of water molecules in DCR kept declining from around 200 K due to temperature rise. It shows an opposite trend of adhesion rate, implying that there is a temperature-dependent peeling for CHT-MMT composites in the range of 200 K ~ 400 K instead of water-induced peeling, which may occur in the earlier time when the number of water molecules in DCR increases. The reduction of water in DCR tends to be slight after 550 K due to water evaporations, since water will fill the region below the reflecting wall, as seen in the last frame. As a consequence, partially stripped NH_3^+ groups unexpectedly started to re-adhere to the MMT surface leading to the increase of adhesion rate of N.

The temperature of water evaporation is predicted to be around 550 K from our results. It is in good agreement with previous experimental results that the weight loss of CHT-montmorillonite nanocomposites between room temperature and about 500 K is attributed to the loss of adsorbed water molecules [193]. Another study also found that the maximum mass loss of CHT-clay beads was around 217.12 °C [190]. The lowest adhesion rate of N is found at near 370 K with a large value of 44.8%. It seems that the

composite structure is hardly affected by water evaporations in an aqueous solution. It is reported that the decomposition of amino units may occur at 135~300 °C [189] and the combustion of the intercalated CHT may occur between 500 and 800 K [193]. However, these phenomena cannot be found in our MD simulations since they were conducted under an aqueous condition.

No considerable desorption or exfoliation phenomena can be found even at extremely high temperatures. Even though some parts of CHT chains still have the potential to be peeled off, the whole CHT backbones remained adsorbed, signifying strong and stabilized coating polymer adhesion to clay layers. Our results indicate that the coating process of monolayer CHT onto clays is irreversible because desorption of this polymer requires the simultaneous desorption of all of the ionic sites in a polymer chain and the diffusion away from the clay surface.

The above continuous linear heating mode does not take contact time into consideration. The microstructure of this composite in water was further evaluated under a series of fixed temperatures at 273K, 298 K, 348 K, and 398 K and the corresponding steady states are shown in Fig. 4-10. The water density declined with increased temperature, leading to a decrease of water number in DCR (Fig. 4-10(b)). It can be noted from Fig. 4-10(a) and (b) that the adhesion rate of N atoms decreases at the beginning for all the cases; whereas the number of water molecules entering DCR gradually increases. This proves the water-caused peeling phenomenon that some NH_3^+ groups would be peeled off from the clay substrate when the dry composite is initially exposed to water.

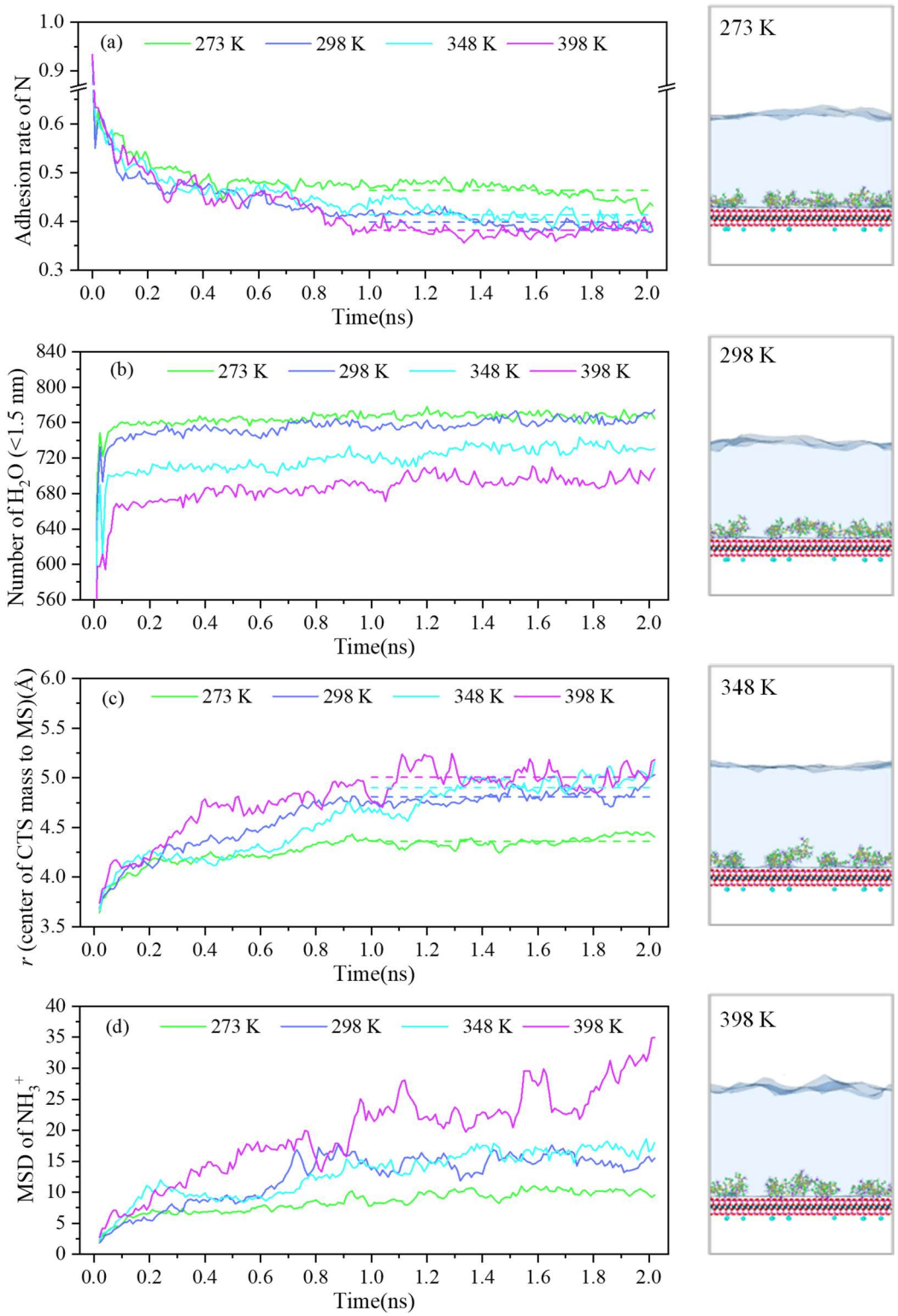

Fig. 4-10 (a) Evolution of adhesion rate of N, (b) Number of H_2O entering into DCR, (c) Distance between CHT and MMT, and (d) MSD curves of NH_3^+ as a function of time. On the right are snapshots of equilibrated states at 273 K, 298 K, 348 K, and 398 K.

When the composite was immersed in water after equilibrium, the adhesion rate of N atoms kept steady, fluctuating around 46.4%, 39.8%, 41.3%, and 38.1% at 273K, 298 K, 348 K, and 398 K, respectively. As temperature increases, the distance (*r*) between the center of mass of six CHT chains and the MS increases to 4.4 Å, 4.8 Å, 4.9 Å and 5.0 Å. The smooth MSD curves of pronated amino groups in Fig. 4-10(d) indicate that CHT is in a relatively stable configuration except at 398 K. Large movement at 398 K suggests these biopolymers become active and unstable. All these indicators show a little difference between 298 K and 348 K.

Therefore, the high thermal stability of the CHT-MMT composite under 398 K was confirmed because no decisive desorption of this biopolymer can be observed. Our result suggests that CHT polymer-modified clay is a thermally stable composite material that will not generate secondary pollutants (CHT) in water.

However, there are some limitations of using the current force field. Thermodynamically consistent force field parameters are sensitive to deviations from the reference state from which they were derived [127]. The simulation phenomenon is found based on the use of SPC model as solvent. A previous study found that at elevated temperatures (> 400 K), the diffusion behaviors of SPC water may deviate from experimental results [210]. At temperatures above 400 K, the possible influence of the properties of the water solvent on the composite structure is not considered in this study. Another limitation of the PCFF-IFF is its inability to simulate the formation and breakage of chemical bonds, especially when studying the coating mechanism of CHT on the MMT. It cannot directly determine whether the possible formation of covalent bonds between the NH3+ groups and the MMT surface or their breakage during peeling process at high temperature. This MD study used the alternative RDF method to investigate their interaction distances to reveal the binding interaction.

4.4 Conclusions

In this chapter, the fabrication of CHT-MMT nanocomposites was simulated based on the protonation rate and drying process of CHT. In addition, the thermal stability of

the CHT-MMT nanocomposite was investigated in an aqueous solution. This study provides insight into the fabrication and design of this type of composites.

As a result of RDF and MSD studies, CHT coating on the MMT surface is mainly contributed to protonated amino groups via electrostatic and hydrogen bonding interactions. Whereas hydroxyl groups and neutral amino groups exhibit little contributions. Our results reveal that higher adhesiveness and more uniform distribution of CHT on the clay surface can be achieved with 100% protonation of CHT by drying completely.

Furthermore, immersion simulations for the dry CHT-MMT composite present both water-induced peeling and temperature-induced peeling of polymer chains from clay substrate. The lowest adhesion rate of NH_3^+ is found at near 370 K with a large value of 44.8%. The composite structure is hardly affected by water evaporations, which occurred at around 550 K in an aqueous solution. Therefore, no considerable desorption or exfoliation phenomena can be found even at extremely high temperatures, despite some parts of CHT chains still having the potential to be peeled off. The whole CHT backbones remained adsorbed.

Chapter 5

Adsorption for cationic MB dye on CHT-modified MMT

5.1 Introduction

In chapter 4, we studied pH and temperature effects on the structural stability of CHT-MMT. To promote the application of this composite in water treatment, more efforts should be made to explore the adsorptive performance and mechanisms of CHT-MMT composites, which can provide insights for optimizing the design of adsorption systems.

In the majority of published research, the evaluation of an adsorbent is usually based on the adsorption isotherm and kinetic models by fitting experimental equilibrium data [211-212]. Adsorption kinetics describe the rate of adsorption, while adsorption isotherms explain how the adsorbates interact with the surface adsorption sites. For example, the Langmuir isotherm model assumes a monolayer of adsorbate on a homogeneous surface with negligible interaction between adsorbed molecules. The Freundlich model indicates multilayer adsorption on a heterogeneous surface, assuming adsorption on different sites with different adsorption energies [213]. However, adsorption modes are not visualized in experimental evaluation methods.

In this chapter, MD simulations are carried out to explore adsorption mechanisms and evaluate the adsorption capacity of CHT-modified MMT (CMMT) for cationic MB considering pH effects. Equilibrium configurations, density profiles, RDF, and interaction energy were studied to reveal adsorption characteristics and mechanisms. Based on the discussion of individual dye diffusion behaviors, an evaluation method of immobilization ability of these surfaces for MB was proposed to quantify the adsorption amount and efficiency.

5.2 Simulation methodology

All the simulations were performed using the LAMMPS code [214]. The hybrid force fields CLAYFF and CVFF were applied to describe the atomic interactions of inorganic and organic components, respectively. Water molecules were described by the rigid SPC model, where the bond distances of water were fixed using the SHAKE algorithm

[215]. A truncation distance of 1.0 nm was set for the calculation of VDW and short-range Coulombic interactions. The long-range electrostatic interactions were computed through the Ewald summation method with an accuracy of 10^{-4} kcal/mol [152]. The periodic boundary conditions were applied the in *x*- and *y*-direction, while the free boundary was applied in *z*-direction, with a reflecting wall at the upper boundary to prevent particles from moving outside the simulation box. The whole simulation consists of two processes: surface modification and adsorption, as presented schematically in Fig. 5-1.

A bilayer MMT modelled by $Na_{0.75}[Si_{7.75}Al_{0.25}](Al_{3.5}Mg_{0.5})O_{20}(OH)_4$ [216] was used as a substrate with dimensions of 4.15 nm × 5.38 nm in the *xy*-plane. The bottom MMT layer was frozen throughout the whole simulation. According to chapter 4, the CMMT surface herein was initially constructed at pH 3.5. There are five steps to prepare CMMT surfaces. In the first step (see Fig. 5-1), the four CHT chains containing with a total of 36 $-NH_3^+$ groups were introduced and equilibrated on the MMT surface, followed by a complete drying procedure which is the second step and equilibration to form the dry CMMT-pH3.5 surface. It is expected to achieve the surface modification of 100% of cation exchange capacity of single layer MMT. Then, the third step is to put the dry CMMT-pH3.5 surface into water and equilibrate to obtain composite solution. The fourth and fifth steps are to obtain CMMT-pH6.5 and CMMT-pH9.5 solutions by converting 50% and 100% of $-NH_3^+$ in the CMMT-pH3.5 solution to $-NH_2$, respectively, and equilibrating. Each of the above equilibration steps started with minimization and was run for 0.5 ns under the NVT ensemble at 298 K. The unmodified MMT solution was also built using the same procedure as the third step.

To start adsorption simulations, 20 methylene blue molecules were added to these systems. The initial dye concentration is 15.09 *wt*%. The dyes have the same initial relative position in each system to eliminate possible position effects. Adsorption simulations were then run under NVT ensemble for a total of 3.1 ns, including a pre-run of 0.1 ns to heat up the systems from 1 K to 298 K and a subsequent run of 3 ns at 298 K.

Fig. 5-2 shows the evolution of total energy of four adsorption systems over the entire 3.1 ns run. All the systems reach their equilibrium state quickly as their total energy converges rapidly.

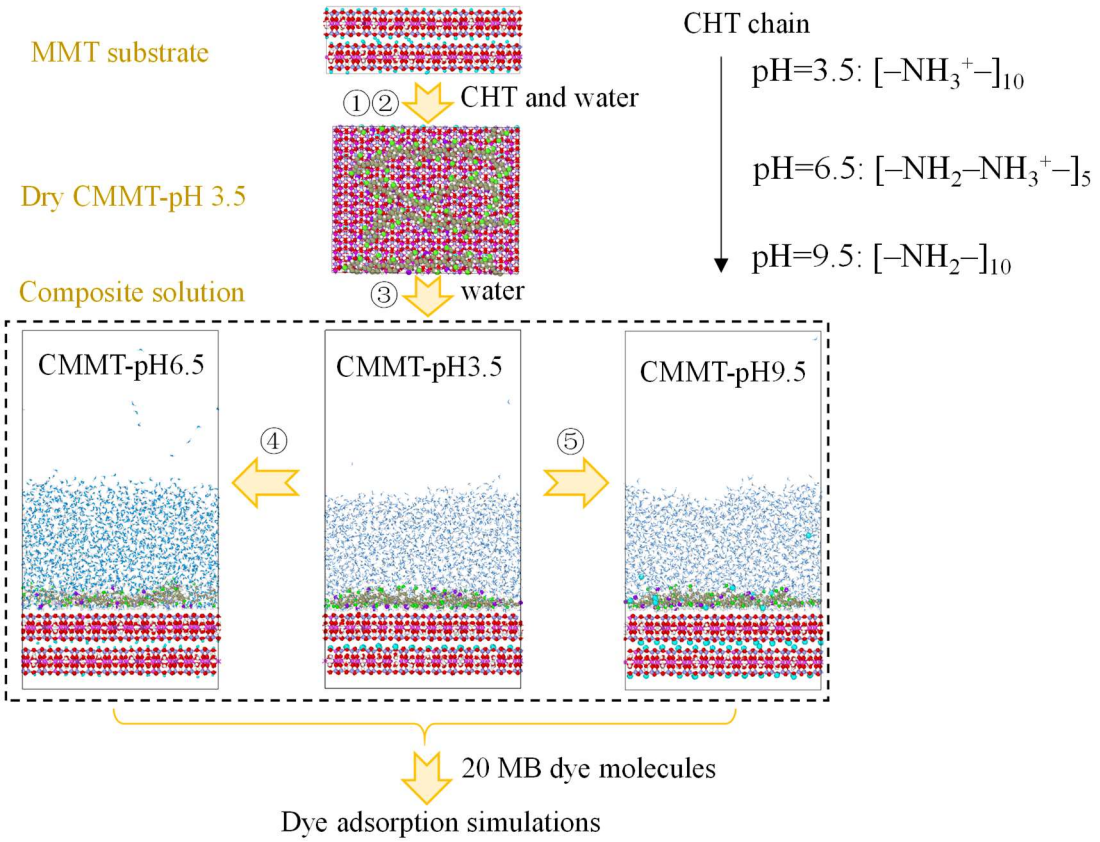

Fig. 5-1 Schematic diagram of CMMT construction and dye adsorption simulation.

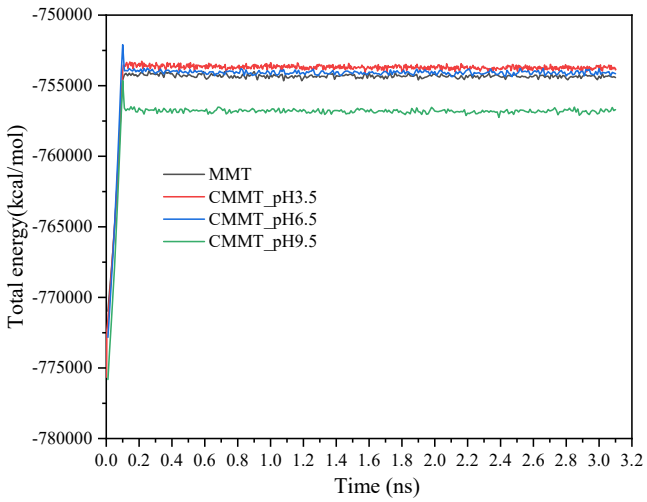

Fig. 5-2 Total energy of four adsorption systems

5.3 Results

5.3.1 Adsorption characteristics

The equilibrated conformations and adsorption sites on the pure and modified MMT surfaces will be discussed in this section. Fig. 5-3 shows the snapshots of four systems extracted from the last frame of atomic trajectories. From these configurations, monolayer coverage of MB is found on the MMT surface. All the MB dyes are in a horizontal orientation and their molecular plane are perpendicular to the surface. However, the multilayer adsorption readily occurs in CMMT systems and is visualized in the form of stacked MB molecules. The observed two adsorption modes correspond to characteristics of the Langmuir and Freundlich isotherm.

The relative position of MB and CHT reflecting the dye adsorption sites and the stability of coated surfaces can be illustrated by *N*-density distribution of MB (middle nitrogen) and CHT (NH_2/NH_3^+), as exhibited in Fig. 5-4. The dashed red line represents the *z*-position of the MMT surface. From Fig. 5-4(a), about 2/3 of the adsorbed dyes face the MMT surface with the N side, while the rest face with S side. The maximum position of N_{MB} to the MMT surface in direct contact is located at $z = 27.5$ Å. The initial distributions of N_{CHT} (dashed pink line) end approximately at $z = 30$ Å, which is the position of CHT surfaces. The equilibrated distributions of N_{CHT} (solid pink line) show that some of the CHT chains are stripped off by adsorption to MB and CHT chains no longer cover the MMT surface perfectly, especially in neutral and basic media. In the CMMT-pH3.5 system, there is no intersection between N-density curves of MB and CHT, indicating that MB does not appear to be directly adsorbed on this surface. For the CMMT-pH6.5 and CMMT-pH9.5 surfaces, the N-density peaks of MB were located at $z = 29.5$ Å and $z = 27.5$ Å, respectively. This suggests that the adsorption sites of MB are only on CHT at pH 6.5, and on both CHT and MMT surface at pH 9.5.

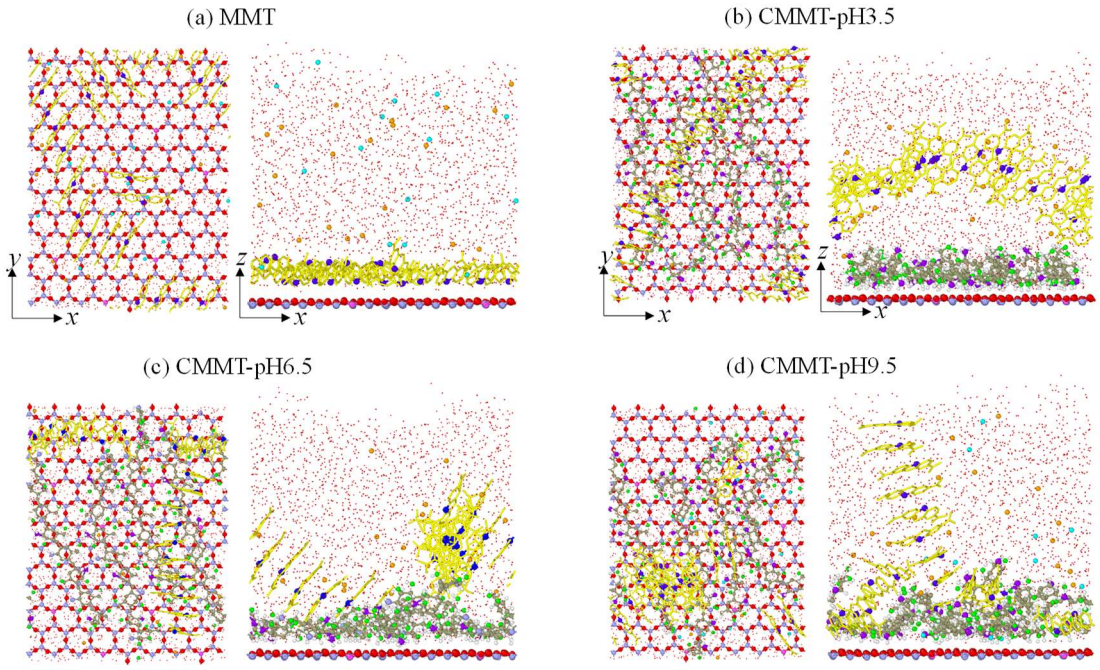

Fig. 5-3 Snapshots of four systems extracted from the last frame of atomic trajectories. For clarity, the MB dyes are colored by yellow and their middle N atoms are marked in blue. MMT is hidden and only its Si-O surface is shown. Water molecules are simply represented by O_{water} with red dots. The light blue atoms are sodium ions and the orange atoms are chloride ions.

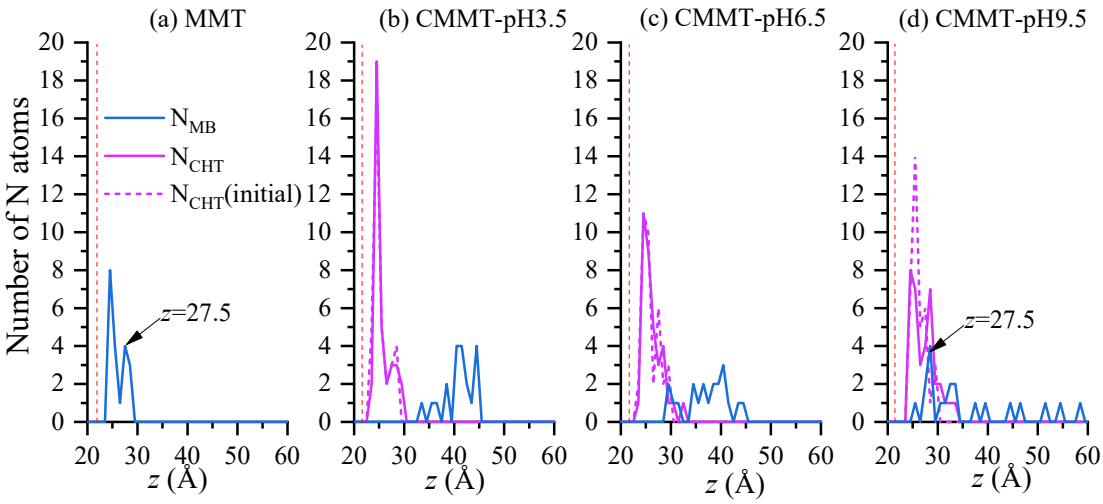

Fig. 5-4 Density profiles of the middle nitrogen atom of MB, and nitrogen atoms in amino groups of CHT.

5.3.2 Interaction mechanisms

The Radial Distribution Function (RDF), g(r), is an important structural indicator that reveals the bonding information. The g(r) of MB-MB and CHT-MB were calculated and plotted in Fig. 5-5. The RDF of the aromatic carbon (C_p) pairs of MB shows that there are strong interactions between MB dyes, indicating a type of non-covalent π–π stacking interactions that occur between the aromatic rings of organic molecules. As a result, MB molecules are easily self-assembled. As for the role of CHT, the negatively charged hydroxyl groups are the main contributors to the attraction of MB, as demonstrated in Fig. 5-5(b), but they only work in neutral and basic media. A distinct peak was found located at 2.65 Å at pH 9.5, indicating strong hydrogen bonding interactions between CHT and MB. According to references [217-218], H-bonds can be formed not only between the free hydrogen of the CHT with electronegative atoms such as nitrogen in the dye structure, namely dipole-dipole H-bonding, but also between the hydrogen of hydroxyl groups and the aromatic rings of MB, called Yoshida H-bonding interaction.

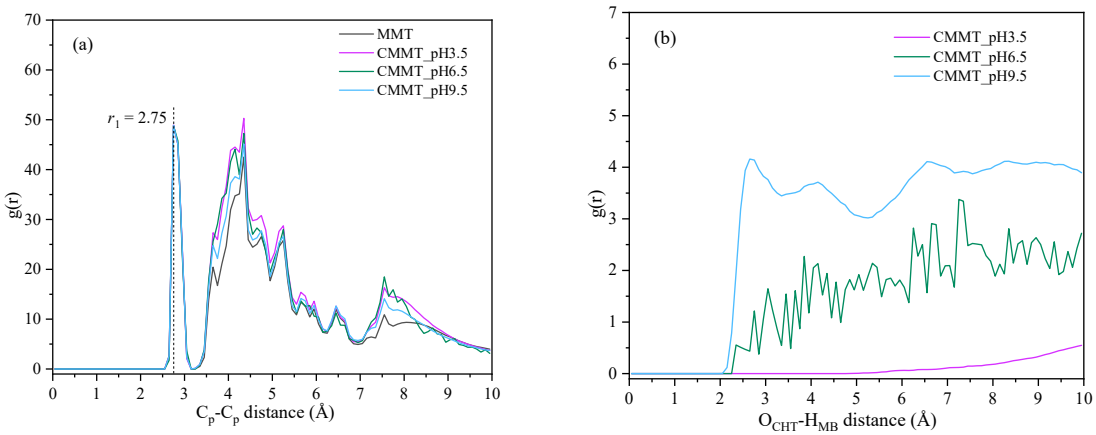

Fig. 5-5 RDF curves of (a) MB-MB, (b) CHT-MB

The adsorption energy of MB on unmodified MMT surface is equal to -185.87 kJ/mol per molecule, which is comparable to our previous results [44]. For CMMT systems, MB can be effectively adsorbed either by the surface (including MMT and CHT) or by surface-adsorbed dyes, which, unlike monolayer adsorption on pure MMT

surface, have different interaction energies at different sites. Accordingly, the assessment of multilayer adsorption strength cannot be based solely on the adsorption energy between dyes and the surface. It is more comprehensive to investigate the non-bonding interaction energy between dyes and other components, which is calculated and illustrated in Fig. 5-6.

A larger absolute value of E_{int}(Surface&Dye) indicates a stronger direct contact between surface and dyes. E_{int}(Dye&Dye) represents the intermolecular interaction between MB molecules. A smaller E_{int}(Water&Dye) reflects less MB dissolved in the solvent. It is observed that the E_{int}(Surface&Dye) increases with pH in modified surfaces and E_{int}(Dye&Dye) is correspondingly weakened. The interaction between dyes and the CMMT surface is much smaller than that without modification. However, the intermolecular interaction between dyes is significantly enhanced. This suggests that monolayer adsorption depends on a strong E_{int}(Surface&Dye), while multilayer adsorption relies on a greater E_{int}(Dye&Dye).

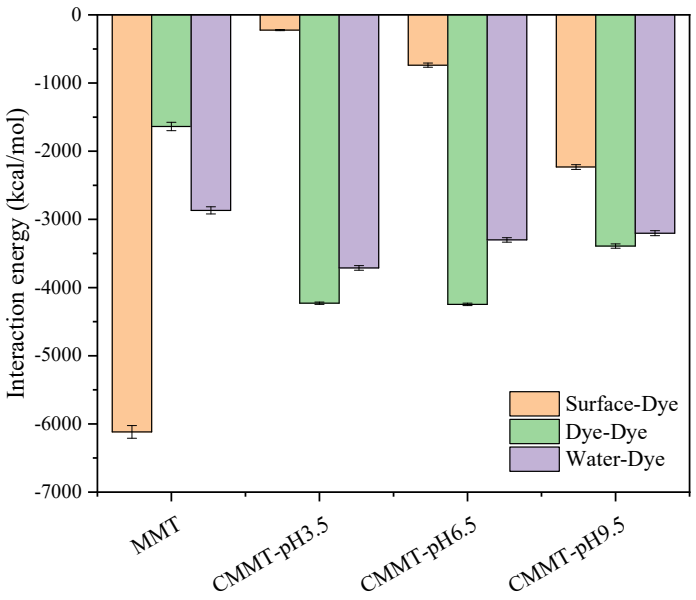

Fig. 5-6 Interaction energy between dyes and other components.

5.3.3 Diffusion and atomic mobility of dyes

The MSD and diffusion coefficients (D) were analyzed to investigate the diffusion

and mobility of dye molecules. The instantaneous MSD values were calculated every 0.01 ns over the whole 3.1 ns trajectories. The average diffusion coefficients of MB (D_{MB}) on four surfaces are obtained from their MSD curves (Fig. 5-7), as listed in Table 5-1. These obtained D_{MB} values are in agreement with the fitted values obtained from the adsorption experiments carried out on other clay adsorbents and bio-adsorbents [163], [219-223]. The values of D_{MB} on three CMMT surfaces are 1.323×10^{-9} m^2/s, 0.888×10^{-9} m^2/s and 0.461×10^{-9} m^2/s at pH 3.5, 6.5 and 9.5, respectively. They are smaller than 1.326×10^{-9} m^2/s calculated in the MMT system, suggesting that CHT modification can provide more diffusion inhibition for MB only at higher pH. However, CHT at pH 3.5 shows little improvement in reducing MB mobility.

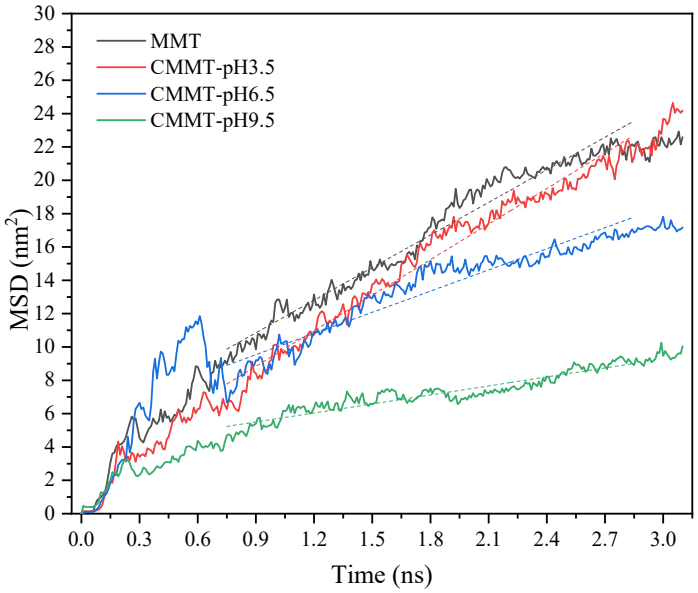

Fig. 5-7 The average MSD of 20 MB dyes in each system.

The diffusion characteristics of single dyes are revealed by studying two transport examples of MB1 and MB2 (see Fig. 5-8(a)) in the CMMT-pH9.5 system. Particularly, the D_{MB1} and D_{MB2} were estimated by fitting the slope of accumulated sets of their MSD values (Fig. 5-8(b)). Furthermore, the positions (x, y, z) of middle nitrogen atom of MB1 and MB2 were recorded every 5 ps to track their motion trajectories, as shown in Fig. 5-8 (c) and (d).

Table 5-1 The diffusion coefficients of MB (D_{MB}).

	D_{MB} ($\times 10^{-9}$ m^2/s)	Reference
MMT	1.326±0.007	This study
CMMT-pH3.5	1.323±0.006	
CMMT-pH6.5	0.888±0.008	
CMMT-pH9.5	0.461±0.003	
MMT and nontronite mixture	0. 016-0.315	[219]
7-nm/9-nm sized silica pore	0.797/1.214	[163]
Bentonite	0.184~0.191 (D_s)	[220]
	0.986~0.995(D_p)	
Bioadsorbent (Enterolobium contortisiliquum)	0.72~0.953 (PVSDM)	[221]
	1.65~2.03 (SDM)	
Paspalum notatum (lignin and cellulose)	0.648~0.986	[222]
stratum corneum	0.22±0.09	[223]

Note: D_s, D_p, PVSDM and SDM for the different theoretical models in fitting D.

The transport of MB1 undergoes from a diffusive state, which is from the solution to the near-surface region to an adsorbed state, which is from the surface to an adsorption site. Correspondingly D_{MB1} increases from the initial 0.6 ns to1.5 ns and slowly decreases over the next 1 ns before stabilizing at an average value of 0.605 ± 0.002 × 10^{-9} m^2/s in the last 0.5 ns. However, D_{MB2} remains constant at approximately 0.028 ± 0.002 × 10^{-9} m^2/s.

Despite MB1 initially being located farther away from the surface than MB2, MB1 was eventually adsorbed to the clay site, whereas MB2 was bound from the start by a cluster of surface-adsorbed MB dyes through π-π stacking interactions. These two adsorption modes appear to be random and independent of the initial distance to the clay surface. On the other hand, MB2 is less diffusive than MB1, indicating that the multilayer-adsorbed MB can also be effectively adsorbed.

(a) Snapshot of CMMT-pH9.5

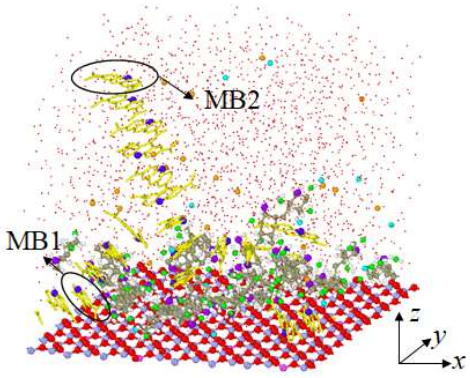

(b) MSD and *D* of MB1 and MB2

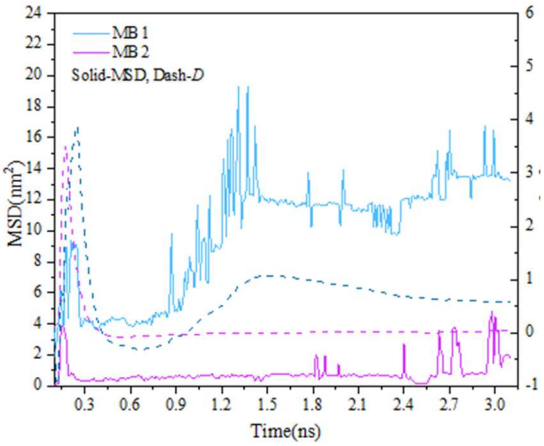

(c) The motion trajectory of MB1

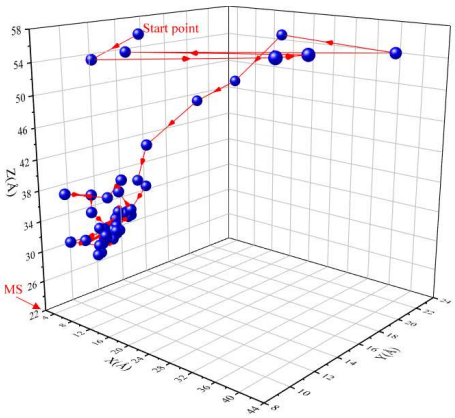

(d) The motion trajectory of MB2

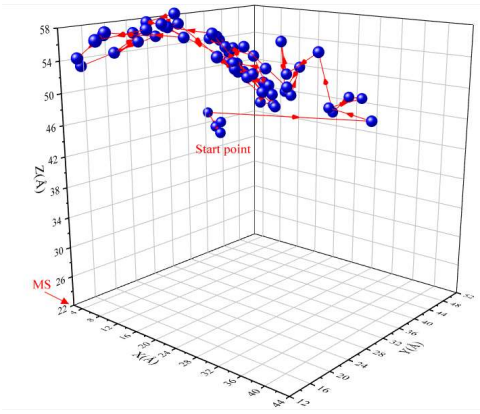

Fig. 5-8 Transport of individual MB1 and MB2 in the CMMT-pH9.5 system.

5.3.4 mobilization ability of surfaces for MB

Quantification of adsorption capacity is the most common way in laboratory experiments to assess adsorbents' adsorption ability. However, it is difficult to identify the adsorbed molecules from visual observations in MD simulations. Calculating the equilibrium concentration after adsorption become the biggest challenge. To address this, an evaluation method of the immobilization ability of surfaces, which refers to the ability to effectively bind or immobilize dye molecules, was proposed for the first time based on the diffusion of individual dyes. The basis for using diffusion properties to distinguish adsorbed molecules is that adsorbed MB can be regarded as inhibited MB by adsorbents with low diffusivity in aqueous systems. The mobility of each MB molecule can be reflected from both its MSD curve and diffusion coefficient.

In Fig. 5-9, MSD curves of 20 individual MB were plotted and offset along the y-axis to distinguish clearly. A plateau in a MSD curve indicates a subdiffusive and inhibited movement of MB. According to reference [224], such a plateau is originated from the cage effect: molecules are trapped in transient cages formed by their neighbors, thereby preventing them from diffusing freely through the medium. Thus, we use a criterion of the error of the mean MSD values (ΔMSD) in a specific time range as an approximate determination of a flat fragment of MSD curves.

To quantify the immobilized MB over time, we divided six time periods from 0.1 ns to 3.1 ns at 0.5 ns intervals and calculated the ΔMSD of each time period. The percentage of motionless MB molecules over time within a threshold of, for instance, ΔMSD < 15 nm^2, is shown in Fig. 5-10. The inhibited MB amount is observed increased from the second time period, indicating the progressive adsorptions of MB molecules on these four surfaces. The immovable MB reaches a maximum of 80~85% on the CMMT-pH9.5 surface. The immobilization capacity to MB is in the following order: CMMT-pH9.5 > CMMT-pH6.5 > CMMT-pH3.5 > MMT, corresponding to equivalent values of 158.79 > 121.29 > 102.63 > 95.00 mg/g. Our result is in good agreement with the previous work conducted by Jawad, et al. [225] finding that the highest removal of MB (156.1 mg/g) onto CHT/zeolite composite is achieved in an alkaline solution with pH 9. Another similar result has also been reported that the amount of MB adsorbed on CHT/bentonite composite increases with pH and is at a maximum at pH 11 [76]. It is clearly shown that CMMT surfaces have a better immobilization capacity for MB than the MMT surface.

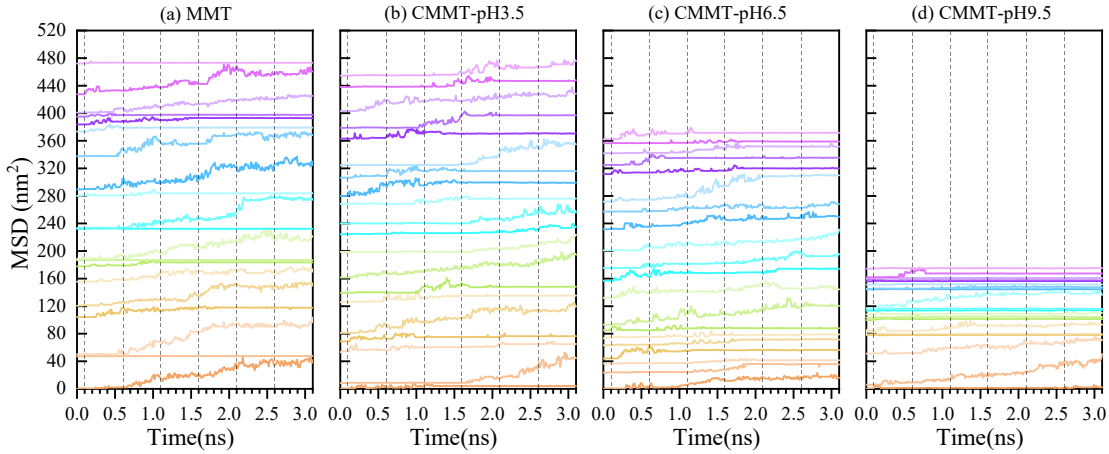

Fig. 5-9 MSD curves of 20 individual MB dyes in four systems.

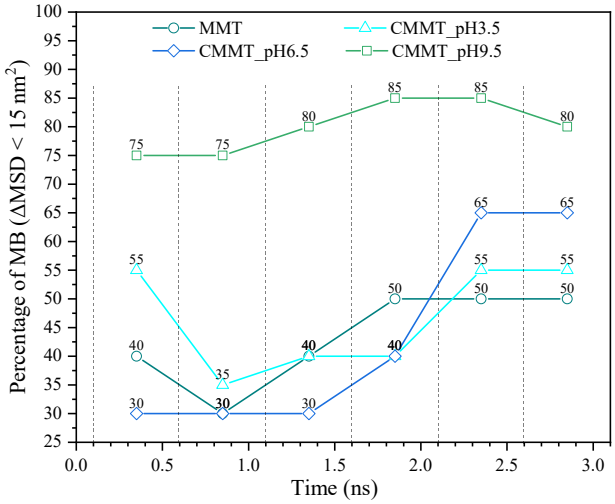

Fig. 5-10 The percentage of possible motionless MB molecules at six time intervals.

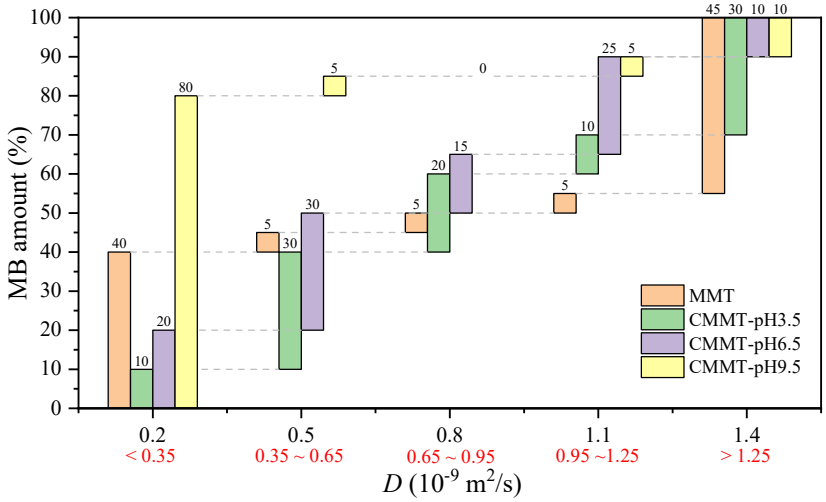

Fig. 5-11 The number frequency of 20 *D* values in each system in five intervals.

If a MSD plateau is maintained over a broad range of time scales, it will result in a relatively small *D*, indicating highly efficient dye adsorption and a rapid kinetic process. In this regard, the adsorption efficiency can be revealed under a criterion of the individual diffusion coefficient (*D*) throughout the process. The *D* values of each MB at time *t* were obtained by fitting the slope of cumulative sets of its MSD values (Fig. 5-9) within *t* and then averaging the *D* over the last 0.5 ns. The number frequency of the 20 *D* values in each system can therefore be divided into five intervals: < 0.35, 0.35 ~ 0.65, 0.65 ~ 0.95, 0.95 ~ 1.25, and > 1.25 with a unit of $\times 10^{-9}$ m^2/s, as illustrated in Fig. 5-11.

It can be seen that 80% of the dye molecules exhibit low diffusion characteristics on the CMMT-pH9.5 surface as their *D* values are less than 0.35 $\times 10^{-9}$ m^2/s. Traced back to the atomic trajectory, these dyes reached equilibrium rapidly due to the combined interaction with both CHT and stacked dyes, whereas the other four molecules (20%) with larger *D* are only adsorbed on the clay sites. However, in the cases of pH 3.5 and pH 6.5, the diffusion coefficients have broad distribution over the five intervals. Dyes on these two surfaces are basically confined by intermolecular dye interactions.

For the unmodified MMT surface, 40% of MB is concentrated in $D < 0.35 \times 10^{-9}$ m^2/s, while 45% has $D > 1.25 \times 10^{-9}$ m^2/s. The reason for this polarization of the *D* distribution is the time it takes for the dye to adhere to the MMT surface. The smaller the *D*, the earlier and easier they are adsorbed. It is seen that almost half of the molecules are immobilized by the surface at a later stage.

The threshold of *D* for effectively adsorbed molecules is crucial and, to the best of our knowledge, has not been reported yet. According to reference [219], the diffusion coefficient of MB on MMT was experimentally estimated to be up to 0.315×10^{-9} m^2/s. This value is closed to the upper range of our first interval of 0.35. Taking the assumption of $D < 0.35 \times 10^{-9}$ m^2/s as a benchmark for effectively adsorbed MB, the order of immobilization efficiency to MB on four surfaces is CMMT-pH9.5 > MMT > CMMT-pH6.5 > CMMT-pH3.5 with amounts of 80%, 40%, 20%, and 10%,

respectively. Moreover, most of the published D_{MB} on other similar adsorbents listed in Table 5-1Table 5-1 The diffusion coefficients of MB (D_{MB}). are less than 1 $\times 10^{-9}$ m^2/s. In this regard, when the threshold extended to the third interval (< 0.95 $\times$ 10^{-9} m^2/s), then the order of immobilization efficiency on four surfaces is CMMT-pH9.5 > CMMT-pH6.5 > CMMT-pH3.5 > MMT with amounts of 85%, 65%, 60%, and 50%, respectively. Hence, based on the above discussion under two thresholds, it can be concluded that the immobilization efficiency on CMMT surfaces is higher with increasing pH. Only in alkaline media can it be guaranteed to be higher than that of MMT. No significant enhancement is found in the strong acidic condition.

5.4 Discussions

5.4.1 The enhancing mechanism of CHT modification

According to the chapter 3, the attraction of MMT to cationic MB is dominated by strong electrostatic interactions. Indeed, in the absence of CHT modification, MB molecules first pile up through strong π–π interactions and then gradually collapse onto the MMT surface, resulting in their molecular planes being perpendicular to the clay and facing it in a random manner. The monolayer MB adsorption on the MMT surface is formed by the combined action of E_{int}(Surface&Dye) and E_{int}(Dye&Dye). The game between the attractions from MMT and stacked dyes is directly responsible for the kinetic rate of individual dye adsorption. On the other hand, such a vertical orientation of the dyes makes them wobble in water owing to a small contact area with MMT. Diffusion analysis in this study has demonstrated that the dyes have larger diffusion coefficients in clay-water systems without CHT.

Competition between clay modifiers and positive contaminants for adsorption sites on clay surfaces has always been an issue, whether the modifier is a surfactant or a polymer. From this study it was found that even though the CHT is not as attractive to MB as the clay, as long as free polar groups are present, the increased surface roughness with the CHT make it readily to capture some MB molecules from water.

Thus, it enables the binding of a cluster of stacked dyes due to the attraction between the aromatic rings of the MB dyes. Therefore, the main role of CHT modification is to expand surface roughness and thus significantly reduce dye mobility and contribute to faster and easier binding of dyes from water. The modified surfaces help to promote the formation of multilayer adsorption.

Although the final configuration on the unmodified clay surface in Fig. 5-3(a) showed that all molecules were adsorbed in a monolayer adsorption mode. The adsorption equilibrium time required is relatively longer than on modified surfaces. Furthermore, all dye planes were found perpendicular to the MMT surface, so it is less likely that the surface will firmly attract extra MB layers as modified surfaces do when higher dye concentrations are added. To verify this, we performed two further adsorption simulations on MMT and CMMT-pH9.5 systems with double dye concentration (40 molecules). The equilibrated conformation (Fig. 5-12**)** on the MMT surface showed that only about half of the dyes are adsorbed in a monolayer adsorption mode, while the rest of the dye is agglomerated and not attracted by the clay surface at all. It is seen from Fig. 5-13 that in the first 1.5 ns the dyes in both cases have similar low MSD values, which is attributed to the high dye concentration. Thereafter, as some MB are adsorbed, those in water exhibit an increasing diffusivity without restraint from CHT. Therefore, CHT-modified clay composites have the potential for cationic dye removal, especially at high dye concentrations.

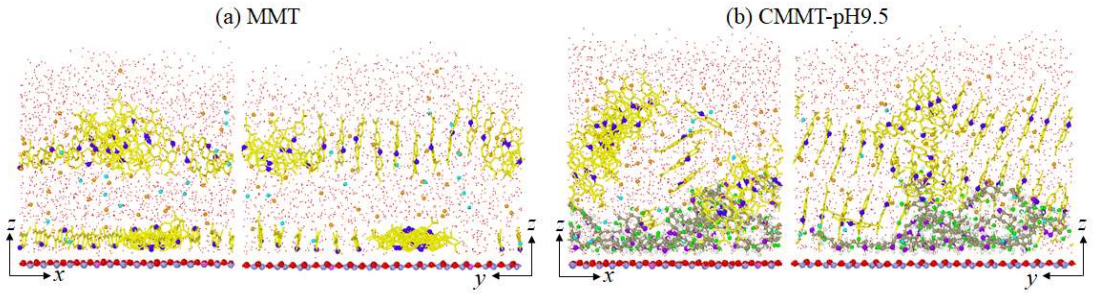

Fig. 5-12 Equilibrated configurations of 40 dyes on (a) MMT and (b) CMMT-pH 9.5 surfaces. For clarity, the MB dyes are colored by yellow and their middle N atoms are marked in blue. MMT is hidden and only its Si-O surface is shown. Water molecules

are simply represented by O_{water} with red dots. The light blue atoms are sodium ions and the orange atoms are chloride ions.

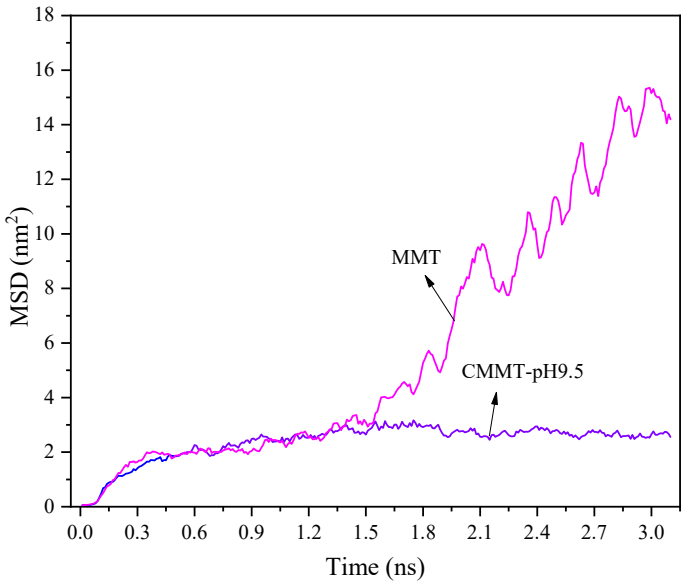

Fig. 5-13 The average MSD curves of 40 MB dyes in MMT and CMMT-pH9.5 systems.

5.4.2 Effects of pH on the stability and sorption efficiency of CMMT

To investigate the stability of CHT-MMT composites in the absence and presence of MB dyes, the interaction energy between CHT and the MMT ($E_{CHT\text{-}MMT}$) in aqueous environment was calculated from the potential energy difference of $E_{CHT\&MMT}$ and the sum of E_{CHT} and E_{MMT}. A lower value of the interaction energy means a more stable CHT-MMT hybrid. As listed in

Table 5-2, the $E_{CHT\text{-}MMT}$ increases when pH rises and after attracting MB, indicating that the CMMT surfaces become unstable during these changes. The stability of the CHT-clay composites can be achieved at lower pH because more $-NH_3^+$ groups can be firmly attached to the negative sites of clay surfaces through cation exchange. Further, as displayed in Fig. 5-4 the density distribution of nitrogen atoms of CHT, some amine groups are detached under basic condition but only when cationic dyes are present. The dominant factor for the retention and stripping of the CHT monolayer is not the pH but

the existence of MB. In fact, the stripping of CHT from MMT surfaces induced by organic contaminations is partial and does not cause stripping of the entire chain. Also, the detachment increases the surface area of the modified surface and at the same time improves the adsorption efficiency. Our results proved that the immobilization efficiency of modified clay surfaces for cationic dyes increases with pH and the optimal pH is in the strong alkaline condition.

Table 5-2 The interaction energy between the clay and CHT ($E_{MMT\text{-}CHT}$, kcal/mol) in aqueous condition before and after adding MB dyes.

	CMMT-pH3.5	CMMT-pH6.5	CMMT-pH9.5
Before adding MB	-45455 ± 32	-12520 ± 13	-986 ± 12
After MB adsorption	-45054 ± 16	-12461 ± 9	-568 ± 6
ΔE	+0.88%	+0.47%	+42.37%

5.4.3 MD simulations for dye adsorption

The database of existing contaminants and potential adsorbents is vast, and with the many environmental variables such as temperature and concentration, the adsorption studies currently available are far from exhaustive. More studies on adsorption of specific hazardous substances or on new adsorbents need to be tested to provide more references for practical applications. Computer simulation can significantly reduce the time and cost of experiments. The MD method has been widely used in this area of research and may be a potential solution.

The effect of other substances present in the real aqueous system on MB adsorption was not considered in this study. Furthermore, when considering the pH conditions, only the structural changes of CMMT were taken into account and the effects of extra ions such as H^+ and OH^- at strong acidic and basic pH were neglected. The research of MD in the quantitative adsorption of complex dye molecules needs to be further developed and this work is a first step.

5.5 Conclusions

In this study, the monolayer coated CMMT surface was first synthesized at pH 3.5 and on this basis the CMMT surfaces at pH 6.5 and 9.5 were constructed. Then, the adsorption process of cationic MB dyes was simulated and the immobilization abilities of CMMT and MMT surfaces were evaluated.

From the density profiles and RDF analysis, it is observed that monolayer adsorption of MB, which is governed by the electrostatic attraction of negatively charged clay, occurs more readily on the pure MMT surface, while multilayer adsorption is found on CMMT surfaces, due to the fact that the intermolecular π-π interactions of the dyes are greater than the attraction of CHT. The hydroxyl group of CHT is the main contributor to attracting MB through H-bonding interactions. This interaction was yet found at pH 3.5.

The immobilization capacity for MB is obtained in the following order: CMMT-pH9.5 > CMMT-pH6.5 > CMMT-pH3.5 > MMT, corresponding to equivalent values of 158.79 > 121.29 > 102.63 > 95.00 mg/g. The maximum immobilization efficiency of 80~85% is achieved on the CMMT-pH9.5 surface, assuming that effectively inhibited MB has $D < 0.35\sim0.95 \times 10^{-9}$ m^2/s. The enhancing mechanism of CHT modification is the expansion of surface roughness to capture MB from water, thereafter attracting a cluster of stacked MB by previously adsorbed molecules. This demonstrates the great potential of organoclay for cationic dye uptake with a multilayer adsorption mechanism, especially at high dye concentrations.

Chapter 6

Adsorption of anionic MO dye by CHT and HDTMA-modified MMT

6.1 Introduction

In chapters 3 to 5, we have demonstrated the effectiveness of CHT and HDTMA-modified MMT for the adsorption of cationic MB dye. In this chapter, we extend the study to evaluate their ability to capture anionic MO dye from water. The CHT cation and HDTMA cations modify MMT surface through cation exchange mechanisms to make MMT surface positively charged, depending on the modification amount. The adsorption mechanisms of outer clay surfaces for MO dyes are studied through MD simulations. The effect of loading of organic cations on the adsorption ability of MO is investigated. Also, the desorption process is simulated and corresponding activation energy of MO in different adsorbed states is calculated.

6.2 Simulation methodology

6.2.1 Materials and Modeling

The MMT substrate consists of an $8a \times 6b \times 2c$ supercell based on the elemental composition: $Na_{0.75}[Si_{7.75}Al_{0.25}](Al_{3.5}Mg_{0.5})O_{20}(OH)_4$. The theoretical surface charge of modified MMT surfaces was determined by the amount of HDTMA and CHT. The CHT chain used in this study was modeled at a theoretical pH of 3.5, where all amine groups are fully protonated to form positive amino groups (NH_3^+) [97]. A CHT consists of seven repeating units, resulting in a net positive charge of $9e$, as shown in Fig. 6-1. A HDTMA [$C_{19}H_{42}N^+$] cation presents a net positive charge of e.

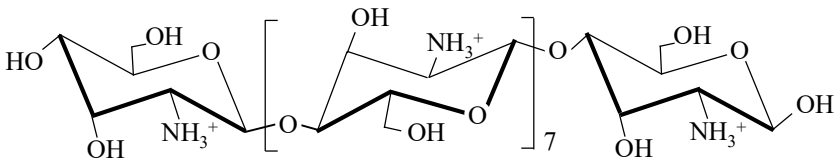

Fig. 6-1 Molecular structures of CHT at pH of 3.5.

Table 6-1 Surface modification conditions. The amount of modifier loading, balancing

ions and overall charges on S1 and S2. A modifier loading of 1 CEC means that all balancing Na^+ on the MMT outer surface are exchanged by two CHT chains or four HDTMA cations.

Modified MMT		Modifier loading and free ions		Surface charge	
		S1	S2	S1	S2
A1	CHT-MMT	2 CEC	-	+18*e*	-18*e*
A2		1 CEC	1 CEC	0	0
A3		1 CEC	Na^+	0	0
B1	HDTMA-MMT	2 CEC	-	+18*e*	-18*e*
B2		1 CEC	1 CEC	0	0
B3		1 CEC	Na^+	0	0

The adsorption process was simulated under aqueous conditions to investigate modified MMT outer surfaces to capture MO dyes from water. Two MMT outer surfaces, labeled S1 (surface 1) and S2 (surface 2), were fully hydrated by a MO solution containing 4000 water molecules. The corresponding water content of MMT (mass ratio of water to MMT) is 100 *wt*%. Each MMT surface carries an average of 18 free sodium ions, which is respect to cation exchange capacity (CEC). A 100% CEC modification of the MMT outer surface means that it can accommodate two CHT chains or 18 HDTMA cations, as they carry a total positive charge of 18*e*. To investigate the effect of organic loading on dye adsorption, three CHT-MMT (A1, A2, and A3) and three HDTMA-MMT (B1, B2, and B3) models were constructed, as summarized in Table 6-1. The systems A1/B1, A2/B2 and A3/B3 correspond to modifier loadings on two MMT outer surfaces (S1, S2) of (2CEC, -), (1CEC, 1CEC), and (1CEC, Na^+) with surface chare of (+18*e,* -18*e*), (0, 0), (0, 0), respectively. The initial adsorption models illustrated shown in Fig. 6-2. To ensure enough dye samples for studying their adsorption behaviors, ten MO dye molecules were placed between the two outer surfaces, with 2000 water molecules on each side, ensuring an approximately equal

separation distance from both surfaces. The corresponding MO concentration is 820 mg/L.

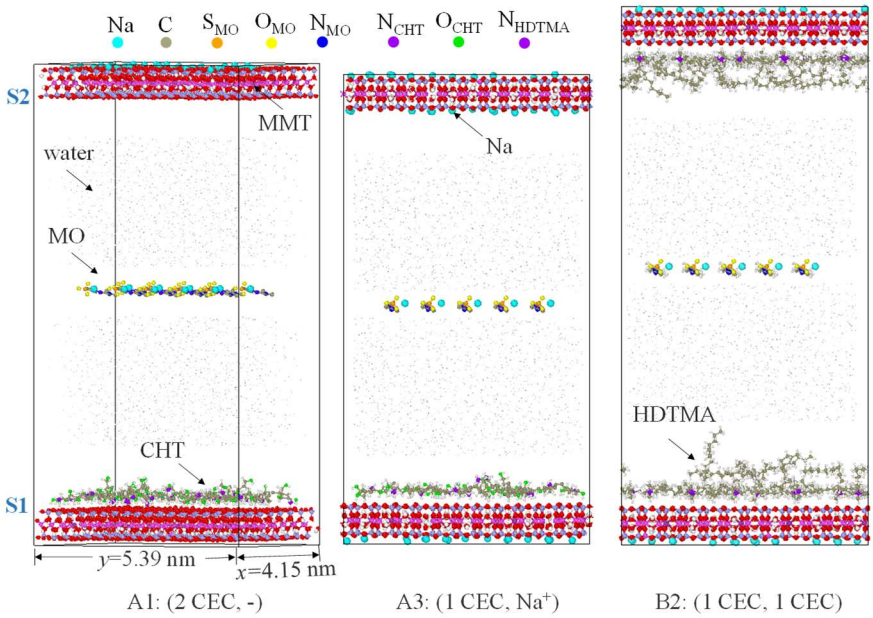

Fig. 6-2 Initial adsorption configurations for A1, A3, and B2 systems, as examples to represent three loading conditions of CHT and HDTMA. A1, B2 and A3 correspond to modifier loadings of (2CEC, -), (1CEC, 1CEC) and (1CEC, Na+) on (S1, S2), respectively. For clarity, water molecules are represented by white dots of O atoms.

6.2.2 Force Fields

The hybrid force fields CLAYFF [121] and CVFF [123] were applied to describe the atomic interactions of inorganic and organic components, respectively. It's worth pointing out that CVFF and other major classic force fields do not include all the potential parameters for MO, especially for six-bonded sulfur and double-bonded nitrogen next to aromatic carbon in MO dye. The dihedral torsion terms should be expressed precisely as they are crucial to maintain and enforcing the planarity of MO structure.

One way to complement those missing parameters is to obtain internal force constants directly from the Hessian matrix (a matrix of Cartesian second derivatives of

the energy) according to the modified Seminario method [226]. Therefore, geometry optimization and vibration frequency calculation for MO were performed via density functional theory (DFT)/B3LYP (Becke, 3-parameter, Lee-Yang-Paar) method under the 6-31G(d, p) basis set [227-228], to obtain the geometric parameters and Hessian matrices. Thus, the force field parameters of MO for equilibrated bond length and angle values were taken from the optimized geometry (Fig. 6-3), and the energy terms were taken from the force constants which were converted from the Hessian matrix. The partial atomic charge of MO anion was assigned by 1.2*CM5 method, which can be used in force field parametrization in MD simulations [229-230].

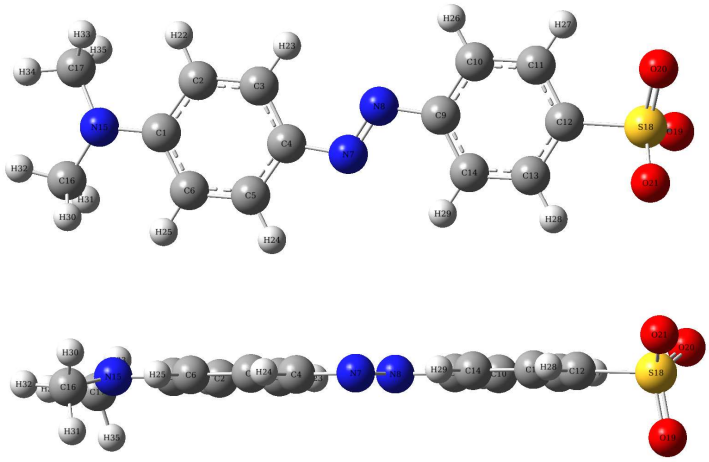

Fig. 6-3 The geometric structure of methyl orange anion obtained by DFT calculations.

6.2.3 Modification and adsorption simulations

The dry modified-MMT surfaces with varying CHT/HDTMA loadings (Table 6-1) were prepared using NVT ensemble at 298 K, involving a 0.5 ns simulation in water followed by a 0.5 ns simulation under dry condition. The detailed modification procedure can be referred to the chapter 4 [97]. To construct adsorption models, water and MO dyes were added to the dry modified MMT surfaces. Subsequently, the six systems were relaxed through an energy minimization procedure, followed by heating for 0.5 ns under NPT ensemble at 298 K and 1 atm. The length of each simulation box in *z*-

direction was recorded and confirmed to be converged after 0.5 ns run (Fig. 6-4). This is essential to ensure the reliability of the data recorded for subsequent adsorption simulation process. Finally, the system ensemble was changed to NVT for an 8 ns simulation at 298 K to investigate the adsorption process.

MD simulations were performed on the LAMMPS platform [214]. Water molecules were described by the rigid SPC model, where the bond distances of water were fixed using the SHAKE algorithm [215]. The inter-molecule interaction is controlled by non-bonded VDW and Coulombic interactions, and for the intra-molecule interaction, the Lennard-Jones (L-J) potential between a pair of bonded atoms will be ignored. A cut-off radius for the calculation of VDW and short-range Coulombic interactions was set at 1.0 nm. L-J parameters for different types of atoms were obtained from the Lorentz-Berthelot mixing rule [122]. The long-range electrostatic interactions were computed through the Ewald summation method [152] with an accuracy of 10^{-4} kcal.mol^{-1}. Three-dimensional periodic boundary condition was applied. A time-step of 1 fs was set.

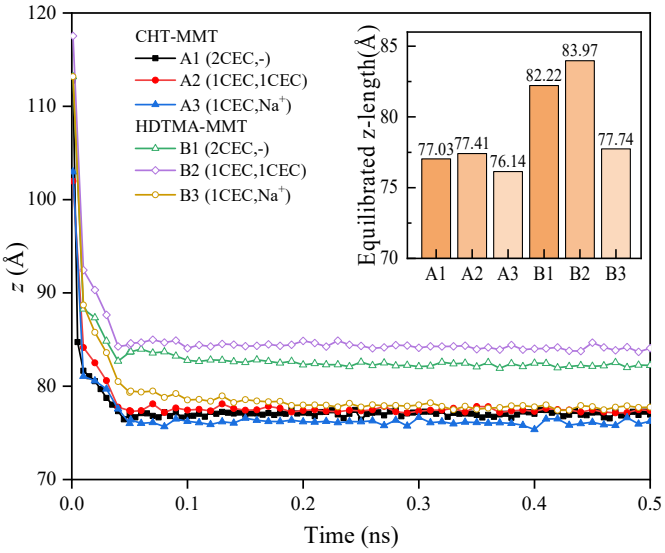

Fig. 6-4 The length evolution of six simulation box in *z*-direction during NPT simulations.

6.3 Results and Discussions

6.3.1 MO adsorption on CHT-MMT surface

6.3.1.1 Equilibrium characteristics

At the molecular level, the convergence of the interaction energy between the adsorbate and adsorbent is indicative of adsorption equilibrium. The interaction energy between the CHT-MMT and MO ($E_{CHT\text{-}MMT...MO}$) was calculated and is plotted in Fig. 6-5. The $E_{CHT\text{-}MMT...MO}$ in the A1 system was found to be converged within 8.5 ns, indicating that MO adsorption reaches equilibrium. However, the $E_{CHT\text{-}MMT...MO}$ obtained for A2 and A3 are much lower compared to A1. To explain differences in interaction energies, the final configurations of adsorption systems and density distributions of Na, S_{MO} and N_{CHT} are analyzed (Fig. 6-6). An intersection of density distributions of S_{MO} and N_{CHT} indicates that MO dyes interact with CHT. In A1, all negative SO_3^- groups of MO molecules are concentrated on the positively charged S1, while balancing Na^+ of MO molecules accumulate on the negatively charged S2. This means that the all MO anions are adsorbed by S1. In contrast, in A1 and A2 systems, where surfaces are neutral though either modified with 1CEC of CHT or balanced by Na^+, MO adsorption is significant reduced. It is seen that only a small part of the SO_3^- group were adsorbed on S2 in A2 and no MO appears to interact with either modified S1 or unmodified S2 in A3. Notably, in A2 the horizontal orientation of adsorbed MO helps to attract free MO dyes with dye-dye interaction. This phenomenon indicates a multi-layer adsorption pattern on S2, as reported in previous studies [22].

The results highlight that both surface charge and organic modifier loading affect the ability of CHT-MMT surface to capture MO from water. The effectiveness of the loading conditions for MO adsorption follows the order: A1 (2CEC, -) > A2 (1CEC, 1CEC) > A3 (1CEC, Na^+). It is recommended that the modifier loading exceeds 1CEC of the MMT to ensure the modified surfaces exhibiting positive charges, thereby promoting the attraction to anionic MO dyes. When neighboring surfaces are both neutral (A2 and A3), Na^+ ions might help neutralize the MO anions, causing them to remain suspended in water.

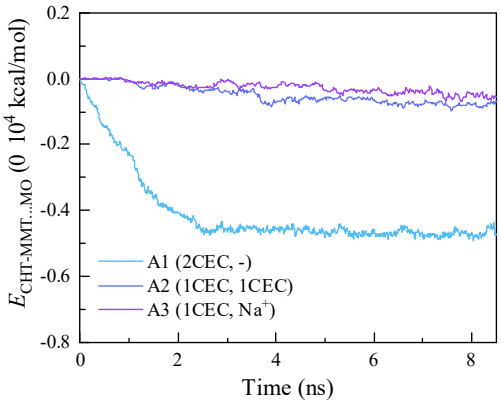

Fig. 6-5 The interaction energy between CHT-MMT and MO in A1, A2, and A3 adsorption systems.

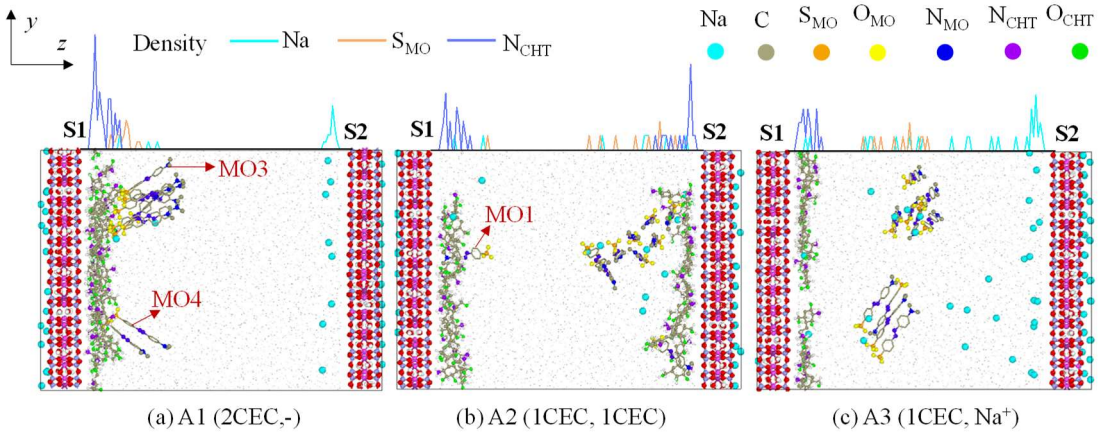

Fig. 6-6 Final configurations of three CHT-MMT systems with different CHT loading conditions and density distributions of sodium ions, S_{MO} and N_{CHT} at 8.5 ns.

6.3.1.2 Adsorption mechanisms

Since in A1 the SO_3 group is the main binding site of MO to CHT, the $g(r)$ (Fig. 6-7) between the SO_3 group and two polar groups (-OH and -NH_3) of CHT are studied to analyze. Distinct first peaks can be observed in $g(r)$ of $O_{CHT\text{-}OH}$…$O_{MO\text{-}SO3}$ and $N_{CHT\text{-}NH3}$…$O_{MO\text{-}SO3}$ in both A1 and A2 and the corresponding locations are around 2.35 and 2.85 Å, respectively. It agrees with previous study that bonding distances between anionic azo dyes and CHT surface are lower than 3.5 Å [231].

Hydrogen bonds can form between strongly electronegative atoms such as O, N, or F. The H-bond donor (D) is covalently bonded to a hydrogen atom and the H-bond acceptor (A) is from a neighboring molecule or ion, as shown in Fig. 6-8. Some available experimental hydrogen bond geometries formed by O-H…O and N-H…O are given in Table 6-2. It is seen that first peak locations of $g(r)$ are comparable with experimental r_{DA}, indicating a high possibility for CHT and MO to form hydrogen bonds.

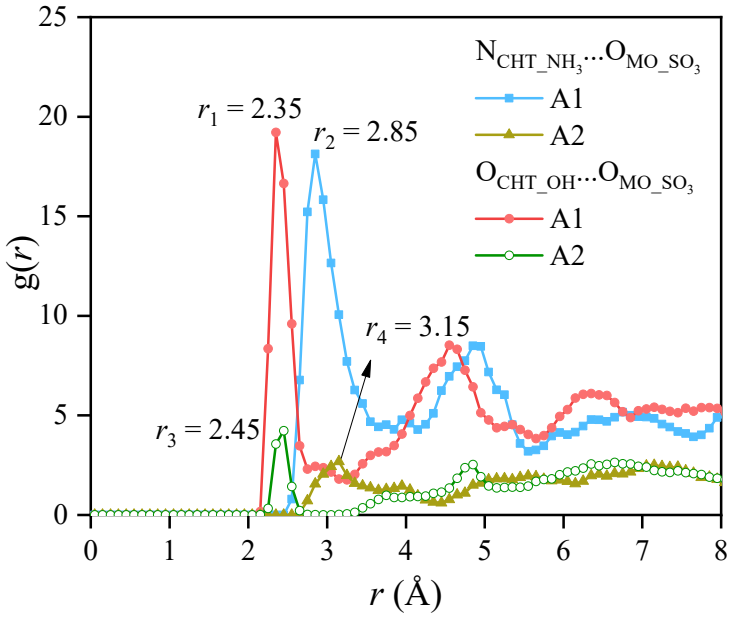

Fig. 6-7 RDF of pair atoms between CHT and MO in A1 and A2.

The number of formed H-bond should be quantified to determine the contribution of -OH and -NH_3 of CHT to the MO adsorption. The formation of hydrogen bond is defined herein using a geometric criterion that r_{DA} is less than 3.5 Å while θ_{DHA} is greater than 150° [232], which can encompass all the possibilities in Table 6-2. The C-H are the least important hydrogen-bonding groups so they are not considered in this study. Therefore, atoms in MO only serve as H-bond acceptor. A sample of 850 frames of trajectories, recorded every 0.01 ns over the entire 8.5 ns simulation process, are included in H-bonds calculation. Table 6-3 lists all possible H-bond donors in CHT and acceptors in MO and their total number of H-bond formed among 850 frames, as well as the average number of stable H-bond in the adsorption process calculated from their

evolution curves over time in Fig. 6-9.

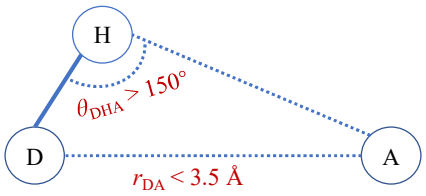

Fig. 6-8 The geometric criteria of hydrogen bonds.

Table 6-2 Comparison of first peak locations of $g(r)$ in A1 and A2 and experimental hydrogen bond length r_{DA} and angles θ_{DHA} formed between N-H…O and O-H…O [233].

Complex	D-H…A	$r_{DA,}$ Å	$\theta_{DHA,}$ °
A1	N-H…O	2.85	
	O-H…O	2.35	
A2	N-H…O	3.15	
	O-H…O	2.45	
(3s.5s7s)-adamantan-1-ammonium 2,5-	N-H…O	2.818	166
dihydroxy-benzoate	O-H…O	2.504	157
Heptan-2-ammonium 2,5-	N-H…O	2.848	163
dihydroxybenzoate	O-H…O	2.544	157
1 -(2-hydroxy-ethyl)pyrrolidine 2,5-	N-H…O	2.778	162
dihydroxy-benzoate	O-H…O	2.766	168
1-(2-hydroxyethyl) pyrrolidine-1-ium 2-	N-H…O	2.697	169
hydroxybenzoate	O-H…O	2.739	176

In A1, about 11 hydrogen bonds are formed and only $-SO_3$ of MO is involved. Since the amount of -OH (80) is 2.22 times higher than that of $-NH_3$ (36), the average number of hydrogen bonds formed with $-SO_3$ is slightly higher at 3.07 times. It suggests that the -OH of CHT is more likely to form a hydrogen bond with MO than the $-NH_3$. In A2, middle double bond N can interact with $-NH_3$ and -OH, indicating a tilted MO orientation to the surface. The total of 2.7 hydrogen bonds formed shows that only up

to 3 MO is directly adsorbed by CHT in a parallel mode.

In conclusion, the controlling mechanism for MO adsorption by CHT-MMT is the strong hydrogen bonding interaction. The hydroxyl group (-OH) and ammonia group (-NH_3) of CHT have approximately equal contributions to the H-bond formation. The major binding site in MO will be negative -SO_3 group, with little or no involvement of N=N and $N(CH_3)_2$.

Table 6-3 The total number of possible H-bonds in the sample of 850 frames in the adsorption process and the average number of stable H-bonds formed.

Donor and H in CHT		Possible acceptor in MO			Criteria
		O in SO_3^-	N in N=N	N in $N(CH_3)_2$	
A1 (2CEC, -)	-NH_3	1739 (ave. 2.7)	0	0	
	-OH	5573 (ave. 8.3)	0	0	$r_{DA} < 3.5$ Å;
A2 (1CEC, 1CEC)	-NH_3	496 (ave. 1.1)	192 (ave. 0.4)	0	$\theta_{DHA} > 150°$
	-OH	408 (ave. 1.2)	9 (ave. 0)	0	

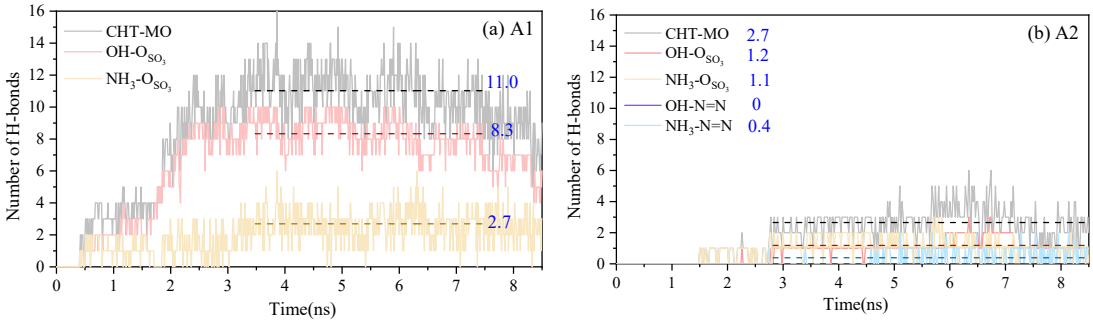

Fig. 6-9 The evolution of possible H-bonds number over time.

6.3.1.3 CHT-MMT stability

The stability of CHT-MMT surfaces during the adsorption process is important to evaluate the effectiveness of the CHT modification. It can be observed from Fig. 6-10(a) that the interaction energy between MMT and CHT, $E_{CHT...MMT}$, remains almost

unchanged whether MO adsorption occurs (A1 and A2) or not (A3). Furthermore, the amount of MO adsorption would not affect the total amount of H-bonds formed between CHT and MMT compared with A1 and A2, as shown in Fig. 6-10(b&c). These results indicate the stability of CHT-MMT and the strong interaction between CHT and MMT.

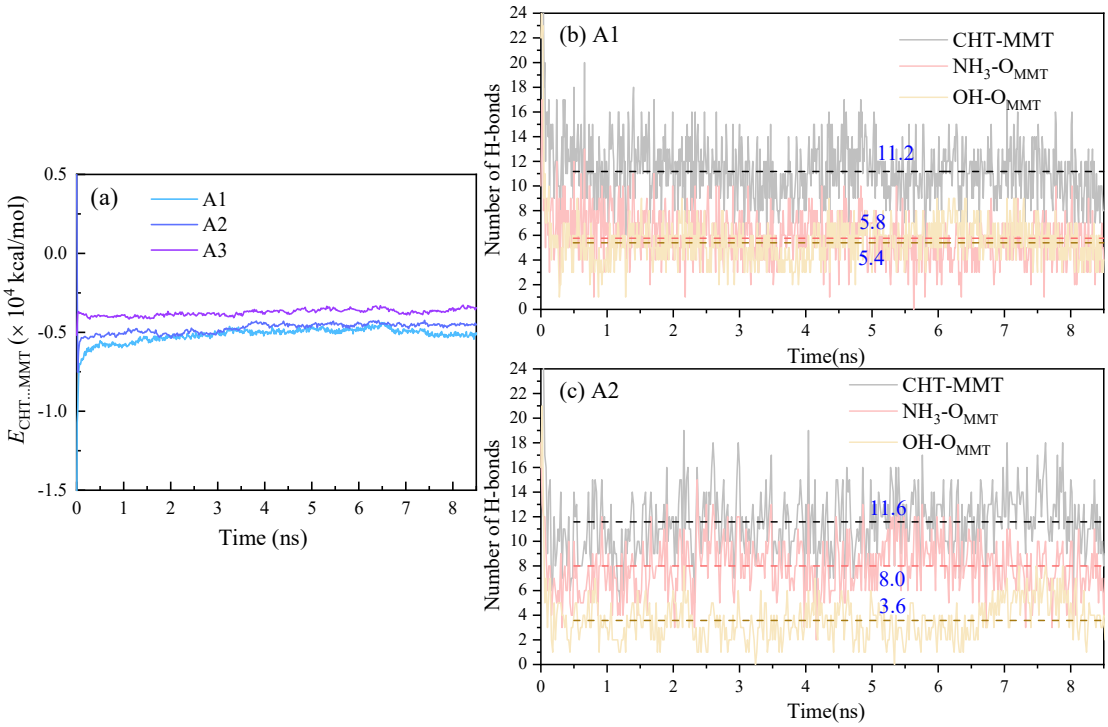

Fig. 6-10 (a) The interaction energy between MMT and CHT in A1, A2 and A3; (b) and (c) the evolution of H-bonds number formed between CHT and MMT in A1 and A2.

6.3.2 MO adsorption on HDTMA-MMT surface

The stability of HDTMA-MMT surfaces should be investigated before studying the adsorption equilibrium. Although $E_{HDTMA\text{-}MMT...MO}$ in B1 reaches equilibrium within 8.5 ns (Fig. 6-11a), the corresponding $E_{HDTMA...MMT}$ increases continuously (Fig. 6-11b). Therefore, the adsorption simulations for B1, B2, and B3 are extended to 11.5 ns. However, this increase in $E_{HDTMA...MMT}$ is still present. From the final configurations (Fig. 6-12), the N_{HDTMA} distribution is found apparently dispersed in B1 and B2, suggesting the detachment of N-head groups. The number of N_{HDTMA} adsorbed on

MMT (Fig. 6-11(d-f)) is counted over time to reflect the desorption of N-heads. The adsorbed N_{HDTMA} is defined as nitrogen atom within the first minimum shell of $O_{MMT...}N_{HDTMA,}$ which is 5.34, 5.85, and 5.45 Å in B1, B2 and B3, respectively, as measured by $g(r)$ (Fig. 6-11(c)).

The adsorbed N-heads are observed unchanged in the last 2 ns in all cases, indicating that HDTMA-MMT stability have been reached by simulating for 11.5 ns. For each 1CEC HDTMA surface, the detachment is rather low, while for 2CEC the detachment is closed to 50 %. This implies that high HDTMA loading especially beyond the 100%CEC of MMT, may cause desorption of N-heads. In addition to the loading rate, water intrusion also plays an important role. The number of water molecules in the first shell of $O_{MMT...}N_{HDTMA}$ correlates well with changes in the number of N_{HDTMA} adsorbed. Water molecules can first easily strip the hydrocarbon tail of HDTMA from MMT surface, and then when the water molecules fill the gap around adsorbed N-heads, it is possible to break the adhesion between the heads and the MMT.

For the adsorption equilibrium, MO adsorption behavior on HDTMA-MMT surfaces is similar to that on CHT-MMT. The $E_{HDTMA\text{-}MMT...MO}$ in B1 is the lowest and converges rapidly while it can be negligible in B2 and B3 (Fig. 6-11(a)). Almost all MO dyes are surrounded by S1 of HDTMA-MMT, and only a few MO are seized by HDTMA in B2 and B3. It is interesting to note that under the same (1CEC, Na^+) loading conditions, HDTMA-MMT is able to seize some MO dyes from water, but CHT-MMT is not. The possible reason for this may be the higher organic carbon content and surface roughness produced by HDTMA. The effectiveness of loading conditions for MO adsorption are ranked as B1 (2CEC, -) > B2 (1CEC, 1CEC) ≈ B3 (1CEC, Na^+).

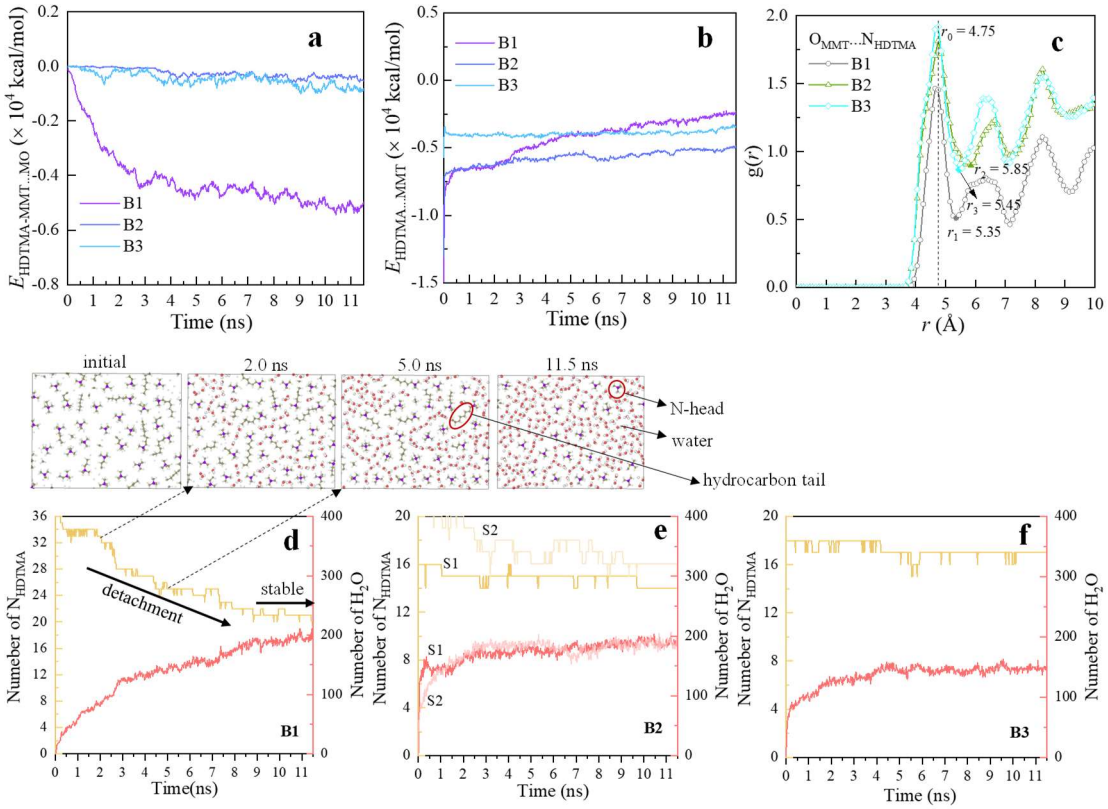

Fig. 6-11 (a) Interaction energy between HDTMA-MMT and MO in B1, B2 and B3 adsorption systems. (b) Interaction energy between MMT and HDTMA. (c) RDF of OMMT…NHDTMA. (d), (e) and (f) display the evolution of number of adsorbed NHDTMA and water molecules in the first shell of OMMT…NHDTMA in B1, B2 and B3, respectively.

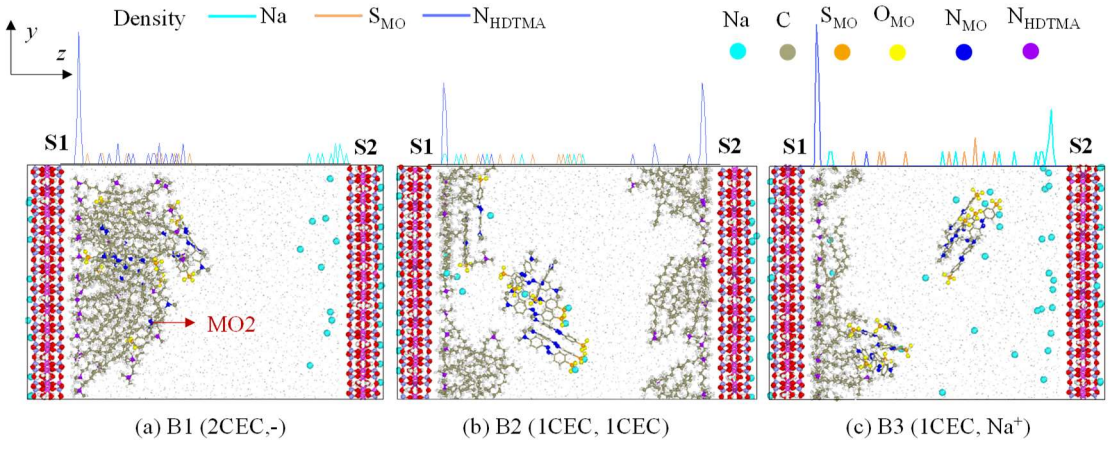

Fig. 6-12 Final configurations of three HDTMA-MMT systems with different

HDTMA loading conditions and distributions of sodium ions, S_{MO} and N_{HDTMA} at 11.5 ns.

In Fig. 6-12, the N_{HDTMA} distribution intersects with that of S_{MO}. The first $g(r)$ peak of N_{HDTMA}…S_{MO} locates at 4.65 Å (Fig. 6-13), showing a strong electrostatic interaction between polar N-head of HDTMA and SO_3 groups of MO. These detached N-heads further contribute to attraction of anionic species. Besides, hydrophobic interaction (van der Waals bonds) plays an indispensable role as C_{HDTMA}…$C_{MO\_aromatic\ C}$ distance is around 5.0 Å.

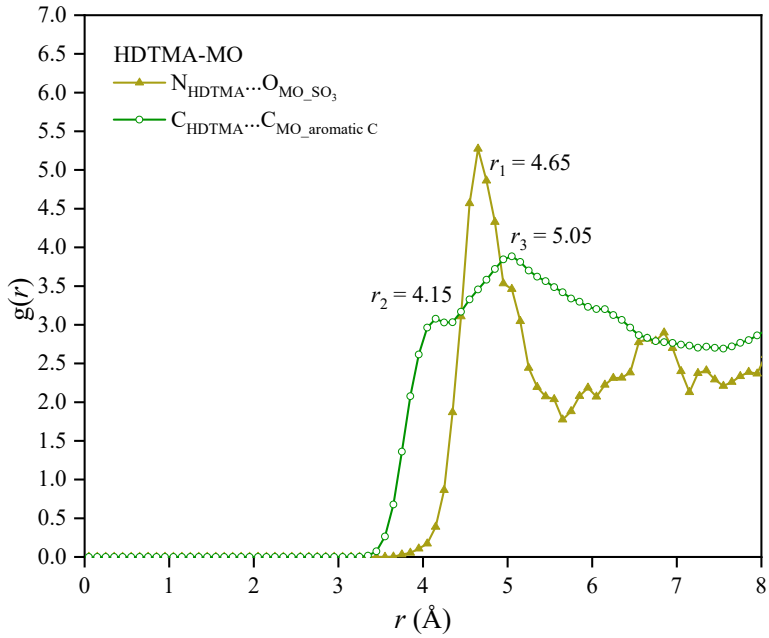

Fig. 6-13 RDF of pair atoms between HDTMA and MO in B1 (1CEC, 1CEC).

6.3.3 Desorption of MO

To study the adsorption strength, the desorption process of adsorbed MO was simulated. Four representative MO molecules adsorbed onto CHT-MMT and HDTMA-MMT surfaces, namely MO1, MO2, MO3, and MO4, as labelled in Fig. 6-6 and Fig. 6-12, are chosen for the study. These representative molecules exhibit different adsorption states, as summarized in Table 6-4. MO1 in A2 is initially attracted by both

CHT and MMT in a tilted mode. MO3 and MO4 in A1 are adsorbed by CHT while MMT is not directly involved, but they additionally interact with nearby adsorbed MO. MO2 in B1 is surrounded by HDTMA. The steer molecular dynamic (SMD) method is a non-equilibrium molecule dynamic method and is used to simulate the interface separation process [234-237]. The concept of SMD procedure is to pull a dye molecule separated from its attached state on the adsorbent surface by applying an external force with a virtual spring. The study of the spring does for separating molecules equals to their activation energy of desorption or adhesion energy. The last snapshot of each NVT adsorption simulation was used as the initial state for SMD simulation. In this study, the middle double-bonded N atom of the chosen MO molecules is tethered and pulled along *z*-direction at a series of constant velocities (1, 2.5, 5, 10, 20, 30, 40, 50, and 60 m/s). The pulling force is recorded in Fig. 6-14 and some snapshots at 1 m/s is given in Fig. 6-15 to show the pulling path. The target pulling distance is set at around 20 Å which is guaranteed beyond the position of the maximum pulling force.

The Bell's model [238] was first proposed in 1978 to the study on adhesion between cells or of cells to surfaces when the adhesion is mediated by reversible bonds. Later in 2007, Ackbarow et al. [239] proposed a modified Bell's model and extended its applicability to the study of adhesion between protein structures. It has been successfully applied to calculate the adhesion energy between silica and epoxy [235], [240]. In this study, the modified Bell's model ((6-1) to (6-3)) is used to measure the energy barrier (adhesion energy) that must be overcome for a MO molecule to desorb from modified MMT surfaces.

$$v = v_0 \exp\left(\frac{f \cdot x_b}{k_B T}\right) \tag{6-1}$$

$$v_0 = \omega_0 \cdot x_b \cdot \exp\left(\frac{-E_b}{k_B T}\right) \tag{6-2}$$

$$f = \left(\frac{k_B T}{x_b}\right) \ln v - \frac{k_B T \ln v_0}{x_b} = A \ln\left(\frac{v}{v^*}\right) + B \tag{6-3}$$

where f is the external applied force and v is the moving velocity, E_b is the energy barrier

and x_b is the transition state. k_B is Boltzmann constant ($1.38064852 \times 10^{-23}$ JK^{-1}), ω_0 is natural vibration frequency ($\approx 1\times 10^{13}$ s^{-1}). T is the temperature and v_0 is the natural bond breaking speed. v^* is equal to 1 m/s used for normalization purpose.

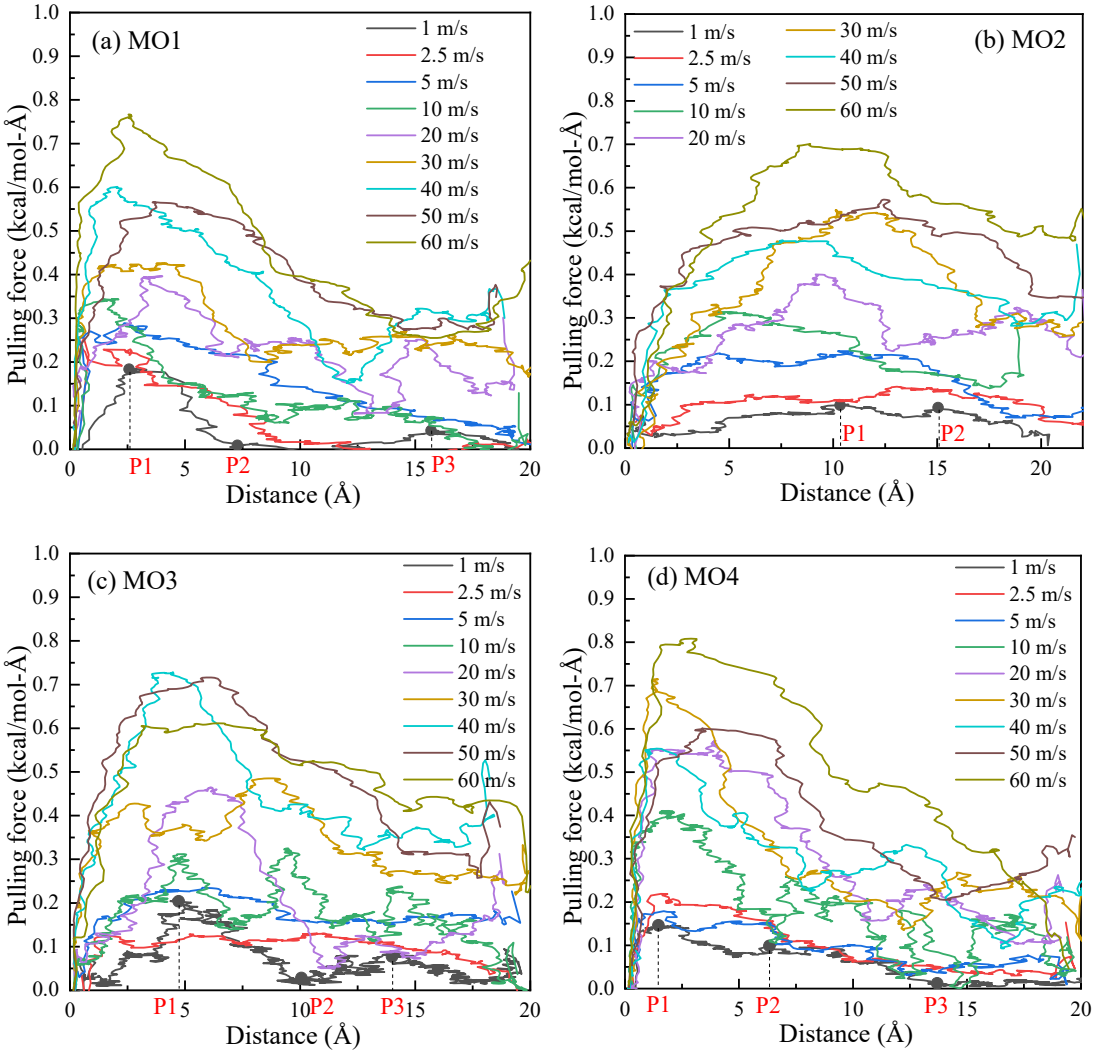

Fig. 6-14 The evolution of pulling force for four representative MO molecules with pulling distance in *z*-direction at various velocities.

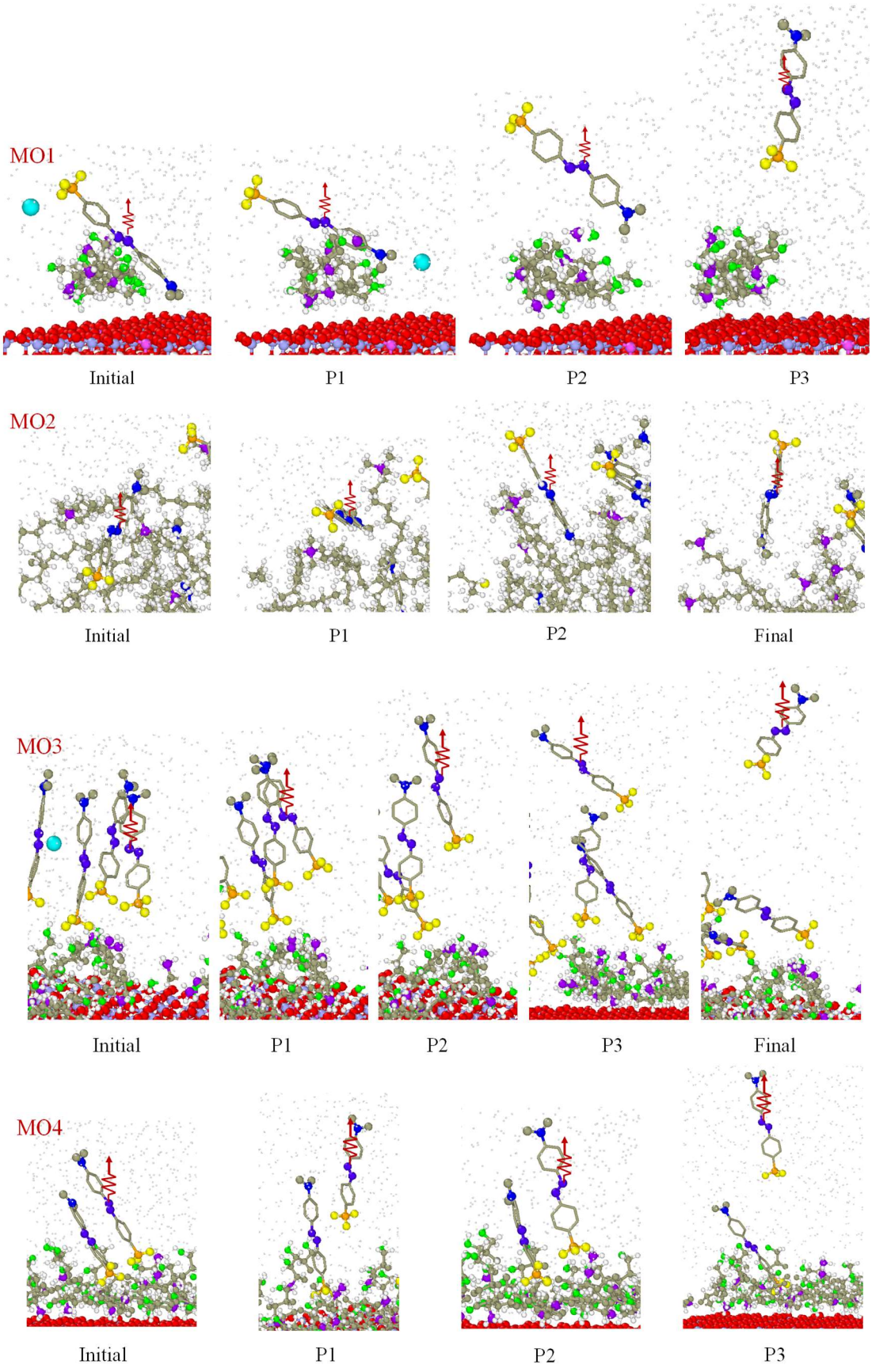

Fig. 6-15 Pulling path of four representative MO molecules at 1 m/s.

The maximum pulling force (Fig. 6-16) is well fitted to Equation 3 at a fast speed (FS) and low speed (LS). The calculated E_b is listed in Table 6-4. The higher the E_b, the stronger the adsorption strength and the harder the desorption process can proceed. It is observed that E_b obtained at LS is higher than that at FS. The E_b obtained from the separation of MO1, MO3, and MO4 from CHT-MMT surfaces is in the range of 14.39~17.91 kJ/mol at $v \leq 30$ m/s. The desorption energy of MO is related to the adsorbed configuration and adsorption force, including π-π interaction from nearby MO and H-bonding with CHT-MMT. In contrast, the E_b obtained from the separation of MO2 (interacting with HDTMA) is 16.28 kJ/mol. The activation energy for desorption is comparable even without involving H-bonding and dye-dye interaction that occur in CHT-modified surfaces. This is because when separating the MO2, those surrounding HDTMA chains move with the MO2 (

Fig. 6-15), resulting in a high pulling force that is maintained over a long pulling distance (Fig. 6-14(b)). The long HDTMA chain does not adhere entirely to the clay surface as CHT does. Such a long hydrocarbon tail provides greater surface roughness and more freedom of movement to continuously interact with contaminants, preventing complete escape of the MO2 from HDTMA.

Therefore, the activation energy of MO desorption from HDTMA-MMT is comparable to that from CHT-MMT at $v \leq 30$ m/s and higher at larger pulling velocities. This suggests that larger contact area provided by the HDTMA-MMT surface compensates for the relatively weaker hydrophobic interactions with MO, compared to the stronger electrostatic interaction provided by CHT-MMT.

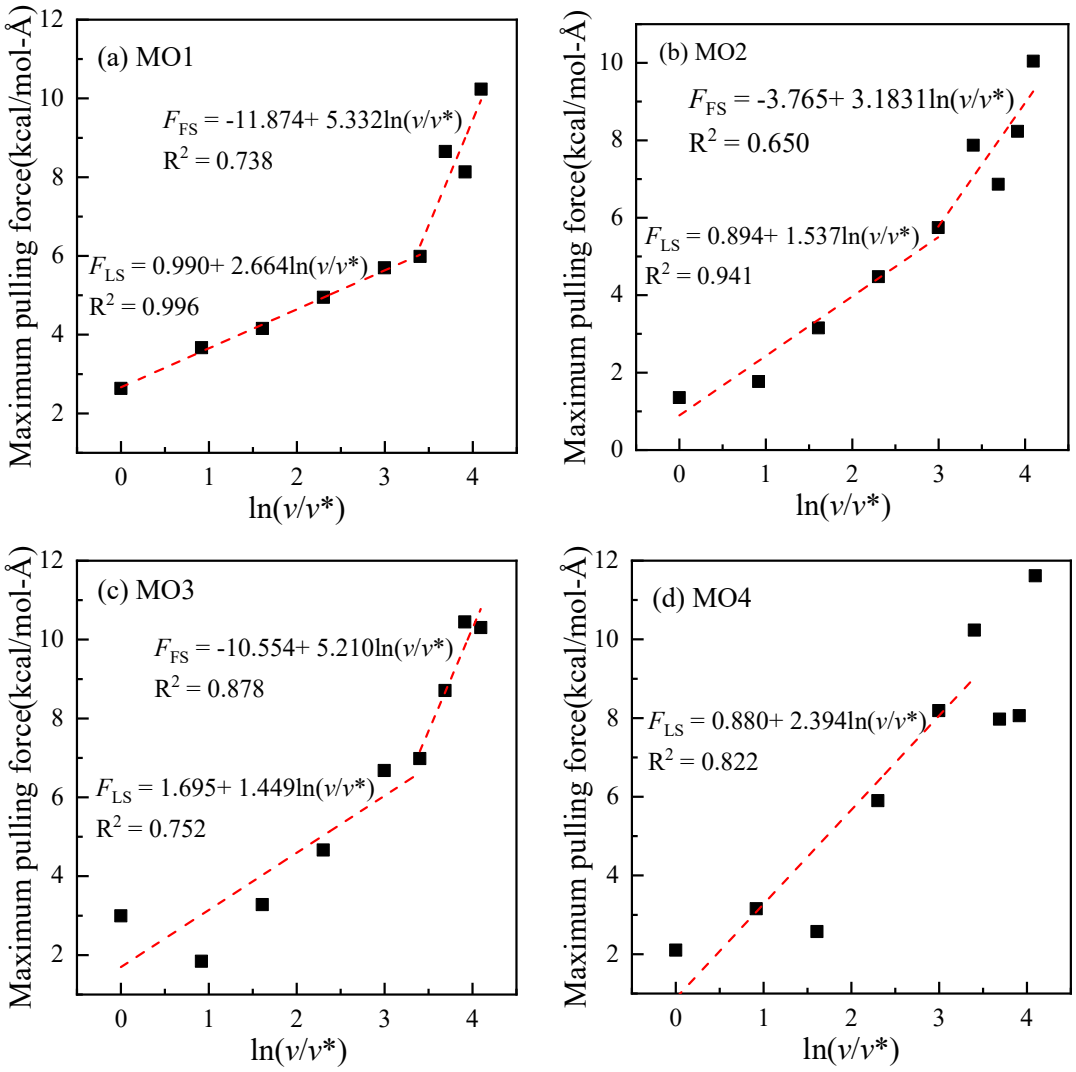

Fig. 6-16 Maximum detaching pulling force of four individual MO molecules as a function of speed variation and the linear fits of modified Bell's model at a fast speed (FS) and low speed (LS).

Table 6-4 Initial interactions involved in the four tethered MO and energy barrier E_b (kJ/mol).

	System	Initial interactions involved	E_b (LS)	E_b (FS)
MO1	A2	H-bonding with CHT&MM	14.39	6.19
MO2	B1	HDTMA	16.28	10.08
MO3	A1	with CHT and π-π interaction		6.78
		from nearby MO	17.91	
MO4	A1	H-bonding with CHT and π-π	14.60	-
		interaction from nearby MO		

6.4 Implications in real applications

The CHT-MMT and HDTMA-MMT have potential for industrial application. Considering that textile wastewater usually contains a variety of dyes including anionic and cationic dyes, developing versatile adsorbents capable of treating a wide range of contaminants is essential for industrial applications. Both HDTMA-MMT and CHT-MMT have previously demonstrated high effectiveness in removing cationic dyes, and this study further confirmed their ability to adsorb anionic dyes, particularly at high organic loading levels (more than 1 CEC of MMT). This addresses a critical limitation of clay-based adsorbents, which are typically ineffective for anionic dye removal, and highlights the potential of these two organoclays to simultaneously adsorb mixed dyes in real wastewater. For HDTMA-MMT, it mainly provides hydrophobic interactions and increases the surface roughness of MMT to capture MO, and the same mechanism for cationic dyes [44]. In the case of CHT-MMT, the adsorption mechanism for anionic MO dyes is mainly due to the strong hydrogen bonding between NH_3^+ of CHT (under acidic conditions) and SO_3^- of anionic dyes. In contrast, for cationic dyes, adsorption is mainly forced by hydroxyl groups (under neutral and alkaline conditions) of CHT [22]. Therefore, HDTMA-MMT is effective in adsorbing both anionic and cationic dyes simultaneously, while CHT-MMT adsorbents can selectively and preferentially remove either cationic or anionic dyes from wastewater effluents by adjusting the pH according

to the pH sensitivity of CHT.

Coagulation is not a major factor in adsorption studies because large aggregates formed as a result of the addition of coagulants usually separate from the water phase prior to the adsorption method. However, potential coagulation effect of dyes caused by high dye concentrations may lead to the formation of small dye aggregates that can affect the uptake of MO dyes. At high dye concentrations, dye molecules tend to self-aggregate through dye-dye interactions, typically involving π–π stacking interactions between aromatic rings [241]. Since the high dielectric constant of dyes reduces the electrostatic repulsion between similarly charged dye molecules in water, most organic dyes form dimers, trimers, and higher aggregates by self-aggregation [242]. Such small aggregates benefit to synergetic adsorption of cationic and anionic dye based on a push-pull mechanism [243-244]. For example, MO can push dimerization of cationic methylene blue and these cationic dimers can pull MO together to adsorb on adsorbents, and vice versa [245]. The two adsorbents studied are for both anionic and cationic dyes, and are therefore more capable to facilitate synergistic effects in the case of dye self-aggregation.

The presence of dissolved or colloidal organic matter (DOM/COM) in real effluents may also induce dye coagulation and, on the other hand, hinder dye adsorption by interacting directly with adsorbents. Previous studies have shown that the presence of DOM can lead to pore blockage and competition for adsorption sites on adsorbents for dye adsorption [246]. Consequently, negatively charged DOM/COM may compete with anionic MO dyes for adsorption sites on positively charged CHT-MMT or HDTMA-MMT surfaces. To further explore adsorption processes for complex wastewater systems, future studies should consider incorporating DOM/COM models to study possible interactions with adsorbents and dyes.

Except the multifunctional adsorption properties, this study showed that two modified clays remained structurally stable during adsorption process and did not cause secondary contamination due to modifier stripping. Additionally, compared to traditional carbon-based materials, clay minerals are naturally abundant, while CHT is

biodegradable and derived from the second most abundant biopolymer [97]. The investigated adsorbent materials are environmentally friendly and cost-effective, making them highly suitable for scale-up. Therefore, the availability and stability of modified MMT supports their use in industrial processes that require the treatment of large volumes of wastewater.

6.5 Conclusions

This chapter investigated the adsorption process and mechanisms of anionic MO dye on CHT-MMT and HDTMA-MMT surfaces at different organic loading (surface charges) using MD method. Equilibrium configurations and intermolecular interaction energy results showed that the ability of both CHT-MMT and HDTMA-MMT to capture MO from water improves with positive surface charges, which is achieved by organic loadings exceeding 1 CEC of MMT. Bonding interaction studies indicated that CHT-MMT composites remain good structural stability when adsorption occurs. In contrast, HDTMA-MMT surfaces presented partial detachment of N-head of HDTMA from the MMT surface. The mechanism of MO adsorption on CHT-MMT is mainly strong hydrogen bonding interaction from -OH and $-NH_3^+$ of CHT to $-SO_3^-$ of MO, whereas on HDTMA-MMT it is hydrophobic interaction provided by HDTMA tails and some strong electrostatic interaction by its head. The calculated E_b of MO desorption from CHT-MMT ranges from 14.39 to 17.91 kJ/mol at $v \leq 30$ m/s, which is comparable to that from HDTMA-MMT (16.28 kJ/mol). This molecule-level study contributes to the design and optimization of CHT-MMT and HDTMA-MMT adsorbents.

Chapter 7

Exfoliated MMT nanofillers role on the high performance of polyamide nanomembranes

7.1 Introduction

Conventional thin-film composite (TFC) membranes are manufactured with a polymeric porous support and a selective layer, usually utilized in pressure-driven nanofiltration and reverse-osmosis separation methods [247]. Polyamide (PA), featuring a thickness ranging from 50 to 100 nm, stands out as the predominant selective layer, particularly in deep water processing such as desalination for drinking water production [101-102]. PA is synthesized via interfacial polymerization (IP) between trimesoyl chloride (TMC) monomers in the organic phase and diamine monomers in the aqueous phase, typically m-phenylenediamine (MPD) or piperazine [27]. The PA formation is governed by the diffusion of MPD towards organic phase and the diffusion of TMC towards aqueous phase. Currently, the key strategy for improving PA structure and performance is to modulate the IP process, predominantly achieved by precise control of the transfer rate of diamine monomers into organic solutions [248-250].

Exfoliated clay nanosheets have the potential as an additive added to the organic/aqueous solution for regulating PA formation. However, when inorganic materials are used as interlayer materials in TFC membranes, an organic coating becomes essential to provide organic affinity with both polymeric PA matrix and substrates, in order to ensure the structural stability of TFCs. However, this organic compatibility issue has received limited attention in the previous studies focusing on the use of nanofillers. To improve the dispersity of exfoliated MMT nanosheets in polymeric matrix, organic modification is needed. PDA is a popular bioinspired hydrophilic coating material that adheres to almost all materials and is formed from the oxidative self-polymerization of dopamine (DA) monomers [251-252]. It has been extensively used as a surface coating for various aluminosilicate interlayers, such as LDH, silica, halloysite nanotubes, and imogolite nanotubes (kaolin polytypes) [253-257]. DA monomers, carrying an amine group and a benzene ring attached to two hydroxyl groups, can enhance the dispersion of MMT in water, even without undergoing self-polymerization, potentially aiding in PA design [258].

It is highly feasible to incorporate exfoliated MMT modified with DA into the

aqueous MPD solution to participate in PA design. Most of the existing studies focus on evaluating the improved water flux and salt rejection rate of modified PA-TFC membranes embedded with nanofillers; however, to the best of our knowledge, the fundamental regulatory mechanism by which MMT fillers operate still remains largely unexplored. The precise effect of the nanofiller on the IP process and PA morphology is unclear and is a critical gap that needs to be addressed to fully exploit the potential of MMT in optimizing PA membranes. Therefore, this chapter aims to unveil molecular insights into the role of exfoliated MMT nanosheets in the perspective of MPD diffusion and distribution, crosslinking degree between MPD and TMC monomers, morphology of formed PA-TFCs, as well as water transport properties.

7.2 Simulation details

7.2.1 Simulation settings

All simulations were performed in LAMMPS platform [214]. The intra-molecular interaction is described by the CLAYFF [121] force field for MMT and the CVFF [123] force field for organic molecules. The CVFF has been successfully used to simulate PA properties [259-260]. A simple point charge model for water was used, which is compatible with CVFF. The inter-molecular interaction is controlled by non-bonding interactions, including van der Waals and electrostatic interaction using a real space cutoff of 12 Å. The Lorentz–Berthelot [261] combining rule was used to determine the L-J parameters for different types of atoms. A three-dimensional periodic boundary condition was used in all simulations to minimize edge effects. The timestep was set to 1 fs.

7.2.2 Exfoliated MMT nanosheets

Pure exfoliated MMT nanosheets can be obtained experimentally by ion exchange using a high-concentration salt solution, rather than by polymer exfoliation [262]. In this study, a single-layer MMT nanosheet in the form of a $5a \times 3b$ supercell was first constructed based on a unit-cell of $Na_{0.6}[Si_{7.74}Al_{0.26}](Al_{3.6}Mg_{0.4})O_{20}(OH)_4$.

Subsequently, the four edges were saturated with H or OH to bond with undercoordinated oxygen or aluminum atoms to cut its periodicity. The partial charges of edge atoms are taken from Ref. [263]. The final MMT nanosheet, depicted in Fig. 7-1, measures 2.95 nm × 2.90 nm in *xy* dimension.

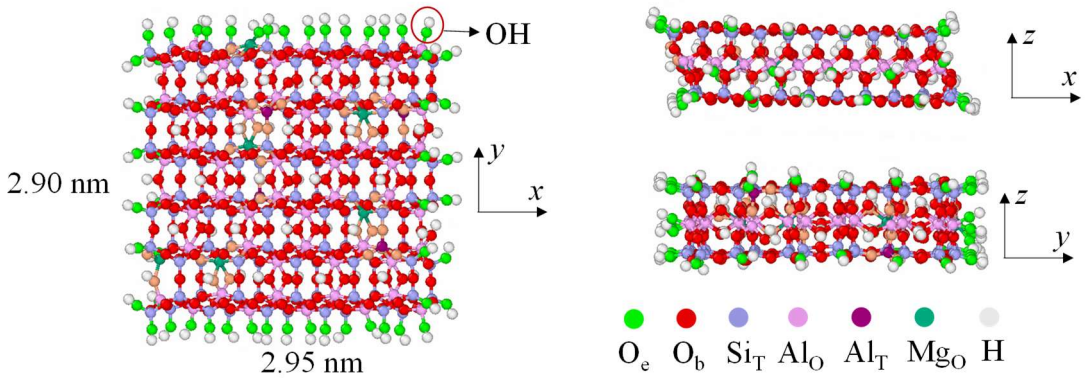

Fig. 7-1 A single-layer MMT nanosheet. O_e: edge hydroxyl oxygen; O_b: bridge oxygen; Si_T: silicon in Tetrahedron; Al_O: aluminum in Octahedron.

7.2.3 MMT/DA aggregates with DA modification

Improving the dispersion of MMT aggregates in an aqueous solution is critical to their effectiveness as fillers in the IP reaction. A high soil porosity may cause greater dispersion of the clay fraction in water and reduce aggregate stability to water [264]. This is primarily because the higher porosity typically results in a larger solvent-accessible surface area which facilitates the penetration of water into the pores and thus minimizes the tendency of nanofillers to agglomerate, a common problem that reduces solubility. It has also been proved that porosity and solubility are positively correlated [265]. Therefore, a higher porosity of nanofiller aggregates is advantageous for their dispersion and solubility in water.

Herein, the structure of exfoliated MMT aggregates under the effect of DA modification was investigated in dry conditions, typically representing the densest state. Firstly, a series of single MMT/DA particles were constructed and then replicated 3 × 3 × 3 times in the *x*, y, and *z* directions, respectively, to form a larger system comprising

27 MMT/DA particles as an aggregate. The simulation box for a single MMT/DA particle was set to a size of 4.2 nm^3 to ensure sufficient space for the free rotation of the MMT sheet within the aggregate system. For modeling a single MMT/DA particle, a monolayer MMT nanosheet and various DA amounts in a mass ratio of 0, 10.37 wt%, 20.74 wt%, 31.11 wt%, and 51.84 *wt*%, corresponding to 0, 9, 18, 27 and 45 DA molecules per MMT nanosheet, respectively, were added in the box. These systems were equilibrated through a minimization procedure followed by a 200 ps run under an NVT ensemble at 298 K. An illustrative example of the equilibrated configuration, specifically MMT/DA-10.37 *wt*%, is presented in Fig. 7-3. The radial distribution function (RDF) $g(r)$ is analyzed to study the interaction type between the MMT and DA molecule. Then, the systems for MMT/DA aggregates were equilibrated under the NVT ensemble for a 200 ps run at 298 K and under the NPT ensemble for 300 ps at 1 atm pressure. The porosity of MMT nanosheet aggregates is studied by pore size distributions (PSD) calculated using Zeo++ [266].

7.2.4 MPD solution with MMT/DA filler

The diffusion behavior of MPD plays a crucial role in controlling the IP process. The fabrication of PA layer is commonly carried out under typical IP reaction conditions, where MPD ≈ 2 *wt*% and TMC ≈ 0.1 *wt*% [103], [267]. Simulations were conducted in MPD solutions (Fig. 7-2(a)) to estimate MPD diffusion properties. The MPD solution were prepared at a concentration of 2 *wt*%, comprising 140 MPD molecules and 4200 H_2O molecules. The solution with an initial density of 1 g/cm^3 was placed in a 5.4 nm^3 simulation box. To investigate the effect of MMT/DA fillers, single equilibrated MMT/DA particles with different amounts of DA (0, 10.37 *wt*%, 20.74 *wt*%, 31.11 *wt*%) were positioned at the bottom of the MPD reservoir. To assess the effect of pure DA addition, the MMT sheet was removed from the MMT/DA particles. A vacuum was added at the top to avoid interaction with periodic images. The MMT nanosheet was fixed and treated as a rigid body in each system during the dynamic simulations to eliminate the possible effect of filler position on the MPD diffusion. Each system was

first simulated under NVT ensemble for 0.1 ns to heat from 1 K to 298 K, followed by 2 ns at the target temperature of 298 K. The mean square displacement (MSD) of MPD during 2 ns simulation was recorded to compute the diffusion coefficients of MPD monomers (D_{MPD}) based on the Einstein equation [143]. The MSD data was segmented into 0.2 ns intervals to minimize the possible long-time effect on the linearity of MSD curves [268].

7.2.5 Interfacial polymerization setup

The PA layer is formed by a crosslinking reaction between MPD and TMC monomers. Typically, PA chains consist of both linear and cross-linked segments because MPD has two active sites and TMC monomer has three involved in covalent bonding. In this study, to simplify the crosslinking simulations, all TMC monomers are only allow up to two reactive sites to be linearly bonded with MPD. The two linear MPD-L and TMC-L reactants are shown in Fig. 7-2(b). MPD-L was prepared by breaking one N-H bond of each -NH_2 groups in MPD, while TMC-L was prepared by breaking one C-Cl bond of each -COCl group in TMC but one broken site is hydrolyzed to COOH as end segment [269]. The atomic charges of MPD-L and TMC-L segments are adopted from Reference [270]. By using reactants, the step of possible bond breaking and removal of the resulting free H atoms in MPD and Cl atoms in TMC is omitted. The crosslinking reaction is assumed to take place in the MPD aqueous solution, so in order to save computational resources, the n-hexane solvent that dissolves the TMC is ignored. The layout of the initial system illustrated in Fig. 7-2(c) is, from top to bottom, a vacuum region, TMC-L reactants, 2 *wt*% MPD-L solution, and the MMT/DA filler. The MPD-L:TMC-L ratio is 1:1 with 140 of each. The 1:1 stoichiometric ratio proved to be crucial in forming highly cross-linked and defect-free PA structure compared to a deficiency and an excess (vs. 1:1) of MPD [271]. The concentration of the MMT nanosheet in the filled-PA complex was 22 *wt*% (excluding DA).

The polymerization process starts with unreacted monomers and ends with no covalent bonds formed. Simulations were performed under NVT ensemble at 298 K for

200 ps, then new bonds were created between reactive atoms (the amino nitrogen of MPD-L and the acyl carbon of TMC-L) within a cutoff distance of 6.25 Å [270]. The reaction distance can be chosen arbitrarily and it has been reported ranging from 3.0 to 13 Å [269, 271-273]. After new bond were created, the new topology of bonds, angles and dihedral angles in the cluster was updated, followed by the energy minimization to avoid unstable configurations. The above three-step crosslinking procedure, a succession of NVT relaxation–bond formation–minimization cycle, was repeated at least 20 times of 2 ns until no new bonds were generated. The number of new bonds formed in each cycle is recorded. The degree of crosslinking (DC) of the PA layer was calculated as the ratio of the number of new bonds formed between MPD-L and TMC-L monomers and the theoretical maximum number of bonds formed.

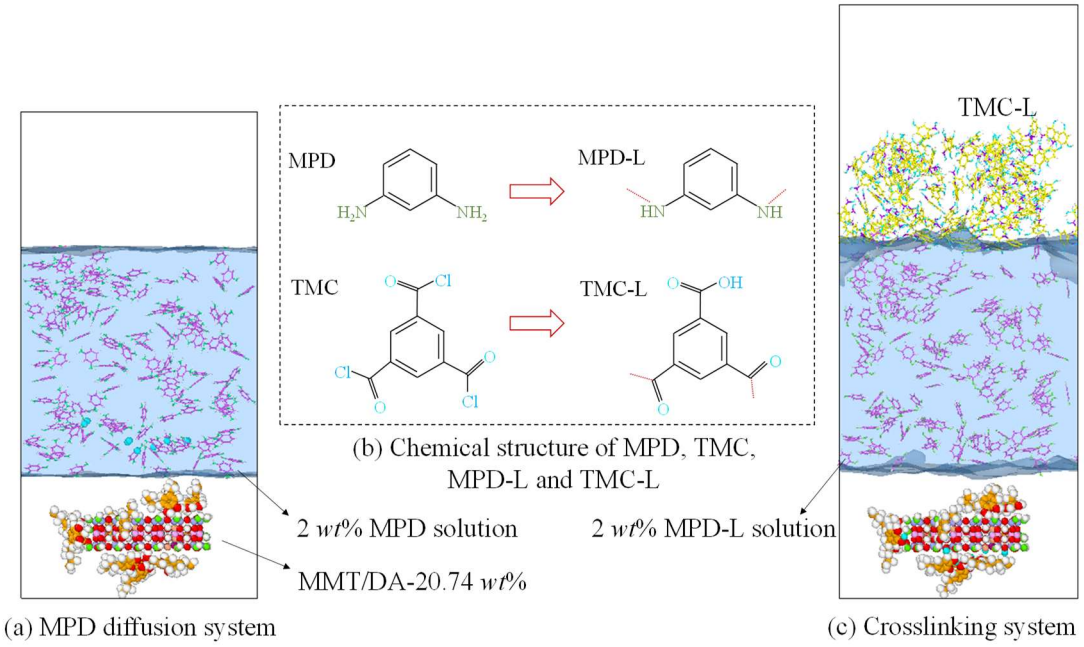

Fig. 7-2 (a) Initial MPD diffusion model; (b) Chemical structure of MPD and TMC monomers and corresponding MPD-L and TMC-L reactants; (c) Initial crosslinking system in aqueous solution.

To evaluate the effect of MMT/DA filler in dry state, water molecules in the last frame of above solution crosslinking simulation were removed and the crosslinking

procedure was continued and repeated until no new bonds formed. Then the dry TFCs with highest DC were obtained. The final DC was calculated. The surface area of dry composites was measured using OVITO on the basis of mathematical alpha complex concept algorithm [274-275].

7.3 Results

7.3.1 MMT-DA bonding interaction and aggregates porosity

As displayed in Fig. 7-3, the equilibrated configuration of MMT/DA-10.37 *wt*% shows a remarkable affinity between DA and MMT. The bonding interaction is revealed by RDF analysis. It is observed that the first peak of the $g(r)$ curve between hydroxyl oxygen atoms of the MMT edge (O_{ME}) and that of DA (O_{DA}) is located at 2.70 Å, indicating a strong hydrogen bonding interaction between DA and MMT. O_{ME} may also form hydrogen bonds with nitrogen atoms of DA (N_{DA}) with an interaction distance within 3.06 Å. The MMT edges exhibit a stronger attraction to hydroxyl and amine groups of DA monomers compared to the MMT surface (MS), owing to higher negative charge concentration of OH groups in the edges. Notably, O_{ME}…O_{DA} pair interaction plays the leading role and O_{ME}…N_{DA} is the secondary. Considering the presence of balanced sodium ions in MMT, it is observed that the Na-O_{DA} bond length is 2.22 Å, highlighting a strong electrostatic interaction. However, such an ionic bridge may occur primarily under dry conditions, as sodium ions are typically dissolved in aqueous solutions.

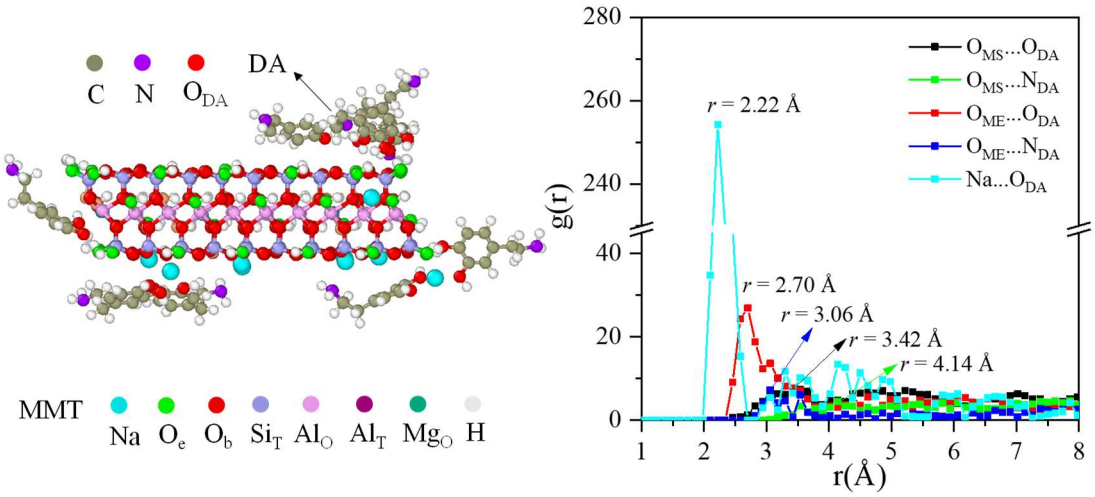

Fig. 7-3 Equilibrated configuration of the MMT/DA-10.37 *wt*% particle and RDF curves between MMT and DA monomers.

To assess the PSD of dry MMT/DA aggregates, a sphere with a diameter of a water molecule (1.4 Å) is used for probing [276]. Particularly, for DA mass ratio of 31.11 wt% and 51.84 wt%, MMT/DA aggregates cannot be detected with the 1.4 Å probe, as no connected voids are found. In these cases, a smaller probe with a radius of 1.0 Å [271] or 0.9 Å is employed to obtain the PSD curves. The obtained PSD curves are illustrated in Fig. 7-4, while the total density within the final simulation box and average pore size are recorded in Table 7-1.

The existence of DA is expected to improve dispersion properties of MMT nanosheets by preventing them from self-adhesion. However, the results from Table 7-1 imply that higher concentration of DA probably narrows interparticle channels of MMT, leading to an increased density and a reduced average pore size of MMT/DA aggregate. This phenomenon arises because, at DA > 20.74 *wt*%, DA molecules are sufficient to fill large voids between the MMT nanosheets, causing the MMT/DA aggregates to attain their densest state and exhibit low inner pore interconnectivity. Conversely, when DA concentration does not exceed 20.74 *wt*%, the adverse effects induced by DA molecules are negligible, and pore sizes of each composite are distributed in the range of 3.2~7.5 Å (Fig. 7-4) with average values of 4.6~5.0 Å. The largest pore diameter of 5.0 Å is achieved within MMT/DA-10.37 *wt*% aggregate.

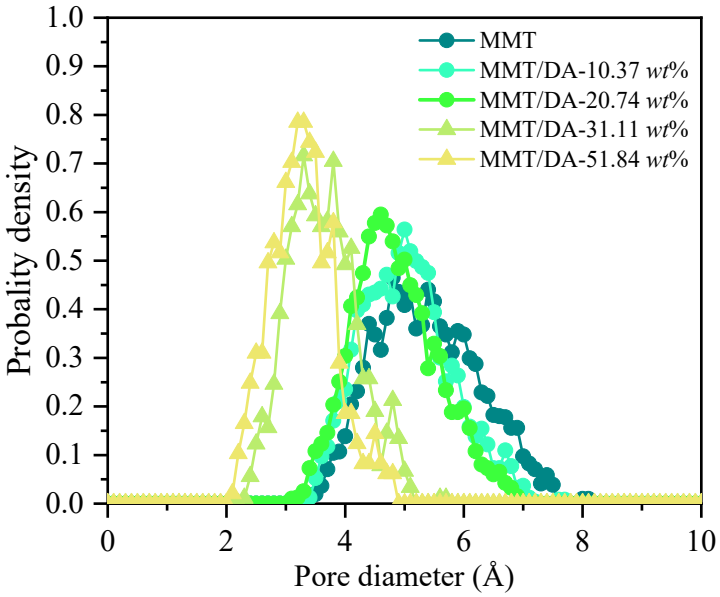

Fig. 7-4 The pore size distributions (PSD) of MMT/DA aggregates with various DA mass ratio.

Table 7-1 The total density and average pore size of MMT/DA aggregates with various DA mass ratio.

DA mass ratio	Density (g/mol)	Average pore size (Å)
0	0.53	4.8
10.37 *wt* %	0.59	5.0
20.74 *wt* %	0.61	4.6
31.11 *wt* %	0.96	3.3
51.84 *wt* %	1.03	3.2

7.3.2 Diffusion characteristics of MPD monomers

Impeding the diffusion of MPD has the potential to inhibit the longitudinal growth of PA layer and form a thinner PA film [250]. As illustrated in Fig. 7-5, the estimated D_{MPD} stabilizes after 0.5 ns and slightly fluctuates around a mean value, while extinct fluctuations are observed in the cases without filler and with 10.37 *wt*% DA. The mean D_{MPD} is calculated to be 8.5 $\times 10^{-10}$ m^2/s in pure water. The incorporation of MMT nanosheet with DA amounts of 0, 10.37 *wt*%, 20.74 *wt*% and 31.11 *wt*% resulted in

reductions in D_{MPD} by 28%, 24%, 55% and 56%, respectively. However, when the MMT sheet was removed, MPD diffusion is only reduced at higher DA concentration (≥ 20.74 *wt*%), and the reduction is smaller than that in the presence of MMT. Therefore, the combination of MMT and DA can effectively reduce MPD diffusion. The lowest D_{MPD} can be obtained with MMT/DA fillers at DA ≥ 20.74 *wt*%. Final snapshots of MPD, MMT and DA (Fig. 7-6) reveal that MPD monomers are attracted by MMT and distributed around MMT. DA molecules might act as an adhesive for MMT and MPD so that the higher DA concentration, the lower the D_{MPD}.

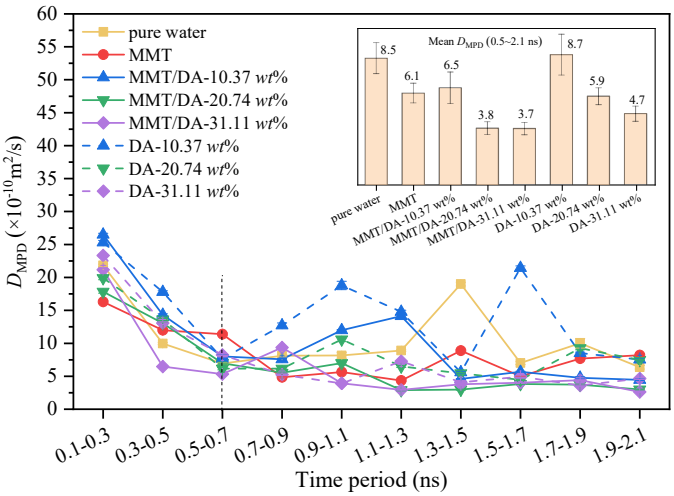

Fig. 7-5 The evolution of computed diffusion coefficients of MPD monomers in water with simulation time period.

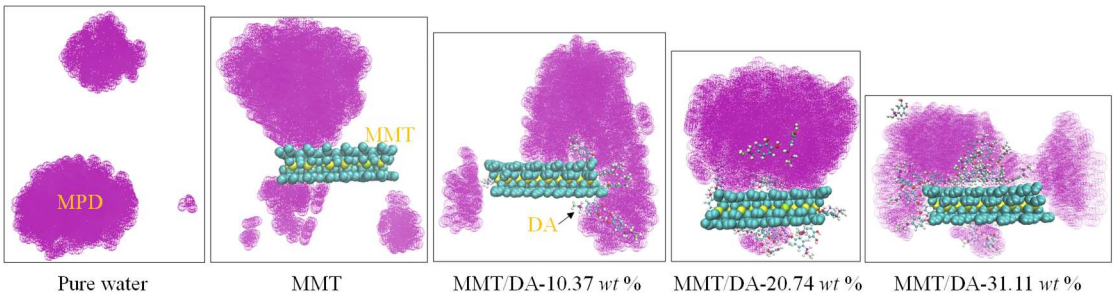

Fig. 7-6 Final configuration of MPD solution and MMT/DA filler rendered by VMD [166]. For clarity, water molecules are hidden to show the distribution of MPD, MMT, and DA components.

7.3.3 Effects on PA formation

The evolution of new bond formation between MPD and TMC reactants (Fig. 7-7(a)) was analyzed to elucidate the crosslinking speed. The degree of crosslinking based on cumulative new bonds (Fig. 7-7(b)) was quantified to evaluate the PA formation. It can be seen that the number of new bonds formed in each cycle showed a general decreasing trend as the reaction proceeds, indicating that the crosslinking process slows down with time for all cases. The system without MMT fillers showed a particularly pronounced deceleration of the reaction within the initial five cycles and the lowest DC. These results suggest that the reaction system without MMT fillers produces fewer polyamide bonds in the early stages, leaving more unreacted agents in the system compared to systems incorporating MMT fillers. Therefore, the presence of MMT fillers accelerates the reaction process and assists PA formation with a significant increase in total DC of at least 44% in the aqueous phase, as observed in Fig. 7-7(b). Regarding the role of DA, a higher DA concentration slightly diminishes the accelerating effect on the crosslinking process facilitated by MMT in first five crosslinking cycles. However, such an effect on total DC appears insignificant when DA ≤ 20.74 *wt*%.

From the morphology of PA network in aqueous solution, as displayed in Fig. 7-8, it becomes apparent that without MMT/DA filler intervention, polymerization zone is naturally concentrated at the contact interface between MPD and TMC. The early IP reaction zone hindered the diffusion of the remaining unreacted monomers, resulting in a low crosslinking rate of 46.45% at a given 1:1 ratio of MPD and TMC sites. This phenomenon has also been proved by Grzebyk et al. [277] that during IP, MPD monomers initially diffuse into the organic layer and react rapidly with TMC, forming an incipient layer of polyamide which further limits polyamide growth. In contrast, when MMT fillers are introduced, the total DC (≥ 67.02%) significantly increases, indicating a more complete reaction and a wider IP reaction zone. The modified PA network exhibits a distinct “leaf-like” and loose structure.

The loose structure of PA monomers can be attributed to two causes. Firstly, the

presence of MMT/DA filler attracts MPD and reduces its diffusion towards TMC. This regulatory effect alters the distribution of MPD, making polymerization sites spread a wider area surrounding the MMT. As a result, this facilitates a more efficient crosslinking process and increases DC in aqueous phase. On the other hand, the strong hydrophilicity of MMT attracts water molecules, preventing dense assembly of MMT and monomers. This tends to create more small voids in the real PA manufacturing. Furthermore, it is worth noting that DA small molecules are dispersed individually within the PA matrix (Fig. 7-8), indicating that the strong interaction between DA and MMT may be broken during the crosslinking process. As such, DA molecules actually serve as independent fillers after the IP process. They mainly function in regulating MPD distribution early in the crosslinking process.

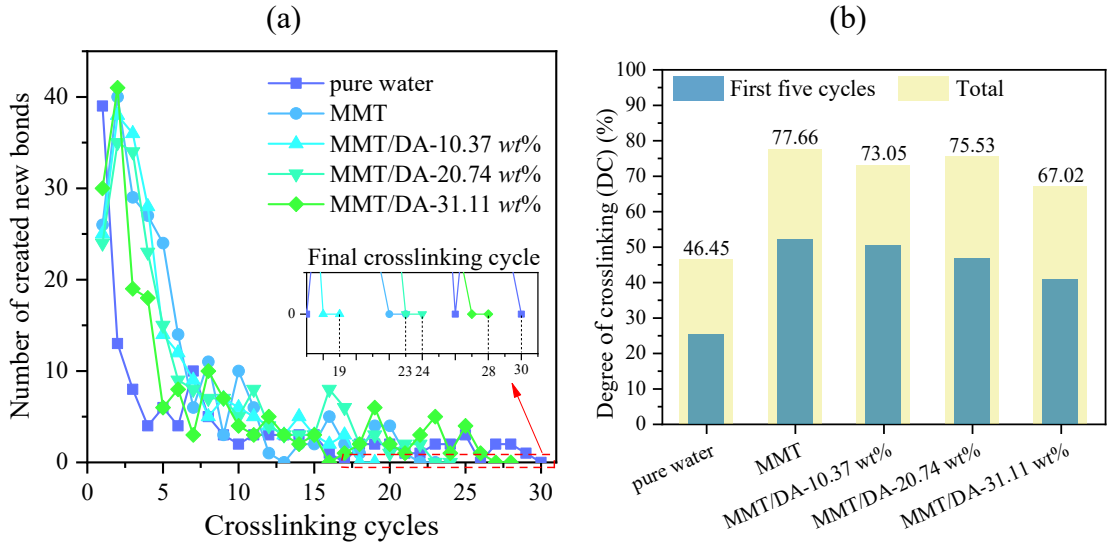

Fig. 7-7 (a) Number of created new bonds between MPD-L and TMC-L in each crosslinking cycle; (b) corresponding degree of crosslinking in aqueous solution.

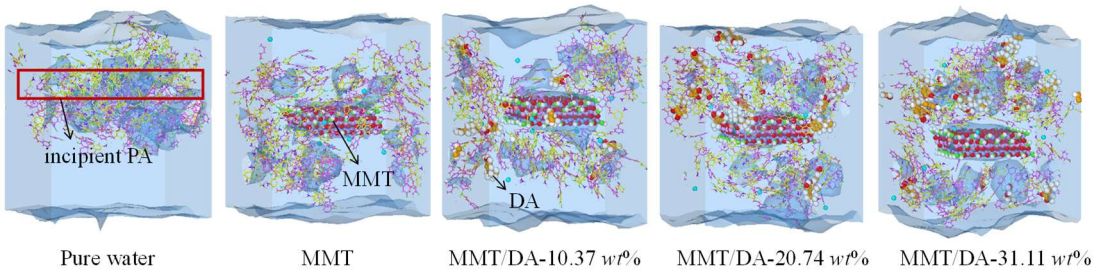

Fig. 7-8 Final configuration after crosslinking reaction in the aqueous solution. The

MPD and TMC reactants are displayed in line type. The benzene ring in TMC-L is colored yellow and in MPD-L is colored pink. MMT and DA molecules are displayed in VDW type.

The water hydration shell inside the PA matrix was analyzed from g(*r*) between oxygen atoms of carboxyl groups (O_{COOH}) and oxygen atoms of water (O_w), as seen in Fig. 7-9. Noting that the first RDF peaks of COOH…O_w center at 2.55~2.65 Å, which corresponds to the first structure shell of COOH. A cut-off distance of 3.35 Å was chosen to evaluate the coordination numbers (CN) of water with -COOH groups in the first solvation shell. The CN of water near the carboxyl segment in pure water was 1.50. This CN increased by 18% to 20% with the addition of MMT nanofillers, reaching values of 1.79, 1.80, 1.77, and 1.78 for DA mass ratios of 0, 10.37 *wt*%, 20.74 *wt*%, and 31.11 *wt*%, respectively. This increase is due to the looser structure of the PA network in the aqueous phase, which allows more water molecules to interact with the PA matrix, thereby enhancing the hydrophilicity of the PA matrix. It can also be found that the CN remains basically unchanged with increasing DA doping, indicating that the increase in hydrophilicity depends more on the presence of MMT rather than the amount of DA. A similar modulation mechanism on the PA structure is reported with hydrophilic nanosphere fillers that their high hydrophilicity could enhance the miscibility of MPD aqueous and TMC organic phases, resulting in the additional breadth of the reaction zone and more pronounced “leaf-like” structure of TFN membranes [278]. Furthermore, the incorporation of silica nanoparticles improves the hydrophilicity of the thin film nanocomposite membrane and contributes to enhanced water flux [279].

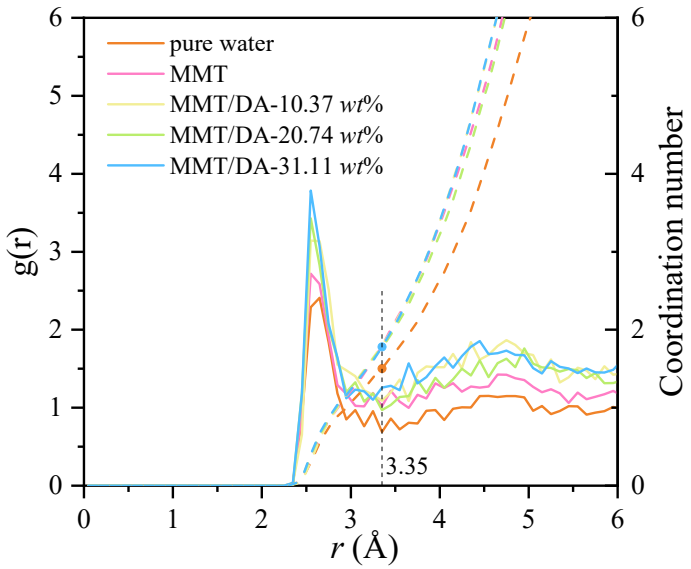

Fig. 7-9 RDF of O_{COOH}…O_{water} and water coordination number.

The crosslinking reaction may continue to occur in the drying process. As the water molecules are removed, the interaction between MPD and TMC reactants is significantly enhanced, making their positional rearrangement easier and thereby driving further crosslinking reactions. After fully idealized drying, all dry PA-TFCs reach a maximum DC with high values above 90% (Fig. 7-10), which is consistent with the range of 91.7~100% of the PA membranes formed by IP reaction reported in prior experimental and computational studies [280-282]. It is noteworthy that the system without MMT fillers showed a significant increase in DC by 111% to almost fully crosslinked state after drying, even exceeding the DC of the system with fillers. The reason for the slightly lower DC due to the MMT/DA fillers may be that these fillers impede the movement of the reactants in the dry state. As the amount of DA increases, the DC of the PA layer tends to decrease under both aqueous and dry conditions. The lower the DC, the higher the porosity. On the other hand, the typical thicknesses of PA layers formed through IP between TMC and MPD range from 100 to 1000 nm [283]. However, the simulated dry PA-TFCs thickness is about 2 nm, which may overestimate the actual crosslinking rates achieved in actual manufacturing especially for dry pristine PA.

In conclusion, the addition of MMT/DA fillers facilitates the IP process in aqueous solutions and produces a PA layer with a lower DC after drying. Furthermore, the

inclusion of MMT/DA fillers increases the surface area (Fig. 7-10), indicating their potential to enhance the surface roughness of the dried PA-TFCs. The simulation result provides valuable insights into the crosslinking process and the effects of MMT/DA fillers for the design and fabrication of novel PA membranes.

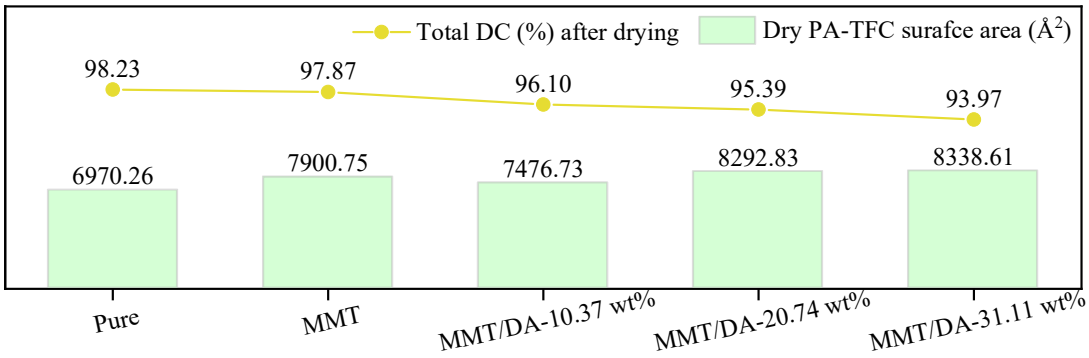

Fig. 7-10 The maximum degree of crosslinking (DC) and surface area of dry PA-TFCs.

7.3.4 Permeability and salt resistance performance

To study the effect on MMT/DA filler on the water transport and desalination performance of TFC, pressure-induced filtration simulations were conducted using the dry unmodified PA-TFC and MMT/DA-20.74 *wt*% modified PA-TFC as virtual membranes. The 10 *wt*% $MgCl_2$ solution containing 88 $MgCl_2$ and 4200 H_2O was constructed as untreated saltwater. A pressure (P) of 10 MPa was exerted on the saltwater solution, which was achieved by applying a uniform external force on a rigid graphene monolayer, calculated as:

$$P = \frac{F_i \cdot N}{A_{xy}} \tag{7-1}$$

where F_i is the external force applied to each atom of graphene; N is the number of graphene atoms; A_{xy} is the area of xy-plane of the simulation box. The graphene layer was positioned on top of the saltwater with a separation distance of 5 Å and treated as a rigid wall. A vacuum region was added on the other side of the dry membranes instead of a pure aqueous solution. The applied vacuum creates a lower pressure on the permeate side of the membrane and an increased transmembrane pressure, which may

lead to faster water transport rates. Fig. 7-11 shows the filtration simulation model of unmodified PA-TFC film.

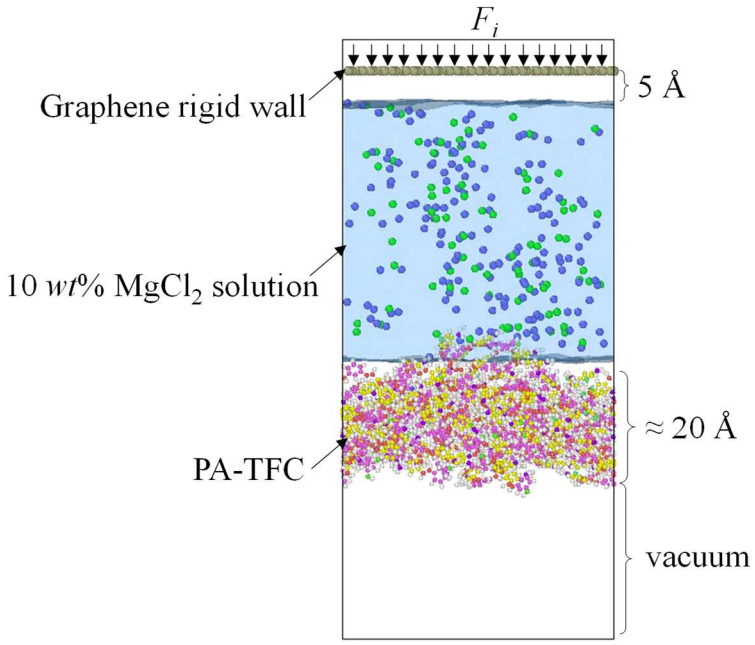

Fig. 7-11 Simulation setup for PA-TFC filtration.

The filtration simulations were performed with a sequence of steps: minimization, 200 ps NVT simulation for pre-hydration, and 30 ns NVT dynamic simulation with applied *P*. To avoid the movement of TFCs, the MMT component was set as a rigid body and 2.8% atoms of the PA network were randomly selected to limit its movement in the *z*-direction. The small fraction of fixed monomers has a negligible effect on the PA-TFC structure [276].

The intermolecular interaction between the PA-TFC and water reflects the amount of water that passes through the composite membrane. As illustrated in Fig. 7-12, the absolute value of interaction energy between PA and water ($E_{(PA\text{-}water)}$) increases rapidly in the early stages (within 6 ns), which is due to the water molecules saturating the dry film and starting to penetrate. Subsequently, the growth rate of $E_{(PA\text{-}water)}$ slows down significantly, especially between 18 and 30 ns where the increase is negligible. This suggests that the water penetration process across two PA-TFCs is a continuous and lengthy process. It is noticed that the water transport rate of the modified membrane is

faster than that of the unmodified membrane in the early stage, but the difference between $E_{1\ (PA\text{-}water)}$ and $E_{2\ (PA\text{-}water)}$ decreases with time. $E_{2\ (PA\text{-}water)}$ is slightly greater than $E_{1\ (PA\text{-}water)}$, and the difference is even larger when the interaction energy between the MMT/DA filler and the water is considered. For example, in the 18-20 ns interval, compared to $E_{1\ (PA\text{-}water)}$, the absolute value of $E_{2\ (PA\text{-}water)}$ is only increased by 3.04% and but $E_{2\ ((PA\ and\ MMT/DA)\text{-}water)}$ is increased by 21.1%. Although MD simulations may not fully capture the dynamic filtration process over long periods of time in reality due to time scale limitations, the 30 ns dynamic simulations performed in this study are sufficient to understand the transport behaviors of water and ions across the PA-TFCs membranes, and to provide valuable insights into molecular interactions and short-term diffusion dynamics.

In order to analyze the effect of MMT/DA filler on water permeability, Fig. 7-13 displays the partial density distribution of water molecules and ions, as well as the corresponding snapshots of two systems (at 30.2 ns). To analyze the evolution of water transport, we added the water density curves at 6.2, 18.2, and 24.2 ns. It is observed that water molecules passing through the PA-TFCs tend to accumulate on the opposite side, evident from the peak in the water density distribution within Region 1. Notably, the enlarged density plot of Region 1 highlights a significant increase in water molecules near the MMT surfaces, suggesting that water penetration is redirected from the PA surface by MMT. Therefore, the hydrophilic MMT have great potential to introduce additional hydrophilic channels within the membrane. Furthermore, the peak density within Region 1 does not show significant change over time from 6.2 ns to 30.2 ns for the modified PA-TFC, contrasting with the increasing trend observed for the pure PA-TFC. Particularly, the water density in the early 6.2 ns is significantly higher than that of the unmodified film. This indicates that the presence of MMT/DA enhances the water transport rate, which contributes to the increased water permeability of the MMT-incorporated membrane.

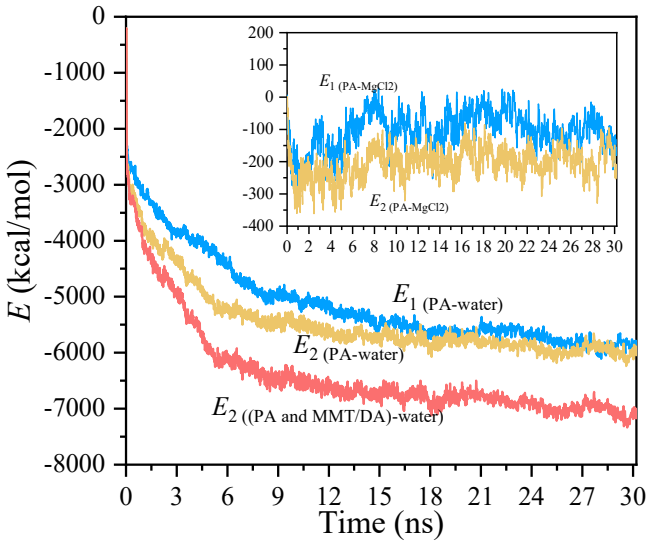

Fig. 7-12 The intermolecular interaction energy between PA-TFCs and water. The subscript 1 is for unmodified PA-TFC system and 2 is for modified system.

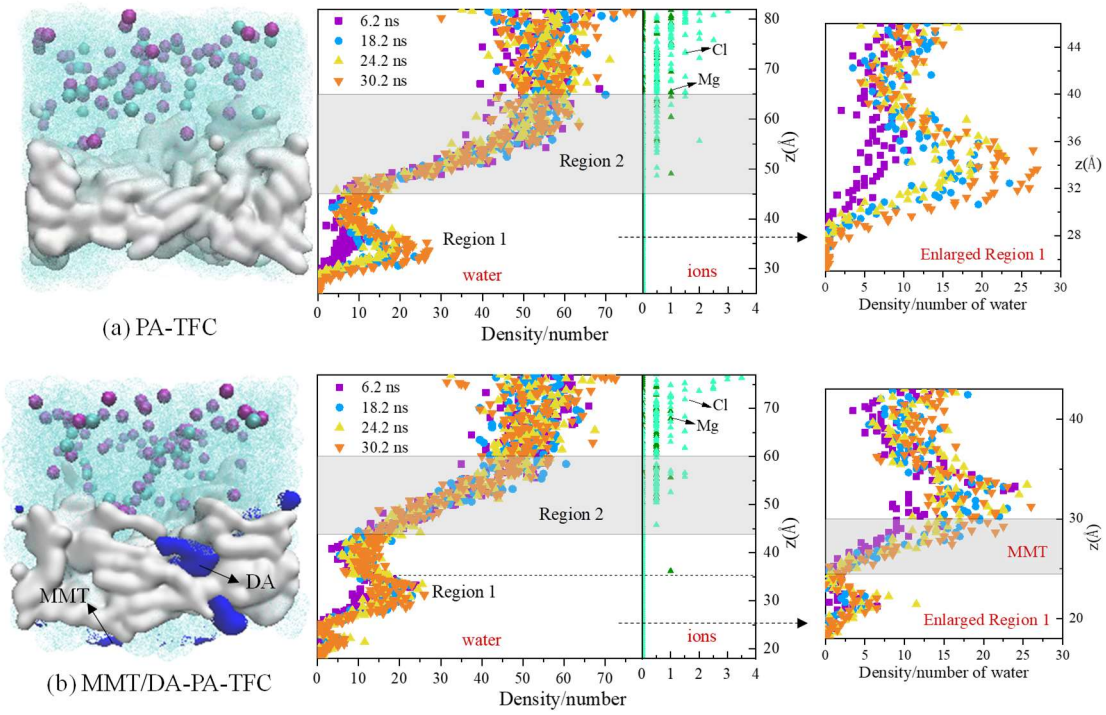

Fig. 7-13 Partial density distribution of water molecules and ions, as well as final configurations of two systems at 30.2 ns, visualized by VMD. In details, PA-TFC is represented in “QuickSurf” mode, water in “Solvent” mode, and ions in “VDW” mode. MMT/DA filler is colored blue.

It is observed from Fig. 7-13 that the density of Mg and Cl ions is zero around the other side of two virtual membranes where the water density peak is. This suggests that no ions pass through the membranes, indicating 100% magnesium and chlorine ion resistances. The result agrees well with previous simulation results that PA membranes with a DC exceeding 90% exhibit an almost perfect rejection of ions [271]. Region 2 represents the PA-water interfaces, where the uneven PA-TFCs surface faces the salt water. It is found that density of ions distributes in Region 2 is not larger that in bulk water, indicating that ions do not accumulate on the PA surfaces. Besides, the absolute value of $E_{1\ (PA\text{-}MgCl2)}$ and $E_{2\ (PA\text{-}MgCl2)}$ also not exhibit an increasing trend over time (Fig. 7-14(c)). Therefore, both two composites demonstrate good antifouling properties. The highly uneven surface of top-view modified composite (color coded from dark blue to red in Fig. 7-14(a) and (b)) may result in slightly larger $E_{2\ (PA\text{-}MgCl2)}$ and $E_{2\ (PA\text{-}water)}$ at the earlier filtration.

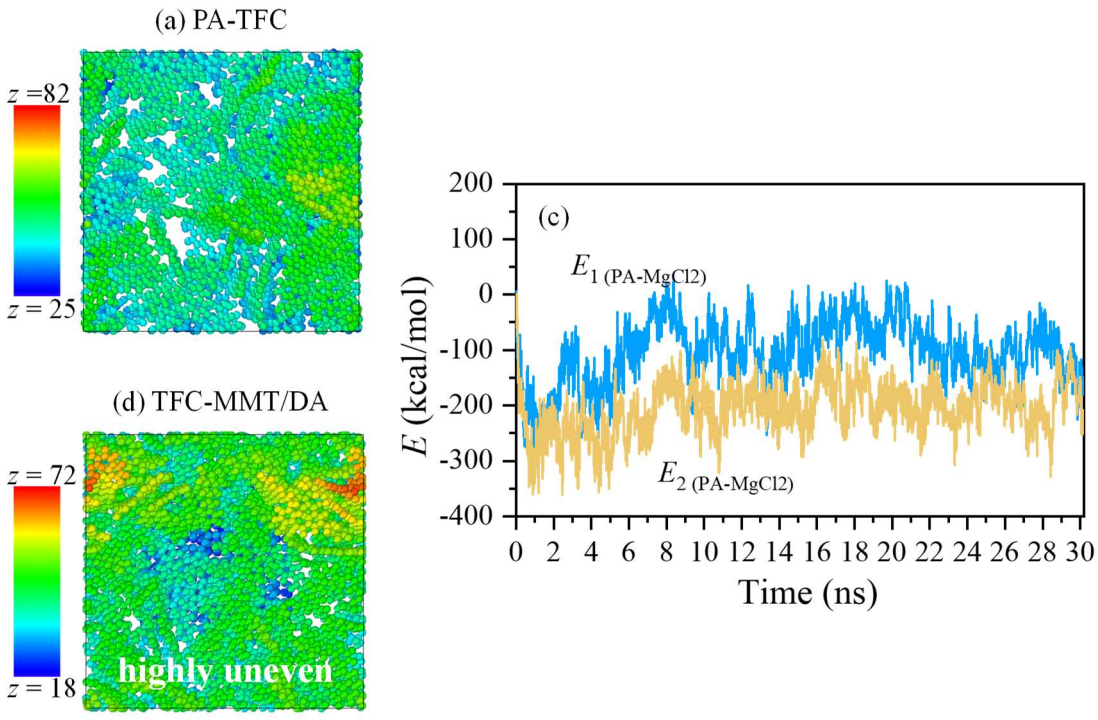

Fig. 7-14 (a) and (b)Top view of PA-TFC and MMT/DA-PA-TFC surface exposed to salt water, color coding based on the atomic *z*-positions; (c) The intermolecular interaction energy between PA-TFCs and ions.

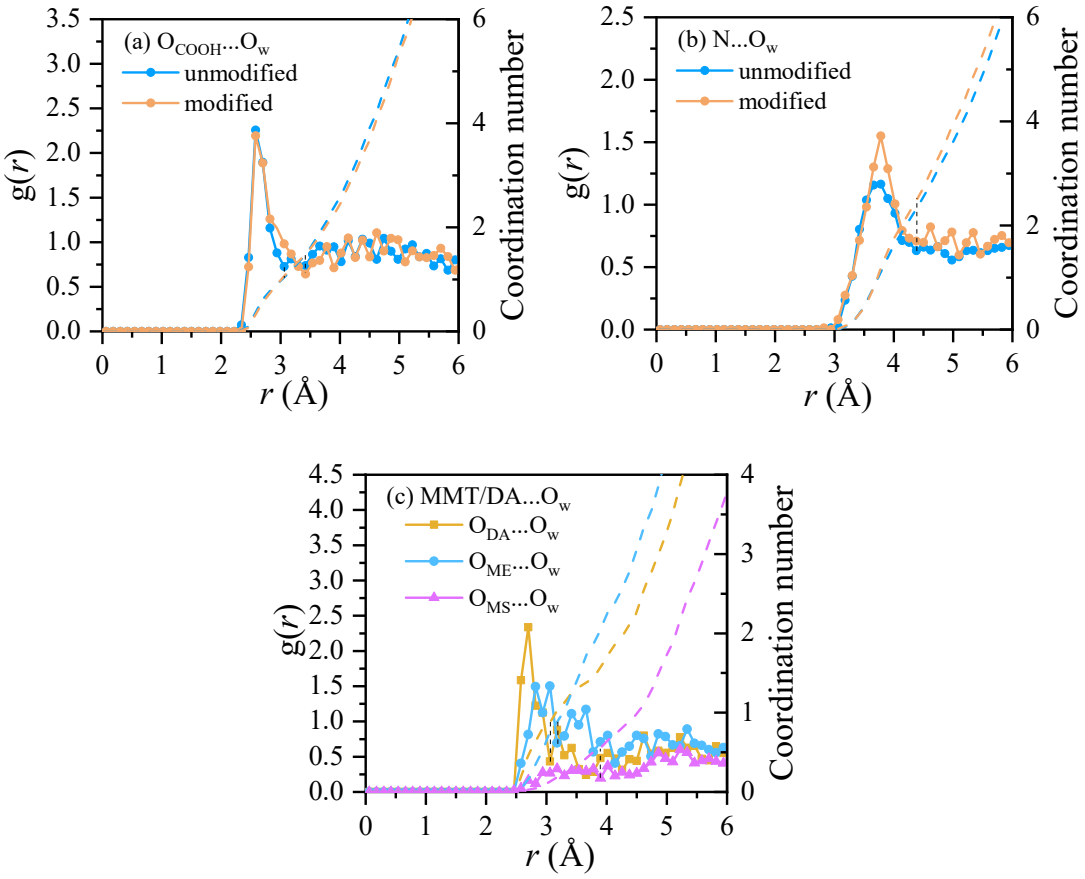

Fig. 7-15 RDFs and water coordination number of (a) O_{COOH}…O_w, (b) N…O_w, and (c) MMT/DA…O_w.

In PA matrix, carboxyl segments provide more strong interaction with water as the first RDF peaks of COOH-O_w center at 2.58 Å and for N-O_w at 3.78 Å (Fig. 7-15(a) and (b)). It is found that the CN of water molecules within the first solvation shell of -COOH segments increases from 1.03 to 1.48 with MMT/DA filler. For reactive nitrogen segment, the CN increases from 2.31 and 2.48. From Fig. 7-15(c), both DA and MMT edge exhibit high hydrophilicity as the CN values of water near oxygen atoms in DA and MMT edge are both 0.88, while MMT surface is less hydrophilic with CN value of 0.55. The incorporation of the MMT/DA filler not only increasing the hydrophilicity of PA matrix, but also provide extra hydrophilicity of itself for the composite membrane. The hydrophilic surface is favorable for water desalination membranes because high affinity for water is associated with higher water solubility. This characteristic typically

results in better water permeability and resistance to fouling in reverse osmosis (RO) desalination applications [284].

7.4 Conclusions

This chapter aims to investigate the effect of exfoliated MMT and MMT/DA nanofillers on the IP process and PA structure and performance using the MD simulation method. The regulatory mechanism of MMT is explored from the MPD diffusion and distribution characteristics, as well as the crosslinking degree between MPD and TMC monomers. Results show that adding an MMT nanosheet with varying DA content of 0, 10.37 *wt*%, 20.74 *wt*% and 31.11 *wt*%, D_{MPD} is reduced by 28%, 24%, 55% and 56%, respectively. DA ≥ 20.74 *wt* % is good to lower D_{MPD} while DA ≤ 20.74 *wt* % maintains better porosity of dry MMT/DA aggregates. The presence of MMT/DA broadens IP reaction zone by reducing MPD diffusion and modulating its distribution, yielding a looser and more hydrophilic "leaf-like" PA morphology with a DC increased by at least 44% in aqueous phase. Surprisingly, the IP reaction is able to break the strong H-bonding interaction between MMT and DA, making DA molecules as individual fillers disperse within the PA matrix after IP process. Furthermore, dry pristine and filled PA-TFCs are produced with high DC > 90 %. According to separation simulation results, MMT/DA have the potential to enhance water transport rate of PA-TFC membrane by providing hydrophilic sites and channels to water, without sacrificing its excellent $MgCl_2$ resistance.

Chapter 8

Ultra-selective bioinspired CNT@MMT dual-channel membrane for highly flux water purification

8.1 Introduction

Seawater and wastewater are available sources of freshwater and their purification is essential for addressing global water scarcity [285]. They can be purified into drinking water and even pure water through membrane-based filtration technologies. Nanofiltration membranes selectively prevent specific molecules or ions from passing through while effectively passing water owing to their nanoscale pores (< 10 nm) [118], [286-287]. Recent studies have highlighted the potential of two-dimensional lamellar membranes (2DLMs) to overcome the key challenge of balancing permeability and selectivity in conventional polymer membranes, due to their unique tunable nanochannels and achievable thinner thicknesses. 2DLMs are typically produced by a top-down fabrication method that exfoliates nanosheets from lamellar materials such as clay minerals, graphene, MXene, molybdenum disulfide (MoS_2), and boron nitride (BN) and reconstructs them into tightly packed nanosheets [114-119]. This assembly yields parallel-stacked nanosheets that generate both transverse (inter-lamellar) and vertical (intra-lamellar) channels [288-289]. Based on the size exclusion and adsorption removal mechanisms of 2DLMs, research to date has emphasized advances in membrane materials, pore size control methods, and contaminant degradation. Specifically, key efforts have focused on: (i) the use of functional and emerging 2D materials or heterogeneous composite membranes [117], [290-292]; (ii) the incorporation of guest species to modulate channels for precise selection [293-296]; (iii) the exploration of self-cleaning functions such as electrocatalysis and photothermal catalysis for contaminant degradation [288], [297-298].

The pore size of membranes is of utmost importance for the size-based selectivity of solute species and the permeation of water. Ensuring precise channel-size regulation and maintaining pore stability during long-time operation remains a challenge, since many lamellar membranes suffer from swelling problems. A widely adopted strategy to address this involves intercalating guest species, such as alkali-metal cations, small organic cations, surfactants, polymers, or nanoparticles, to support and bridge adjacent layers after exfoliation [32-33]. However, current research has largely focused on

controlling interlayer spacing (*h*) by chemical modification of exfoliated nanosheets, while intralayer channels (*d*), typically larger than 1 nm depending on the lateral dimensions of the nanosheets and the membrane fabrication process, is still difficult to manipulate (Fig. 8-1(a)) [287]. Consequently, most 2DLMs possess single-size selective channels, which may restrict their permeability-selectivity performance when exposed to flux containing a mixture of small salts and larger organic molecules. A more effective approach would involve designing hierarchical structures or multi-channel systems to facilitate mass transport across different length scales [299-300]. On the other hand, it is reported that the introduced intercalators within channels may impede mass transport kinetics to some extent, this strategy often requiring further assessment [33-34]. Additionally, reconstructed membranes also encounter issues such as non-uniform channels due to reassembly defects, alongside scalability challenges arising from the complexity and time demands of the fabrication process. As a result, existing single-pore size modulation and top-down fabrication is insufficient to achieve high efficiency and scale-up applications. Innovative structures and fabrication methods for 2DLMs need to be further explored.

To address the aforementioned limitations of channel-size control, co-existing pollutant removal, anti-fouling and scalability, we propose a non-exfoliated type of montmorillonite (MMT) membrane with hydroxyl carbon nanotubes (CNTs) assisted dual-selective channel design for separately selection of small ion and large organic. Naturally occurring clay minerals such as MMT and vermiculite are promising sustainable 2DLMs materials due to their layered structure and excellent adsorption capacity [22], [44]. Clay particles are hexagonal-shape crystals and have intrinsic nanoconfined channels formed by the stacking of adjacent layers that are ideal molecule selective pathways (Fig. 8-1(b) and (c)). Due to their swelling properties, the produce of clay membranes often requires exfoliation and intercalation treatment to stabilize channel size [30-31]. To avoid these steps and take advantage of the intrinsic interlayers, our design draw inspiration from fern structure (Fig. 8-1(d)), where a central axis (rachis) laterally supports and organizes the lamellar leaflets in an ordered arrangement.

Similarly, the proposed CNT@MMT membrane features an axis-supported structure, with 1D hydroxyl-CNTs serving as the axis (Fig. 8-1(e) and (f)). These hydroxyl-CNTs facilely form covalent bonds with the edge faces of clay nanosheets, maintaining MMT interlayer spacing which is controlled by hydration. Apart from the stabilizing function, the introduction of hydroxyl-CNTs also create tunable inter-edge channels between MMT particles for the first time. These channels can be tailored by the diameter of CNTs, thereby exploiting the specific adsorption and photocatalytic properties of CNTs for the adsorption and subsequent degradation of large organic molecules. These favorable functions brought by CNTs are crucial to enhance water flow and improve contaminant retention with enlarged intralayer size (< 2nm) while maintaining intrinsic uniform interlayer channels (< 1nm) of MMT for ion selectivity (Fig. 8-1(g)). The dual-channel design is the key to address the persistent challenge of trade-off between permeability and rejection efficiency in membrane technologies. Finally, unlike reconstructed membranes, this approach proposes opens a new avenue for fabricating ceramic membranes that are simpler, scalable, and adaptable to diverse separation needs from desalination to large molecule separation.

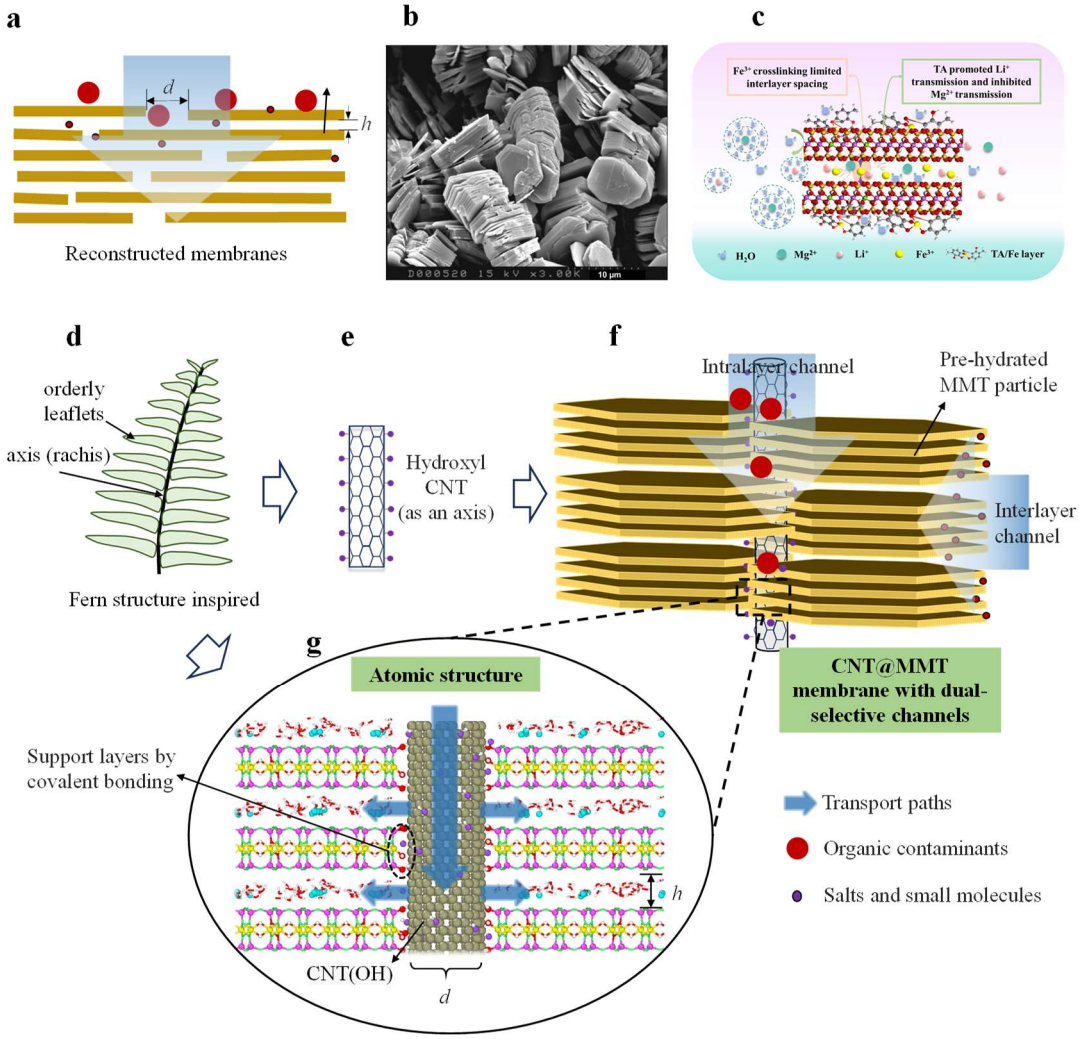

Fig. 8-1 Design concept of dual-channel CNT(OH)@MMT membrane. (a) Reconstructed 2DLMs with interlayer (*h*) and intralayer (*d*) channels. (b) SEM image of well crystallized clay particles with hexagonal morphology [301]. (c) Interlayer channels of MMT for ion separation. (d)-(f) Scheme of proposed MMT membrane design assisted by CNTs inspired by the fern structure. The hierarchical structure of CNT(OH)@MMT membrane consists of interlayer channel within MMT particles and intralayer channel between particles separated by CNTs. (g) Atomic structure of CNT(OH)@MMT membrane.

8.2 Modelling of materials and methods

8.2.1 Atomic structure

The Na-MMT model was built based on the unit cell formula of $Na_{0.75}[Si_{7.75}Al_{0.25}](Al_{3.5}Mg_{0.5})O_{20}(OH)_4$. A MMT monolayer consists of a 10*a* × 6*b* supercell cleaved along [010] face (*y*-direction), which is then terminated on both sides by Si-O-H and Al-O-H (under neutral conditions) [302-304]. The final dimension was 5.2 nm × 5.4 nm in *xy*-plane. Single-wall hydroxyl-CNT were built in armchair modes (*n* = *m* = 10) with a periodic boundary in the *z*-direction, corresponding to diameters of 11.61 Å. 10 *wt*% of hydroxyl groups were randomly distributed along the sidewalls of CNTs.

8.2.2 Reactive MD simulations

To investigate the bonding interactions between CNTs and MMT edges, reactive MD simulations were performed using the ReaxFF. The ReaxFF parameters used to model the interactions in the CNT@MMT water system in this chapter are based on reference [305]. A three-dimensional periodic boundary was applied. The edge contact model using a three-layer Na-MMT (*w* = 3.2 %) and a (10,10) CNT(OH) periodic in *z*-direction. Enough vacuum region was added in the simulation cell in *y*-dimension to eliminate interface periodic image. The face contact model using a two-layer *xy*-periodic Na-MMT supercell (*w* = 3.2 %) and a (10,10) CNT(OH) periodic in *y*-direction and vacuum region was added in *z*-dimension. Systems were equilibrated using NVT ensemble for 0.3 ns, with a time step of 0.5 fs.

8.2.3 Non-reactive MD simulations

Non-reactive force fields CLAYFF [121] and CVFF [123] have been extensively employed in systems involving clay and organic-clay composites, enabling the study of clay hydration, mechanical properties, and interfacial interactions [44], [237], [306-308]. Only non-bonding interactions, such as VDW and electrostatic interactions, are considered

for the intermolecular interactions between MMT and CNTs. The partial charges of edge atoms of MMT were taken from a quantum calculation [263]. Lennard–Jones (L–J) parameters for different atom types were calculated using the Lorentz–Berthelot rule [261]. The timestep was set to 1 fs.

The interlayer channel size of MMT depends on its hydration level. Here, hydrated MMT systems were constructed based on a three-layer Na-MMT and 0 to 18 H_2O per unit cell in the interlayer, corresponding to water content $w = m_{water}/m_{MMT} = 0 – 43.7\%$. These systems were equilibrated in a minimization procedure, followed by 100 ps of relaxation under NVE ensemble, and 500 ps of pressure control in z-direction using NPT ensemble. As ambient water is not considered in the system, virtual 12–6 L–J walls were set at the y-positions of MMT edges to confine water and Na ions within the interlayer region. The equilibrated d_{001} of Na-MMT systems was recorded.

8.3 Results and discussion

8.3.1 Structural characteristics of CNT@MMT composites

To ensure the formation of a dual-channel structure in CNT@MMT composites, hydroxyl-modified CNTs (CNT(OH)) are expected to chemically bond with the edges of the clay. To verify this, reactive molecular dynamics (MD) simulations were performed to investigate the interaction mechanisms between CNT(OH) and MMT at both the edges and basal surfaces. Fig. 8-2(a) and (b) show the binding energies for the edge and face contact modes at different initial distances between MMT and CNT(OH). The binding energies were calculated from the total potential energy difference between composite system and the sum of the individual energies of CNT(OH) and MMT in the final geometry snapshot. These values exclude relaxation of the MMT or CNT(OH) when the interface is broken and thus isolate the instantaneous bond strength at the interface [309]. The negative values of binding energies indicate that the combination of CNT(OH) and MMT is an exothermic process. Notably, the lower binding energy observed in the edge contact model (with a 3.8-nm-long CNT) signifies stronger

bonding at the interface compared to the face contact model (with a 5.2-nm-long CNT), despite the smaller contact area of (CNT(OH). This is attributed to the abundance of hydroxyl groups exposed at the edges of clay particles at neutral pH, making them more reactive than the basal planes to interact with both CNT(OH) and pristine CNT. Pristine CNT shows weaker binding affinity than CNT(OH) in both contact models at the same initial distance between C atoms and the MMT. It is reported that oxygen functionalization brings better dispersion for CNTs in organic and inorganic matrices and compatibility with hydrophilic clay minerals [310-311]. Since MMT edges are hydrophilic and rich in reactive –OH groups, incorporated CNT(OH) preferentially interacts with the edges rather than the basal faces.

To investigate the bonding mechanisms in the two contact models, we calculated the number of reactive bonds between CNT(OH) and MMT. No bonds are observed between CNT(OH) and MMT basal face, even at dry interface (Fig. 8-2(d)). In contrast, Si/Al–O–C linkages are found between CNT(OH) and MMT edges, where bridging hydroxyl oxygen can be part of either the MMT edge (O_M) or CNT(OH)) (O_C), as seen in the topological structure (Fig. 8-2(c)). The low binding energy in the edge contact mode is directly associated to interfacial bonding. In the edge contact mode, closer initial Si…C distances promote bond formation and yields lower binding energy. As shown in Fig. 8-2(e), the number of various bonds remain unchanged after 50 ps over the 300-ps simulation, indicating that the bonding reaction reaches equilibrium, and corresponding equilibrated number of each type of bond is shown in Fig. 8-2(f). Shorter initial Si…C distances results in an increased number of O_C–Si/Al and C–O_M bonds between CNT(OH) and MMT, which correlates with enhanced binding energy. However, when the Si–C distance is greater than 4 Å, these bonds are not found. The CNT(OH) originally carries 38 –OH groups with 10% modification, so the change in number of C–O_C bonds can reveal the structure integrity of CNT(OH). It is suggested that the original hydroxyl groups on the CNT sidewall have a slight loss as the initial Si…C distance decreases, indicating that the bonding is accompanied by slight deformation of the CNT at the interface. When the Si…C distance reduces to as small

as 1 Å, C-Si/Al bonds may form (Fig. 8-2(f)).

The results confirm that CNT(OH) can successfully create covalent bonds with MMT edges by forming Si–O–C or Al–O–C linkages, ensuring the establishment of inter-edge channels. The functional hydroxyl groups on CNTs promote the bond formation due to their hydrophilicity and high electronegativity [312].

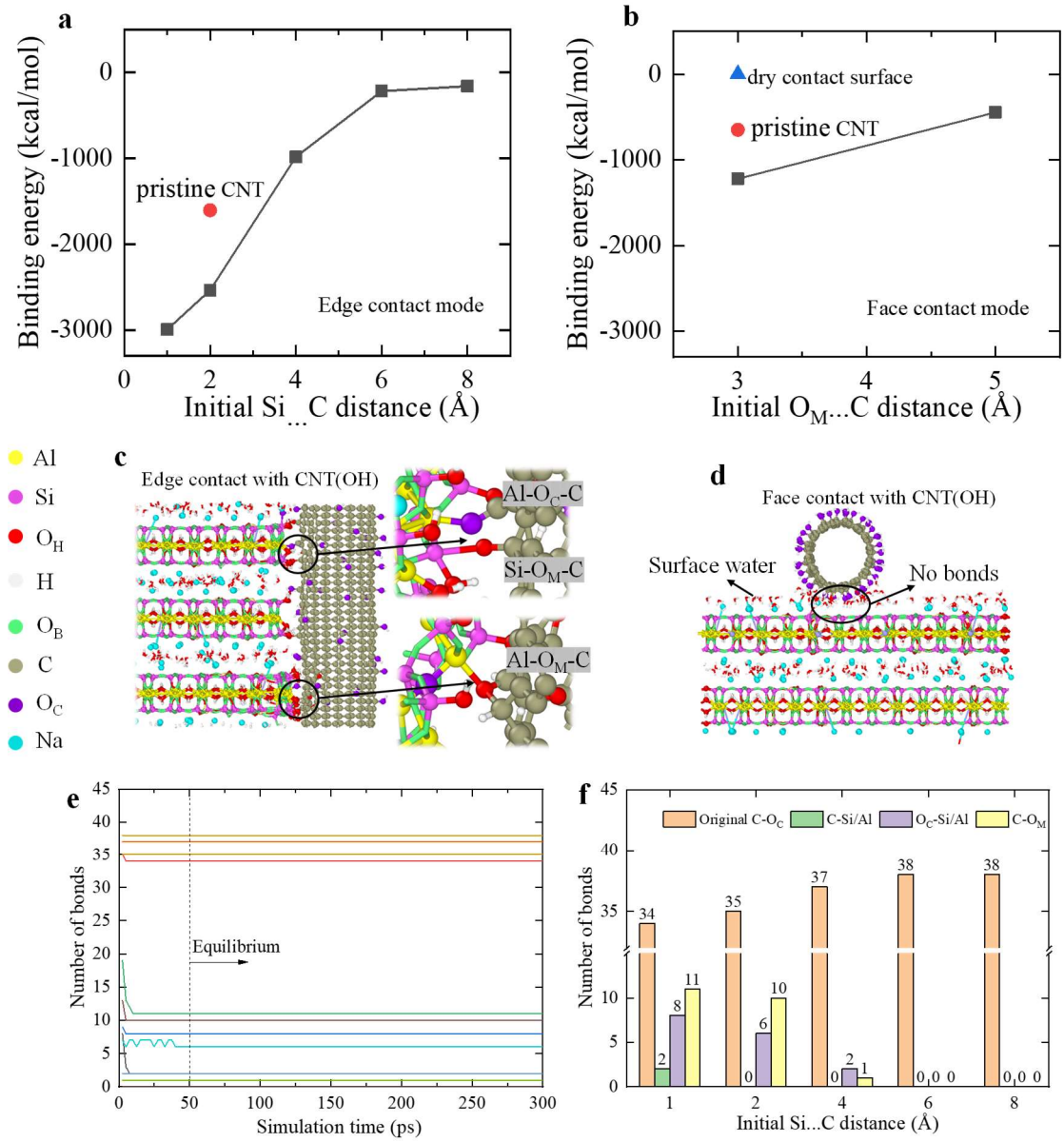

Fig. 8-2 Bonding characteristics of CNT@MMT composites. (a) Binding energy between MMT edge and CNT(OH) at different initial Si…C distances. (b) Binding energy between MMT basal surface and CNT(OH) at different initial O_M…C distances,

where O_M represents hydroxyl oxygen atoms at the MMT edges. (c) Topological configuration of edge contact model between MMT and CNT(OH) at initial Si…C distance of 2 Å. (d) Topological configuration of face contact model between MMT and CNT(OH) at initial O_M…C distance of 3 Å. Color code: yellow-Si; pink-Al; red-hydroxyl O in MMT; green-bridging O; cyan-sodium; olive-C; purple-hydroxyl O in CNT(OH); white-hydroxyl H. (e) Time evolution of the number of various bond types, and **f** corresponding bond counts after equilibrium is reached.

8.3.2 Interlayer size control of CNT@MMT membrane

Unlike common intercalation strategies, the interlayer channels within the CNT@MMT membrane take advantage of inherent structures of MMT crystals and are subsequently stabilized by CNTs. To be ion-selective channels, the interlayer spacing should be smaller than the Debye length (~20 Å), where DLVO theory breaks down and ion-specific and hydration effects become significant [313]. It can be precisely controlled by water content (w) when the MMT interlayer accommodates no more than three layers of water molecules (3W), corresponding to basal spacings (d_{001}) of 18.8 Å [314]. Non-reactive MD simulations were conducted to find the relationship between d_{001} and w. As shown in Fig. 8-3, the obtained d_{001} of Na-MMT is less than 12.4 Å at $w <$ 0.097, which aligns well with the experimental values of bulk Na-MMT powder, indicating the presence of a single layer of water molecules (1W) in the interlayer region (Table 8-1) [262, 315-317]. For $w \geq 0.097$, the calculated d_{001} of Na-MMT agrees with experimental data for Wyoming-type Na-montmorillonite [318] and simulation values for smectite [314], following a linear relationship of $d_{001} = 0.97 + 2.47w$ with a high correlation coefficient ($R^2 = 0.996$). The thickness of a single MMT layer is approximately 9.6 Å. Consequently, by controlling the w, the interlayer height can be quantitatively adjusted from 2.8 Å and 9.2 Å (1W ~ 3W). This precise control is crucial for ion sieving, since the channel sizes should be controlled to be smaller than the hydration diameter of target ions, e.g., 7.6 Å for Li^+ and 8.5 Å for Mg^{2+}, in order to efficiently select ions according to the dehydration barriers that need to be overcome

[319]. For example, vermiculite membranes with and without intercalation can control the interlayer channel to 3-5 Å, achieving high rejection efficiencies for dyes (> 98%) and salts (~ 95%). [285], [320-321]. However, reported pure MMT membranes have a wide range of interlayer heights from 4 to 9.5 Å (Table 8-1) [262], [315], [322-326]. It suggests that the interlayer spacing of MMT membranes varies greatly due to uncertainties in morphologies of exfoliated nanosheets and reassembly process. When modified with polymers, salts or nanoparticles, the range can be fixed to vary from 4 to 7.5 Å, providing more predictable control [32], [316], [319], [325-326]. In contrast, the proposed pre-hydration and stabilizing method is more flexible and precise in regulating interlayer height of the MMT membrane compared to the layer-by-layer assembly.

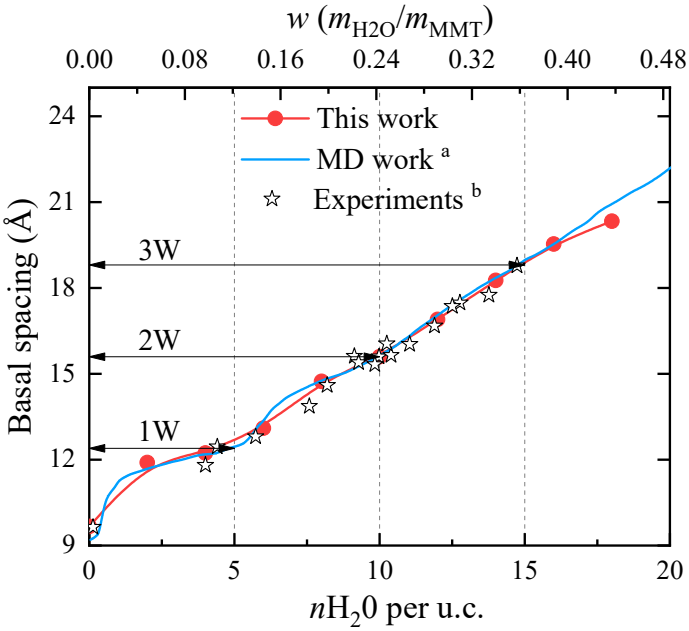

Fig. 8-3 Basal spacing of Na-MMT as a function of water content *w* and number of water molecules per unit cell. a is for Ref. [314] and b is for Ref. [318].

Table 8-1 Basal spacing of Na-MMT crystal and existing reconstructed MMT membranes. The corresponding interlayer height of the membranes is calculated based on the thickness of an MMT layer of ~9.6 Å.

d_{001} of Na-MMT crystals (Å)	d_{001} of MMT membranes (with intercalation) (Å)	Interlayer height of membranes (Å)	Ref.
< 12.4 (1W) (w < 0.097)	9.7 + 24.7w ($w \geq 0.097$)	2.8 ~ 9.2 (1W~3W)	This study
12.4	14.7	5.1	[315]
12.3	17.5	7.9	[262]
14.9	17.9	8.3	[322]
12.2–11.5	13.6–15.2	4–5.6	[324]
12.2	17.1 (CTAB)	7.5	[316]
	14.3	4.7	[323]
	14.1	4.5	[325]
	13.7 (PDA/PEI)	4.1	[325]
	19.1	9.5	[326]
	16.8 ($Fe(OH)_3$)	7.2	[326]
	13.6–14.8 (CTAC)	4–5.2	[327]
	14.4–14.9 (Fe^{3+})	4.8–5.3	[319]

8.3.3 Water and dye transport properties

The dual channels are designed to separate ion selectivity from organic contaminant selectivity. Specifically, interlayer channels in clays are dedicated to small molecule and ion selection, whereas intralayer channels, which can be larger than the interlayer spacing, allow the free passage of water molecules and ions, but restrict the

movement of large organic contaminants. This approach ensures that, during ion selection, water flow can be enhanced through enlarged intralayer channels, and when ensuring effective organic pollutant filtration can simultaneously maintain efficient ion selectivity.

To verify the ability of intralayer channels of the CNT@MMT membranes for organic selectivity and higher water permeation, non-equilibrium molecular dynamics (NEMD) simulations were performed up to 10 ns under NVT ensemble to study the diffusion of water and methylene blue (MB). MB (319.85 g mol^{-1}) is a cationic dye with a dimension of 1.6 × 0.8 nm [328]. The setup of filtration simulations is illustrated in Fig. 8-4(a). The system consists of an equilibrated CNT@MMT membrane positioned between feed and permeate reservoirs, bounded by graphene sheets for implementing pressure. In the membrane section, the transport network includes a 1.2-nm-width intralayer channel created by an open-ended (10,10) CNT with 10 *wt*% hydroxyl functionalization, and 0.74-nm-height interlayer channels (corresponding to d_{001}= 17.2 Å at *w*=29%), consistent with the sub-1 nm channel observed in most MMT membranes (Table 8-1). Between the MMT and CNT(OH), Si/Al -O-C bonds were manually created. In the NEMD simulations, mass transport was driven by a pressure difference across the membrane, with feed side pressure set at 100 MPa, while the permeate side was fixed at 0.1 MPa. Note that the pressure difference applied at the molecular level is more than an order of magnitude higher than that typically used in nanofiltration, which is necessary to ensure a statistically meaningful number of molecules passing through the membrane in the very short time [287]. To analyze the water flux (J_w), the quantity of permeate water that passed through the membrane was calculated as the increase of water molecules in the permeate reservoir. The number water flux ($nm^{-2}\cdot ns^{-1}$) can be calculated by normalizing the number of permeate water molecules by simulation time (ns) and the membrane surface area (36.88 nm^2), and then it can be converted to a volumetric water flux (L h^{-1} m^{-2} bar^{-1}) using molar volume of water [329]. The rejection rate of MB molecules was determined by subtracting the MB amount presented in the permeate reservoir from the initial MB amount in the feed reservoir.

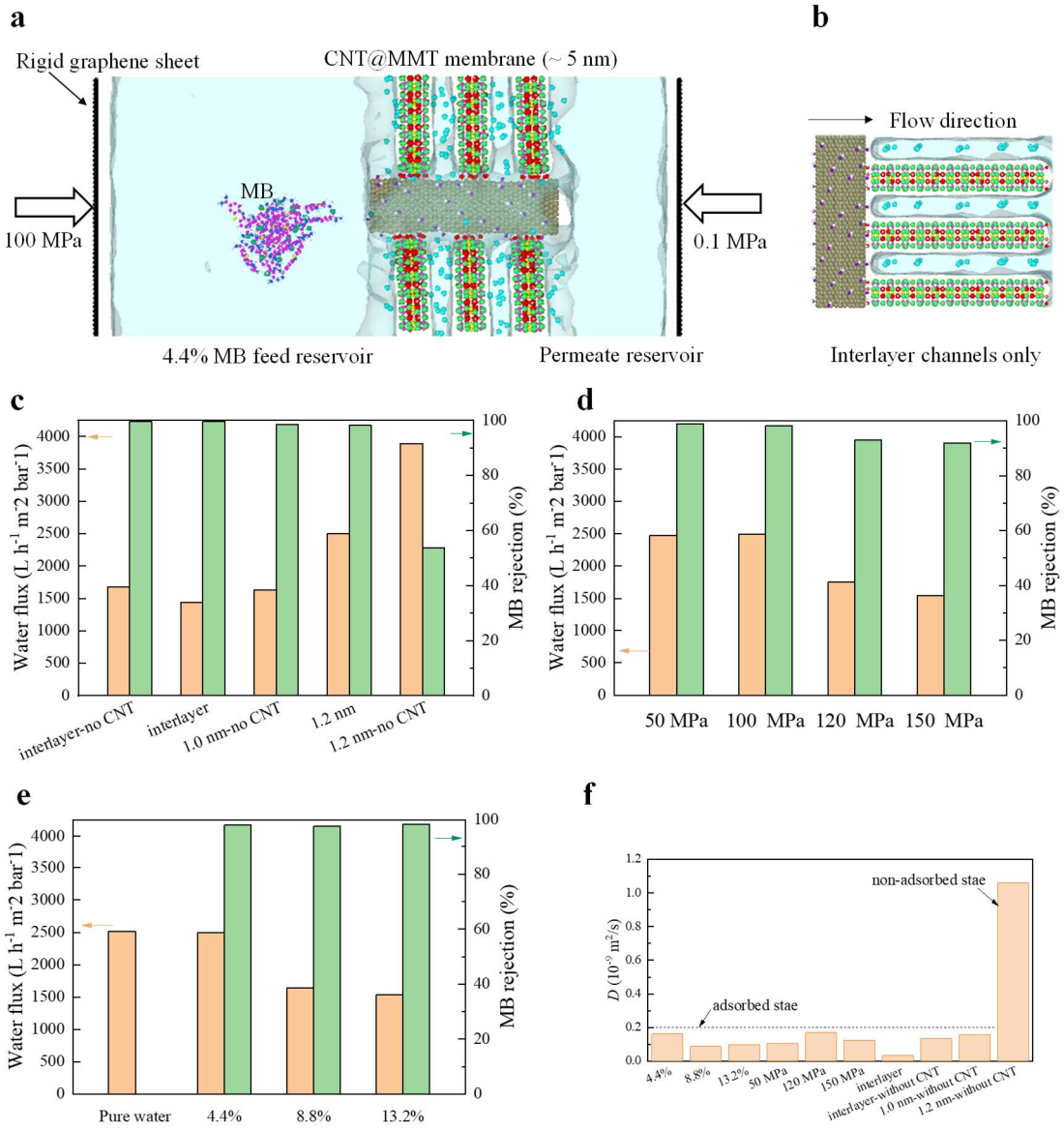

Fig. 8-4 Simulation setup and membrane performance. (a) Simulation setup for NEMD at initial configuration for CNT@MMT membrane. The feed reservoir is a 4.4 % MB solution consisting of 8000 water molecules and 20 MB molecules. Color code for the CNT@MMT membrane: yellow-Si; pink-Al; red-hydroxyl O in MMT; green-bridging O; cyan-sodium; olive-C; purple-hydroxyl O in CNT(OH); white-hydroxyl H. The light green transparent surface mesh is a water molecule rendered by OVITO [274]. (b) The membrane model used to study interlayer-only transport where water flow is parallel to the clay layer. (c) Water flux and MB rejection rate through interlayer-only channels and intralayer-included channels in the presence and absence of CNT(OH) at a pressure of 100 MPa and a MB concentration of 4.4%. Water flux and MB rejection rate through

1.2-nm intralayer-included channels with CNT(OH) (d) at a pressure of 100 MPa and (e) at a MB concentration of 4.4%. (f) Diffusion coefficients of MB molecules.

To emphasize the significant enhancement of water transport and dye rejection in intralayer channels achieved by incorporating CNT(OH), we evaluated the J_w and MB rejection rate in intralayer channels with or without CNTs support at 100 MPa. For comparison, the J_w and MB rejection rate were also calculated through interlayer-only channels, where the flow direction is parallel to the clay layers (Fig. 8-4(b)). As shown in Fig. 8-4(c), MB rejection approaches 100% when water flow only through interlayer gaps, indicating that a 0.74-nm clay interlayer effectively blocks MB in aqueous phase either with or without CNTs. Including a 1-nm intralayer channel maintains high selectivity (> 98%), but the permeability has no significant increase. When the intralayer channel size increases to 1.2 nm, the permeability improves significantly. However, MB rejection differs notably between cases with and without CNTs. With CNT(OH) support, the MB rejection rate exceeds 95% with the J_w increased by ~50%, while without CNTs, it drops to around 50%, despite a 200% rise in J_w. It suggests that although a narrower 1-nm interlayer channel can achieve 98% rejection via size exclusion, it limits water flux compared to the 1.2-nm channel. Results highlights the critical role of CNT(OH) in expanding intralayer channels for higher water flux, and particularly in enhancing selectivity for organic pollutants.

We further examined the effect of high solute concentration and pressure on membrane transport performance in a 1.2-nm intralayer pore supported by CNT(OH). To assess pressure effects, 50, 100, 120, and 150 MPa were applied to the feed side with a 4.4% MB. As shown in Fig. 8-4(d), the selectivity for MB decreases with increasing pressure but remains above 92%. Water permeability shows a declining trend from 100 MPa, with J_w decreasing by 30% at 120 MPa and 38% at 150 MPa, compared to 2496 L h^{-1} m^{-2} bar^{-1} at 100 MPa. To evaluate concentration effects, we tested MB concentrations of 4.4%, 8.8%, and 13.2% under 100MPa. It is found that MB rejection maintains over 97% even at highest MB concentrations of 13.2%, but J_w was

significantly impeded at higher MB concentrations exceeding 4.4% (Fig. 8-4(e)). These results demonstrate that the CNT@MMT membrane enable fast water transport and high MB exclusion at pressures up to 100 MPa and concentration up to 4.4% (44.46g/L). In practical applications, nanofiltration and reverse osmosis typically operate at pressures of 1-10 bar and 10-150 bar, respectively, with MB contamination levels of 50-500mg/L [287]. These conditions are far smaller than the tested limits, confirming the effectiveness of CNT@MMT membrane in balancing of permeability and selectivity under normal operating conditions.

8.3.4 Mechanisms of enhanced membrane performance

To investigate the mechanism behind the enhanced MB selectivity in the presence of CNT(OH), the diffusion behavior of MB in each system was analyzed. Previous studies indicate that diffusion coefficients (D) of MB below 0.35×10^{-9} m^2/s reflect a restricted movement due to adsorption on MMT surface [22]. As shown in Fig. 8-4(f), the D values of MB passing through 1.2-nm intralayer channel with CNT(OH) fall below 0.2×10^{-9} m^2/s, which can be regarded as they are in the adsorbed state on the CNT@MMT framework. In contrast, in the absence of CNT(OH), the diffusion coefficient of MB through a 1.2-nm intralayer channel exceeds 1.0×10^{-9} m^2/s, indicating large mobility during filtration and in a non-adsorbed state. In contrast to the adsorption mechanism in the 1.2 nm channel, for the other cases involving only interlayer channels or smaller 1.0-nm intralayer channels, the D values remain low in the presence and absence of CNT(OH), reflecting a size-exclusion mechanism (>98%).

Further, we investigated the retention of MB molecules within the membrane region and the corresponding rejection rate as a function of permeate percentage (Fig. 8-5(b-d)). Fig. 8-5(a) shows the variation with simulation time of the permeate percentage, which is defined as the ratio of the number of permeate water molecules to the initial number in feed reservoir. As shown in Fig. 5(b), in the absence of CNTs, approximately 50% of MB molecules penetrate the 1.2-nm intralayer pore of MMT during the initial 15% of water permeation and quickly pass through the membrane as

water permeation reaches 30%. Once MB leaves the membrane, water permeation is greatly accelerated (Fig. 8-5(a)). Mechanisms of improved MB rejection can be attributed to the fact that the added CNT(OH) significantly impedes the passage of MB molecules. Fig. 8-5(c) shows that even with increased MB concentrations, the total amount of MB (just 10%) retained within the membrane rise insignificantly. Notably, elevated pressures (>100 MPa) are more likely to facilitate the MB intrusion, with around 40% of MB molecules penetrating the membrane intralayer region (Fig. 8-5(d). However, despite the increased MB accumulation inside membrane, most MB molecules are trapped within the membrane due to the adsorption by CNT@MMT framework, as evidenced by the stable number of MB molecules retained within the membrane.

Studying the contribution of CNT(OH) and MMT edges to MB adsorption is essential to understand the retention mechanism of MB within the membrane. The binding energy for a MB molecule on CNT(OH) sidewall and at the MMT edge face are calculated to be -306 kJ/mol and -209 kJ/mol, respectively. CNT(OH) exhibits a stronger attraction to MB compared to MMT, indicating MB molecules preferentially adsorb onto CNT(OH). This can be attributed to π-π interaction arising from the aromatic benzene rings in both MB and CNT(OH). Previous studies have shown that larger-size and an oppositely charged molecules tend to block nanochannels, leading to reduced permeability [316], [330]. This often take place in the negatively charged clay membranes used for the removal of positively charged dyes. Owing to the great affinity for organic molecules, CNT(OH)s serving as effective adsorbents not only prevent MB from passing through intralayer channels, but also avoiding the blockage of channel entrances by adsorbed on the MMT edges.

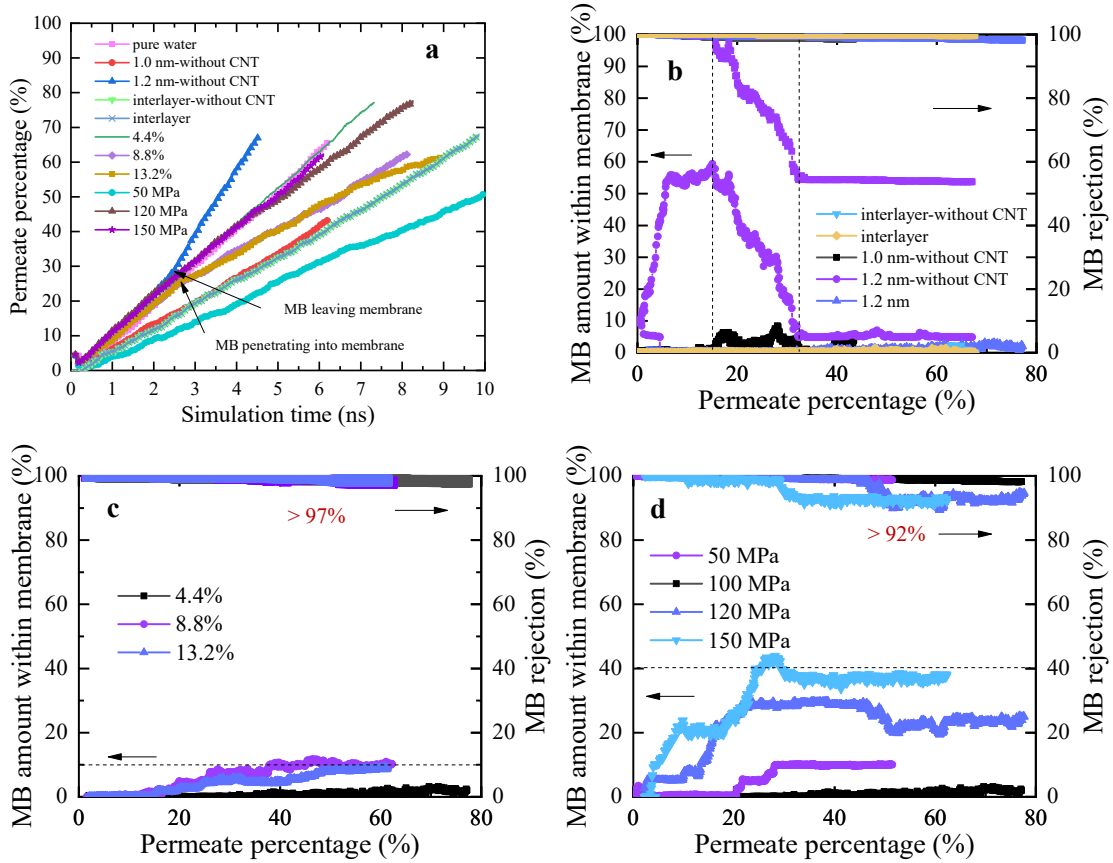

Fig. 8-5 MB retention within membranes. (a) Permeate percentage as a function of time. The retention of MB molecules within the membrane region and the corresponding rejection rate as a function of permeate percentage through (b) interlayer-only channels and intralayer-included channels in the presence and absence of CNT(OH) at a pressure of 100 MPa and a MB concentration of 4.4%, and through 1.2-nm intralayer-included channels (c) at a MB concentration of 4.4% and (d) at a pressure of 100 MPa.

8.3.5 Structural stability

The structural response of the CNT@MMT membrane to the pressure-driven flow is also a great concern in membrane performance. To investigate the role of CNT(OH) in maintaining channel gaps, an additional filtration simulation was conducted on MMT model without CNT(OH) support. Unlike the previously described setup for pure MMT membranes with all layers fixed, this simulation allowed the outer MMT layers to move freely while fixing only the middle layer. In the CNT-containing models, all MMT

layers free to move. Fig. 8-6(a) shows the change in interlayer height of MMT, measured as the difference between instantaneous and initial height, for membrane models with CNT(OH) at 120 MPa and without CNT(OH) at 100 MPa. Results show that the presence of CNT(OH) limits the fluctuations of interlayer spacing to less than 0.5 Å, providing sufficient support to prevent significant movement of the MMT sheets. In contrast, the absence of CNTs leads in pronounced variations in interlayer spacing. It is seen that the interlayer spacing near the feed side (D_1) decreases by more than 2 Å due to hydraulic pressure, while near the outlet side, it (D_2) sharply increases, indicating a pressure-induced delamination of the clay sheets, as illustrated in Fig. 8-6(b). Furthermore, the intralayer channel becomes narrower due to the movement of clay layers without CNT support. These results demonstrate the effectiveness of CNT(OH) in maintaining structural integrity and ensuring the stability of both interlayer and intralayer channels during cross-flow filtration.

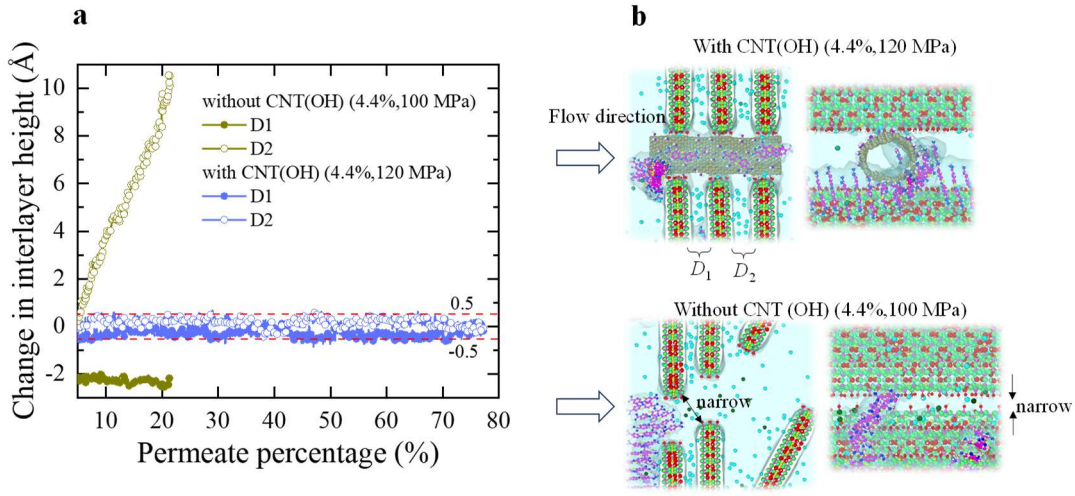

Fig. 8-6 (a) The evolution of the change in interlayer height of MMT with and without (10,10) CNT(OH) in the intralayer region. (b) Configurations of the two models at the final points in curves.

8.3.6 Performance comparison with other membranes

To compare the calculated membrane performance with experimentally measured

data of other membranes, it is necessary to predict the water flux with real clay particles from water flux calculated by atomic models. Clay particles typically range in size from 10 to 100 nm with an aspect ratio (width-to-thickness ratio) of 5 to 30 [317]. The atomic MMT model used in calculations has dimensions of x:y:z ≈ 1:1:1 (~5 nm), which is an order of magnitude smaller than the size of real clay platelets. The obtained volumetric water flux is calculated based on an atomic-scale separation area of A_1 = 5.2 nm × 7.1 nm. Given the model thickness of 5 nm, the xy-plane area of a real particle (A_2) is estimated to be at least 25 times larger than A_1, as illustrated in Fig. 8-7(a). Since the sizes of the intralayer channels are wider and paths are shorter than those of the interlayer channels, the calculated J_w can be considered as the J_w through a single intralayer channel. Due to the hexagonal structure of MMT particles, each particle has six edge surfaces, which can form six intralayer channels with adjacent particles. As a result, a single particle accounts for three intralayer paths for mass transport. Thus, the real water flux (J_w*) can be scaled down from the atomic-scale J_w by the formula J_w* = (J_w / 25) × 3, which considers the scaled area and the number of pathways. The values of J_w* are presented in Fig. 8-7(b). It is shown that the CNT@MMT membrane exhibits an impressive water permeance of 180~300 $L \cdot m^{-2} \cdot h^{-1} \cdot bar^{-1}$, higher than 122.4 $L \cdot m^{-2} \cdot h^{-1} \cdot bar^{-1}$ of VMT membrane with the interlayers spacing of 1.51 nm and intralayer of 1.21 nm. The membrane can achieve high permeability and MB rejection under pressures up to 100 MPa. This performance is also an order of magnitude higher than most of reported polymer and other 2D membranes.

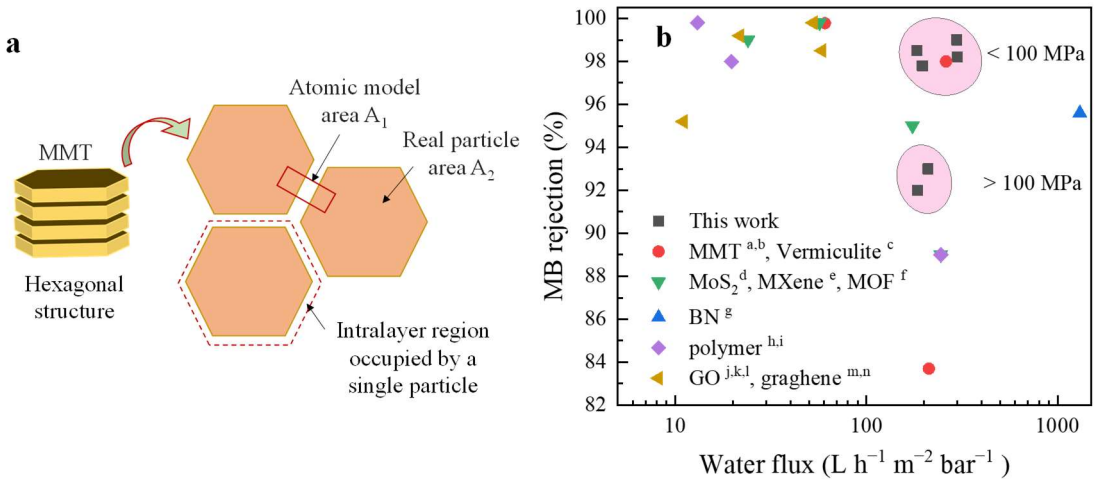

Fig. 8-7 (a) Relationship of filtration area of atomic models and area of real clay particles. (b) Comparison of MB rejection and water flux with other membranes. References: a [315], b [326], c [321], d [331], e [332], f [333], g [334], h [335], i [336], j [328], k [337], l [338], m [339], and n [340].

8.3.7 Membrane regeneration

Fouling caused by dye adsorption in membranes is a critical problem that affecting the long-time performance of membranes. CNT(OH) effectively adsorbs organic contaminants, preventing their transport through the membrane or accumulation at MMT edges. The strong adsorption of CNTs to organic pollutants makes composite membranes easier to clean and regenerate. This can be achieved either by separating the pollutant-adsorbed CNTs from the clay matrix or by utilizing the photocatalytic properties of the CNTs to degrade methylene blue. The latter method can maintain the composite structure without causing physical damage and is a promising approach. Photocatalysis involves absorption of visible or UV light by semiconductor materials, using solar radiation and catalysts to generate hydroxyl radicals that oxidize and decompose chemical contaminants. The dual role of CNTs as both adsorbent and photocatalyst is attributed to their graphitic structure, which facilitates π-π and dipole-dipole interactions [341]. Previous studies have shown that CNTs can directly degrade MB

via photocatalysis and this photocatalytic activity stems from the sp^2 hybridized lattice of the graphitic framework [342]. Adding catalysts can accelerate the reaction. For example, N-doped CNTs exhibit stronger photocatalytic degradation of MB than pure CNTs [342]. Also, this catalytic approach offers an eco-friendly cleaning solution by converting organic pollutants into clean byproducts, such as CO_2 and H_2O.

8.4 Conclusions

In this chapter, we proposed a novel clay-based membrane that combines CNT(OH) adsorption and dual-channel design for multifunctional decontamination. The structure of the CNT@MMT membranes and mass transport properties through intralayer channels were evaluated using reactive and non-reactive MD simulations. Main conclusions are as follows:

1) Reactive MD studies confirmed that Si/Al-O-C linkages are formed between hydroxyl-CNT and MMT [010] edge faces, which are sufficiently robust to stabilize the MMT interlayer and intralayer structure during filtration.
2) The non-exfoliated method of the MMT membrane is more flexible and precise in regulating interlayer height from 2.8 Å and 9.2 Å by controlling *w* compared to most exfoliated MMT membranes.
3) Mass transport studies highlight the ability of the CNT@MMT membrane with 1.2-nm intralayer pore and 0.74-nm interlayer to overcome the permeability-selectivity trade-off under high pressure up to 100 MPa. It achieves a remarkable MB rejection rate of > 97% and a water flux of 180~300 $L \cdot m^{-2} \cdot h^{-1} \cdot bar^{-1}$ predicted from the molecular level. The enhanced mechanism is attributed to the good adsorption properties of CNT(OH) for MB than MMT edges.

General conclusion

This thesis systematically investigates the development of organically modified MMT composites for enhanced adsorption and membrane-based filtration in water purification. For adsorption properties, we demonstrated that HDTMA-MMT both HDTMA-MMT and unmodified Na-MMT are highly effective for MB removal, exhibiting adsorption energies ranging from -100 to -250 kJ/mol. MB adsorption mechanisms is chemisorption dominated by strong electrostatic interaction between CH_3 groups of MB and oxygen atoms of MMT surfaces. However, HDTMA modification enhances adsorption only at $w > 50\%$, as low w (< 50%) causes site-blocking effects. To overcome this limitations, CHT-MMT composites were explored, focusing on coating mechanisms, thermal stability, and adsorption performance. The CHT-MMT interaction is mainly generated by $-NH_3^+$ via electrostatic and hydrogen bonding interactions at acidic condition where CHT has higher protonation rate, and the strong interaction ensure high-temperature stability (up to 800 K) of this composite in water. The CHT-MMT shows superior MB immobilization capacities up to 80% (158.79 mg/g) at pH 9.5, driving by multilayer adsorption via hydrogen bonding and π-π stacking interactions. Furthermore, adsorption performance for anionic MO was investigated, revealing that CHT-MMT captures MO predominantly through strong hydrogen bonding, while HDTMA-MMT relies on hydrophobic and electrostatic interactions. MO desorption energies from CHT-MMT and HDTMA are comparable, demonstrating stable MO adsorption. The research demonstrates that modification enables multilayer adsorption, significantly improving dye removal at high concentrations compared to unmodified MMT. Additionally, positively charged CHT-MMT and HDTMA-MMT exhibit strong anionic dye uptake, highlighting their potential for treating mixed dye systems in real wastewater applications.

To improve membrane performance, we incorporated exfoliated MMT nanosheets into PA membranes, where MMT and DA modifications reduced MPD diffusion and broadened interfacial polymerization zones. The modified PA membranes exhibited a looser and more hydrophilic “leaf-like” PA morphology with a crosslinking degree increased by at least 44% in aqueous phase. Separation simulation showed that

MMT/DA have the potential to enhance water transport rate of PA membrane by providing hydrophilic sites and channels to water, without sacrificing its excellent $MgCl_2$ resistance.

To further address the challenge of selectivity-permeability balance in membrane techniques, we inspired by the fern structure in nature and successfully designed a non-exfoliated MMT membrane with CNT(OH)-assisted dual-selective channels for highly flux water purification. MD simulations reveal that the CNT@MMT membrane with an interlayer height of 0.74 nm and an intralayer width of 1.2 nm can achieve exceptional water flux (180~300 $L \cdot m^{-2} \cdot h^{-1} \cdot bar^{-1}$) and high methylene blue rejection (> 97%) under pressures below 100 MPa. It avoids common exfoliation and intercalation strategies, paving the way for a facile and scalable fabrication method for clay-based membranes for efficient and scalable water purification.

Future studies will focus on tailoring CNT@MMT membranes for the removal of pollutants with varying molecular sizes, including small organic molecules, heavy metals, salts, and microplastics. This will be achieved by designing membranes with tunable pore sizes through controlled CNT diameters and incorporating functionalized adsorption sites. Additionally, long-term stability tests under varying pH and pressure conditions will be conducted to ensure their practical applicability in real-world water treatment systems.

References

(1) Katheresan, V.; Kansedo, J.; Lau, S. Y. Efficiency of various recent wastewater dye removal methods: A review. *J. Environ. Chem. Eng.* **2018**, *6*, 4676-4697.

(2) Polajnar Horvat, K.; Šrimpf Vendramin, K. Issues Surrounding Behavior towards Discarded Textiles and Garments in Ljubljana. *Sustainability-Basel* **2021**, *13*, 6491.

(3) Yaseen, D. A.; Scholz, M. Treatment of synthetic textile wastewater containing dye mixtures with microcosms. *Environ. Sci. Pollut. R.* **2018**, *25*, 1980-1997.

(4) Solayman, H. M.; Hossen, M. A.; Abd Aziz, A.; Yahya, N. Y.; Leong, K. H.; Sim, L. C.; Monir, M. U.; Zoh, K. Performance evaluation of dye wastewater treatment technologies: A review. *J. Environ. Chem. Eng.* **2023**, *11*, 109610.

(5) Wang, Q.; Lai, Z.; Luo, C.; Zhang, J.; Cao, X.; Liu, J.; Mu, J. Honeycomb-like activated carbon with microporous nanosheets structure prepared from waste biomass cork for highly efficient dye wastewater treatment. *J. Hazard. Mater.* **2021**, *416*, 125896.

(6) Huang, H.; Li, Y.; Jiang, G.; Wang, H.; Jiang, W. In Situ Construction of Dye-Sensitized BiOCl/Rutile-TiO2 Nanorod Heterojunctions with Highly Enhanced Photocatalytic Activity for Treating Persistent Organic Pollutants. *Inorg. Chem.* **2021**, *60*, 17325-17338.

(7) Hassan, M. M.; Carr, C. M. A critical review on recent advancements of the removal of reactive dyes from dyehouse effluent by ion-exchange adsorbents. *Chemosphere* **2018**, *209*, 201-219.

(8) Shindhal, T.; Rakholiya, P.; Varjani, S.; Pandey, A.; Ngo, H. H.; Guo, W.; Ng, H. Y.; Taherzadeh, M. J. A critical review on advances in the practices and perspectives for the treatment of dye industry wastewater. *Bioengineered* **2021**, *12*, 70-87.

(9) Biswas, S.; Fatema, J.; Debnath, T.; Rashid, T. U. Chitosan–clay composites for wastewater treatment: a state-of-the-art review. *ACS ES&T Water* **2021**, *1*, 1055-

1085.

(10) Robinson, T.; McMullan, G.; Marchant, R.; Nigam, P. Remediation of dyes in textile effluent: a critical review on current treatment technologies with a proposed alternative. *Bioresource Technol.* **2001**, *77*, 247-255.

(11) Mahida, V. P.; Patel, M. P. Removal of some most hazardous cationic dyes using novel poly (NIPAAm/AA/N-allylisatin) nanohydrogel. *Arab. J. Chem.* **2016**, *9*, 430-442.

(12) Belkassa, K.; Khelifa, M.; Batonneau-Gener, I.; Marouf-Khelifa, K.; Khelifa, A. Understanding of the mechanism of crystal violet adsorption on modified halloysite: Hydrophobicity, performance, and interaction. *J. Hazard. Mater.* **2021**, *415*, 125656.

(13) Patanjali, P.; Chopra, I.; Mandal, A.; Singh, R. Kinetics and isotherm studies for adsorptive removal of methylene blue from aqueous solutions using organoclay. *Indian J. Chem. Techn.* **2021**, *28*, 86-93.

(14) Olusegun, S. J.; Mohallem, N. D. S. Comparative adsorption mechanism of doxycycline and Congo red using synthesized kaolinite supported CoFe2O4 nanoparticles. *Environ. Pollut.* **2020**, *260*, 114019.

(15) Khnifira, M.; Boumya, W.; Abdennouri, M.; Sadiq, M.; Achak, M.; Serdaroğlu, G.; Kaya, S.; Şimşek, S.; Barka, N. A combined molecular dynamic simulation, DFT calculations, and experimental study of the eriochrome black T dye adsorption onto chitosan in aqueous solutions. *Int. J. Biol. Macromol.* **2021**, *166*, 707-721.

(16) Natarajan, S.; Bajaj, H. C.; Tayade, R. J. Recent advances based on the synergetic effect of adsorption for removal of dyes from waste water using photocatalytic process. *J. Environ. Sci.-China* **2018**, *65*, 201-222.

(17) Piaskowski, K.; Świderska-Dąbrowska, R.; Zarzycki, P. K. Dye Removal from Water and Wastewater Using Various Physical, Chemical, and Biological Processes. *J. Aoac Int.* **2018**, *101*, 1371-1384.

(18) Katheresan, V.; Kansedo, J.; Lau, S. Y. Efficiency of various recent wastewater

dye removal methods: A review. *J. Environ. Chem. Eng.* **2018**, *6*, 4676-4697.

(19) Liao, Y.; Loh, C.; Tian, M.; Wang, R.; Fane, A. G. Progress in electrospun polymeric nanofibrous membranes for water treatment: Fabrication, modification and applications. *Prog. Polym. Sci.* **2018**, *77*, 69-94.

(20) Amrhar, O.; Berisha, A.; El Gana, L.; Nassali, H.; S. Elyoubi, M. Removal of methylene blue dye by adsorption onto Natural Muscovite Clay: experimental, theoretical and computational investigation. *Int. J. Environ. An. Ch.* **2021**, 1-26.

(21) Bingül, Z. Determination of affecting parameters on removal of methylene blue dyestuff from aqueous solutions using natural clay: Isotherm, kinetic, and thermodynamic studies. *J. Mol. Struct.* **2022**, *1250*, 131729.

(22) Zhang, L.; Zaoui, A.; Sekkal, W. Adsorption efficiency of highly methylene blue dye concentrations with multilayer chitosan-modified clays for a precise nanofiltration performance of polluted water. *Journal of Water Process Engineering* **2024**, *57*, 104651.

(23) Awad, A. M.; Shaikh, S. M.; Jalab, R.; Gulied, M. H.; Nasser, M. S.; Benamor, A.; Adham, S. Adsorption of organic pollutants by natural and modified clays: a comprehensive review. *Sep. Purif. Technol.* **2019**, *228*, 115719.

(24) Elemen, S.; Kumbasar, E. P. A.; Yapar, S. Modeling the adsorption of textile dye on organoclay using an artificial neural network. *Dyes Pigments* **2012**, *95*, 102-111.

(25) Anirudhan, T. S.; Ramachandran, M. Adsorptive removal of basic dyes from aqueous solutions by surfactant modified bentonite clay (organoclay): kinetic and competitive adsorption isotherm. *Process Saf. Environ.* **2015**, *95*, 215-225.

(26) Keshmiri-Naqab, R.; Taghavijeloudar, M. Could organoclay be used as a promising natural adsorbent for efficient and cost-effective dye wastewater treatment? *J. Environ. Manage.* **2023**, *342*, 118322.

(27) Ismail, A. F.; Padaki, M.; Hilal, N.; Matsuura, T.; Lau, W. J. Thin film composite membrane—Recent development and future potential. *Desalination* **2015**, *356*, 140-148.

(28) Xie, T.; Li, F.; Chen, K.; Zhao, S.; Chen, Y.; Sun, H.; Li, P.; Niu, Q. J. Fabrication of novel thin-film nanocomposite polyamide membrane by the interlayer approach: A review. *Desalination* **2023**, *554*, 116509.

(29) Lau, W. J.; Gray, S.; Matsuura, T.; Emadzadeh, D.; Chen, J. P.; Ismail, A. F. A review on polyamide thin film nanocomposite (TFN) membranes: History, applications, challenges and approaches. *Water Res.* **2015**, *80*, 306-324.

(30) Xiao, T.; Li, X.; Liu, Z.; Lu, B.; Zhai, J. The nanoscale modulation of interlayer space in two-dimensional nanoclay membranes for osmotic energy conversion. *J. Membrane Sci.* **2024**, *695*, 122456.

(31) Tian, M.; Wang, L.; Wang, J.; Zheng, S.; Wang, F.; Shao, N.; Wang, L. A Two-Dimensional Lamellar Vermiculite Membrane for Precise Molecular Separation and Ion Sieving. *Acs Sustain. Chem. Eng.* **2022**, *10*, 1137-1148.

(32) Zhang, T.; Ren, B.; Bai, H.; Wen, T.; Chen, L.; Ma, S.; Wang, X.; Wang, S.; Zhao, Y. Subnanometer-scale control of channel height in two-dimensional montmorillonite membrane for ion separation. *J. Membrane Sci.* **2023**, *675*, 121573.

(33) Han, B.; Sun, X.; Fan, Z.; Jiang, H.; Wang, Z.; Zhang, W.; He, M.; Ma, J. Enhanced Mono/Divalent Ion Separation via Charged Interlayer Channels in Montmorillonite-Based Membranes. *Environ. Sci. Technol.* **2024**, *58*, 4415-4427.

(34) Wen, T.; Zhao, Y.; Wang, X.; Chen, L.; Gao, R.; Wang, S.; Zhang, T. Efficient and ultrafast separation of Li+ and Mg2+ by the porous two-dimensional nanochannel of perm-selective montmorillonite membrane. *Chem. Eng. J.* **2023**, *475*, 146101.

(35) Elwakeel, K. Z.; Elgarahy, A. M.; Elshoubaky, G. A.; Mohammad, S. H. Microwave assist sorption of crystal violet and Congo red dyes onto amphoteric sorbent based on upcycled Sepia shells. *Journal of Environmental Health Science and Engineering* **2020**, *18*, 35-50.

(36) Elgarahy, A. M.; Elwakeel, K. Z.; Mohammad, S. H.; Elshoubaky, G. A. Multifunctional eco-friendly sorbent based on marine brown algae and bivalve

shells for subsequent uptake of Congo red dye and copper(II) ions. *J. Environ. Chem. Eng.* **2020**, *8*, 103915.

(37) Attarki, J.; Khnifira, M.; Boumya, W.; Mahsoune, A.; Lemdek, E. M.; Sadiq, M.; Abdennouri, M.; Kaya, S.; Barka, N. Adsorption mechanism investigation of methylthioninium chloride dye onto some metal phosphates using Monte Carlo dynamic simulations and DFT calculations. *Inorg. Chem. Commun.* **2023**, *149*, 110436.

(38) Madkour, L. H.; Kaya, S.; Guo, L.; Kaya, C. Quantum chemical calculations, molecular dynamic (MD) simulations and experimental studies of using some azo dyes as corrosion inhibitors for iron. Part 2: Bis–azo dye derivatives. *J. Mol. Struct.* **2018**, *1163*, 397-417.

(39) Khnifira, M.; El Hamidi, S.; Mahsoune, A.; Sadiq, M.; Serdaroğlu, G.; Kaya, S.; Qourzal, S.; Barka, N.; Abdennouri, M. Adsorption of methylene blue cationic dye onto brookite and rutile phases of titanium dioxide: Quantum chemical and molecular dynamic simulation studies. *Inorg. Chem. Commun.* **2021**, *129*, 108659.

(40) Dadashi Firouzjaei, M.; Akbari Afkhami, F.; Rabbani Esfahani, M.; Turner, C. H.; Nejati, S. Experimental and molecular dynamics study on dye removal from water by a graphene oxide-copper-metal organic framework nanocomposite. *Journal of Water Process Engineering* **2020**, *34*, 101180.

(41) Zhang, C.; Chen, H.; Xue, G.; Liu, Y.; Chen, S.; Jia, C. A critical review of the aniline transformation fate in azo dye wastewater treatment. *J. Clean. Prod.* **2021**, *321*, 128971.

(42) Benkhaya, S.; M'Rabet, S.; El Harfi, A. Classifications, properties, recent synthesis and applications of azo dyes. *Heliyon* **2020**, *6*.

(43) Alsantali, R. I.; Raja, Q. A.; Alzahrani, A. Y. A.; Sadiq, A.; Naeem, N.; Mughal, E. U.; Al-Rooqi, M. M.; El Guesmi, N.; Moussa, Z.; Ahmed, S. A. Miscellaneous azo dyes: a comprehensive review on recent advancements in biological and industrial applications. *Dyes Pigments* **2022**, *199*, 110050.

(44) Zhang, L.; Zaoui, A.; Sekkal, W.; Zheng, Y. Interlayer adsorption of cationic dye on cationic surfactant-modified and unmodified montmorillonite. *J. Hazard. Mater.* **2023**, *442*, 130107.

(45) Zeng, Q. H.; Yu, A. B.; Lu, G. Q.; Standish, R. K. Molecular dynamics simulation of organic− inorganic nanocomposites: layering behavior and interlayer structure of organoclays. *Chem. Mater.* **2003**, *15*, 4732-4738.

(46) Adeyemo, A. A.; Adeoye, I. O.; Bello, O. S. Adsorption of dyes using different types of clay: a review. *Applied Water Science* **2017**, *7*, 543-568.

(47) Zheng, Y.; Zaoui, A.; Shahrour, I. A theoretical study of swelling and shrinking of hydrated Wyoming montmorillonite. **2011**, *51*, 177-181.

(48) Wei, P.; Zhang, L.; Zheng, Y.; Diao, Q.; Zhuang, D.; Yin, Z. Nanoscale friction characteristics of hydrated montmorillonites using molecular dynamics. *Appl. Clay Sci.* **2021**, *210*, 106155.

(49) Viani A, G. A. F. A. The nature of disorder in montmorillonite by simulation of X-ray powder patterns. *Am. Mineral.* **2002**, *87*, 966-975.

(50) Xiaoying Jin, M. J. X. S. Adsorption of methylene blue and orange II onto unmodified and

surfactant-modified zeolite. *J. Colloid Interf. Sci.* **2008**, 243-247.

(51) Anirudhan, T. S.; Ramachandran, M. Adsorptive removal of basic dyes from aqueous solutions by surfactant modified bentonite clay (organoclay): kinetic and competitive adsorption isotherm. *Process Saf. Environ.* **2015**, *95*, 215-225.

(52) Pentrák, M.; Czímerová, A.; Madejová, J.; Komadel, P. Changes in layer charge of clay minerals upon acid treatment as obtained from their interactions with methylene blue. *Appl. Clay Sci.* **2012**, *55*, 100-107.

(53) El Mouzdahir, Y.; Elmchaouri, A.; Mahboub, R.; Gil, A.; Korili, S. A. Equilibrium modeling for the adsorption of methylene blue from aqueous solutions on activated clay minerals. *Desalination* **2010**, *250*, 335-338.

(54) Cottet, L.; Almeida, C.; Naidek, N.; Viante, M. F.; Lopes, M. C.; Debacher, N. A. Adsorption characteristics of montmorillonite clay modified with iron oxide

with respect to methylene blue in aqueous media. *Appl. Clay Sci.* **2014**, *95*, 25-31.

(55) Mao, S.; Gao, M. Functional organoclays for removal of heavy metal ions from water: A review. *J. Mol. Liq.* **2021**, *334*, 116143.

(56) Jia, S.; Yang, Z.; Ren, K.; Tian, Z.; Dong, C.; Ma, R.; Yu, G.; Yang, W. Removal of antibiotics from water in the coexistence of suspended particles and natural organic matters using amino-acid-modified-chitosan flocculants: A combined experimental and theoretical study. *J. Hazard. Mater.* **2016**, *317*, 593-601.

(57) Zhang, T.; Wang, W.; Zhao, Y.; Bai, H.; Wen, T.; Kang, S.; Song, G.; Song, S.; Komarneni, S. Removal of heavy metals and dyes by clay-based adsorbents: From natural clays to 1D and 2D nano-composites. *Chem. Eng. J.* **2021**, *420*, 127574.

(58) Yu, X.; Wei, C.; Ke, L.; Hu, Y.; Xie, X.; Wu, H. Development of organovermiculite-based adsorbent for removing anionic dye from aqueous solution. *J. Hazard. Mater.* **2010**, *180*, 499-507.

(59) Juang, R.; Lin, S.; Tsao, K. Mechanism of Sorption of Phenols from Aqueous Solutions onto Surfactant-Modified Montmorillonite. *J. Colloid Interf. Sci.* **2002**, *254*, 234-241.

(60) He, H.; Zhou, Q.; Martens, W. N.; Kloprogge, T. J.; Yuan, P.; Xi, Y.; Zhu, J.; Frost, R. L. Microstructure of HDTMA+-modified montmorillonite and its influence on sorption characteristics. *Clay Clay Miner.* **2006**, *54*, 689-696.

(61) Zhao, Q.; Burns, S. E. Modeling Sorption and Diffusion of Organic Sorbate in Hexadecyltrimethylammonium-Modified Clay Nanopores – A Molecular Dynamics Simulation Study. *Environ. Sci. Technol.* **2013**, *47*, 2769-2776.

(62) Liang, Y.; Li, H. A comparison of trimeric surfactant intercalated montmorillonite with its gemini modified one: Characterization and application in methyl orange removal. *J. Mol. Liq.* **2017**, *227*, 139-146.

(63) Geroeeyan, A.; Niazi, A.; Konoz, E. Removal of Basic Orange 2 dye and Ni2+ from aqueous solutions using alkaline-modified nanoclay. *Water Sci. Technol.*

2021, *83*, 2271-2286.

(64) Olcay, A. N.; Polat, M.; Polat, H. Ancillary effects of surfactants on filtration of low molecular weight contaminants through cellulose nitrate membrane filters. *Colloids and Surfaces A: Physicochemical and Engineering Aspects* **2016**, *492*, 199-206.

(65) Burns, S. E.; Bartelt-Hunt, S. L.; Smith, J. A.; Redding, A. Z. Coupled mechanical and chemical behavior of bentonite engineered with a controlled organic phase. *J. Geotech. Geoenviron.* **2006**, *132*, 1404-1412.

(66) Bhatt, A. S.; Sakaria, P. L.; Vasudevan, M.; Pawar, R. R.; Sudheesh, N.; Bajaj, H. C.; Mody, H. M. Adsorption of an anionic dye from aqueous medium by organoclays: equilibrium modeling, kinetic and thermodynamic exploration. *Rsc Adv.* **2012**, *2*, 8663-8671.

(67) Saavedra-Labastida, E.; Díaz-Nava, M. C.; Illescas, J.; Muro, C. Comparison of the removal of an anionic dye from aqueous solutions by adsorption with organically modified clays and their composites. *Water, Air, & Soil Pollution* **2019**, *230*, 88.

(68) Gamoudi, S.; Srasra, E. Adsorption of organic dyes by HDPy+-modified clay: effect of molecular structure on the adsorption. *J. Mol. Struct.* **2019**, *1193*, 522-531.

(69) Zhu, L.; Chen, B. Sorption behavior of p-nitrophenol on the interface between anion− cation organobentonite and water. *Environ. Sci. Technol.* **2000**, *34*, 2997-3002.

(70) Wibulswas, R. Batch and fixed bed sorption of methylene blue on precursor and QACs modified montmorillonite. *Sep. Purif. Technol.* **2004**, *39*, 3-12.

(71) Jourvand, M.; Ghodratollah, S. K.; Omidi-Khaniabadi, Y.; Godini, H.; Nourmoradi, H. Removal of methylene blue from aqueous solutions using modified clay. *J Bas Res Med Sci* **2015**, *2*, 32-41.

(72) Alkizwini, R. S. The Use of an Organo-Kaolinite Sorbent in a Permeable Reactive Barrier for Remediating Groundwater Contaminated with Methylene Blue Dye:

Experimental and Theoretical Investigation. *Environmental Processes* **2021**, *8*, 889-910.

(73) Crini, G.; Badot, P. Application of chitosan, a natural aminopolysaccharide, for dye removal from aqueous solutions by adsorption processes using batch studies: A review of recent literature. *Prog. Polym. Sci.* **2008**, *33*, 399-447.

(74) El-Kousy, S. M.; El-Shorbagy, H. G.; El-Ghaffar, M. A. A. Chitosan/montmorillonite composites for fast removal of methylene blue from aqueous solutions. *Mater. Chem. Phys.* **2020**, *254*, 123236.

(75) Pereira, F. A. R.; Sousa, K. S.; Cavalcanti, G. R. S.; França, D. B.; Queiroga, L. N. F.; Santos, I. M. G.; Fonseca, M. G.; Jaber, M. Green biosorbents based on chitosan-montmorillonite beads for anionic dye removal. *J. Environ. Chem. Eng.* **2017**, *5*, 3309-3318.

(76) Bulut, Y.; Karaer, H. Adsorption of methylene blue from aqueous solution by crosslinked chitosan/bentonite composite. *J. Disper. Sci. Technol.* **2015**, *36*, 61-67.

(77) Marrakchi, F.; Khanday, W. A.; Asif, M.; Hameed, B. H. Cross-linked chitosan/sepiolite composite for the adsorption of methylene blue and reactive orange 16. *Int. J. Biol. Macromol.* **2016**, *93*, 1231-1239.

(78) Eltaweil, A. S.; Ibrahim, K.; Abd El-Monaem, E. M.; El-Subruiti, G. M.; Omer, A. M. Phosphate removal by Lanthanum-doped aminated graphene oxide@aminated chitosan microspheres: Insights into the adsorption mechanism. *J. Clean. Prod.* **2023**, *385*, 135640.

(79) Omer, A. M.; Elgarhy, G. S.; El-Subruiti, G. M.; Abd El-Monaem, E. M.; Eltaweil, A. S. Construction of efficient Ni-FeLDH@MWCNT@Cellulose acetate floatable microbeads for Cr(VI) removal: Performance and mechanism. *Carbohyd. Polym.* **2023**, *311*, 120771.

(80) Jawad, A. H.; Malek, N. N. A.; Abdulhameed, A. S.; Razuan, R. Synthesis of magnetic chitosan-fly ash/Fe 3 O 4 composite for adsorption of reactive orange 16 dye: optimization by Box–Behnken design. *J. Polym. Environ.* **2020**, *28*, 1068-

1082.

(81) Chang, M.; Juang, R. Adsorption of tannic acid, humic acid, and dyes from water using the composite of chitosan and activated clay. *J. Colloid Interf. Sci.* **2004**, *278*, 18-25.

(82) Ahmad, R.; Ansari, K. Comparative study for adsorption of congo red and methylene blue dye on chitosan modified hybrid nanocomposite. *Process Biochem.* **2021**, *108*, 90-102.

(83) Karimi-Maleh, H.; Ayati, A.; Davoodi, R.; Tanhaei, B.; Karimi, F.; Malekmohammadi, S.; Orooji, Y.; Fu, L.; Sillanpää, M. Recent advances in using of chitosan-based adsorbents for removal of pharmaceutical contaminants: A review. *J. Clean. Prod.* **2021**, *291*, 125880.

(84) Bleiman, N.; Mishael, Y. G. Selenium removal from drinking water by adsorption to chitosan–clay composites and oxides: Batch and columns tests. *J. Hazard. Mater.* **2010**, *183*, 590-595.

(85) Kang, S.; Zhao, Y.; Wang, W.; Zhang, T.; Chen, T.; Yi, H.; Rao, F.; Song, S. Removal of methylene blue from water with montmorillonite nanosheets/chitosan hydrogels as adsorbent. *Appl. Surf. Sci.* **2018**, *448*, 203-211.

(86) Bahrudin, N. N.; Nawi, M. A.; Jawad, A. H.; Sabar, S. Adsorption Characteristics and Mechanistic Study of Immobilized Chitosan-Montmorillonite Composite for Methyl Orange removal. *J. Polym. Environ.* **2020**, *28*, 1901-1913.

(87) Kang, S.; Qin, L.; Zhao, Y.; Wang, W.; Zhang, T.; Yang, L.; Rao, F.; Song, S. Enhanced removal of methyl orange on exfoliated montmorillonite/chitosan gel in presence of methylene blue. *Chemosphere* **2020**, *238*, 124693.

(88) Ulu, A.; Alpaslan, M.; Gultek, A.; Ates, B. Eco-friendly chitosan/κ-carrageenan membranes reinforced with activated bentonite for adsorption of methylene blue. *Mater. Chem. Phys.* **2022**, *278*, 125611.

(89) Kurczewska, J. Chitosan-montmorillonite hydrogel beads for effective dye adsorption. *Journal of Water Process Engineering* **2022**, *48*, 102928.

(90) Nesic, A. R.; Velickovic, S. J.; Antonovic, D. G. Characterization of

chitosan/montmorillonite membranes as adsorbents for Bezactiv Orange V-3R dye. *J. Hazard. Mater.* **2012**, *209-210*, 256-263.

(91) Kang, S.; Zhao, Y.; Wang, W.; Zhang, T.; Chen, T.; Yi, H.; Rao, F.; Song, S. Removal of methylene blue from water with montmorillonite nanosheets/chitosan hydrogels as adsorbent. *Appl. Surf. Sci.* **2018**, *448*, 203-211.

(92) Mourya, V. K.; Inamdar, N. N. Chitosan-modifications and applications: Opportunities galore. *Reactive and Functional polymers* **2008**, *68*, 1013-1051.

(93) Mourya, V. K.; Inamdar, N. N. Chitosan-modifications and applications: Opportunities galore. *Reactive and Functional Polymers* **2008**, *68*, 1013-1051.

(94) Synowiecki, J.; Al-Khateeb, N. A. Production, properties, and some new applications of chitin and its derivatives. **2003**.

(95) Adnan, A.; Lam, R.; Chen, H.; Lee, J.; Schaffer, D. J.; Barnard, A. S.; Schatz, G. C.; Ho, D.; Liu, W. K. Atomistic Simulation and Measurement of pH Dependent Cancer Therapeutic Interactions with Nanodiamond Carrier. *Mol. Pharmaceut.* **2011**, *8*, 368-374.

(96) Bravo-Osuna, I.; Vauthier, C.; Farabollini, A.; Palmieri, G. F.; Ponchel, G. Mucoadhesion mechanism of chitosan and thiolated chitosan-poly(isobutyl cyanoacrylate) core-shell nanoparticles. *Biomaterials* **2007**, *28*, 2233-2243.

(97) Zhang, L.; Zaoui, A.; Sekkal, W. Synthesis of a chitosan-clay nanomembrane by pH control and its thermal stability in aqueous environments. *Appl. Clay Sci.* **2023**, *243*, 107089.

(98) Daraei, P.; Madaeni, S. S.; Salehi, E.; Ghaemi, N.; Ghari, H. S.; Khadivi, M. A.; Rostami, E. Novel thin film composite membrane fabricated by mixed matrix nanoclay/chitosan on PVDF microfiltration support: Preparation, characterization and performance in dye removal. *J. Membrane Sci.* **2013**, *436*, 97-108.

(99) Ghaemi, N.; Daraei, P.; Akhlaghi, F. S. Polyethersulfone nanofiltration membrane embedded by chitosan nanoparticles: Fabrication, characterization and performance in nitrate removal from water. *Carbohyd. Polym.* **2018**, *191*, 142-

151.

(100) Liao, Z.; Zhu, J.; Li, X.; Van der Bruggen, B. Regulating composition and structure of nanofillers in thin film nanocomposite (TFN) membranes for enhanced separation performance: A critical review. *Sep. Purif. Technol.* **2021**, *266*, 118567.

(101) Freger, V.; Ramon, G. Z. Polyamide desalination membranes: Formation, structure, and properties. *Prog. Polym. Sci.* **2021**, *122*, 101451.

(102) Jiang, Z.; Karan, S.; Livingston, A. G. Water transport through ultrathin polyamide nanofilms used for reverse osmosis. *Adv. Mater.* **2018**, *30*, 1705973.

(103) Dong, H.; Wu, L.; Zhang, L.; Chen, H.; Gao, C. Clay nanosheets as charged filler materials for high-performance and fouling-resistant thin film nanocomposite membranes. *J. Membrane Sci.* **2015**, *494*, 92-103.

(104) Zhao, Y.; Li, N.; Xia, S. Polyamide nanofiltration membranes modified with Zn–Al layered double hydroxides for natural organic matter removal. *Compos. Sci. Technol.* **2016**, *132*, 84-92.

(105) Yadav, D.; Borpatra Gohain, M.; Karki, S.; Ingole, P. G. A Novel Approach for the Development of Low-Cost Polymeric Thin-Film Nanocomposite Membranes for the Biomacromolecule Separation. *ACS omega* **2022**.

(106) Nidhi Maalige, R.; Aruchamy, K.; Mahto, A.; Sharma, V.; Deepika, D.; Mondal, D.; Nataraj, S. K. Low operating pressure nanofiltration membrane with functionalized natural nanoclay as antifouling and flux promoting agent. *Chem. Eng. J.* **2019**, *358*, 821-830.

(107) Dong, H.; Wu, L.; Zhang, L.; Chen, H.; Gao, C. Clay nanosheets as charged filler materials for high-performance and fouling-resistant thin film nanocomposite membranes. *J. Membrane Sci.* **2015**, *494*, 92-103.

(108) Ingole, P. G.; Pawar, R. R.; Baig, M. I.; Jeon, J. D.; Lee, H. K. Thin film nanocomposite (TFN) hollow fiber membranes incorporated with functionalized acid-activated bentonite (ABn-NH) clay: towards enhancement of water vapor permeance and selectivity. *J. Mater. Chem. A* **2017**, *5*, 20947-20958.

(109) Ang, M. B.; Deang, A. B.; Aquino, R. R.; Basilia, B. A.; Huang, S.; Lee, K.; Lai, J. In *Membranes*, 2020; Vol. 10.

(110) Tian, M.; Meng, X.; Liu, Q.; Li, W.; You, X.; Liu, C.; Fortner, J. D. Hydrophilic montmorillonite in tailoring the structure and selectivity of polyamide membrane. *J. Membrane Sci.* **2022**, *657*, 120674.

(111) Ang, M. B. M. Y.; Deang, A. B. G.; Chiao, Y.; Aquino, R. R.; Millare, J. C.; Huang, S.; Tsai, H.; Lee, K. Integrating nanoclay intercalated with interlayers of cationic surfactant into thin-film nanocomposite nanofiltration membranes to improve performance and antifouling property. *Sep. Purif. Technol.* **2022**, *285*, 120360.

(112) You, H.; Zhang, X.; Zhu, D.; Yang, C.; Chammingkwan, P.; Taniike, T. Advantages of polydopamine coating in the design of ZIF-8-filled thin-film nanocomposite (TFN) membranes for desalination. *Colloids and Surfaces A: Physicochemical and Engineering Aspects* **2021**, *629*, 127492.

(113) Zhang, G.; Zhang, J.; Lv, P.; Sun, J.; Zhao, P.; Yang, L. Modifying thin film composite membrane with zeolitic imidazolate framework-8@polydopamine for enhanced antifouling property. *Chemosphere* **2020**, *248*, 125956.

(114) Tang, X.; Guo, B.; Zhang, S.; Tan, X.; Zheng, H. Layer-by-layer repaired lamellar membrane for low stacking defect of MXene nanosheets and efficient separation performance in water purification. *J. Environ. Chem. Eng.* **2023**, *11*, 109450.

(115) Shahzad, M. K.; Memon, F. H.; Soomro, F.; Iqbal, M.; Ibrar, A.; Memon, A. A.; Lim, J. H.; Choi, K. H.; Thebo, K. H. MoS2-based lamellar membranes for mass transport applications: Challenges and opportunities. *J. Environ. Chem. Eng.* **2023**, *11*, 109329.

(116) Vafa, N.; Firoozabadi, B.; Nejat Pishkenari, H. Confined water transport and desalination mechanism through lamellar Boron-Nitride Channels: A molecular dynamics simulation study. *Comp. Mater. Sci.* **2023**, *226*, 112208.

(117) Tang, J.; Wang, Y.; Yang, H.; Zhang, Q.; Wang, C.; Li, L.; Zheng, Z.; Jin, Y.; Wang, H.; Gu, Y. All-natural 2D nanofluidics as highly-efficient osmotic energy

generators. *Nat. Commun.* **2024**, *15*, 3649.

(118) Shah, I. A.; Bilal, M.; Almanassra, I. W.; Ihsanullah, I. A comprehensive review of graphene oxide-based membranes for efficient dye removal from water sources. *Sep. Purif. Technol.* **2024**, *330*, 125277.

(119) Chen, L.; Shi, G.; Shen, J.; Peng, B.; Zhang, B.; Wang, Y.; Bian, F.; Wang, J.; Li, D.; Qian, Z. Ion sieving in graphene oxide membranes via cationic control of interlayer spacing. *Nature* **2017**, *550*, 380-383.

(120) Fatima, J.; Shah, A. N.; Tahir, M. B.; Mehmood, T.; Shah, A. A.; Tanveer, M.; Nazir, R.; Jan, B. L.; Alansi, S. Tunable 2D nanomaterials; their key roles and mechanisms in water purification and monitoring. *Frontiers in Environmental Science* **2022**, *10*, 766743.

(121) Cygan, R. T.; Liang, J.; Kalinichev, A. G. Molecular Models of Hydroxide, Oxyhydroxide, and Clay Phases and the Development of a General Force Field. *The Journal of Physical Chemistry B* **2004**, *108*, 1255-1266.

(122) Allen, M. P.; Tildesley, D. J. *Computer simulation of liquids*; Oxford university press, 2017.

(123) Dauber Osguthorpe, P.; Roberts, V. A.; Osguthorpe, D. J.; Wolff, J.; Genest, M.; Hagler, A. T. Structure and energetics of ligand binding to proteins: Escherichia coli dihydrofolate reductase-trimethoprim, a drug-receptor system. *Proteins: Structure, Function, and Bioinformatics* **1988**, *4*, 31-47.

(124) Sun, H. COMPASS: an ab initio force-field optimized for condensed-phase applications overview with details on alkane and benzene compounds. *The Journal of Physical Chemistry B* **1998**, *102*, 7338-7364.

(125) Razmimanesh, F.; Amjad-Iranagh, S.; Modarress, H. Molecular dynamics simulation study of chitosan and gemcitabine as a drug delivery system. *J. Mol. Model.* **2015**, *21*, 165.

(126) Chávez, E. L.; Oviedo-Roa, R.; Contreras-Pérez, G.; Martínez-Magadán, J. M.; Castillo-Alvarado, F. L. Theoretical studies of ionic conductivity of crosslinked chitosan membranes. *Int. J. Hydrogen Energ.* **2010**, *35*, 12141-12146.

(127) Heinz, H.; Lin, T.; Kishore Mishra, R.; Emami, F. S. Thermodynamically consistent force fields for the assembly of inorganic, organic, and biological nanostructures: the INTERFACE force field. *Langmuir* **2013**, *29*, 1754-1765.

(128) Heinz, H.; Castelijns, H. J.; Suter, U. W. Structure and Phase Transitions of Alkyl Chains on Mica. *J. Am. Chem. Soc.* **2003**, *125*, 9500-9510.

(129) Heinz, H.; Koerner, H.; Anderson, K. L.; Vaia, R. A.; Farmer, B. L. Force Field for Mica-Type Silicates and Dynamics of Octadecylammonium Chains Grafted to Montmorillonite. *Chem. Mater.* **2005**, *17*, 5658-5669.

(130) Heinz, H.; Vaia, R. A.; Krishnamoorti, R.; Farmer, B. L. Self-assembly of alkylammonium chains on montmorillonite: effect of chain length, head group structure, and cation exchange capacity. *Chem. Mater.* **2007**, *19*, 59-68.

(131) Senftle, T. P.; Hong, S.; Islam, M. M.; Kylasa, S. B.; Zheng, Y.; Shin, Y. K.; Junkermeier, C.; Engel-Herbert, R.; Janik, M. J.; Aktulga, H. M. The ReaxFF reactive force-field: development, applications and future directions. *npj Computational Materials* **2016**, *2*, 1-14.

(132) Pitman, M. C.; Van Duin, A. C. Dynamics of confined reactive water in smectite clay–zeolite composites. *J. Am. Chem. Soc.* **2012**, *134*, 3042-3053.

(133) Manzano, H.; Moeini, S.; Marinelli, F.; Van Duin, A. C.; Ulm, F.; Pellenq, R. J. Confined water dissociation in microporous defective silicates: mechanism, dipole distribution, and impact on substrate properties. *J. Am. Chem. Soc.* **2012**, *134*, 2208-2215.

(134) Rahaman, O.; Van Duin, A. C.; Goddard III, W. A.; Doren, D. J. Development of a ReaxFF reactive force field for glycine and application to solvent effect and tautomerization. *The Journal of Physical Chemistry B* **2011**, *115*, 249-261.

(135) Monti, S.; Corozzi, A.; Fristrup, P.; Joshi, K. L.; Shin, Y. K.; Oelschlaeger, P.; Van Duin, A. C.; Barone, V. Exploring the conformational and reactive dynamics of biomolecules in solution using an extended version of the glycine reactive force field. *Phys. Chem. Chem. Phys.* **2013**, *15*, 15062-15077.

(136) Fogarty, J. C.; Aktulga, H. M.; Grama, A. Y.; Van Duin, A. C.; Pandit, S. A. A

reactive molecular dynamics simulation of the silica-water interface. *The Journal of chemical physics* **2010**, *132*.

(137) Van Duin, A. C.; Dasgupta, S.; Lorant, F.; Goddard, W. A. ReaxFF: a reactive force field for hydrocarbons. *The Journal of Physical Chemistry A* **2001**, *105*, 9396-9409.

(138) Allen, M. P.; Tildesley, D. J. *Computer simulation of liquids*; Oxford university press, 2017.

(139) Hoover, W. G. Canonical dynamics: Equilibrium phase-space distributions. *Physical review A* **1985**, *31*, 1695-1697.

(140) Schneider, T.; Stoll, E. Molecular-dynamics study of a three-dimensional one-component model for distortive phase transitions. *Physical Review B* **1978**, *17*, 1302.

(141) Berendsen, H. J.; Postma, J. V.; Van Gunsteren, W. F.; DiNola, A.; Haak, J. R. Molecular dynamics with coupling to an external bath. *The Journal of chemical physics* **1984**, *81*, 3684-3690.

(142) Frenkel, D.; Smit, B. *Understanding molecular simulation: from algorithms to applications*; Elsevier, 2001.

(143) Allen, M. P.; Tildesley, D. J. *Computer simulation of liquids*; Oxford university press, 1987.

(144) Ekramipooya, A.; Valadi, F. M.; Latifi Pour, M.; Rashtchian, D.; Gholami, M. R. Effect of the Pyrrolic Nitrogen Functional Group in the Selective Adsorption of CO2: GCMC, MD, and DFT Studies. *Energ. Fuel.* **2021**, *35*, 15918-15934.

(145) Johnson, E. R.; Keinan, S.; Mori-Sánchez, P.; Contreras-García, J.; Cohen, A. J.; Yang, W. Revealing Noncovalent Interactions. *J. Am. Chem. Soc.* **2010**, *132*, 6498-6506.

(146) Liu, X.; Lu, X.; Wang, R.; Zhou, H.; Xu, S. Molecular dynamics insight into the cointercalation of hexadecyltrimethyl-ammonium and acetate ions into smectites. *Am. Mineral.* **2009**, *94*, 143-150.

(147) Zhao, Q.; Burns, S. E. Microstructure of Single Chain Quaternary Ammonium

Cations Intercalated into Montmorillonite: A Molecular Dynamics Study. *Langmuir* **2012**, *28*, 16393-16400.

(148) Gładysz-Płaska, A.; Majdan, M.; Pikus, S.; Sternik, D. Simultaneous adsorption of chromium(VI) and phenol on natural red clay modified by HDTMA. *Chem. Eng. J.* **2012**, *179*, 140-150.

(149) Zhao, Q.; Burns, S. E. Molecular Dynamics Simulation of Secondary Sorption Behavior of Montmorillonite Modified by Single Chain Quaternary Ammonium Cations. *Environ. Sci. Technol.* **2012**, *46*, 3999-4007.

(150) Berendsen, H. J. C.; Grigera, J. R.; Straatsma, T. P. The missing term in effective pair potentials. *The Journal of Physical Chemistry* **1987**, *91*, 6269-6271.

(151) Boecker, J.; Schlenkrich, M.; Bopp, P.; Brickmann, J. Molecular dynamics simulation of a n-hexadecyltrimethylammonium chloride monolayer. *The Journal of Physical Chemistry* **1992**, *96*, 9915-9922.

(152) Darden, T.; York, D.; Pedersen, L. Particle mesh Ewald: An N· log (N) method for Ewald sums in large systems. *The Journal of chemical physics* **1993**, *98*, 10089-10092.

(153) Bourg, I. C.; Sposito, G. Connecting the Molecular Scale to the Continuum Scale for Diffusion Processes in Smectite-Rich Porous Media. *Environ. Sci. Technol.* **2010**, *44*, 2085-2091.

(154) Houhoune, F.; Nibou, D.; Chegrouche, S.; Menacer, S. Behaviour of modified hexadecyltrimethylammonium bromide bentonite toward uranium species. *J. Environ. Chem. Eng.* **2016**, *4*, 3459-3467.

(155) Yapar, S. Physicochemical study of microwave-synthesized organoclays. *Colloids and Surfaces A: Physicochemical and Engineering Aspects* **2009**, *345*, 75-81.

(156) Burns, S. E.; Bartelt-Hunt, S. L.; Smith, J. A.; Redding, A. Z. Coupled mechanical and chemical behavior of bentonite engineered with a controlled organic phase. *J. Geotech. Geoenviron.* **2006**, *132*, 1404-1412.

(157) Guediri, A.; Bouguettoucha, A.; Chebli, D.; Chafai, N.; Amrane, A. Molecular

dynamic simulation and DFT computational studies on the adsorption performances of methylene blue in aqueous solutions by orange peel-modified phosphoric acid. *J. Mol. Struct.* **2020**, *1202*, 127290.

(158) Benjelloun, M.; Miyah, Y.; Akdemir Evrendilek, G.; Zerrouq, F.; Lairini, S. Recent Advances in Adsorption Kinetic Models: Their Application to Dye Types. *Arab. J. Chem.* **2021**, *14*, 103031.

(159) Zheng, Y.; Zaoui, A. How water and counterions diffuse into the hydrated montmorillonite. **2011**, *203*, 80-85.

(160) Chang, F. C.; Skipper, N. T.; Sposito, G. Computer simulation of interlayer molecular structure in sodium montmorillonite hydrates. *Langmuir* **1995**, *11*, 2734-2741.

(161) Gürses, A.; Doğar, Ç.; Yalçın, M.; Açıkyıldız, M.; Bayrak, R.; Karaca, S. The adsorption kinetics of the cationic dye, methylene blue, onto clay. *J. Hazard. Mater.* **2006**, *131*, 217-228.

(162) Amrhar, O.; Berisha, A.; El Gana, L.; Nassali, H.; S. Elyoubi, M. Removal of methylene blue dye by adsorption onto Natural Muscovite Clay: experimental, theoretical and computational investigation. *Int. J. Environ. An. Ch.* **2021**, 1-26.

(163) Boukoussa, B.; Mokhtar, A.; El Guerdaoui, A.; Hachemaoui, M.; Ouachtak, H.; Abdelkrim, S.; Addi, A. A.; Babou, S.; Boudina, B.; Bengueddach, A.et al. Adsorption behavior of cationic dye on mesoporous silica SBA-15 carried by calcium alginate beads: Experimental and molecular dynamics study. *J. Mol. Liq.* **2021**, *333*, 115976.

(164) Jeffrey, G. A. *An Introduction to Hydrogen Bonding*; Oxford University Press, 1997.

(165) Lu, T.; Chen, F. Multiwfn: A multifunctional wavefunction analyzer. *J. Comput. Chem.* **2012**, *33*, 580-592.

(166) Humphrey, W.; Dalke, A.; Schulten, K. VMD: visual molecular dynamics. *Journal of molecular graphics* **1996**, *14*, 33-38, 27-28.

(167) Yang, Y.; Yu, W.; He, S.; Yu, S.; Chen, Y.; Lu, L.; Shu, Z.; Cui, H.; Zhang, Y.;

Jin, H. Rapid adsorption of cationic dye-methylene blue on the modified montmorillonite/graphene oxide composites. *Appl. Clay Sci.* **2019**, *168*, 304-311.

(168) Liu, L.; Luo, X.; Ding, L.; Luo, S. In *4 - Application of Nanotechnology in the Removal of Heavy Metal From Water*; Luo, X.; Deng, F., Eds.; Elsevier, 2019.

(169) Abidi, N.; Duplay, J.; Errais, E.; Jada, A.; Trabelsi-Ayadi, M. Discoloration of textile effluent by natural clay improved through the presence of dyeing additives. *Desalin. Water Treat.* **2016**, *57*, 27954-27968.

(170) Li, Z.; Chang, P.; Jiang, W.; Jean, J.; Hong, H. Mechanism of methylene blue removal from water by swelling clays. *Chem. Eng. J.* **2011**, *168*, 1193-1200.

(171) Rafatullah, M.; Sulaiman, O.; Hashim, R.; Ahmad, A. Adsorption of methylene blue on low-cost adsorbents: A review. *J. Hazard. Mater.* **2010**, *177*, 70-80.

(172) Fan, H.; Zhou, L.; Jiang, X.; Huang, Q.; Lang, W. Adsorption of Cu2+ and methylene blue on dodecyl sulfobetaine surfactant-modified montmorillonite. *Appl. Clay Sci.* **2014**, *95*, 150-158.

(173) Weng, C.; Pan, Y. Adsorption of a cationic dye (methylene blue) onto spent activated clay. *J. Hazard. Mater.* **2007**, *144*, 355-362.

(174) Yener, N.; Biçer, C.; Önal, M.; Sarıkaya, Y. Simultaneous determination of cation exchange capacity and surface area of acid activated bentonite powders by methylene blue sorption. *Appl. Surf. Sci.* **2012**, *258*, 2534-2539.

(175) Zhu, J.; Tian, M.; Zhang, Y.; Zhang, H.; Liu, J. Fabrication of a novel “loose” nanofiltration membrane by facile blending with Chitosan–Montmorillonite nanosheets for dyes purification. *Chem. Eng. J.* **2015**, *265*, 184-193.

(176) Rekik, S. B.; Gassara, S.; Bouaziz, J.; Deratani, A.; Baklouti, S. Development and characterization of porous membranes based on kaolin/chitosan composite. *Appl. Clay Sci.* **2017**, *143*, 1-9.

(177) Ngah, W. W.; Teong, L. C.; Hanafiah, M. M. Adsorption of dyes and heavy metal ions by chitosan composites: A review. *Carbohyd. Polym.* **2011**, *83*, 1446-1456.

(178) Nesic, A. R.; Velickovic, S. J.; Antonovic, D. G. Characterization of chitosan/montmorillonite membranes as adsorbents for Bezactiv Orange V-3R

dye. *J. Hazard. Mater.* **2012**, *209-210*, 256-263.

(179) Hu, C.; Zhu, P.; Cai, M.; Hu, H.; Fu, Q. Comparative adsorption of Pb(II), Cu(II) and Cd(II) on chitosan saturated montmorillonite: Kinetic, thermodynamic and equilibrium studies. *Appl. Clay Sci.* **2017**, *143*, 320-326.

(180) Gogoi, P.; Thakur, A. J.; Devi, R. R.; Das, B.; Maji, T. K. A comparative study on sorption of arsenate ions from water by crosslinked chitosan and crosslinked chitosan/MMT nanocomposite. *J. Environ. Chem. Eng.* **2016**, *4*, 4248-4257.

(181) Futalan, C. M.; Kan, C.; Dalida, M. L.; Hsien, K.; Pascua, C.; Wan, M. Comparative and competitive adsorption of copper, lead, and nickel using chitosan immobilized on bentonite. *Carbohyd. Polym.* **2011**, *83*, 528-536.

(182) de Lima, P. H. C.; Tavares, A. A.; de Lima Silva, S. M.; de Moura, M. R.; Aouada, F. A.; Grillo, R. Recent advances on nanohybrid systems constituting clay–chitosan with organic molecules – A review. *Appl. Clay Sci.* **2022**, *226*, 106548.

(183) Moussout, H.; Ahlafi, H.; Aazza, M.; El Akili, C. Performances of local chitosan and its nanocomposite 5%Bentonite/Chitosan in the removal of chromium ions (Cr(VI)) from wastewater. *Int. J. Biol. Macromol.* **2018**, *108*, 1063-1073.

(184) Zhang, H.; Ma, J.; Wang, F.; Chu, Y.; Yang, L.; Xia, M. Mechanism of carboxymethyl chitosan hybrid montmorillonite and adsorption of Pb(II) and Congo red by CMC-MMT organic-inorganic hybrid composite. *Int. J. Biol. Macromol.* **2020**, *149*, 1161-1169.

(185) Dlamini, D. S.; Li, J.; Mamba, B. B. Critical review of montmorillonite/polymer mixed-matrix filtration membranes: Possibilities and challenges. *Appl. Clay Sci.* **2019**, *168*, 21-30.

(186) Han, Y.; Lee, S.; Choi, K. H.; Park, I. Preparation and characterization of chitosan–clay nanocomposites with antimicrobial activity. *J. Phys. Chem. Solids* **2010**, *71*, 464-467.

(187) Cavallaro, G.; Micciulla, S.; Chiappisi, L.; Lazzara, G. Chitosan-based smart hybrid materials: A physico-chemical perspective. *J. Mater. Chem. B* **2021**, *9*, 594-611.

(188) Rubilar, J. F.; Candia, D.; Cobos, A.; Díaz, O.; Pedreschi, F. Effect of nanoclay and ethyl-Nα-dodecanoyl-l-arginate hydrochloride (LAE) on physico-mechanical properties of chitosan films. *LWT - Food Science and Technology* **2016**, *72*, 206-214.

(189) Martínez-Camacho, A. P.; Cortez-Rocha, M. O.; Ezquerra-Brauer, J. M.; Graciano-Verdugo, A. Z.; Rodriguez-Félix, F.; Castillo-Ortega, M. M.; Yépiz-Gómez, M. S.; Plascencia-Jatomea, M. Chitosan composite films: Thermal, structural, mechanical and antifungal properties. *Carbohyd. Polym.* **2010**, *82*, 305-315.

(190) Tirtom, V. N.; Dinçer, A.; Becerik, S.; Aydemir, T.; Çelik, A. Comparative adsorption of Ni(II) and Cd(II) ions on epichlorohydrin crosslinked chitosan–clay composite beads in aqueous solution. *Chem. Eng. J.* **2012**, *197*, 379-386.

(191) Sun, W.; Zeng, H.; Tang, T. Synergetic adsorption of polymers on montmorillonite: Insights from molecular dynamics simulations. *Appl. Clay Sci.* **2020**, *193*, 105654.

(192) Tiraferri, A.; Maroni, P.; Caro Rodríguez, D.; Borkovec, M. Mechanism of Chitosan Adsorption on Silica from Aqueous Solutions. *Langmuir* **2014**, *30*, 4980-4988.

(193) Darder, M.; Colilla, M.; Ruiz-Hitzky, E. Biopolymer−Clay Nanocomposites Based on Chitosan Intercalated in Montmorillonite. *Chem. Mater.* **2003**, *15*, 3774-3780.

(194) Wang, Y.; Wohlert, J.; Bergenstråhle-Wohlert, M.; Tu, Y.; Ågren, H. Molecular mechanisms for the adhesion of chitin and chitosan to montmorillonite clay. *Rsc Adv.* **2015**, *5*, 54580-54588.

(195) Zhu, S.; Khan, M. A.; Wang, F.; Bano, Z.; Xia, M. Exploration of adsorption mechanism of 2-phosphonobutane-1,2,4-tricarboxylic acid onto kaolinite and montmorillonite via batch experiment and theoretical studies. *J. Hazard. Mater.* **2021**, *403*, 123810.

(196) Silva, F. A. R.; Sales, M. J. A.; Paterno, L. G.; Ghoul, M.; Chebil, L.; Maia, E. R.

Preliminary Molecular Dynamics Studies of the Montmorillonite, Amylose, Fatty Acids and Water for Polymer-Clay Nanocomposite Modeling. *MRS Advances* **2018**, *3*, 1659-1663.

(197) Zhao, H.; Yang, Y.; Zhou, D.; Shu, X.; Ran, Q. Molecular dynamic simulations of montmorillonite contact with polycarboxylate superplasticizer at solid-liquid interface. *Materials Today Communications* **2021**, *28*, 102538.

(198) Xie, G.; Xiao, Y.; Deng, M.; Luo, Y.; An, W.; Yu, H.; Luo, P. Investigation on the inhibition mechanism of alkyl diammonium as montmorillonite swelling inhibitor: Experimental and molecular dynamics simulations. *Fuel* **2020**, *282*, 118841.

(199) Da Silva, J. C. S.; França, D. B.; Rodrigues, F.; Oliveira, D. M.; Trigueiro, P.; Silva Filho, E. C.; Fonseca, M. G. What happens when chitosan meets bentonite under microwave-assisted conditions? Clay-based hybrid nanocomposites for dye adsorption. *Colloids and Surfaces A: Physicochemical and Engineering Aspects* **2021**, *609*, 125584.

(200) Xu, Y.; Ren, X.; Hanna, M. A. Chitosan/clay nanocomposite film preparation and characterization. *J. Appl. Polym. Sci.* **2006**, *99*, 1684-1691.

(201) Lee, D. W.; Lim, C.; Israelachvili, J. N.; Hwang, D. S. Strong Adhesion and Cohesion of Chitosan in Aqueous Solutions. *Langmuir* **2013**, *29*, 14222-14229.

(202) Bondi, A. van der Waals Volumes and Radii. *The Journal of Physical Chemistry* **1964**, *68*, 441-451.

(203) Rowland, R. S.; Taylor, R. Intermolecular Nonbonded Contact Distances in Organic Crystal Structures: Comparison with Distances Expected from van der Waals Radii. *The Journal of Physical Chemistry* **1996**, *100*, 7384-7391.

(204) Sogias, I. A.; Khutoryanskiy, V. V.; Williams, A. C. Exploring the Factors Affecting the Solubility of Chitosan in Water. *Macromol. Chem. Phys.* **2010**, *211*, 426-433.

(205) Hsu, S.; Hsu, S.; Chang, S. Effect of pH on Molecular Structures and Network of Glycol Chitosan. *ACS Biomaterials Science & Engineering* **2020**, *6*, 298-307.

(206) Wang, J.; Zhuang, S. Removal of various pollutants from water and wastewater by modified chitosan adsorbents. *Crit. Rev. Env. Sci. Tec.* **2017**, *47*, 2331-2386.

(207) Kyung, D.; Lim, H.; Kim, H.; Lee, W. CO2 Hydrate Nucleation Kinetics Enhanced by an Organo-Mineral Complex Formed at the Montmorillonite–Water Interface. *Environ. Sci. Technol.* **2015**, *49*, 1197-1205.

(208) Monvisade, P.; Siriphannon, P. Chitosan intercalated montmorillonite: Preparation, characterization and cationic dye adsorption. *Appl. Clay Sci.* **2009**, *42*, 427-431.

(209) Zhu, C.; Wang, Q.; Huang, X.; Yun, J.; Hu, Q.; Yang, G. Adsorption of amino acids at clay surfaces and implication for biochemical reactions: Role and impact of surface charges. *Colloids and Surfaces B: Biointerfaces* **2019**, *183*, 110458.

(210) Walser, R.; Mark, A. E.; van Gunsteren, W. F. On the Temperature and Pressure Dependence of a Range of Properties of a Type of Water Model Commonly Used in High-Temperature Protein Unfolding Simulations. *Biophys. J.* **2000**, *78*, 2752-2760.

(211) Abushawish, A.; Almanassra, I. W.; Backer, S. N.; Jaber, L.; Khalil, A. K. A.; Abdelkareem, M. A.; Sayed, E. T.; Alawadhi, H.; Shanableh, A.; Atieh, M. A. High-efficiency removal of hexavalent chromium from contaminated water using nitrogen-doped activated carbon: kinetics and isotherm study. *Mater. Chem. Phys.* **2022**, *291*, 126758.

(212) Chatla, A.; Almanassra, I. W.; Jaber, L.; Kochkodan, V.; Laoui, T.; Alawadhi, H.; Atieh, M. A. Influence of calcination atmosphere on Fe doped activated carbon for the application of lead removal from water. *Colloids and Surfaces A: Physicochemical and Engineering Aspects* **2022**, *652*, 129928.

(213) Dada, A. O.; Olalekan, A. P.; Olatunya, A. M.; Dada, O. Langmuir, Freundlich, Temkin and Dubinin–Radushkevich isotherms studies of equilibrium sorption of Zn2+ unto phosphoric acid modified rice husk. *IOSR Journal of applied chemistry* **2012**, *3*, 38-45.

(214) Plimpton, S. Fast Parallel Algorithms for Short-Range Molecular Dynamics. *J.*

Comput. Phys. **1995**, *117*, 1-19.

(215) Ryckaert, J.; Ciccotti, G.; Berendsen, H. J. C. Numerical integration of the cartesian equations of motion of a system with constraints: molecular dynamics of n-alkanes. *J. Comput. Phys.* **1977**, *23*, 327-341.

(216) Wei, P.; Zheng, Y.; Zaoui, A.; Yin, Z. Atomistic study on thermo-mechanical behavior and structural anisotropy of montmorillonite under triaxial tension and compression. *Appl. Clay Sci.* **2023**, *233*, 106817.

(217) Bahrudin, N. N.; Nawi, M. A.; Jawad, A. H.; Sabar, S. Adsorption Characteristics and Mechanistic Study of Immobilized Chitosan-Montmorillonite Composite for Methyl Orange removal. *J. Polym. Environ.* **2020**, *28*, 1901-1913.

(218) Miao, J.; Ren, J.; Li, H.; Wu, D.; Wu, Y. Mesoporous crosslinked chitosan-activated clinoptilolite biocomposite for the removal of anionic and cationic dyes. *Colloids and Surfaces B: Biointerfaces* **2022**, *216*, 112579.

(219) Gürses, A.; Doğar, Ç.; Yalçın, M.; Açıkyıldız, M.; Bayrak, R.; Karaca, S. The adsorption kinetics of the cationic dye, methylene blue, onto clay. *J. Hazard. Mater.* **2006**, *131*, 217-228.

(220) Souza, P. R.; Dotto, G. L.; Salau, N. P. G. Experimental and mathematical modeling of hindered diffusion effect of cationic dye in the adsorption onto bentonite. *J. Environ. Chem. Eng.* **2019**, *7*, 102891.

(221) Lima, J. P.; Alvarenga, G.; Goszczynski, A. C. F.; Rosa, G. R.; Lopes, T. J. Batch adsorption of methylene blue dye using Enterolobium contortisiliquum as bioadsorbent: Experimental, mathematical modeling and simulation. *J. Ind. Eng. Chem.* **2020**, *91*, 362-371.

(222) Kumar, K. V.; Porkodi, K. Mass transfer, kinetics and equilibrium studies for the biosorption of methylene blue using Paspalum notatum. *J. Hazard. Mater.* **2007**, *146*, 214-226.

(223) Genina, E. A.; Bashkatov, A. N.; Tuchin, V. V. Effect of ethanol on the transport of methylene blue through stratum corneum. *Medical Laser Application* **2008**, *23*, 31-38.

(224) Weeks, E. R.; Weitz, D. A. Subdiffusion and the cage effect studied near the colloidal glass transition. *Chem. Phys.* **2002**, *284*, 361-367.

(225) Jawad, A. H.; Abdulhameed, A. S.; Reghioua, A.; Yaseen, Z. M. Zwitterion composite chitosan-epichlorohydrin/zeolite for adsorption of methylene blue and reactive red 120 dyes. *Int. J. Biol. Macromol.* **2020**, *163*, 756-765.

(226) Allen, A. E. A.; Payne, M. C.; Cole, D. J. Harmonic Force Constants for Molecular Mechanics Force Fields via Hessian Matrix Projection. *J. Chem. Theory Comput.* **2018**, *14*, 274-281.

(227) Becke, A. D. Density-functional exchange-energy approximation with correct asymptotic behavior. *Physical review A* **1988**, *38*, 3098.

(228) Yang, W.; Parr, R. G.; Lee, C. Development of the Colle-Salvetti correlation-energy formula into a functional of the electron density. *Physical Review B* **1988**, *37*, 785-789.

(229) Marenich, A. V.; Jerome, S. V.; Cramer, C. J.; Truhlar, D. G. Charge Model 5: An Extension of Hirshfeld Population Analysis for the Accurate Description of Molecular Interactions in Gaseous and Condensed Phases. *J. Chem. Theory Comput.* **2012**, *8*, 527-541.

(230) Dodda, L. S.; Vilseck, J. Z.; Cutrona, K. J.; Jorgensen, W. L. Evaluation of CM5 Charges for Nonaqueous Condensed-Phase Modeling. *J. Chem. Theory Comput.* **2015**, *11*, 4273-4282.

(231) Khnifira, M.; Boumya, W.; Attarki, J.; Mahsoune, A.; Abdennouri, M.; Sadiq, M. H.; Kaya, S.; Barka, N. Elucidating the adsorption mechanisms of anionic dyes on chitosan (110) surface in aqueous medium by quantum chemical and molecular dynamics. *Materials Today Communications* **2022**, *33*, 104488.

(232) Luzar, A.; Chandler, D. Hydrogen-bond kinetics in liquid water. *Nature* **1996**, *379*, 55-57.

(233) Stoimenovski, J.; Dean, P. M.; Izgorodina, E. I.; MacFarlane, D. R. Protic pharmaceutical ionic liquids and solids: aspects of protonics. *Faraday Discuss.* **2012**, *154*, 335-352.

(234) Gao, P.; Pu, W.; Wei, P.; Kong, M. Molecular dynamics simulations on adhesion energy of PDMS-silica interface caused by molecular structures and temperature. *Appl. Surf. Sci.* **2022**, *577*, 151930.

(235) Yaphary, Y. L.; Yu, Z.; Lam, R. H. W.; Hui, D.; Lau, D. Molecular dynamics simulations on adhesion of epoxy-silica interface in salt environment. *Composites Part B: Engineering* **2017**, *131*, 165-172.

(236) Park, S.; Schulten, K. Calculating potentials of mean force from steered molecular dynamics simulations. *The Journal of chemical physics* **2004**, *120*, 5946-5961.

(237) Wan, J.; Zaoui, A. Insight into enhancing foundation stability with rubber-soil mixtures: A nanofriction study. *Comput. Geotech.* **2024**, *166*, 105971.

(238) Bell, G. Models for the Specific Adhesion of Cells to Cells. *Science* **1978**, *200*, 618-627.

(239) Ackbarow, T.; Chen, X.; Keten, S.; Buehler, M. J. Hierarchies, multiple energy barriers, and robustness govern the fracture mechanics of α-helical and β-sheet protein domains. *Proceedings of the National Academy of Sciences* **2007**, *104*, 16410.

(240) Büyüköztürk, O.; Buehler, M. J.; Lau, D.; Tuakta, C. Structural solution using molecular dynamics: Fundamentals and a case study of epoxy-silica interface. *Int. J. Solids Struct.* **2011**, *48*, 2131-2140.

(241) Wang, B.; Yang, X.; Ma, L.; Zhai, L.; Xuan, J.; Liu, C.; Bai, Z. Ultra-high efficient pH induced selective removal of cationic and anionic dyes from complex coexisted solution by novel amphoteric biocomposite microspheres. *Sep. Purif. Technol.* **2020**, *231*, 115922.

(242) Florence, N.; Naorem, H. Dimerization of methylene blue in aqueous and mixed aqueous organic solvent: A spectroscopic study. *J. Mol. Liq.* **2014**, *198*, 255-258.

(243) Wu, J.; Liu, J.; Wen, B.; Li, Y.; Zhou, B.; Wang, Z.; Yang, S.; Zhao, R. Nitrogen-rich covalent triazine frameworks for high-efficient removal of anion dyes and the synergistic adsorption of cationic dyes. *Chemosphere* **2021**, *272*, 129622.

(244) Zhang, Q.; Jing, R.; Zhao, S.; Wu, M.; Liu, X.; Shao, Y.; Lv, F.; Liu, A.; Meng, Z. Adsorption of cationic and anionic dyes on montmorillonite in single and mixed wastewater. *J. Porous Mat.* **2019**, *26*, 1861-1867.

(245) Li, H.; Cao, X.; Zhang, C.; Yu, Q.; Zhao, Z.; Niu, X.; Sun, X.; Liu, Y.; Ma, L.; Li, Z. Enhanced adsorptive removal of anionic and cationic dyes from single or mixed dye solutions using MOF PCN-222. *Rsc Adv.* **2017**, *7*, 16273-16281.

(246) Guillossou, R.; Le Roux, J.; Mailler, R.; Pereira-Derome, C. S.; Varrault, G.; Bressy, A.; Vulliet, E.; Morlay, C.; Nauleau, F.; Rocher, V.et al. Influence of dissolved organic matter on the removal of 12 organic micropollutants from wastewater effluent by powdered activated carbon adsorption. *Water Res.* **2020**, *172*, 115487.

(247) Geng, C.; Zhao, F.; Niu, H.; Zhang, J.; Dong, H.; Li, Z.; Chen, H. Enhancing the permeability, anti-biofouling performance and long-term stability of TFC nanofiltration membrane by imidazole-modified carboxylated graphene oxide/polyethersulfone substrate. *J. Membrane Sci.* **2022**, *664*, 121099.

(248) Li, X.; Wang, Z.; Han, X.; Liu, Y.; Wang, C.; Yan, F.; Wang, J. Regulating the interfacial polymerization process toward high-performance polyamide thin-film composite reverse osmosis and nanofiltration membranes: A review. *J. Membrane Sci.* **2021**, *640*, 119765.

(249) Freger, V.; Ramon, G. Z. Polyamide desalination membranes: Formation, structure, and properties. *Prog. Polym. Sci.* **2021**, *122*, 101451.

(250) Han, S.; Zhu, J.; Uliana, A. A.; Li, D.; Zhang, Y.; Zhang, L.; Wang, Y.; He, T.; Elimelech, M. Microporous organic nanotube assisted design of high performance nanofiltration membranes. *Nat. Commun.* **2022**, *13*, 7954.

(251) Guo, H.; Deng, Y.; Tao, Z.; Yao, Z.; Wang, J.; Lin, C.; Zhang, T.; Zhu, B.; Tang, C. Y. Does hydrophilic polydopamine coating enhance membrane rejection of hydrophobic endocrine-disrupting compounds? *Environmental Science & Technology Letters* **2016**, *3*, 332-338.

(252) Phua, S. L.; Yang, L.; Toh, C. L.; Huang, S.; Tsakadze, Z.; Lau, S. K.; Mai, Y.;

Lu, X. Reinforcement of Polyether Polyurethane with Dopamine-Modified Clay: The Role of Interfacial Hydrogen Bonding. *Acs Appl. Mater. Inter.* **2012**, *4*, 4571-4578.

(253) Hu, M.; Li, X.; Tao, R.; Mai, Z.; Chen, X.; Gui, S.; Matsuyama, H.; Li, J. Highly permeable polyamide nanofiltration membranes with crumpled structures regulated by polydopamine-piperazine-halloysite interlayer. *Desalination* **2023**, *565*, 116862.

(254) Han, J.; Wang, S.; Deng, R.; Wu, Q. Polydopamine/Imogolite Nanotubes (PDA/INTs) Interlayer Modulated Thin Film Composite Forward Osmosis Membrane For Minimizing Internal Concentration Polarization. *Chinese J. Polym. Sci.* **2022**, *40*, 1233-1241.

(255)Abdollahzadeh, M.; Hosseini, E.; Ahmadi, H.; Lim, S.; Korayem, A. H.; Razmjou, A.; Asadnia, M. Low humid transport of anions in layered double hydroxides membranes using polydopamine coating. *J. Membrane Sci.* **2021**, *624*, 118974.

(256) He, G.; Li, Z.; Liu, Y.; Liu, M.; Zhu, C.; Zhang, L.; Zhang, H. A novel lithium ion-imprinted membrane with robust adsorption capacity and anti-fouling property based on the uniform multilayered interlayer. *Desalination* **2022**, *539*, 115973.

(257) Shah, A. A.; Cho, Y. H.; Choi, H.; Nam, S.; Kim, J. F.; Kim, Y.; Park, Y.; Park, H. Facile integration of halloysite nanotubes with bioadhesive as highly permeable interlayer in forward osmosis membranes. *J. Ind. Eng. Chem.* **2019**, *73*, 276-285.

(258) Cao, S.; Yang, Y.; Zhang, S.; Liu, K.; Chen, J. Multifunctional dopamine modification of green antibacterial hemostatic sponge. *Materials Science and Engineering: C* **2021**, *127*, 112227.

(259) Ridgway, H. F.; Orbell, J.; Gray, S. Molecular simulations of polyamide membrane materials used in desalination and water reuse applications: Recent developments and future prospects. *J. Membrane Sci.* **2017**, *524*, 436-448.

(260) Kotelyanskii, M. J.; Wagner, N. J.; Paulaitis, M. E. Molecular dynamics

simulation study of the mechanisms of water diffusion in a hydrated, amorphous polyamide. *Computational and Theoretical Polymer Science* **1999**, *9*, 301-306.

(261) Frenkel, D.; Smit, B. *Understanding molecular simulation: From algorithms to applications*; Academic Press, 2001.

(262) Liu, Y.; Xia, Z.; Wang, Y.; Rozyyev, V.; Kazi, O. A.; Gao, F.; Wang, D.; Lee, S. S.; Koritala, R.; Wen, J.et al. Montmorillonite Membranes with Tunable Ion Transport by Controlling Interlayer Spacing. *Acs Appl. Mater. Inter.* **2023**, *15*, 57144-57152.

(263) Underwood, T. R.; Bourg, I. C. Large-Scale Molecular Dynamics Simulation of the Dehydration of a Suspension of Smectite Clay Nanoparticles. *The Journal of Physical Chemistry C* **2020**, *124*, 3702-3714.

(264) Barral, M. T.; Arias, M.; Guérif, J. Effects of iron and organic matter on the porosity and structural stability of soil aggregates. *Soil and Tillage Research* **1998**, *46*, 261-272.

(265) Fridland, M.; Rosado, R. Mineral Trioxide Aggregate (MTA) Solubility and Porosity with Different Water-to-Powder Ratios. *J. Endodont.* **2003**, *29*, 814-817.

(266) Willems, T. F.; Rycroft, C. H.; Kazi, M.; Meza, J. C.; Haranczyk, M. Algorithms and tools for high-throughput geometry-based analysis of crystalline porous materials. *Micropor. Mesopor. Mat.* **2012**, *149*, 134-141.

(267) Chai, G.; Krantz, W. B. Formation and characterization of polyamide membranes via interfacial polymerization. *J. Membrane Sci.* **1994**, *93*, 175-192.

(268) Michalet, X. Mean square displacement analysis of single-particle trajectories with localization error: Brownian motion in an isotropic medium. *Physical Review E* **2010**, *82*, 41914.

(269) Ding, M.; Ghoufi, A.; Szymczyk, A. Molecular simulations of polyamide reverse osmosis membranes. *Desalination* **2014**, *343*, 48-53.

(270) Liyana-Arachchi, T. P.; Sturnfield, J. F.; Colina, C. M. Ultrathin Molecular-Layer-by-Layer Polyamide Membranes: Insights from Atomistic Molecular Simulations. *The Journal of Physical Chemistry B* **2016**, *120*, 9484-9494.

(271) Li, N.; Li, M.; Lin, S.; Cui, S.; Zhang, X. Stoichiometric effect on the structural transformation and spatial variation of polyamide reverse osmosis membranes: A molecular dynamics study. *J. Membrane Sci.* **2023**, *686*, 121980.

(272) Kolev, V.; Freger, V. Hydration, porosity and water dynamics in the polyamide layer of reverse osmosis membranes: A molecular dynamics study. *Polymer* **2014**, *55*, 1420-1426.

(273) Zhang, C.; Bu, G.; Sajib, M. S. J.; Meng, L.; Xu, S.; Zheng, S.; Zhang, L.; Wei, T. PXLink: A simulation program of polymer crosslinking to study of polyamide membrane. *Comput. Phys. Commun.* **2023**, *291*, 108840.

(274) Stukowski; Alexander. Visualization and analysis of atomistic simulation data with OVITO–the Open Visualization Tool. *Model. Simul. Mater. Sc.* **2010**, *18*, 15012.

(275) Stukowski, A. Computational analysis methods in atomistic modeling of crystals. *Jom-Us* **2014**, *66*, 399-407.

(276) Shen, M.; Keten, S.; Lueptow, R. M. Dynamics of water and solute transport in polymeric reverse osmosis membranes via molecular dynamics simulations. *J. Membrane Sci.* **2016**, *506*, 95-108.

(277) Grzebyk, K.; Armstrong, M. D.; Coronell, O. Accessing greater thickness and new morphology features in polyamide active layers of thin-film composite membranes by reducing restrictions in amine monomer supply. *J. Membrane Sci.* **2022**, *644*, 120112.

(278) Wang, Y.; Zhang, H.; Song, C.; Gao, C.; Zhu, G. Effect of aminophend/formaldehyde resin polymeric nanospheres as nanofiller on polyamide thin film nanocomposite membranes for reverse osmosis application. *J. Membrane Sci.* **2020**, *614*, 118496.

(279) Niksefat, N.; Jahanshahi, M.; Rahimpour, A. The effect of SiO2 nanoparticles on morphology and performance of thin film composite membranes for forward osmosis application. *Desalination* **2014**, *343*, 140-146.

(280) Zhang, H.; Wu, M. S.; Zhou, K.; Law, A. W. Molecular Insights into the

Composition–Structure–Property Relationships of Polyamide Thin Films for Reverse Osmosis Desalination. *Environ. Sci. Technol.* **2019**, *53*, 6374-6382.

(281) Coronell, O.; Mariñas, B. J.; Cahill, D. G. Depth Heterogeneity of Fully Aromatic Polyamide Active Layers in Reverse Osmosis and Nanofiltration Membranes. *Environ. Sci. Technol.* **2011**, *45*, 4513-4520.

(282) Suzuki, Y.; Koyano, Y.; Nagaoka, M. Influence of Monomer Mixing Ratio on Membrane Nanostructure in Interfacial Polycondensation: Application of Hybrid MC/MD Reaction Method with Minimum Bond Convention. *The Journal of Physical Chemistry B* **2015**, *119*, 6776-6785.

(283) Jadav, G. L.; Singh, P. S. Synthesis of novel silica-polyamide nanocomposite membrane with enhanced properties. *J. Membrane Sci.* **2009**, *328*, 257-267.

(284) Vrijenhoek, E. M.; Hong, S.; Elimelech, M. Influence of membrane surface properties on initial rate of colloidal fouling of reverse osmosis and nanofiltration membranes. *J. Membrane Sci.* **2001**, *188*, 115-128.

(285) Suvigya, K.; Lalita, S.; Gopinadhan, K. Membranes for desalination and dye separation: Are 2D materials better than polymers? A critical comparison. *Sep. Purif. Technol.* **2023**, *325*, 124693.

(286) Zhu, Y.; Jian, M.; Meng, N.; Ji, Y.; Bai, X.; Wu, L.; Yang, H.; Tan, C.; Li, H. Recent progress in developing 2D MOFs/COFs/Zeolites nanosheets membranes for water purification. *Sep. Purif. Technol.* **2024**, *337*, 126404.

(287) Liu, X.; Zhang, L.; Cui, X.; Zhang, Q.; Hu, W.; Du, J.; Zeng, H.; Xu, Q. 2D Material Nanofiltration Membranes: From Fundamental Understandings to Rational Design. *Advanced Science* **2021**, *8*, 2102493.

(288) Tian, M.; Liu, Y.; Zhang, S.; Yu, C.; Ostrikov, K.; Zhang, Z. Overcoming the permeability-selectivity challenge in water purification using two-dimensional cobalt-functionalized vermiculite membrane. *Nat. Commun.* **2024**, *15*, 391.

(289) Liu, J.; Wang, N.; Yu, L.; Karton, A.; Li, W.; Zhang, W.; Guo, F.; Hou, L.; Cheng, Q.; Jiang, L.et al. Bioinspired graphene membrane with temperature tunable channels for water gating and molecular separation. *Nat. Commun.* **2017**, *8*, 2011.

(290) Wang, R.; Qian, J.; Chen, X.; Low, Z.; Chen, Y.; Ma, H.; Wu, H.; Doherty, C. M.; Acharya, D.; Xie, Z. Pyro-layered heterostructured nanosheet membrane for hydrogen separation. *Nat. Commun.* **2023**, *14*, 2161.

(291) Wang, R.; Qian, J.; Chen, X.; Low, Z.; Chen, Y.; Ma, H.; Wu, H.; Doherty, C. M.; Acharya, D.; Xie, Z. Pyro-layered heterostructured nanosheet membrane for hydrogen separation. *Nat. Commun.* **2023**, *14*, 2161.

(292) Wang, J.; Cui, Z.; Li, S.; Song, Z.; He, M.; Huang, D.; Feng, Y.; Liu, Y.; Zhou, K.; Wang, X. Unlocking osmotic energy harvesting potential in challenging real-world hypersaline environments through vermiculite-based hetero-nanochannels. *Nat. Commun.* **2024**, *15*, 608.

(293) Wang, Y.; Lian, T.; Tarakina, N. V.; Yuan, J.; Antonietti, M. Lamellar carbon nitride membrane for enhanced ion sieving and water desalination. *Nat. Commun.* **2022**, *13*, 7339.

(294) Xu, R.; Kang, Y.; Zhang, W.; Pan, B.; Zhang, X. Two-dimensional MXene membranes with biomimetic sub-nanochannels for enhanced cation sieving. *Nat. Commun.* **2023**, *14*, 4907.

(295) Zhang, P.; Zhang, Y.; Wang, L.; Qiu, K.; Tang, X.; Gibson, J. K.; Liu, X.; Mei, L.; An, S.; Huang, Z. Bioinspired macrocyclic molecule supported two-dimensional lamellar membrane with robust interlayer structure for high-efficiency nanofiltration. *Advanced Science* **2023**, *10*, 2206516.

(296) Wang, W.; Onofrio, N.; Petit, E.; Karamoko, B. A.; Wu, H.; Liu, J.; Li, J.; Qi, K.; Zhang, Y.; Gervais, C. High-surface-area functionalized nanolaminated membranes for energy-efficient nanofiltration and desalination in forward osmosis. *Nature Water* **2023**, *1*, 187-197.

(297) Qu, J.; Li, S.; Zhong, B.; Deng, Z.; Shu, Y.; Cai, Y.; Hu, J.; Li, C. M. Two-dimensional nanomaterials: synthesis and applications in photothermal catalysis. *Nanoscale* **2023**, *15*, 2455-2469.

(298) Meng, C.; Ding, B.; Zhang, S.; Cui, L.; Ostrikov, K. K.; Huang, Z.; Yang, B.; Kim, J.; Zhang, Z. Angstrom-confined catalytic water purification within Co-TiO

x laminar membrane nanochannels. *Nat. Commun.* **2022**, *13*, 4010.

(299) Yang, H.; Yang, L.; Wang, H.; Xu, Z.; Zhao, Y.; Luo, Y.; Nasir, N.; Song, Y.; Wu, H.; Pan, F.et al. Covalent organic framework membranes through a mixed-dimensional assembly for molecular separations. *Nat. Commun.* **2019**, *10*, 2101.

(300) Yang, L.; Xiao, H.; Qian, Y.; Zhao, X.; Kong, X.; Liu, P.; Xin, W.; Fu, L.; Jiang, L.; Wen, L. Bioinspired hierarchical porous membrane for efficient uranium extraction from seawater. *Nature Sustainability* **2022**, *5*, 71-80.

(301) Wilson, M. J.; Wilson, L.; Patey, I. The influence of individual clay minerals on formation damage of reservoir sandstones: a critical review with some new insights. *Clay Miner.* **2014**, *49*, 147-164.

(302) Zhang, L.; Zaoui, A.; Sekkal, W. Exfoliated montmorillonite nanofillers role on the high performance and the permeability of polyamide nanofiltration membrane. *J. Membrane Sci.* **2025**, *713*, 123303.

(303) Kon Kova, T. V.; Rysev, A. P. Inversion of Montmorillonite Ion-Exchange Characteristics. *Colloid J.*+ **2020**, *82*, 130-135.

(304) HOCKING, M. B.; KLIMCHUK, K. A.; LOWEN, S. Polymeric Flocculants and Flocculation. *Journal of Macromolecular Science, Part C* **1999**, *39*, 177-203.

(305) Muraleedharan, M. G.; Herz-Thyhsen, R.; Dewey, J. C.; Kaszuba, J. P.; van Duin, A. C. T. Understanding the chemistry of cation leaching in illite/water interfacial system using reactive molecular dynamics simulations and hydrothermal experiments. *Acta Mater.* **2020**, *186*, 564-574.

(306) Wan, J.; Zaoui, A. Mechanical resistance behind fiber-reinforced polymer pile: Role of clay minerals. *Comput. Geotech.* **2024**, *168*, 106158.

(307) Zhang, L.; Zheng, Y.; Yin, Z.; Zaoui, A. Interparticle friction behaviors of kaolinite: Insights into macroscale friction from nanoscale. *Appl. Clay Sci.* **2024**, *261*, 107571.

(308) Zheng, Y.; Zaoui, A. Mechanical behavior in hydrated Na-montmorillonite clay. **2018**, *505*, 582-590.

(309) Bhati, M.; Senftle, T. P. Identifying Adhesion Properties at Si/Polymer Interfaces

with ReaxFF. *The Journal of Physical Chemistry C* **2019**, *123*, 27036-27047.

(310) Kim, S. W.; Kim, T.; Kim, Y. S.; Choi, H. S.; Lim, H. J.; Yang, S. J.; Park, C. R. Surface modifications for the effective dispersion of carbon nanotubes in solvents and polymers. *Carbon* **2012**, *50*, 3-33.

(311) Kim, G. M.; Nam, I. W.; Yang, B.; Yoon, H. N.; Lee, H. K.; Park, S. Carbon nanotube (CNT) incorporated cementitious composites for functional construction materials: The state of the art. *Compos. Struct.* **2019**, *227*, 111244.

(312) Qiu, C.; Jiang, L.; Gao, Y.; Sheng, L. Effects of oxygen-containing functional groups on carbon materials in supercapacitors: A review. *Materials & Design* **2023**, *230*, 111952.

(313) Boek, E. S. Molecular dynamics simulations of interlayer structure and mobility in hydrated Li-, Na-and K-montmorillonite clays. *Mol. Phys.* **2014**, *112*, 1472-1483.

(314) Holmboe, M.; Bourg, I. C. Molecular Dynamics Simulations of Water and Sodium Diffusion in Smectite Interlayer Nanopores as a Function of Pore Size and Temperature. *The Journal of Physical Chemistry C* **2014**, *118*, 1001-1013.

(315) Huang, M.; Chen, Y.; Yan, X.; Guo, X.; Dong, L.; Lang, W. Two-dimensional Montmorillonite membranes with efficient water filtration. *J. Membrane Sci.* **2020**, *614*, 118540.

(316) Zhou, Y.; Ding, H.; Smith, A. T.; Jia, X.; Chen, S.; Liu, L.; Chavez, S. E.; Hou, Z.; Liu, J.; Cheng, H.et al. Nanofluidic energy conversion and molecular separation through highly stable clay-based membranes. *J. Mater. Chem. A* **2019**, *7*, 14089-14096.

(317) Bergaya, F.; Jaber, M.; Lambert, J. F. Clays and clay minerals. *Rubber-Clay Nanocomposites: Science, Technology, and Applications* **2011**, 1-44.

(318) Holmboe, M.; Wold, S.; Jonsson, M. Porosity investigation of compacted bentonite using XRD profile modeling. *J. Contam. Hydrol.* **2012**, *128*, 19-32.

(319) Liu, J.; Zhao, Y.; Gao, R.; Zhang, L.; Jiang, X.; Miao, Y.; Cheng, S.; Dong, G.; Zhang, T. Efficient Li+/Mg2+ separation by two-dimensional montmorillonite

membrane with stable channel structure through ion exchange and metal–organic coordination strategy. *Sep. Purif. Technol.* **2025**, *358*, 130141.

(320) Tian, M.; Wang, L.; Wang, J.; Zheng, S.; Wang, F.; Shao, N.; Wang, L. A Two-Dimensional Lamellar Vermiculite Membrane for Precise Molecular Separation and Ion Sieving. *Acs Sustain. Chem. Eng.* **2022**, *10*, 1137-1148.

(321) Wei, X.; Liu, Y.; Zhang, Z.; Zhao, F.; Li, Z.; Fan, C.; Yang, Y.; Jiang, Z. 2D vermiculite nanofiltration membrane with TiO2 nanoparticles as versatile intercalator for enhanced water purification. *J. Membrane Sci.* **2024**, *695*, 122461.

(322) Liu, M.; Huang, M.; Tian, L.; Zhao, L.; Ding, B.; Kong, D.; Yang, Q.; Shao, J. Two-Dimensional Nanochannel Arrays Based on Flexible Montmorillonite Membranes. *Acs Appl. Mater. Inter.* **2018**, *10*, 44915-44923.

(323) Zhang, T.; Bai, H.; Zhao, Y.; Ren, B.; Wen, T.; Chen, L.; Song, S.; Komarneni, S. Precise Cation Recognition in Two-Dimensional Nanofluidic Channels of Clay Membranes Imparted from Intrinsic Selectivity of Clays. *Acs Nano* **2022**, *16*, 4930-4939.

(324) Huang, K.; Rowe, P.; Chi, C.; Sreepal, V.; Bohn, T.; Zhou, K. G.; Su, Y.; Prestat, E.; Pillai, P. B.; Cherian, C. T.et al. Cation-controlled wetting properties of vermiculite membranes and its promise for fouling resistant oil–water separation. *Nat. Commun.* **2020**, *11*, 1097.

(325) Han, B.; Sun, X.; Fan, Z.; Jiang, H.; Wang, Z.; Zhang, W.; He, M.; Ma, J. Enhanced Mono/Divalent Ion Separation via Charged Interlayer Channels in Montmorillonite-Based Membranes. *Environ. Sci. Technol.* **2024**, *58*, 4415-4427.

(326) Zhang, Y.; Tang, J.; Li, N.; Wang, S.; Zhou, L.; Gu, Y.; Jin, Y.; Zhang, Q.; Wang, H.; Liu, J. Anti-swelling 2D clay nanofiltration with interlamellar fixation for efficient dye separation. *J. Membrane Sci.* **2024**, *709*, 123141.

(327) Zhang, T.; Ren, B.; Bai, H.; Wen, T.; Chen, L.; Ma, S.; Wang, X.; Wang, S.; Zhao, Y. Subnanometer-scale control of channel height in two-dimensional montmorillonite membrane for ion separation. *J. Membrane Sci.* **2023**, *675*, 121573.

(328) Goh, K.; Jiang, W.; Karahan, H. E.; Zhai, S.; Wei, L.; Yu, D.; Fane, A. G.; Wang, R.; Chen, Y. All-Carbon Nanoarchitectures as High-Performance Separation Membranes with Superior Stability. *Adv. Funct. Mater.* **2015**, *25*, 7348-7359.

(329) Liu, S.; Ganti-Agrawal, S.; Keten, S.; Lueptow, R. M. Molecular insights into charged nanofiltration membranes: Structure, water transport, and water diffusion. *J. Membrane Sci.* **2022**, *644*, 120057.

(330) Huang, H.; Song, Z.; Wei, N.; Shi, L.; Mao, Y.; Ying, Y.; Sun, L.; Xu, Z.; Peng, X. Ultrafast viscous water flow through nanostrand-channelled graphene oxide membranes. *Nat. Commun.* **2013**, *4*, 2979.

(331) Chen, Y.; Zhang, G.; Liu, H.; Qu, J. Confining Free Radicals in Close Vicinity to Contaminants Enables Ultrafast Fenton-like Processes in the Interspacing of MoS2 Membranes. *Angewandte Chemie International Edition* **2019**, *58*, 8134-8138.

(332) Pandey, R. P.; Rasool, K.; Madhavan, V. E.; Aïssa, B.; Gogotsi, Y.; Mahmoud, K. A. Ultrahigh-flux and fouling-resistant membranes based on layered silver/MXene (Ti 3 C 2 T x) nanosheets. *J. Mater. Chem. A* **2018**, *6*, 3522-3533.

(333) Sheng, F.; Li, X.; Li, Y.; Afsar, N. U.; Zhao, Z.; Ge, L.; Xu, T. Cationic covalent organic framework membranes for efficient dye/salt separation. *J. Membrane Sci.* **2022**, *644*, 120118.

(334) Guo, Q.; Xu, M.; Tang, Q.; Liu, Y.; Zhang, W.; Guo, C.; Zhao, X.; Zhu, Y.; Ye, S.; Liu, D.et al. Advanced hybrid nanosheet membranes with stable nanochannels for ultrafast molecular separation. *npj Clean Water* **2023**, *6*, 38.

(335) Liu, M.; Chen, Q.; Lu, K.; Huang, W.; Lü, Z.; Zhou, C.; Yu, S.; Gao, C. High efficient removal of dyes from aqueous solution through nanofiltration using diethanolamine-modified polyamide thin-film composite membrane. *Sep. Purif. Technol.* **2017**, *173*, 135-143.

(336) Zhang, Y.; Zhao, K.; Zhang, Z.; Xie, H.; Li, Z.; Lin, Z.; Mo, C.; Yang, W.; Wang, X.; Wei, J. Polypropylene non-woven supported calcium alginate hydrogel filtration membrane for efficient separation of dye/salt at low salt concentration.

Desalination **2021**, *500*, 114845.

(337) Feng, X.; Yu, Z.; Long, R.; Sun, Y.; Wang, M.; Li, X.; Zeng, G. Polydopamine intimate contacted two-dimensional/two-dimensional ultrathin nylon basement membrane supported RGO/PDA/MXene composite material for oil-water separation and dye removal. *Sep. Purif. Technol.* **2020**, *247*, 116945.

(338) Chen, L.; Wang, W.; Fang, Q.; Zuo, K.; Hou, G.; Ai, Q.; Li, Q.; Ci, L.; Lou, J. High performance hierarchically nanostructured graphene oxide/covalent organic framework hybrid membranes for stable organic solvent nanofiltration. *Applied Materials Today* **2020**, *20*, 100791.

(339) Han, Y.; Xu, Z.; Gao, C. Ultrathin graphene nanofiltration membrane for water purification. *Adv. Funct. Mater.* **2013**, *23*, 3693-3700.

(340) Jia, F.; Yang, L.; Sun, L.; Yu, D.; Song, Y.; Wang, Y.; Kipper, M. J.; Tang, J.; Huang, L. Efficient separation of dyes using two-dimensional heterogeneous composite membranes. *Water Res.* **2023**, *247*, 120693.

(341) Osorio-Aguilar, D.; Saldarriaga-Noreña, H.; Murillo-Tovar, M.; Vergara-Sánchez, J.; Ramírez-Aparicio, J.; Magallón-Cacho, L.; García-Betancourt, M. In *Catalysts*, 2023; Vol. 13.

(342) Ramírez-Aparicio, J.; Samaniego-Benítez, J. E.; Murillo-Tovar, M. A.; Benítez-Benítez, J. L.; Muñoz-Sandoval, E.; García-Betancourt, M. L. Removal and surface photocatalytic degradation of methylene blue on carbon nanostructures. *Diam. Relat. Mater.* **2021**, *119*, 108544.